The Dissertation Committee for Nicholas Pacheco Dana Certifies that this is the approved version of the following dissertation:

Photoacoustic Image Guidance and Tissue Characterization in Cardiovascular Applications

Committee:

Laura Suggs, Supervisor

Stanislav Emelianov, Co-Supervisor

Andrew Dunn

James Tunnell

Richard Bouchard

Photoacoustic Image Guidance and Tissue Characterization in Cardiovascular Applications

by

Nicholas Pacheco Dana, B.S.; M.S.E.

Dissertation

Presented to the Faculty of the Graduate School of

The University of Texas at Austin

in Partial Fulfillment

of the Requirements

for the Degree of

Doctor of Philosophy

The University of Texas at Austin

December 2016

Acknowledgements

When work such as this comes to fruition, it is impossible acknowledge everyone who has made a worthy contribution. Still, the generosity of a several people stand out and deserve recognition.

I'd like to thank the colleagues I've worked with in the various ultrasound and biomaterials labs incarnations. Your support and assistance, as well as your patience and tolerance of my incoherent mumblings in our shared workspace, cannot be overstated. I'd also like to thank Tera Sherrard and Marissa Canales, whose friendship and diligence allowed this work to continue.

I'd like to thank Dr. Jason Cook, who has often been my unofficial mentor as I've stumbled along. I wish to thank Joshua Gray and Trevor Mitcham, for their help with work done far afield. For the inelegant composition before you, I'd like to thank Timothy Sowers, who has been a terrific boon composing this work.

Of course, I owe much to my committee members, Dr. Andrew Dunn and Dr. James Tunnell, for their tutelage and insight over the years. For Dr. Richard Bouchard, much thanks is owed as an early mentor of mine. To my advisors, Dr. Laura Suggs and Dr. Stanislav Emelianov, innumerable accolades are due. Their insight, gentleness, guidance and thoughtful mentorship have been gifts that cannot be adequately repaid.

Lastly, I wish to thank my many friends and loved ones, both present and absent. Heather's unending love and patience is forever an inspiration to me. The fidelity of my brother, Terry, and my sister, Sherry, of which I am undeserving and grateful. And lastly, for my son, Nathaniel, in whose hands I lay my legacy.

May this work serve as a testimony your collective contributions. Thank you.

PHOTOACOUSTIC IMAGE GUIDANCE AND TISSUE CHARACTERIZATION IN CARDIOVASCULAR APPLICATIONS

Nicholas Pacheco Dana, Ph. D.

The University of Texas at Austin, 2016

Supervisor: Laura Suggs

Co-Supervisor: Stanislav Emelianov

Collectively, cardiovascular diseases continue to be the leading cause of death, across nations and across decades. Improved diagnostic imaging methods offer promise to alleviate the morbidity associated with these diseases. Photoacoustic (PA) imaging is one such method, poised to make a significant impact on cardiovascular imaging, both as a research tool, as well as a clinical imaging modality. Offering the potential of molecular imaging in real-time, PA methods have been demonstrated in proof-of-concept studies tracking myocyte calcium dynamics. These results open the door to non-invasive longitudinal assessment of cardiac electrophysiological function, with implications for drug and contrast agent development. PA image guidance has also been extended to the characterization of cardiac radiofrequency ablation lesions. This method has been demonstrated to utilize endogenous chromophore changes resulting from ablation for the generation of depth-resolved tissue characterization maps, capable of assessing lesion extent. The technique has been subsequently validated by assessing high-intensity focused ultrasound ablation lesions in myocardium, with the hope for offering thermographic capabilities as well. While PA imaging offers such promise in cardiac ablation procedures, it is also in the process of clinical translation for image guidance and

characterization in coronary artery disease applications. Research has shown, using Monte Carlo optical modeling, that using a simple dual-wavelength PA imaging technique has great potential for successful visualization of atherosclerotic plaques across multiple tissue types and at clinically relevant multiple millimeters of depth. Collectively these results offer a suite of PA imaging tools with the potential for molecular and thermographic imaging across a broad range of cardiovascular applications.

Table of Contents

List of Tables

List of Figures

Chapter 1: Introduction To Photoacoustic Imaging For Cardiovascular Applications[1]

1.1 INTRODUCTION

Photoacoustic (PA) imaging (also called optoacoustic imaging) is a hybrid optical-ultrasound imaging modality that relies on optical excitation to generate ultrasonic waves in tissue. PA signal generation depends upon optical absorption, making PA imaging a molecular imaging modality. By observing PA pressure-transients using an ultrasound (US) system, and because PA signal generation relies only on absorbed photons, PA imaging is able to overcome the imaging depth limitations common to optical techniques that rely on ballistic photon propagation. It is also well suited to take advantage of the reduced optical absorption of tissues in the near-infrared (NIR), as well as to utilize various contrast agents for improved imaging. For these reasons it has become a promising medical imaging modality, with applications that include the evaluation of coronary heart disease (CHD), stem cell treatment monitoring, cancer diagnosis, and treatment guidance, just to name a few. For context, a brief history of PA imaging is provided in Appendix A.

This chapter serves to outline the contents of this dissertation and provide a foundation to understand the overall goals of the research presented. It begins with an outline of the fundamental physics involved in the production of a PA wave, followed by a brief examination of how the physics can be exploited to allow for specific techniques, such as molecular or thermographic imaging. The discussion of those techniques will pay particular attention to how they can apply to cardiovascular imaging applications and will segue into the main theme of this dissertation; PA imaging for cardiovascular image

[1] This chapter is adapted in part from a textbook chapter 'Overview of Photoacoustic Imaging' (Dana, Dumani, Cook, and Emelianov 2016). Nicholas Dana is the primary author of this textbook chapter.

guidance and tissue characterization. The two primary areas of PA cardiovascular imaging will be discussed; image guidance for cardiac electrophysiology (EP) studies and intravascular photoacoustic (IVPA) imaging for coronary artery disease. An overview of the research and goals that comprise Chapters 2, 3, 4 and 5 is provided. The chapter will conclude with a summary that will be expanded in Chapter 6 to address the limitations of this research, as well as directions of future studies.

1.2 PHYSICS OF PHOTOACOUSTICS

Several physical phenomena dictate the manner in which PA signals are generated and sensed. Due to photoacoustics being a hybrid imaging modality that relies upon light to generate a signal within the tissue, a strong understanding of light transport in tissue is necessary.

1.2.1 Optical Transport in Tissue

Before we can reliably utilize the photoacoustic effect for imaging, we first must have some understanding of light propagation in tissue. The Radiative Transport Equation (RTE, also called the Boltzmann Equation) is an analytical model to express the fluence (or fluence rate) within a given region or voxel. While this model is comprehensive in its treatment of wavelength (λ, [nm]), scattering ($\mu_s(\vec{r},\lambda)$, [cm^{-1}]), absorption ($\mu_a(\vec{r},\lambda)$, [cm^{-1}]), and anisotropy ($g(\vec{r})$, unitless), it is often very difficult to solve without considerable simplification. Below we will briefly discuss each term and what it represents in terms of optical fluence ($F(\vec{r},\lambda)$ [J/m^2]), as well as two common methods used to more easily elucidate the light distribution in tissue.

$$dP = -dP_{div} - dP_{ext} + dP_{sca} + dP_{src} \qquad \text{Equation 1}$$

In Equation 1, the term dP represents the change in power of the volume element dV within the solid angle dΩ (Figure 1). Power loss from beam divergence is accounted for by the term dP_{div}. The term dP_{ext} accounts for losses due to optical extinction, which includes absorption and scattering.

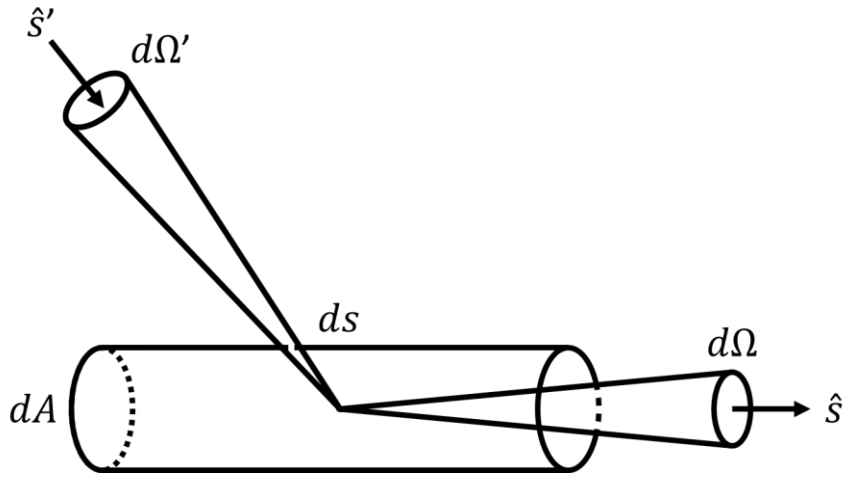

Figure 1.1: Diagram of infinitesimal volume of optically scattering and absorbing medium. For transiting photons $d\Omega$ and $d\Omega'$ represent outgoing and incoming solid angles, respectively, while $\hat{s}$ and $\hat{s}'$ represent outgoing and incoming vectors, respectively. The total volume $dV = ds \cdot dA$.

Gains due to photons scattered into dΩ from angle dΩ′ are represented by the scattering term dP_{sca}, while photons generated within dV are accounted for by the source term dP_{src}. This derives from energy conservation, which assumes a steady-state system (i.e. constant illumination source and time-independent optical parameters). By integrating over time, and all angles of dΩ′ and dΩ (and optical wavelength, for polychromatic sources), we can obtain an expression for fluence that accounts for optical energy delivered through a unit area at a given location. Often an exact solution to the RTE is unattainable and approximate solutions are needed. One such simplified solution, a diffusion approximation, treats photons as diffusing particles in a medium. It is less

accurate than the RTE (Andreas, Raymond, and Randall 1998), but more straightforward. Another alternative is to use Monte Carlo modeling to stochastically simulate photon transport. This typically yields more accurate results than diffusion approximations (Flock et al. 1989), but is more computationally demanding. For a thorough treatment of optical transport in tissue I direct readers to Wang and Wu, 2007 (Wang and Wu 2007).

1.2.1.1 Simplification of the Radiative Transport Equation

In typical PA applications, there is no internal source, and the external source can be easily characterized for energy output and beam divergence. This resolves part of the RTE, but, if absolute fluence is desired, absorption and scattering must often be approximated using methods mentioned above. Still, even if absolute fluence is unknown, semi-quantitative results may be obtained using relative differences in PA signal. These methods utilize spectroscopic PA (sPA, also called multi-wavelength PA) imaging, and often assume that fluence spatial-distribution varies little between wavelengths. That assumption relies upon $\mu_s(\vec{r},\lambda)$, $\mu_a(\vec{r},\lambda)$ and $g(\vec{r})$, remaining relatively constant across wavelength and time, and may not be valid for all applications.

1.2.2 Derivation of tissue-heating function

Once fluence has been accounted for, we can determine the energy deposited into a unit volume. The optical absorption coefficient represents the fraction of light that will be absorbed as it propagates. Thus, the product of fluence and optical absorption represents the fraction of absorbed light energy (Welch et al. 1989). It is treated as if this energy is entirely converted to heat, resulting in a tissue heating function ($F(\vec{r},\lambda) \cdot \mu_a(\vec{r},\lambda) = H(\vec{r},\lambda)$ [J/m^3]), which can be related to particle velocity of the acoustic medium-(u [m/s]) and pressure (p, [Pa]) of the medium.

$$\nabla u = -\frac{p}{\underbrace{\rho v_s^2}_{\nabla u_p}} + \underbrace{\beta T}_{\nabla u_T} - \frac{\gamma H}{\underbrace{2nc_L \rho v_s^2}_{\nabla u_{ER}}} \qquad \text{Equation 2}$$

$$\rho \frac{\partial^2 u}{\partial t^2} = -\nabla p \qquad \text{Equation 3}$$

1.2.2.1 Heating and Pressure-Velocity Relationship

Equations 2 and 3 represent the expansion equation and linear equation of motion, respectively. Equation 2 relates the spatial gradient of displacement (∇u) to individual contributions from pressure (∇u_p), thermal expansion (∇u_T) and electrostriction (∇u_{ER}), which is the process of displacement in dielectric materials in response to an external electric field. Equation 3 relates acceleration ($\partial^2 u/\partial t^2$) to the spatial gradient of pressure (∇p). This model assumes that displacements and particle velocities are small, and that the medium is acoustically isotropic and homogenous. For biological applications, electrostriction is typically several orders of magnitude less than the other terms (Tam 1986), and so is neglected. The model also ignores shear and volume viscosities, as well as shear elasticity. Other important parameters are mass density (ρ, [kg/m^3]), the linear thermal expansion coefficient (β, [K^{-1}]) and sound velocity (v_s, [m/s], $v_{H_2O} \approx 1480$ m/s, $v_{tissue} \approx 1540$ m/s).

$$\left(\nabla^2 - \frac{1}{v_s^2}\frac{\partial^2}{\partial t^2}\right) p = -\rho\beta \frac{\partial^2 T}{\partial t^2} \qquad \text{Equation 4}$$

By applying the gradient operator to Equation 3, combining that with Equation 2, and rearranging terms, we obtain Equation 4.

$$\frac{\partial T}{\partial t} = \frac{-k_{th}\nabla^2 T + H}{\rho C_p} \qquad \text{Equation 5}$$

Lastly, by relating temperature change to thermal conduction and heating through Equation 5 (Wang and Wu 2007), using thermal conductivity (k_{th}, [W/(m K)]) and specific heat capacity at constant pressure (C_p, [J/(kg K)]), we obtain the following expression for PA pressure which relates to energy deposition derived from optical transport:

$$\left(\nabla^2 - \frac{1}{v_s^2}\frac{\partial^2}{\partial t^2}\right)p = \frac{\beta}{C_p}\frac{\partial}{\partial t}(k_{th}\nabla^2 T - H) \qquad \text{Equation 6}$$

1.2.3 Photoacoustic Equation

A few conditions must be met in order for a significant PA signal to be generated. This is primarily a function of the laser pulse duration.

1.2.3.1 Thermal Confinement

Utilizing short-duration optical excitation is paramount to achieving efficient PA energy conversion. Tissue thermal conductivity governs the heat diffusion within the tissue. For length d_c, [m], the thermal relaxation time (τ_{th}, [s]) needed for a thermal gradient to diffuse across that length is:

$$\tau_{th} = d_c^2\frac{\rho C_p}{k_{th}} \qquad \text{Equation 7}$$

If the laser pulse duration (τ_p, [s]), is much less than thermal relaxation time ($\tau_p \ll \tau_{th}$), then very little absorbed energy can diffuse away from the absorbing region during excitation, making the heat "confined" to the absorber. When thermal confinement is satisfied, the Laplacian temperature term ($k_{th}\nabla^2 T$) is eliminated from Equation 6, and the pressure is solely a function of the heating term, as shown below. For a more detailed derivation, we refer to (Tam 1986) and (Wang and Wu 2007).

$$\left(\nabla^2 - \frac{1}{v_s^2}\frac{\partial^2}{\partial t^2}\right)p = -\frac{\beta}{C_p}\frac{\partial H}{\partial t} \qquad \text{Equation 8}$$

1.2.3.2 Stress Confinement

Another important parameter is the stress relaxation time (τ_{st}, [s]), which is the time needed for a pressure wave to propagate distance d_c, such that:

$$\tau_{st} = \frac{d_c}{v_s} \qquad \text{Equation 9}$$

When optical excitation is much quicker than stress relaxation ($\tau_p \ll \tau_{st}$) the system is said to be in stress confinement. In such a case PA pressure waves constructively interfere across the absorber region. The result is the equivalent of a Green's function solution to Equation 8 (i.e. a delta heating pulse) (Diebold and Sun 1994). Equation 8 therefore reduces to a straightforward expression for the peak pressure (p_0, [Pa]) immediately after optical excitation, often referred to as the PA equation.

$$p_0(\vec{r},\lambda,T) = \frac{\beta(T)v_s^2(T)}{C_p(T)}F(\vec{r},\lambda)\mu_a(\vec{r},\lambda) = \Gamma(T)F(\vec{r},\lambda)\mu_a(\vec{r},\lambda) \qquad \text{Equation 10}$$

The parameters β, v_s and C_p are often combined into a single term, the Grüneisen parameter ($\Gamma(T)$, unitless) and their temperature dependence is expressly written in Equation 10. This result outlines PA pressure dependence on fluence, optical absorption and temperature. Table 1.1 shows examples of thermal- and stress-confinement times using parameters for water.

Confinement condition	Absorber size			
	1 mm	30 μm	1 μm	100 nm
Thermal confinement (τ_{th})	70 s	60 ms	70 μs	700 ns
Stress confinement (τ_{st})	700 ns	20 ns	0.7 ns	70 ps

Table 1.1: Example thermal and stress confinement times for various absorber sizes. Represents the upper-limit of laser-pulse duration for optical excitation if ideal PA signal generation is to be achieved.

1.2.4 Photoacoustic Imaging Data

Figure 2 is a schematic of a typical PA imaging system and highlights the primary components. The resulting PA data is capable of providing an image, or map, of the tissue optical absorption. Recall that the PA signals are proportional to the product of the fluence and optical absorption. As such, spatial inhomogeneity in fluence can mask the underlying optical absorption information, which is of principal interest. For this reason it is desirable to spatially decouple optical absorption from fluence. If the fluence distribution can be accounted for using modeling or other methods (Cook, Frey, and Emelianov 2013), then more accurate quantitative PA (qPA) absorption estimates can be made.

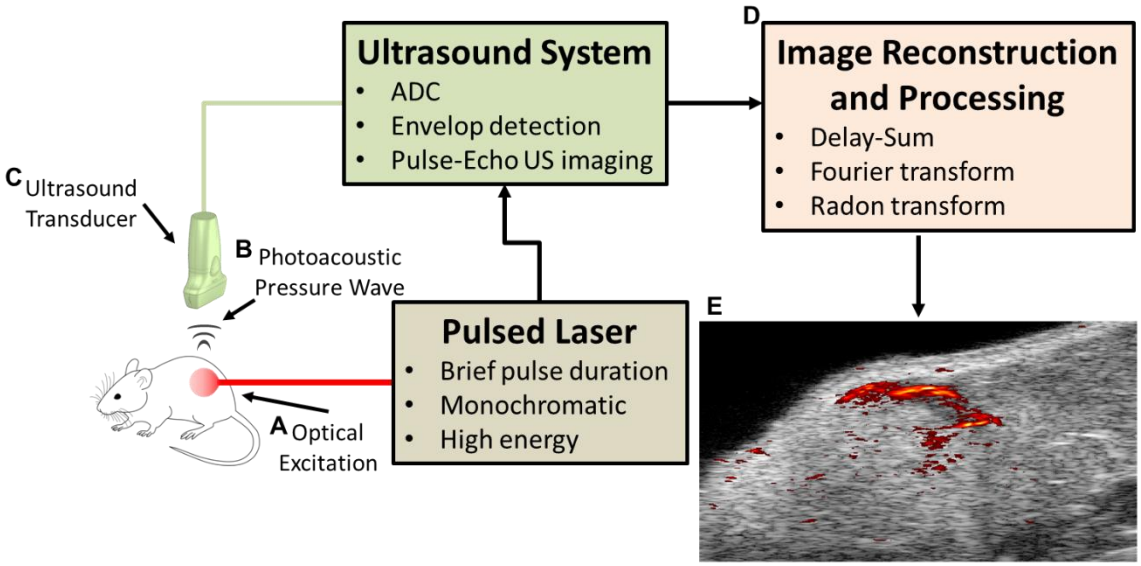

Figure 1.2: Example of typical PA imaging system components. Diagram highlights optical excitation (A), followed by generation of PA pressure waves (B), which are then received and digitized using a US transducer and system, respectively (C), before image reconstruction/processing (D) and final image rendering (E, showing combined US-PA image).

1.2.4.1 Molecular Imaging

As mentioned above, tissue optical absorption is the pertinent information that PA imaging is capable of supplying. Optical absorption is determined by the particular molecules present in tissue, which each contribute a unique spectrum capable of identifying the particular absorber, or chromophore. For this reason, PA imaging is a molecular imaging modality, and by properly leveraging PA imaging techniques, we can determine the particular molecular constituents which are present in a given tissue region.

For a given wavelength, the local optical absorption is the sum of the contribution from each individual absorber in the interrogated region of space, resulting in a function dependent on both wavelength and absorber concentration (Wang and Wu 2007), as shown in Equation 11:

$$\mu_a(\vec{r},\lambda) = \sum_{i=1}^{n} \mu_a^i(\vec{r},\lambda) = \sum_{i=1}^{n} \epsilon^i(\lambda) \cdot C^i(\vec{r}) = \sum_{i=1}^{n} \sigma^i(\lambda) \cdot N^i(\vec{r}) \qquad \text{Equation 11}$$

Where absorption ($\mu_a^i(\vec{r},\lambda)$, [cm^{-1}]) represents the individual contribution from the i^{th} chromophore. The product of molar absorptivity ($\epsilon^i(\lambda)$ [m^2/mol]) and molar concentration ($C^i(\vec{r})$, [mol/m^3]), and the product of optical cross-section ($\sigma^i(\lambda)$, [m^2]) and chromophore number ($N^i(\vec{r})$, [m^{-3}]) are equivalent expressions for absorption.

Because optical absorption represents a linear sum of chromophores, various techniques can be used to estimate concentration. sPA can be used to estimate chromophore concentration, provided fluence differences across wavelengths and time-dependent concentration changes can be accounted for, or are nearly negligible. If the fluence is absolutely known, then true concentration estimates can be made (Cook, Frey, and Emelianov 2013). Otherwise, concentration estimates are typically relative to one another. Either way, such information yields valuable insight into tissue function.

1.2.4.2 Thermosensitive Photoacoustic Response

As seen from Equation 10, the PA signal generation depends upon the Grüneisen parameter, which is comprised of temperature-dependent variables that are tissue specific and, together, lend PA imaging its temperature sensitivity.

Tissue Type (~37 °C)	ρ [g/cm^3]	C_p [J/(g K)]	v_s [m/s]
Muscle	1.07	3.6	1575 - 1590
Fat	0.95	2.3	1450
Liver	1.06	3.6	1590
Blood	1.06	3.8	1575
Water	0.99	4.2	1500

Table 1.2: Typical thermal and acoustic properties for various tissue types.

Table 1.2 highlights typical physical properties for select tissue types measured at 37°C (Duck 1990b, 1990a). Note that lipid-based tissues exhibit markedly distinct thermal and acoustic properties from most other tissue types. Specific heat capacity and speed of sound values typically vary by less than 5% across tissue types in the temperature range of 20 – 70 °C, which is not the case for thermal expansion. The thermal expansion coefficient of water varies from 0 [K^{-1}] at 4 °C to 5.85×10-4 [K^{-1}] at 70 °C, and is approximately linear in this range. The Grüneisen parameter for water-based tissues is often approximated using the behavior of water, and an empirical formula has been derived for temperatures measured in degrees Celsius (Oraevsky, Jacques, and Tittel 1997).

$$\Gamma(T) \approx 0.0043 + 0.0053 \cdot T \qquad \text{Equation 12}$$

Due to the large temperature dependence of the Grüneisen parameter, the PA signal amplitude is coupled to temperature. Once a baseline tissue PA signal is measured at a known temperature (usually assumed to be body temperature), changes in tissue temperature can be remotely observed by comparing PA signals to baseline. This temperature dependence operates independent of wavelength and can be used to estimate changes in tissue temperature (Irina, Kirill, and Rinat 2005; Shah et al. 2008).

Additionally, the Grüneisen temperature dependence of lipid-based tissues is opposite that of water-based tissues in the physiologic range and has been used to characterize tissues based on lipid content (Wang and Emelianov 2011). Thus, thermosensitive PA imaging has great utility for tissue characterization and image guidance.

1.3 PHOTOACOUSTIC IMAGING TECHNIQUES

Due to the hybrid nature of photoacoustic imaging, as well as the sensitivity of the modality to multiple tissue parameters, there exist several different approaches to generating a desirable image. These approaches can vary in which chromophore of interest is being imaged (e.g. exogenous vs. endogenous chromophores), how those chromophores are visualized (e.g. single-wavelength vs. multiple-wavelength acquisition) as well as how the system is configured in order to acquire image data (e.g. single-element vs. element-array implementations). Often it is preferable to combine multiple techniques in order to optimize contrast, resolution or sensitivity (e.g. contrast-enhanced spectroscopic imaging using a 1D array transducer). What follows is a brief discussion of common techniques and what insight each may offer.

1.3.1 Photoacoustic Contrast Agents

Because photoacoustic contrast is based on optical absorption, useful information can be gleaned both from visualizing the distribution of endogenous chromophores, as well as tracking signal from exogenous contrast agents. The most commonly imaged endogenous chromophore is hemoglobin, but other absorbers of interest include melanin, and lipid, while common exogenous absorbers include dyes, porphyrins, and nanoparticles (NPs). The ideal contrast agent will have a strong, spectrally unique NIR absorption. Furthermore, exogenous agents must be bio-compatible, stable, and easily cleared or degraded through normal metabolism. Development of agents with said

attributes is an intense area of research (Wang, Chuang, and Ho 2012). Figure 1.3 illustrates the absorption spectra of common tissue components and contrast agents.

1.3.1.1 Hemoglobin Imaging

Hemoglobin-variants (i.e. Hb and HbO2) exhibit distinct optical absorption spectra in the NIR regime up to approximately 1100 nm, at which point the absorption of water begins to dominate and hemoglobin variants appear indistinguishable. As such, sPA imaging can be used to determine SpO2 by comparing spectroscopic data to Hemoglobin spectra (Prahl 1999; Wang et al. 2006) to determine the relative amounts of oxygenated vs. deoxygenated hemoglobin. Since oxygenation has been closely linked to tissue function and disease state, Hb has become the most utilized endogenous absorber for PA imaging applications. While Hb absorption can confound imaging with exogenous contrast agents, studies have shown that proper wavelength and/or contrast agent selection can be done to optimize combined Hb and exogenous contrast imaging (Kim et al. 2011).

1.3.1.2 Plasmonic Nanoparticle Agents

For noble metals, optical properties are determined by their degree of electron confinement, which is strongly influenced by their dimensions (El-Sayed 2001). Gold and silver NPs can exhibit surface-plasmon resonance (SPR), a phenomenon where the electronic state can strongly couple across the surface of the particle. This result allows for the electrons to oscillate coherently at particular frequencies which happen to correspond to NIR optical frequencies. This results in highly efficient optical absorption and scattering at the resonant frequency, which is dependent upon the particle geometry and can be selected for by varying particle size and shape (Kelly et al. 2003). Additionally, many surface modification protocols exist for NPs. As such, they can be

functionalized to improve cytotoxicity, circulation time, stability, aggregation prevention, and enable molecular-specific targeting (Niidome et al. 2006; Kumar, Aaron, and Sokolov 2008). NPs as PA contrast agents have been synthesized in a variety of geometries, including nanospheres (NSs) (Ji et al. 2007), nanorods (NRs) (Nikoobakht and El-Sayed 2003), nanoshells (Xiang et al. 2006) and nanocages (Chen et al. 2005), with absorption peaks ranging from 500 – 1100 nm and sizes from 2 – 200 nm. These represent just a few of the potential NP configurations.

As mentioned above, when the electron clouds of plasmonic NPs in close proximity can interact. This coupling affects the resonant frequency of oscillating electrons, and can result in spectral changes in absorption and scattering. This can be exploited to detect physiological events in tissue, such as aggregation due to changes in endocytosis (Nam et al. 2012), temperature (Zhao et al. 2011) and pH (Wu et al. 2010). The podocytes, which are responsible for glomerular filtration, are typically separated by a covered filtration slit roughly 25–60 nm wide (Haraldsson, Nyström, and Deen 2008). As such, particles smaller than 5 nm have been shown to clear the body through renal filtration, whereas larger particles are sequestered by the reticuloendothelial system, leading to accumulation in the liver and spleen (Longmire, Choyke, and Kobayashi 2008). Unfortunately, reducing particle size, which improves renal clearance, tends to limit particle tunability and functionalization. Biodegradable clusters of small NPs may be a solution. This approach aims to solve the clearance issue while maintaining particle function and facilitating translatability of NPs and potential FDA approval (Yoon et al. 2012).

1.3.1.3 Non-plasmonic Nanoparticle Agents

Non-plasmonic NPs can exhibit strong optical absorption in the NIR regime, and because they do not exhibit the characteristic spectral shifts at high densities that occur with plasmonic-coupling particles, they can be useful in many applications (Cook, Frey, and Emelianov 2013). In addition, they can have distinct features like super-paramagnetism and broad absorption spectra, opening up applications that would otherwise be unavailable using plasmonic NPs alone. Materials include carbon-sheets, iron oxide, and copper sulfide. Unfortunately, many of these particles share the same biocompatibility and clearance concerns as mentioned previously, requiring careful synthesis.

Single-walled carbon nanotubes (SWNTs) exhibit a broad absorption spectrum that allows imaging with optical, NIR, and microwave radiation (Pramanik et al. 2009). Generally speaking, broad absorption is problematic for spectral unmixing techniques, but SWNTs can be conjugated with dyes to considerably enhance absorption at particular wavelengths (Zerda et al. 2010). Super-paramagnetic iron oxide nanoparticles (SPIONs) have been used for quantitative PA microscopy where plasmonic coupling from NPs would otherwise produce non-linear results (Cook, Frey, and Emelianov 2013). SPIONs exhibit magnetic properties, which can be useful both for targeting the particles to a particular region, through the use of localized magnetic fields, as well as a multimodal imaging contrast agent. However their poor NIR optical absorption makes them undesirable solo-contrast agents for most PA applications. SPIONs are currently the only FDA-approved medical imaging NPs for human use (Tassa, Shaw, and Weissleder 2011). Alternatively, copper sulfide nanoparticles have been synthesized in small sizes around 10 nm with strong NIR absorption peaks (Ku et al. 2012). Their ease of synthesis and

relative low cost represents an advantage compared to other NP systems (Goel, Chen, and Cai 2014).

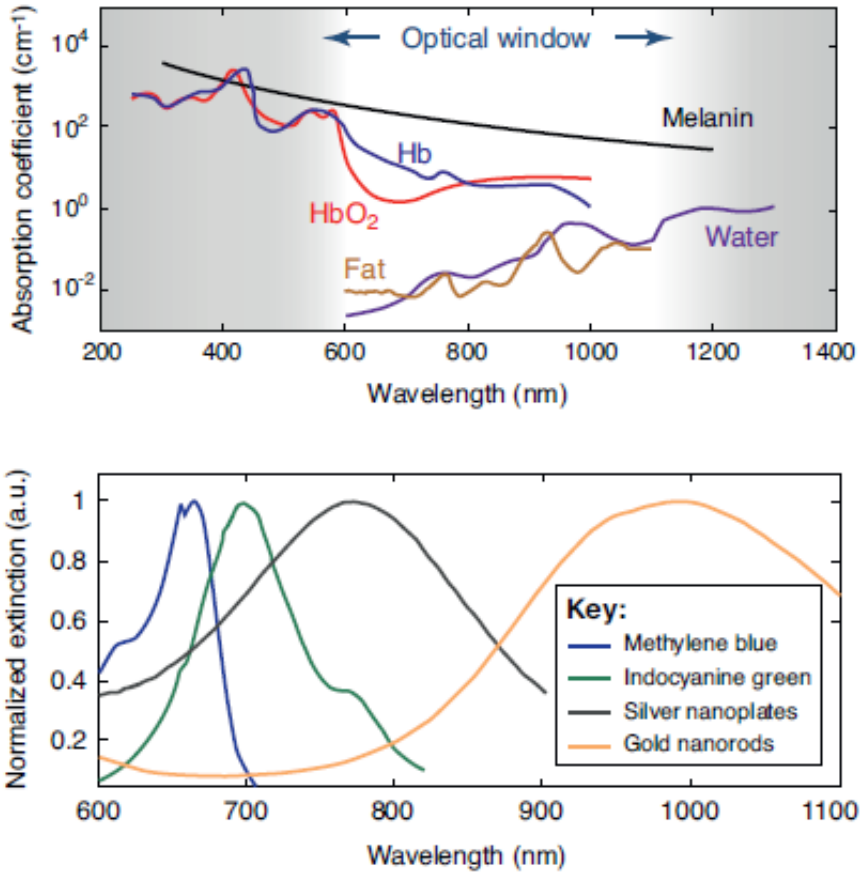

Figure 1.3. Absorption (top) and normalized extinction (bottom) spectra of some common tissue components and contrast agents. (Partially reproduced from (Mallidi, Luke, and Emelianov 2011)).

1.3.1.4 Dye-based Contrast Agents

Dyes are typically small molecules and offer advantages such as rapid clearance and biocompatibility over other contrast agents. They can also be molecularly targeted (Bhattacharyya et al. 2008) or combined with other particles for increased absorption, stability, targeting or delivery capabilities (Akers et al. 2010; Zerda et al. 2010). A variety

of dyes absorbing in the NIR have been used for PA and combined PA-fluorescence imaging (Kim et al. 2010). While dyes possess many advantages over other agents, they exhibit molar absorption values several orders of magnitude lower than other NPs (Jain et al. 2006), and they are susceptible to photo-bleaching (Laufer, Zhang, and Beard 2010).

Indocyanine green (ICG) is a fluorescent dye extensively explored for PA imaging. It has been embedded in NPs for cancer-specific targeting (Kim et al. 2007) and encapsulated in nanodroplets (NDs) for multimodal imaging (Hannah et al. 2013). ICG's spectral absorption varies with concentration and environment, and may be exploited to track dynamic changes (Rajian et al. 2011).

1.3.2 Tomographic and illumination methods

Just as the imaging target will dictate what endogenous or exogenous chromophores are of interest, so too will it determine the optimal PA imaging setup for a particular application. The two actions that must be performed to gather PA information, pulsed light delivery and acoustic reception, can be accomplished in several different ways. Typically, pulsed lasers come in one of three varieties: mode-locking lasers (pulse duration $\leq$ 10-10 s), pulsed LEDs (pulse duration $\geq$ 10-9 s), and Q-switching lasers (pulse duration $\approx$ 10-9 s). As previously stated, PA pressure intensities are largest when both stress and thermal confinement are satisfied. Therefore, mode-locking lasers would theoretically generate the highest PA signals. However, the optical linewidth (also called spectral bandwidth) generated from mode-locking lasers is very broad due to the inverse time and frequency domain relationship. Mode-locked lasers also typically have lower overall pulse energies (pico- to nano-Joules). For these reasons, mode-locked lasers are sub-optimal for PA applications. Some PA systems utilize pulsed LEDs; however, the pulse energies of these light sources is also typically low (nano- to micro -Joules),

limiting their use to applications such as needle and biopsy guidance, where high absorption is assured. Therefore, the bulk of PA imaging applications utilize nanosecond Q-switching lasers capable of milli-Joule or greater pulse energies, with typical pulse-repetition rates of 10s of Hertz.

Because the pressure waves are acoustic, PA acquisition can be performed using current US technology; however, instead of an ultrasonic pulse-send and subsequent echo-receive, the "pulse" is performed by optical excitation and the US system is used only for the acoustic receive. Because of their similarities, PA imaging can be implemented using a single element, a 1-D array, or even a 2-D array, as is the case for US imaging.

1.3.2.1 Single-element solutions

The most basic receiver is a single element transducer. This type of receiver measures PA signals along a single line, analogous to an US A-line. In order to produce an image, the transducer must be moved to acquire multiple A-line positions and ultimately form an image. Although primitive and cumbersome, single element transducer systems are used in some applications today - the most common being intravascular photoacoustic (IVPA) imaging. Single elements are advantageous here because they can be made very compact, despite the mechanical components required to move the single element. For IVPA applications a single element transducer is combined with a small fiber optic (FO) cable used for light delivery. Images are formed by rotating the element and FO cable and acquiring US amplitude-lines (A-lines) at several rotational positions (Karpiouk, Wang, and Emelianov 2010). The A-lines can be used to then reconstruct a traditional brightness-mode (B-mode) US-PA image, as shown in Figure 1.4. IVPA imaging receivers can be rotated extremely fast (1000s of revolutions per

minute) enabling the potential for real-time imaging. This form of imaging will be discussed in greater detail in Chapter 4.

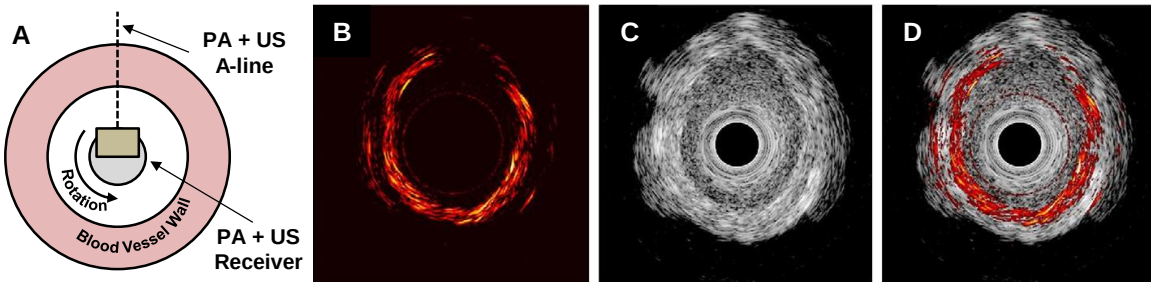

Figure 1.4. Schematic of IVPA catheter inside of the blood vessel (A). The catheter rotates inside of the blood vessel and captures a PA and US A-line at multiple positions. A-lines are used to provide a PA image (B), an US image (C), then overlaid for a co-registered PA/US image (D). Adapted from (Wang et al. 2012b; Dana, Dumani, et al. 2016).

1.3.2.2 One-dimensional Array Transducers

The vast majority of PA applications utilize 1-D array receivers because they do not require moving parts to render 2-D US or PA images. Linear-array PA transducers are very similar to ultrasound transducers in that there is a linear-array of piezoelectric elements, allowing multiple simultaneous received positions and more sophisticated image processing (e.g., beamforming) to render higher quality images. To provide the illumination, optical fibers are placed around the transducer elements in order to optimize light delivery within a particular region of the imaging plane. In addition to real-time 2-D B-mode images, linear array PA transducers can also be used to generate 3-D image volumes by mechanically translating the array orthogonal to the imaging plane (Hoelen and de Mul 2000). The resulting data set is a 3-D image stack, comparable to what is generated using X-ray computed tomography (CT) or MRI imaging systems. Resolution in the elevational dimension (i.e. the dimension of array translation) is limited by

transducer element elevational-size in that dimension, though poor spatial sampling can further reduce resolution. This is an example of photoacoustic tomography (PAT)

1.3.3 Photoacoustic Microscopy Methods

Unlike US imaging, PA imaging is not limited to the macroscale. PA microscopy (PAM) typically uses a single-element receiver and interrogates the tissue using highly focused light. Because PA signals are generated only in the light's focal zone, optical resolution can be achieved, provided optical scattering is minimized. Like optical imaging, PAM is limited to superficial structures. Microvasculature and superficial pathology can be easily visualized and characterized (Wang 2009; Zhang et al. 2009). Because the resolution is subcellular, there is potential to detect in-vivo circulating tumor cells (CTCs, indicators of metastasis and disease aggression) for more accurate staging of cancer (Galanzha et al. 2009; Weight et al. 2006; Hu et al. 2013; Wu et al. 2014), or to monitor highly localized cellular activity (Dana, Fowler, et al. 2016). In addition, quantification of absorbers can be performed with PAM, allowing for accurate molecular imaging and the potential for in-vivo histology (Cook, Frey, and Emelianov 2013). Examples of PA microscopy systems and images are shown in Figure 1.5.

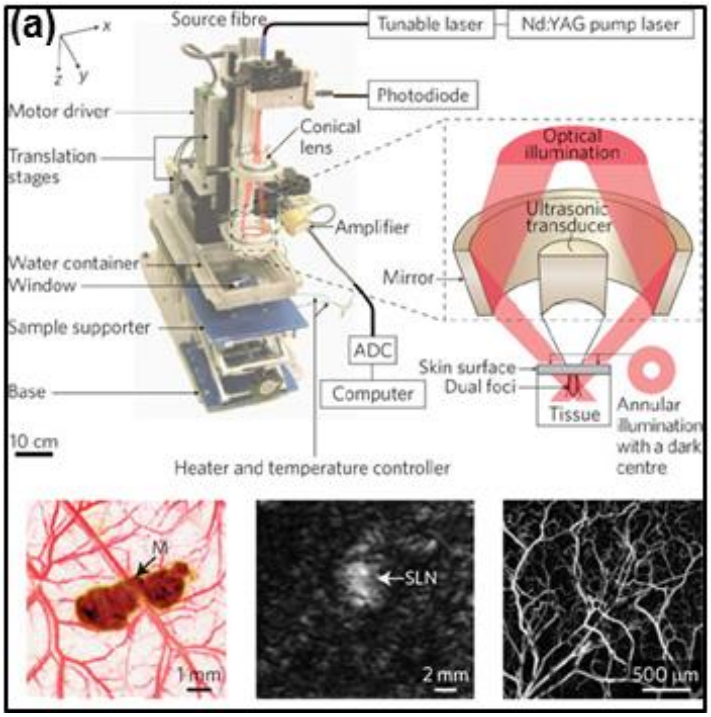

Figure 1.5. Examples of PA microscope systems. Adapted with permission from (Wang 2009).

1.3.4 Spectroscopic and Multiplex Photoacoustic Methods

As discussed in above, the total optical absorption spectrum of a region is the linear sum of all the absorbers therein. As such, if the chromophore spectra are sufficiently distinct (i.e. they can be easily distinguished, such as that of oxygenated and deoxygenated Hb at certain wavelengths), then sPA methods can be leveraged to estimate the concentration (relative or absolute) of each absorber. Such techniques typically require statistical methods, such as linear regression, to spectrally unmix the individual contributions in the overall PA image. This is commonly called multiplex imaging.

Multiplex imaging represents the most versatile application of sPA imaging, as it has the capacity to distinguish multiple chromophores of interest in the field of view (FOV). This technique can be used with endogenous chromophores to estimate oxygen

saturation percentage (SpO2) (Wang et al. 2006), or with exogenous contrast agents, to identify the presence of multiple contrast agents in a single FOV (Bayer et al. 2011), as shown in Figure 1.6.

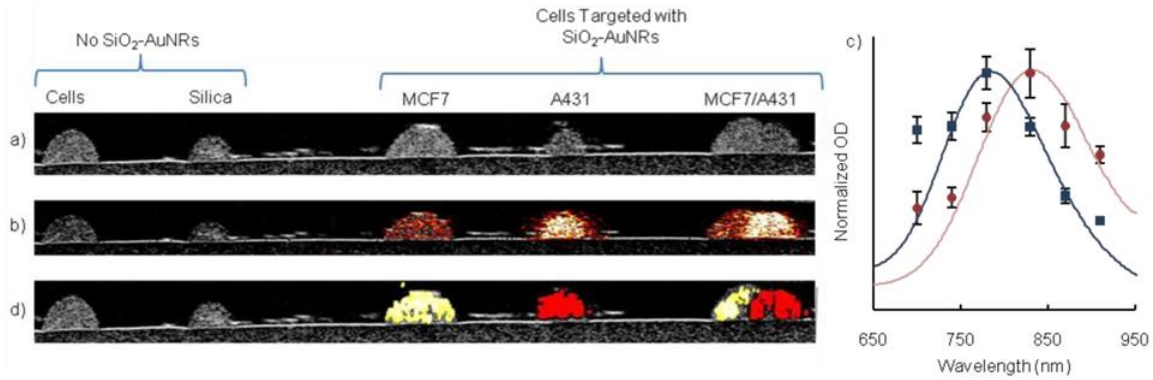

Figure 1.6. US image of phantoms containing inclusions with cells loaded with silica-coated gold NRs (SiO2-AuNRs, a). US image overlaid with 830 nm PA image (b). Plot of PA spectra (points) and UV-Vis (lines) of two SiO2-AuNRs contrast agents tuned to have peak absorptions at 780 nm (blue) and 830 nm (red, c). Molecular map of cells overlaid on US image with inclusions containing either 830 nm SiO2-AuNRs (red), 780 nm SiO2-AuNRs (yellow), or both, after processing multi-wavelength PA data using correlation analysis (d). Figure adapted with permission from (Bayer et al. 2011).

Proper wavelength selection is paramount for reliable spectral unmixing of multiplex PA image data (Luke, Nam, and Emelianov 2013). If wavelengths are selected that do not adequately differentiate chromophores of interest, then spectral unmixing algorithms may yield ambiguous results. With respect to absorption, exogenous contrast agents used for multiplexed PA imaging should be spectrally distinguishable from one another and from endogenous chromophores, such as Hb or lipids. Refer to Figure 1.3 for the spectra of common chromophores.

1.3.5 Multimodal Photoacoustic Imaging

PA imaging is a hybrid imaging modality, making it well suited to incorporate additional imaging functionality. There are several benefits to the addition of optical or ultrasonic capability. Often though, this requires careful design to balance the needs of multiple imaging modalities. Accommodating these conflicts can pose considerable engineering challenges; still, several attempts have been made toward the realization of synergistic multi-modal PA imaging.

1.3.5.1 Combined Photoacoustic-Ultrasound Imaging

US imaging makes an ideal candidate for integration with a PA imaging system as it can use the same components for US detection as are used for PA detection, making the two datasets inherently co-registered. Image reconstruction for both modalities can also be performed using the same hardware and software, making combined PA and US based imaging relatively straightforward and reducing the hardware costs.

Because US imaging is sensitive to tissue mechanical properties (Szabo 2004), the information provided by US imaging is complementary to PA data. Traditional pulse-echo US reconstructs an image of backscattered US energy resulting from acoustic impedance variations within the tissue (Szabo 2004). This is commonly called US B-mode imaging and provides good morphological and structural information to complement the molecular-based PA imaging data. Examples can be seen in Figures 1.2, 1.4 and 1.6.

1.4 Cardiovascular Applications of Photoacoustic Imaging

Cardiovascular medicine has benefitted from US imaging for decades and thus the introduction of PA to the clinically familiar imaging modality was a natural extension of the new technology. The three primary applications of US imaging in the cardiovascular

realm are: echocardiography, the assessment of cardiac function; intravascular ultrasound (IVUS) for the detection and image guidance of vulnerable plaque in coronary heart disease (CHD); and vascular ultrasound for the diagnosis and staging of peripheral and carotid artery disease. Though some research has explored applying PA imaging to the problem of peripheral and carotid artery disease (Kruizinga et al. 2014), the vast majority of research has focused on the development of intravascular photoacoustic (IVPA) imaging of coronary arteries (Su, Wang, and Emelianov 2009; Wang et al. 2010; VanderLaan et al. 2014; Yeager et al. 2014; Jansen, van der Steen, et al. 2014; Jansen, Wu, et al. 2014; Abran et al. 2014; Wang et al. 2012b), though studies have investigated the potential of using PA imaging for image guidance and tissue characterization purposes in cardiac arrhythmia applications (Dana et al. 2014; Dana, Fowler, et al. 2016; Gray et al. 2015).

1.4.1 Overview of Cardiac Arrhythmia

The heart is unique in that it is a vital organ that relies on automatic electro-mechanical (also called excitation-contraction) coupling to function. Cardiac electrophysiology (EP) function differs from that of skeletal muscle in that calcium ions (Ca) play a vital role in both cardiac cell automaticity (the ability of cardiac cells to spontaneously depolarize) and the propagation of action potentials across cells. Normal cardiac rhythm functions as follows (Fogoros 1999):

- The resting membrane potential in the cell is disrupted by changes in the ion concentration within the cell, such that the threshold to reach an action potential is reached.

- Triggering of an action potential (Phase 0) results in a rapid change in cytosolic ion concentration, causing rapid depolarization (~ 10 ms) from the resting membrane potential of the cell (-90 mV) to the action potential (+50 mV).
- The rapid depolarization of the action potential completes, resulting in a slight decrease in membrane potential as the initial ion channels close and new ones open (Phase 1).
- The action potential is maintained by the delayed and sustained opening of ion channels, which causes the membrane potential to plateau for approximately 150 ms (Phase 2). This phase differs from typical neuronal or skeletal muscle electrophysiological function.
- The resting membrane potential repolarizes as ion channels and ion pumps restore the normal electro-chemical gradient of the cell (Phase 3).
- The myocyte stays at its normal resting membrane potential (Phase 4) until an action potential is initiated either through leaky ion channels within the cell itself (automaticity of cardiac cells) or through the propagation of electric potentials from neighboring cells.

The initial rapid depolarization of a cardiac cell occurs from the voltage-gated opening of sodium (Na) channels, allowing Na influx into the cytosol and increasing the membrane potential during Phase 0. Phase 1 represents the closure of Na channels and the delayed opening of voltage-gated potassium (K) and chlorine (Cl) ion channels. Phase 2, which is unique to cardiac cells, is typified by the protracted opening of Ca ion-channels which allows for the protracted influx in cytosolic Ca, which changes Ca concentration by several orders of magnitude. Ca influx itself induces further Ca release from intracellular stores, which helps account for the magnitude and duration of Ca cytosolic concentration changes. Ca is responsible for electro-mechanical coupling within

the myocardial cell, for the prolonged duration of Phase 2 (which determines the cell refractory period) and also plays a role in conducting the action potential between adjacent cells via gap junctions. Resting membrane potential is restored during Phase 3 largely by the cytosolic efflux of K and influx of Cl, which result in a net increase of negative ions within the cytoplasm which restore the membrane potential. Figure 1.7 details the entirety of the myocardial action potential and the ions associated with each phase.

Normally, all cardiac cells exhibit automaticity and have the potential to auto-induce membrane depolarization, known as the pacemaker potential. Therefore, the cells with fastest "clock" will determine the cardiac rhythm, as their depolarization initiates action potentials in neighboring cells and propagates a depolarization wave throughout the myocardium. In normal sinus rhythm (NSR) the pacemaker cells of the sino-atrial (SA) node exhibit the most rapid spontaneous depolarization, occurring approximately 50-60 times a minute under normal conditions, though this can vary considerably across individuals and is heavily influenced by the sympathetic and parasympathetic nervous system. The SA node determines the heart rate, and initiates depolarization that propagates; first through both atria, then onto the atrio-ventricular (AV) node (where there is a slight pause), then down through the bundle of His in the ventricular septum, and finally through the Purkinje fibers in the ventricular walls. The depolarization is followed by mechanical contraction of myocytes that results in the pumping action of the heart. This process relies on cytosolic Ca to unlock binding sites on actin filaments so that myosin fibers may engage them to initiate contraction (Lehman, Craig, and Vibert 1994), thus allowing electro-mechanical coupling within the cell.

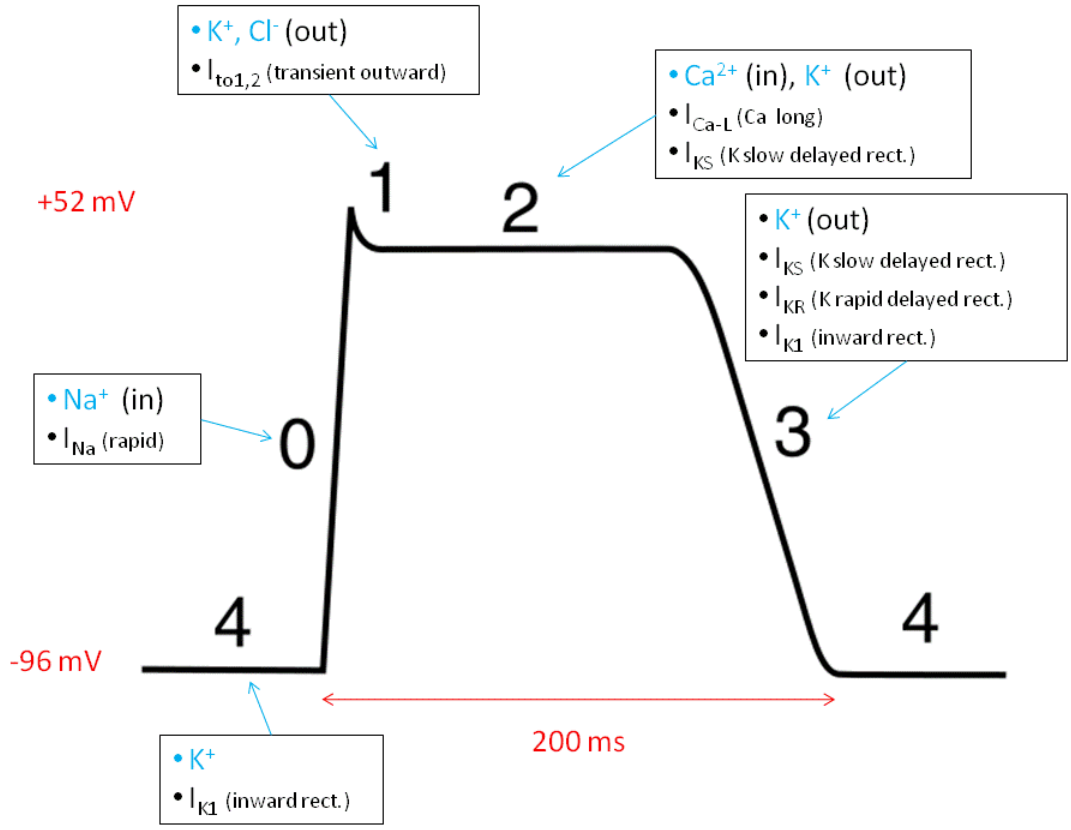

Figure 1.7. Diagram of cardiac action potential and ion fluxes that result in myocardial depolarization and repolarization. Provided by (Wikipedia.org 2016).

1.4.1.1 Atrial Fibrillation

Cardiac arrhythmia occurs when NSR is disrupted. This can occur when non-SA node pacemaker cells, often referred to as ectopic foci, usurp the pacemaker role of the SA node and initiate depolarization signals to adjacent cells. This is the case with atrial fibrillation (AF), the most common arrhythmia encountered clinically (Mozaffarian et al. 2015). During AF, ectopic foci, typically located around the pulmonary veins in the left atrium, initiate arrhythmogenic electrical signals which disrupt NSR in the atria (Pappone et al. 2000). The result is disorganized electrical propagation throughout the atria. This prevents orderly contraction of the atria and undermines the ability of the heart to

properly fill the ventricles. Patient experiences of AF vary; for some, the result may be minor and go unnoticed, while other patients experience severe debilitation or fatigue (Mozaffarian et al. 2015). Regardless of patient experience, AF carries significant risks for other cardiovascular diseases, such as stroke and coronary heart disease (CHD) (Mozaffarian et al. 2015). AF is treated both with antiarrhythmic drugs, as well as with surgical intervention.

1.4.1.2 Current State of Atrial Fibrillation Treatment

Currently antiarrhythmic drugs represent the first line of treatment for AF, as well as other arrhythmias (Santangeli et al. 2011). Unfortunately, many of these drugs are burdened with either poor efficacy, severe side-effects, or both (Santangeli et al. 2011). Only approximately 1 in 4 AF sufferers is able to maintain NSR using only antiarrhythmic drugs (Mozaffarian et al. 2015). For most AF patients a minimally invasive surgical procedure, trans-catheter ablation (TCA), represents the best opportunity for long-term maintenance of NSR. This procedure introduces one or more catheters into the patient's body, typically through the femoral veins. The catheters are then directed to the heart, penetrate through the atrial septum (if needed) and apply some form of energy (radiofrequency (Petersen, Chen, Pietersen, Svendsen, and Haunso 1999), focused US (Mitnovetski et al. 2009) or cryoablation (Tse et al. 2003)) to destroy the offending tissue that is initiating or maintaining arrhythmia. Unfortunately, due to limitations of current image guidance tools, the efficacy of these procedures varies greatly (Shah 2011).

1.4.2 Image Guidance for Cardiac Arrhythmia Procedures

Currently echocardiography (either trans-esophageal or intracardiac) (Marrouche et al. 2003) and fluoroscopy are the primary imaging modalities used during TCA

procedures, although pre-procedural MRI or CT scans can be used to generate the 3D cardiac anatomy for reference. Electro-anatomical mapping systems can also be used to reconstruct the cardiac geometry in interactive software, as well as tag locations with electrocardiogram measurements (Natale et al. 1998). While these systems are useful for visualizing cardiac geometry and structure, they cannot reliably characterize the cardiac tissue (Shah 2011), which is necessary to determine if the desired therapeutic endpoint has been achieved. Investigations into potential imaging techniques is underway to address these limitations, one of which involves PA image guidance.

1.4.2.1 Visualization of Myocyte Depolarization

In order to reconstruct the spatio-temporal propagation of depolarization within the myocardium, physicians must make some measurement of the electric potential at different positions and time-points in the tissue. During electrophysiology (EP) studies of AF physicians typically do this by navigating a catheter to different sites within the heart and measuring the electric field with the catheter-tip electrode while simultaneously measuring the time with respect to the pulse at the SA node. The catheter position is recorded by an electro-anatomical mapping (EAM) system, which can attempt to reconstruct electrical depolarization once a sufficient number of measurements have been made (Natale et al. 1998). Cardiac tissue is typically represented as a 2D surface in the 3D model space and electrical propagation is projected onto that 2D surface. A similar method could be used in a laboratory setting to examine animal EP function for assessing novel pharmacotherapeutics. Unfortunately, measurements of electric potential integrate the EM field over the volume surrounding the electrode and typically provide only a coarse map. A method to visualize EP function with improved resolution and that is sensitive to 3D position may provide useful insight into cardiac EP and

pharmacotheraputic function. Photoacoustics may be able to add insight so as to provide quantitative results that can be scaled from cell studies up to animal studies.

1.4.2.2 Tissue Characterization for Guided Cardiac Ablation Procedures

Once the offending tissue is identified, physicians can then target the tissue for destruction via catheter ablation. Ablation treats arrhythmia by generating non-conductive lesions within the tissue that disrupt or isolate arrhythmogenic signals. If durable lesions aren't generated (i.e. if lesions aren't transmural and contiguous) then the risk that the ablated tissue will recover electrical conductivity becomes high, which could render the procedure ineffective. Alternatively, if too much energy is applied, then the risk of damage to peripheral tissues, as well as complications such as cardiac tamponade, increase (Mozaffarian et al. 2015; Go et al. 2013). As such, it is vital to monitor the tissue temperature and function to achieve optimal results (Shah 2011). Physicians currently lack a reliable method to characterize the ablation substrate to determine when a durable lesion has been generated (Shah 2011). PA imaging is being studied as a means to address this deficiency.

1.4.2.3 Thermographic Visualization for Ablation Temperature Monitoring

Despite the safety of TCA, potentially fatal complications can arise from the procedure. Atrioesophageal fistula, which describes a fissure between the left atrium and the esophagus, is still a particular danger for AF ablation procedures (Chavez et al. 2015), as the esophagus lies directly posterior to the left atrial pulmonary veins. Another potential complication that may arise from TCA is cardiac tamponade, which occurs from bleeding into the pericardial sack, and can be caused from mechanical trauma or from overheating that generates a steam pocket that ruptures the atrial wall (Hsu et al. 2005). Partially in an attempt to limit such complications, physicians will often monitor catheter-

tip temperature. Studies have shown that catheter-tip temperature monitoring improves lesion durability, but can also increase the rate of complication, as catheter-tip temperature is loosely correlated with tissue temperature (Schwartzman et al. 2001). Direct monitoring of tissue temperature would likely both improve TCA efficacy and reduce complications (Shah 2011). The temperature sensitivity of PA and US based techniques suggests such a method may be able to provide thermographic image guidance during procedures in addition to tissue characterization (Pramanik and Wang 2009; Chitnis et al. 2010; Dana et al. 2014; Dana 2014).

1.4.3 Overview of Coronary Heart Disease

In 2015 an estimated 635,000 Americans experienced a new coronary event linked to coronary artery disease, with an American experiencing a myocardial infarction approximately every 43 seconds (Mozaffarian et al. 2015). This emphasizes the impact that coronary heart disease (CHD) places on our healthcare system. As such, visualization of coronary arteries represents an arena where the recent advent of high-resolution molecular imaging modalities shows particular promise to have significant impacts (MacNeill et al. 2003; Sanz and Fayad 2008).

1.4.3.1 Summary of Coronary Heart Disease

At its heart (pun!) CHD is typified by the buildup of lipid and cholesterol deposits, or atherosclerotic plaques, on the lumen of the coronary arteries. This buildup can lead to stenosis of the artery, which can impede the supply of oxygenated blood to myocardial tissue downstream of the occluded area. While severe stenosis can be life threatening in itself, plaques can also rupture, leading to the formation of thrombus which can completely block the artery and lead to myocardial infarction. Fortunately, the formation of atherosclerotic plaques is a protracted process that occurs over a lifetime

(Sanz and Fayad 2008), which affords opportunity for diagnosis and treatment. As the lipid pool in the plaque increases and/or the fibrous cap which constrains the plaque weakens, the risk of rupture and a subsequent acute myocardial event significantly increases (Sanz and Fayad 2008; Davies et al. 1994; Muller et al. 1994; Hellings et al. 2010). Specifically, plaques which have a large (≥3.5 mm^2 cross-section, representing ≥70% stenosis (Narula et al. 2013)) lipid rich pool along with a thin fibrous-cap (≤85 μm (Narula et al. 2013)) are particularly rupture prone. Being able to differentiate a rupture-prone plaque from its stable counterpart could allow additional prophylactic treatment options for CHD patients (Wilensky 2013). For that reason, considerable resources have been invested toward methods capable of characterizing and stabilizing at-risk plaques.

1.4.3.2 Current Treatment Practices

It has been shown that pharmacotherapeutics, such as statins, can improve outcomes for patients suffering from CHD (Jain and Ridker 2005; Cannon et al. 2006) by both reducing cholesterol production and as anti-inflammatories. Unfortunately, acute events, such as thrombus formation due to a ruptured plaque, typically require an immediate and invasive response to both clear the thrombus and stabilize any plaques that may still pose a threat. This is referred to as percutaneous coronary intervention (PCI). While many advances in recent years, such as drug-eluting stents, have made PCI very effective at treating ruptured plaques, there still remains a need to better identify high-risk plaques for treatment (Sousa et al. 2005). In particular, it has been shown that plaque content (i.e. size and composition of plaque) is a valuable predictor of future coronary events (Hellings et al. 2010), suggesting that real-time molecular imaging would be a valuable tool for PCI procedures. Intravascular photoacoustic (IVPA) imaging is one of the modalities being investigated to address this need.

1.4.4 Intravascular Photoacoustic Imaging

PCI procedures have benefitted from intravascular ultrasound (IVUS) imaging for decades, making the introduction of PA molecular imaging onto US imaging represent a natural extension of a clinically familiar imaging modality. Though some research has explored applying PA imaging to the problem of peripheral and carotid artery disease (Kruizinga et al. 2014), the vast majority of research has focused on the development of intravascular photoacoustic (IVPA) imaging of coronary arteries (VanderLaan et al. 2014; Abran et al. 2014; Karpiouk, Wang, and Emelianov 2010). These studies have focused on exploring methods to characterize plaque content (Jansen, van der Steen, et al. 2014; Jansen, Wu, et al. 2014; Wang et al. 2010; Wang et al. 2012b; Yeager et al. 2012; Yeager et al. 2014), as well as determine the extent of local inflammation (Wang et al. 2009), both of which influence plaque vulnerability (Hellings et al. 2010; Libby 2002). Additionally, IVPA imaging has also been used to visualize coronary stent placement (Su, Wang, and Emelianov 2009), which, along with other factors such as vessel size, can predict long-term negative outcomes (Elezi et al. 1998). An IVPA system and catheter can be implemented with relative ease, with most designs opting to introduce a fiber optic (FO) cable for light delivery into an existing IVUS system, as shown in Figure 1.8 (Karpiouk, Wang, and Emelianov 2010). This approach uses the IVUS transducer and system for the detection and processing of PA signals and represents a minimalistic approach to introduce molecular imaging to PCI procedures.

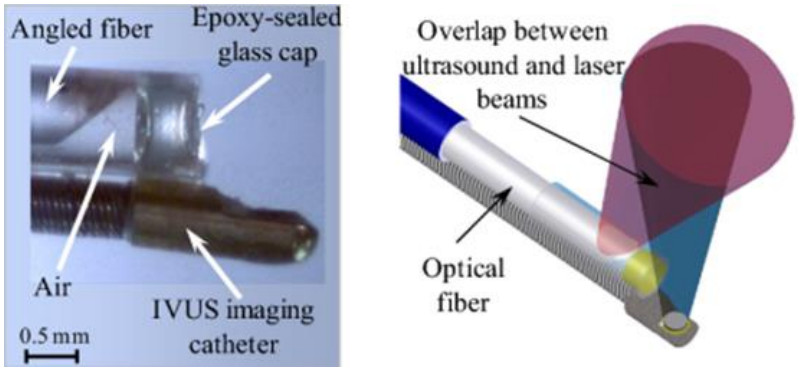

Figure 1.8. Diagram of an integrated IVUS and IVPA imaging catheter (left) and schematic (right). Adapted with permission from (Karpiouk, Wang, and Emelianov 2010).

1.4.4.1 Spectroscopic Photoacoustic Tissue Characterization

The most useful addition of IVPA imaging comes allows for spectroscopic intravascular photoacoustic (sIVPA) imaging for tissue characterization. sIVPA imaging provides molecular information to complement the structural information gathered from IVUS imaging (MacNeill et al. 2003). While the optical absorption of lipid is relatively low in the wavelength range of 700 – 1000 nm, absorption tends to increase with increasing wavelength (Bashkatov et al. 2005a), as is also the case with water (Hale and Querry 1973). However, there are two wavelength regions in the NIR where the optical absorption of lipid peaks relative to water (Hale and Querry 1973; Bashkatov et al. 2005a): 1210 and 1720 nm. These wavelengths represent spectral regions where good contrast between lipid- and water-based tissues is expected (VanderLaan et al. 2014; Jansen, Wu, et al. 2014). Figure 1.9 highlights the potential of combined IVPA/IVUS imaging at these wavelengths.

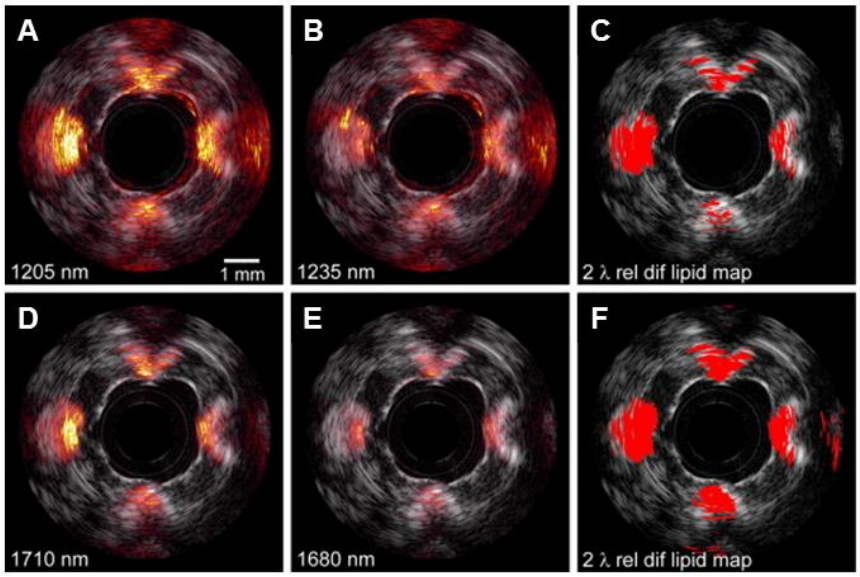

Figure 1.9. Combined IVPA + IVUS images of cholesterol and lipid phantom at 1210 (A), 1235 (B), 1710 (D) and 1680 nm (E). 1235 and 1680 nm represent poor lipid-water contrast and were used to generate lipid maps (C and F) using a difference method. Adapted with permission from (Jansen, Wu, et al. 2014).

The contrast between water and lipid is greatest at 1720 nm, but the overall tissue optical absorption is approximately 10x greater at 1720 nm than at 800 nm (the center of the optical window), making depth penetration a concern (Roggan et al. 1999). Furthermore, high-energy, high repetition-rate, pulsed laser sources operating in the 1720 nm range are limited. Still, research has shown the potential of IVPA imaging at 1720 nm and 1210 nm, visualizing plaque-laden arteries through luminal blood, both in vivo and ex vivo, using an atherosclerotic animal model (Wang et al. 2012a; Wang et al. 2012b).

Depth penetration is less of a concern for PA imaging at 1210 nm, and more laser sources exist at this wavelength. For this reason, 1210 nm IVPA imaging is also under investigation and has shown promise in identifying cholesterol and lipid inclusions in an imaging phantom (Jansen, Wu, et al. 2014). Building upon these results, imaging systems are currently being developed to provide combined IVUS/IVPA imaging of

atherosclerotic plaque in real-time for translation into clinical environments (VanderLaan et al. 2014). While these two wavelength bands represent promising wavelength regimes for sIVPA imaging, studies have yet to conclusively determine which wavelengths are optimal in terms of balancing contrast, imaging depth and sensitivity to atherosclerotic disease state (i.e. being able differentiate high-risk, lipid rich plaques from smaller, stable plaques).

1.4.4.2 Thermal Intravascular Photoacoustic Imaging

As discussed above the mechanism of PA signal generation is temperature dependent (Tam 1986). Tissue characterization using Grüneisen thermal dependence is possible and has been demonstrated using thermal intravascular photoacoustic (tIVPA) imaging (Wang and Emelianov 2011). By modulating the temperature ($17.5\,℃ \leq T \leq 38\,℃$) while performing IVPA imaging at 1210 nm, lipid deposits in an ex vivo atherosclerotic animal model were characterized and differentiated from the nearby water-based tissue components (Wang and Emelianov 2011). Furthermore, results indicate that the Grüneisen thermal-response of lipid-rich plaques differs from that of periadventitial- and abdominal-fat, despite spectroscopic imaging struggling to differentiate the lipid types (Wang and Emelianov 2011). While tIVPA imaging may be a valuable tool to characterize atherosclerotic tissue, questions still remain as to the sensitivity and specificity of this technique.

1.4.4.3 Modeling of Light Transport for Photoacoustic Imaging

Despite the initial promise presented by both sIVPA and tIVPA imaging, there remain several questions which must be addressed before a full clinical system can be developed. Due to various limitations an exhaustive exploration of both the optical parameter space, as well as various different pathological states, to optimize IVPA

imaging has yet to be done. IVPA imaging typically needs a high-energy (≥1 mJ), short-duration (<10 ns) laser pulse to generate a sufficiently strong PA signal that can be reliably detected. Furthermore, as a medical imaging modality, real-time capabilities (~ 25 frames per second, >3200 Hz laser-pulse repetition rate) are necessary to have a significant impact in the clinical space. Currently there are few, if any, tunable-laser sources that meet the above requirements. For that reason, there remains a need to optimize IVPA imaging methods before clinical translation can proceed. The advent of a means to offer quantified assessment of this problem space would be a boon. Optical transport simulation techniques, such as Monte Carlo (MC) modeling, may be able to address this need without necessity for costly equipment and lengthy experimentation.

MC optical modeling has been around since the 1980's (Wilson and Adam 1983), but only in recent years, as computational power has increased, has it become a practical method to explore a large parameter space. Studies have shown that MC optical modeling tends to produce more accurate results than analytical methods (Flock et al. 1989), which rely on simplifying assumptions to generate a solution to the RTE (Wang and Wu 2007). Due to the versatility and the reliability of MC optical modeling, considerable research has gone into developing MC optical modeling tools. MC software tools have been developed for 2D simulation of layered tissues (e.g. skin) (Wang, Jacques, and Zheng 1995), up to 3D simulations of arbitrary heterogeneous volumes (Jacques 2014). Additional models have been developed that account for differences in refractive index across tissue-types (Fang and Boas 2009). In terms of improving efficiency, models have been adapted to reconstruct the tissue as a surface mesh (Fang 2010), as well as a means to parallelize MC simulations on GPUs (Fang and Boas 2009; Fang 2010). The availability of reliable MC optical modeling tools makes this method promising as a means of simulating IVPA imaging results for different wavelengths and tissue

geometries in order to optimize imaging parameters and guide the development of a clinically translatable IVPA imaging system.

1.5 Overview of Research Goals

The overall goal of the research contained herein is to facilitate the clinical translation of PA imaging as it pertains to cardiovascular applications. To pare down such a broad goal, the research thrusts are sub-divided into two application spaces: image guidance for treatment of arrhythmia and image guidance for treatment of coronary heart disease. While these two research pursuits are diverse in the application space, they are unified in that they often rely upon the same fundamental techniques (e.g. spectroscopic PA imaging) to improve PA image guidance. Additionally, some of the tools discussed herein (e.g. MC optical modeling), once developed, can be readily applied to a variety of PA imaging applications in the cardiovascular realm and beyond. In that regard the two parallel research interests support the comprehensive goal of developing PA imaging methods for tissue characterization and image guidance in cardiovascular applications.

1.5.1 Image Guidance of Arrhythmia Treatment Goals

The research herein aims to address two applications of PA imaging with respect to image guidance for cardiac arrhythmia applications. The first research discussed in this dissertation examines a preliminary PA method to monitor cardiac depolarization. Additionally, also explored is a spectroscopic PA imaging method designed to characterize ablation lesions in myocardium as a potential means of image guidance for ablation procedures.

1.5.1.1 Visualization of Myocyte Depolarization and Cardiac Electric Potential

Ca exchange is fundamental to cardiac EP function and is responsible for electro-mechanical coupling in cardiac myocytes. Additionally, the cytosolic Ca concentration

changes by several orders of magnitude during the cardiac cycle. For these reasons, Ca is a promising imaging target. As a first step toward PA-based monitoring of myocardial EP function, this research explores proof-of-concept PA tracking of myocyte cytosolic Ca fluctuations. An appropriate Ca-sensitive PA contrast agent could serve as a probe for monitoring Ca levels in the cytosol. Arsenazo III (Asz) is dye which exhibits a shift in absorption spectrum as a result of binding Ca ions. Initial investigations using Asz as a PA contrast agent for active cardiac myocytes were done with an experimental PA microscopy setup, with results discussed in Chapter 2.

1.5.1.2 Toward Tissue Characterization of Cardiac Ablation Lesions

PA imaging also has potential to characterize cardiac tissue during the ablation process, in order to provide online feedback to physicians for TCA guidance. The process of TCA RF-ablation involves targeted hyperthermia at a particular tissue locus. The hyperthermia results in a combination of protein denaturation and membrane disruption (Thomsen, Jacques, and Flock 1990; Thomsen 1991) that often trigger cellular apoptotic and necrotic pathways that eventually heal by replacing damaged myocardium with non-conductive scar tissue. If PA imaging is going to have a lasting impact as an image guidance modality, it must be able to accurately monitor this process and provide meaningful information to the physician while ablation is underway. The research herein explores a spectroscopic method to improve the sensitivity, specificity and depth at which cardiac tissue can be accurately characterized as ablated or non-ablated. By examining multiple wavelengths to characterize tissue, such a method can help overcome the changes in the fluence distribution that result from tissue hyperthermia. Results from ex vivo studies, along with a discussion of translating results to in vivo studies, are presented in Chapter 3.

1.5.2 Image Guidance of Coronary Heart Disease

As discussed above, IVPA imaging has undergone several studies to explore its ability to visualize atherosclerotic plaques (Wang and Emelianov 2011; Wang et al. 2012a; Wang et al. 2012b; Jansen, van der Steen, et al. 2014; Jansen, Wu, et al. 2014), implantable stents (Su, Wang, and Emelianov 2009) and exogenous contrast agents (Yeager et al. 2012; Yeager et al. 2014). While the various studies have effectively demonstrated the potential for IVPA imaging to visualize plaques, there has yet to be a comprehensive examination across the NIR spectrum to determine optimal NIR wavelengths for maximizing imaging depth and assessing plaque content and burden, in order to determine which plaques require intervention. Research discussed herein aims to provide an examination of those parameters in order to guide translation of IVPA imaging into the clinical realm.

1.5.2.1 Model-based Optimization of Intravascular Photoacoustic Imaging

In an ideal situation an exhaustive examination of PA results would be obtained from conducting PA imaging studies on various tissue and plaque geometries, at many wavelengths throughout the NIR spectrum, followed up with histopathological examination of all tissue samples to confirm PA imaging results. Unfortunately, due to various limitations on time, expense and the availability of equipment and tissue samples, such an approach is beyond realization. As an alternative, research in this dissertation attempts to replicate those findings through MC simulation of optical transport and the resulting PA signal generation for a variety of tissue types, across many wavelengths in the NIR regime. In this way, this research approximates the extensive studies discussed above, with the intent to optimize IVPA imaging for translational studies. These results are discussed in Chapter 4.

1.5.3 Summary of Research Goals

While the studies discussed herein address different applications of PA imaging, they are united in that they attempt to advance PA imaging for cardiovascular applications, facilitating translation into the clinical realm. This is done initially by exploring the potential of PA image guidance for cardiac arrhythmia procedures. The exploration of proof-of-concept PA sensing of Ca dynamics aims to determine, as a first step, if PA techniques can monitor myocyte EP activity. As TCA treatment often follows the initial arrhythmia diagnosis, the next set of PA studies discussed explores a multi-wavelength method to characterize TCA lesions in ex vivo myocardial samples, with the goal of developing a reliable PA protocol for image guidance during cardiac ablation procedures. The last study discussed in this dissertation is a thorough exploration of IVPA imaging by simulating light propagation and PA imaging results from an IVPA system, across a broad spectral range in the NIR. The results of this comprehensive simulation can then be used to guide the development of an optimized IVPA system for clinical translation. This dissertation concludes in the final chapter by summarizing results, particularly as they pertain to PA applications in cardiovascular imaging as a whole. This includes a discussion of the limitations of the presented results, as well as future studies that capitalize on results presented and a vision of the future of cardiovascular PA imaging as a whole.

1.6 REFERENCES

Abran, M., G. Cloutier, M. H. R. Cardinal, B. Chayer, J. C. Tardif, and F. Lesage. 2014. 'Development of a Photoacoustic, Ultrasound and Fluorescence Imaging Catheter for the Study of Atherosclerotic Plaque', Biomedical Circuits and Systems, IEEE Transactions on, 8: 696-703.

Akers, Walter J, Chulhong Kim, Mikhail Berezin, Kevin Guo, Ralph Fuhrhop, Gregory M Lanza, Georg M Fischer, Ewald Daltrozzo, Andreas Zumbusch, and Xin Cai. 2010. 'Noninvasive photoacoustic and fluorescence sentinel lymph node

identification using dye-loaded perfluorocarbon nanoparticles', ACS Nano, 5: 173-82.

Andreas, H. Hielscher, E. Alcouffe Raymond, and L. Barbour Randall. 1998. 'Comparison of finite-difference transport and diffusion calculations for photon migration in homogeneous and heterogeneous tissues', Physics in Medicine and Biology, 43: 1285.

Bashkatov, A. N., E. A. Genina, V. I. Kochubey, and V. V. Tuchin. 2005. 'Optical properties of human skin, subcutaneous and mucous tissues in the wavelength range from 400 to 2000 nm', Journal of Physics D: Applied Physics, 38: 2543.

Bayer, Carolyn L., Yun-Sheng Chen, Seungsoo Kim, Srivalleesha Mallidi, Konstantin Sokolov, and Stanislav Emelianov. 2011. 'Multiplex photoacoustic molecular imaging using targeted silica-coated gold nanorods', Biomedical Optics Express, 2: 1828-35.

Bhattacharyya, Sibaprasad, Shuyan Wang, Daniel Reinecke, William Kiser Jr, Robert A Kruger, and Timothy R DeGrado. 2008. 'Synthesis and evaluation of near-infrared (NIR) dye− herceptin conjugates as photoacoustic computed tomography (PCT) probes for HER2 expression in breast cancer', Bioconjugate chemistry, 19: 1186-93.

Cannon, Christopher P., Benjamin A. Steinberg, Sabina A. Murphy, Jessica L. Mega, and Eugene Braunwald. 2006. 'Meta-Analysis of Cardiovascular Outcomes Trials Comparing Intensive Versus Moderate Statin Therapy', Journal of the American College of Cardiology, 48: 438-45.

Chavez, Patricia, Franz H Messerli, Abel Casso Dominguez, Emad F Aziz, Tina Sichrovsky, Daniel Garcia, Connor D Barrett, and Stephan Danik. 2015. 'Atrioesophageal fistula following ablation procedures for atrial fibrillation: systematic review of case reports', Open Heart, 2.

Chen, Jingyi, Fusayo Saeki, Benjamin J Wiley, Hu Cang, Michael J Cobb, Zhi-Yuan Li, Leslie Au, Hui Zhang, Michael B Kimmey, and Xingde Li. 2005. 'Gold nanocages: bioconjugation and their potential use as optical imaging contrast agents', Nano Letters, 5: 473-77.

Chitnis, Parag V., Hans-Peter Brecht, Richard Su, and Alexander A. Oraevsky. 2010. 'Feasibility of optoacoustic visualization of high-intensity focused ultrasound-induced thermal lesions in live tissue', Journal of Biomedical Optics, 15: 021313-13-5.

Cook, Jason R., Wolfgang Frey, and Stanislav Emelianov. 2013. 'Quantitative Photoacoustic Imaging of Nanoparticles in Cells and Tissues', ACS Nano, 7: 1272-80.

Dana, N., L. Di Biase, A. Natale, S. Emelianov, and R. Bouchard. 2014. 'In vitro photoacoustic visualization of myocardial ablation lesions', Heart Rhythm, 11: 150-7.

Dana, N., R. A. Fowler, A. Allen, J. Zoldan, L. Suggs, and S. Emelianov. 2016. 'In vitro photoacoustic sensing of calcium dynamics with arsenazo III', Laser Physics Letters, 13: 075603.

Dana, Nicholas P., Diego S. Dumani, Jason R. Cook, and Stanislav Emelianov. 2016. 'Overview of Photoacoustic Imaging.' in Devon J. Godfrey, Jacob Van Dyk, Shiva K. Das, Bruce H. Curran and Anthony B. Wolbarst (eds.), Advances in Medical Physics (Medical Physics Publishing: Madison, WI).

Dana, Nicholas; Bouchard, Richard; Di Biase, Luigi; Natale, Andrea; Emelianov, Stanislav. 2014. "Characterization of myocardial ablation lesions using multi-wavelength photoacoustic imaging." In SPIE Photons Plus Ultrasound: Imaging and Sensing 2014. San Francisco, California United States.

Davies, M. J., N. Woolf, P. Rowles, and P. D. Richardson. 1994. 'Lipid and cellular constituents of unstable human aortic plaques.' in, Arteriosclerosis (Springer).

Diebold, G. J., and T. Sun. 1994. 'PROPERTIES OF PHOTOACOUSTIC WAVES IN ONE-DIMENSION, 2-DIMENSION, AND 3-DIMENSION', Acustica, 80: 339-51.

Duck, Francis A. 1990a. 'Chapter 8 - Nuclear Magnetism of Tissue.' in Francis A. Duck (ed.), Physical Properties of Tissues (Academic Press: London).

———. 1990b. 'Chapter 9 - Tissue Composition.' in Francis A. Duck (ed.), Physical Properties of Tissues (Academic Press: London).

El-Sayed, Mostafa A. 2001. 'Some interesting properties of metals confined in time and nanometer space of different shapes', Accounts of chemical research, 34: 257-64.

Elezi, Shpend, Adnan Kastrati, Franz-Josef Neumann, Martin Hadamitzky, Josef Dirschinger, and Albert Schömig. 1998. 'Vessel Size and Long-Term Outcome After Coronary Stent Placement', Circulation, 98: 1875-80.

Fang, Qianqian. 2010. 'Mesh-based Monte Carlo method using fast ray-tracing in Plücker coordinates', Biomedical Optics Express, 1: 165-75.

Fang, Qianqian, and David A. Boas. 2009. 'Monte Carlo Simulation of Photon Migration in 3D Turbid Media Accelerated by Graphics Processing Units', Optics express, 17: 20178-90.

Flock, S. T., M. S. Patterson, B. C. Wilson, and D. R. Wyman. 1989. 'Monte Carlo modeling of light propagation in highly scattering tissues. I. Model predictions and comparison with diffusion theory', Biomedical Engineering, IEEE Transactions on, 36: 1162-68.

Fogoros, Richard N. 1999. Electrophysiologic Testing (Blackwell Publishing).

Galanzha, Ekaterina I, Evgeny V Shashkov, Thomas Kelly, Jin-Woo Kim, Lily Yang, and Vladimir P Zharov. 2009. 'In vivo magnetic enrichment and multiplex photoacoustic detection of circulating tumour cells', Nature nanotechnology, 4: 855-60.

Go, Alan S, Dariush Mozaffarian, Véronique L Roger, Emelia J Benjamin, Jarett D Berry, William B Borden, Dawn M Bravata, Shifan Dai, Earl S Ford, and Caroline S Fox. 2013. 'Heart disease and stroke statistics—2013 update a report from the American Heart Association', Circulation, 127: e6-e245.

Goel, Shreya, Feng Chen, and Weibo Cai. 2014. 'Synthesis and biomedical applications of copper sulfide nanoparticles: from sensors to theranostics', Small, 10: 631-45.

Gray, J. P., N. Dana, K. L. Dextraze, F. Maier, S. Emelianov, and R. R. Bouchard. 2015. 'Multi-Wavelength Photoacoustic Visualization of High Intensity Focused Ultrasound Lesions', Ultrasonic Imaging.

Hale, George M., and Marvin R. Querry. 1973. 'Optical Constants of Water in the 200-nm to 200-μm Wavelength Region', Applied optics, 12: 555-63.

Hannah, Alexander, Geoffrey Luke, Katheryne Wilson, Kimberly Homan, and Stanislav Emelianov. 2013. 'Indocyanine green-loaded photoacoustic nanodroplets: dual contrast nanoconstructs for enhanced photoacoustic and ultrasound imaging', ACS Nano, 8: 250-59.

Haraldsson, Börje, Jenny Nyström, and William M. Deen. 2008. 'Properties of the Glomerular Barrier and Mechanisms of Proteinuria', Physiological Reviews, 88: 451-87.

Hellings, Willem E., Wouter Peeters, Frans L. Moll, Sebastiaan R.D. Piers, Jessica van Setten, Peter J. Van der Spek, Jean-Paul P.M. de Vries, Kees A. Seldenrijk, Peter C. De Bruin, Aryan Vink, Evelyn Velema, Dominique P.V. de Kleijn, and Gerard Pasterkamp. 2010. 'Composition of Carotid Atherosclerotic Plaque Is Associated With Cardiovascular Outcome: A Prognostic Study', Circulation, 121: 1941-50.

Hoelen, Christoph G. A., and Frits F. M. de Mul. 2000. 'Image reconstruction for photoacoustic scanning of tissue structures', Applied optics, 39: 5872-83.

Hsu, Li-Fern, Pierre JaÏS, MÉLÈZe Hocini, Prashanthan Sanders, Christophe ScavÉE, Frederic Sacher, Yoshihide Takahashi, Martin Rotter, Jean-Luc Pasquie, Jacques ClÉMenty, and Michel HaÏSsaguerre. 2005. 'Incidence and Prevention of Cardiac Tamponade Complicating Ablation for Atrial Fibrillation', Pacing and Clinical Electrophysiology, 28: S106-S09.

Hu, Xiaoge, Chen-Wei Wei, Jinjun Xia, Ivan Pelivanov, Matthew O'Donnell, and Xiaohu Gao. 2013. 'Trapping and Photoacoustic Detection of CTCs at the Single Cell per

Milliliter Level with Magneto-Optical Coupled Nanoparticles', Small (Weinheim an der Bergstrasse, Germany), 9: 2046-52.

Irina, V. Larina, V. Larin Kirill, and O. Esenaliev Rinat. 2005. 'Real-time optoacoustic monitoring of temperature in tissues', Journal of Physics D: Applied Physics, 38: 2633.

Jacques, Steven L. 2014. 'Coupling 3D Monte Carlo light transport in optically heterogeneous tissues to photoacoustic signal generation', Photoacoustics, 2: 137-42.

Jain, Mukesh K., and Paul M. Ridker. 2005. 'Anti-Inflammatory Effects of Statins: Clinical Evidence and Basic Mechanisms', Nat Rev Drug Discov, 4: 977-87.

Jain, Prashant K., Kyeong Seok Lee, Ivan H. El-Sayed, and Mostafa A. El-Sayed. 2006. 'Calculated Absorption and Scattering Properties of Gold Nanoparticles of Different Size, Shape, and Composition: Applications in Biological Imaging and Biomedicine', The Journal of Physical Chemistry B, 110: 7238-48.

Jansen, Krista, Antonius F. W. van der Steen, Min Wu, Heleen M. M. van Beusekom, Geert Springeling, Xiang Li, Qifa Zhou, K. Kirk Shung, Dominique P. V. de Kleijn, and Gijs van Soest. 2014. 'Spectroscopic intravascular photoacoustic imaging of lipids in atherosclerosis', Journal of Biomedical Optics, 19: 026006-06.

Jansen, Krista, Min Wu, Antonius F. W. van der Steen, and Gijs van Soest. 2014. 'Photoacoustic imaging of human coronary atherosclerosis in two spectral bands', Photoacoustics, 2: 12-20.

Ji, Xiaohui, Xiangning Song, Jun Li, Yubai Bai, Wensheng Yang, and Xiaogang Peng. 2007. 'Size control of gold nanocrystals in citrate reduction: the third role of citrate', Journal of the American Chemical Society, 129: 13939-48.

Karpiouk, Andrei B., Bo Wang, and Stanislav Y. Emelianov. 2010. 'Development of a catheter for combined intravascular ultrasound and photoacoustic imaging', Review of Scientific Instruments, 81: 014901.

Kelly, K Lance, Eduardo Coronado, Lin Lin Zhao, and George C Schatz. 2003. 'The optical properties of metal nanoparticles: the influence of size, shape, and dielectric environment', The Journal of Physical Chemistry B, 107: 668-77.

Kim, Chulhong, Kwang Hyun Song, Feng Gao, and Lihong V Wang. 2010. 'Sentinel lymph nodes and lymphatic vessels: noninvasive dual-modality in vivo mapping by using indocyanine green in rats—volumetric spectroscopic photoacoustic imaging and planar fluorescence imaging 1', Radiology, 255: 442-50.

Kim, Gwangseong, Sheng-Wen Huang, Kathleen C Day, Matthew O'Donnell, Rodney R Agayan, Mark A Day, Raoul Kopelman, and Shai Ashkenazi. 2007. 'Indocyanine-

green-embedded PEBBLEs as a contrast agent for photoacoustic imaging', Journal of Biomedical Optics, 12: 044020-20-8.

Kim, S., Y. S. Chen, G. P. Luke, and S. Y. Emelianov. 2011. 'In vivo three-dimensional spectroscopic photoacoustic imaging for monitoring nanoparticle delivery', Biomed Opt Express, 2: 2540-50.

Kruizinga, Pieter, Antonius F. W. van der Steen, Nico de Jong, Geert Springeling, Jan Lukas Robertus, Aad van der Lugt, and Gijs van Soest. 2014. 'Photoacoustic imaging of carotid artery atherosclerosis', Journal of Biomedical Optics, 19: 110504-04.

Ku, Geng, Min Zhou, Shaoli Song, Qian Huang, John Hazle, and Chun Li. 2012. 'Copper sulfide nanoparticles as a new class of photoacoustic contrast agent for deep tissue imaging at 1064 nm', ACS Nano, 6: 7489-96.

Kumar, S, J Aaron, and K Sokolov. 2008. 'Directional conjugation of antibodies to nanoparticles for synthesis of multiplexed optical contrast agents with both delivery and targeting moieties', Nature Protocols, 3: 314-20.

Laufer, Jan, Edward Zhang, and Paul Beard. 2010. 'Evaluation of absorbing chromophores used in tissue phantoms for quantitative photoacoustic spectroscopy and imaging', Selected Topics in Quantum Electronics, IEEE Journal of, 16: 600-07.

Lehman, William, Roger Craig, and Peter Vibert. 1994. 'Ca2+-induced tropomyosin movement in Limulus thin filaments revealed by three-dimensional reconstruction', Nature, 368: 65-67.

Libby, Peter. 2002. 'Inflammation in atherosclerosis', Nature, 420: 868-74.

Longmire, Michelle, Peter L Choyke, and Hisataka Kobayashi. 2008. 'Clearance properties of nano-sized particles and molecules as imaging agents: considerations and caveats'.

Luke, Geoffrey P., Seung Yun Nam, and Stanislav Y. Emelianov. 2013. 'Optical wavelength selection for improved spectroscopic photoacoustic imaging', Photoacoustics, 1: 36-42.

MacNeill, Briain D., Harry C. Lowe, Masamichi Takano, Valentin Fuster, and Ik-Kyung Jang. 2003. 'Intravascular Modalities for Detection of Vulnerable Plaque: Current Status', Arteriosclerosis, Thrombosis, and Vascular Biology, 23: 1333-42.

Mallidi, S., G. P. Luke, and S. Emelianov. 2011. 'Photoacoustic imaging in cancer detection, diagnosis, and treatment guidance', Trends Biotechnol, 29: 213-21.

Marrouche, N. F., D. O. Martin, O. Wazni, A. M. Gillinov, A. Klein, M. Bhargava, E. Saad, D. Bash, H. Yamada, W. Jaber, R. Schweikert, P. Tchou, A. Abdul-Karim, W. Saliba, and A. Natale. 2003. 'Phased-array intracardiac echocardiography

monitoring during pulmonary vein isolation in patients with atrial fibrillation: impact on outcome and complications', Circulation, 107: 2710-6.

Mitnovetski, S., A. A. Almeida, J. Goldstein, A. W. Pick, and J. A. Smith. 2009. 'Epicardial high-intensity focused ultrasound cardiac ablation for surgical treatment of atrial fibrillation', Heart Lung Circ, 18: 28-31.

Mozaffarian, Dariush, Emelia J. Benjamin, Alan S. Go, Donna K. Arnett, Michael J. Blaha, Mary Cushman, Sarah de Ferranti, Jean-Pierre Després, Heather J. Fullerton, Virginia J. Howard, Mark D. Huffman, Suzanne E. Judd, Brett M. Kissela, Daniel T. Lackland, Judith H. Lichtman, Lynda D. Lisabeth, Simin Liu, Rachel H. Mackey, David B. Matchar, Darren K. McGuire, Emile R. Mohler, Claudia S. Moy, Paul Muntner, Michael E. Mussolino, Khurram Nasir, Robert W. Neumar, Graham Nichol, Latha Palaniappan, Dilip K. Pandey, Mathew J. Reeves, Carlos J. Rodriguez, Paul D. Sorlie, Joel Stein, Amytis Towfighi, Tanya N. Turan, Salim S. Virani, Joshua Z. Willey, Daniel Woo, Robert W. Yeh, and Melanie B. Turner. 2015. 'Heart Disease and Stroke Statistics—2015 Update: A Report From the American Heart Association', Circulation, 131: e29-e322.

Muller, James E, George S Abela, Richard W Nesto, and Geoffrey H Tofler. 1994. 'Triggers, acute risk factors and vulnerable plaques: the lexicon of a new frontier', Journal of the American College of Cardiology, 23: 809-13.

Nam, Seung Yun, Laura M Ricles, Laura J Suggs, and Stanislav Y Emelianov. 2012. 'Nonlinear photoacoustic signal increase from endocytosis of gold nanoparticles', Optics Letters, 37: 4708-10.

Narula, Jagat, Masataka Nakano, Renu Virmani, Frank D. Kolodgie, Rita Petersen, Robert Newcomb, Shaista Malik, Valentin Fuster, and Aloke V. Finn. 2013. 'Histopathologic Characteristics of Atherosclerotic Coronary Disease and Implications of the Findings for the Invasive and Noninvasive Detection of Vulnerable Plaques', Journal of the American College of Cardiology, 61: 1041-51.

Natale, Andrea, Larry Breeding, Gery Tomassoni, Kathleen Rajkovich, Mark Richey, Salwa Beheiry, Katie Martinez, Lisa Cromwell, Brandon Wides, and Fabio Leonelli. 1998. 'Ablation of right and left ectopic atrial tachycardias using a three-dimensional nonfluoroscopic mapping system', The American Journal of Cardiology, 82: 989-92.

Niidome, Takuro, Masato Yamagata, Yuri Okamoto, Yasuyuki Akiyama, Hironobu Takahashi, Takahito Kawano, Yoshiki Katayama, and Yasuro Niidome. 2006. 'PEG-modified gold nanorods with a stealth character for in vivo applications', Journal of Controlled Release, 114: 343-47.

Nikoobakht, Babak, and Mostafa A El-Sayed. 2003. 'Preparation and growth mechanism of gold nanorods (NRs) using seed-mediated growth method', Chemistry of Materials, 15: 1957-62.

Oraevsky, Alexander A., Steven L. Jacques, and Frank K. Tittel. 1997. 'Measurement of tissue optical properties by time-resolved detection of laser-induced transient stress', Applied optics, 36: 402-15.

Pappone, C., S. Rosanio, G. Oreto, M. Tocchi, F. Gugliotta, G. Vicedomini, A. Salvati, C. Dicandia, P. Mazzone, V. Santinelli, S. Gulletta, and S. Chierchia. 2000. 'Circumferential radiofrequency ablation of pulmonary vein ostia: A new anatomic approach for curing atrial fibrillation', Circulation, 102: 2619-28.

Petersen, H. H., X. Chen, A. Pietersen, J. H. Svendsen, and S. Haunso. 1999. 'Temperature-controlled radiofrequency ablation of cardiac tissue: an in vitro study of the impact of electrode orientation, electrode tissue contact pressure and external convective cooling', J Interv Card Electrophysiol, 3: 257-62.

Prahl, Scott. 1999. 'Optical absorption of hemoglobin', Oregon Medical Laser Center, http://omlc. ogi. edu/spectra/hemoglobin/index. html, 15.

Pramanik, M., and L. V. Wang. 2009. 'Thermoacoustic and photoacoustic sensing of temperature', J Biomed Opt, 14: 054024.

Pramanik, Manojit, Magdalena Swierczewska, Danielle Green, Balaji Sitharaman, and Lihong V Wang. 2009. 'Single-walled carbon nanotubes as a multimodal-thermoacoustic and photoacoustic-contrast agent', Journal of Biomedical Optics, 14: 034018-18-8.

Rajian, Justin Rajesh, Mario L. Fabiilli, J. Brian Fowlkes, Paul L. Carson, and Xueding Wang. 2011. 'Drug delivery monitoring by photoacoustic tomography with an ICG encapsulated double emulsion', Optics express, 19: 14335-47.

Roggan, A., M. Friebel, K. Do Rschel, A. Hahn, and G. Mu Ller. 1999. 'Optical Properties of Circulating Human Blood in the Wavelength Range 400-2500 nm', J Biomed Opt, 4: 36-46.

Santangeli, P., L. Di Biase, G. Pelargonio, J. D. Burkhardt, and A. Natale. 2011. 'The pharmaceutical pipeline for atrial fibrillation', Ann Med, 43: 13-32.

Sanz, Javier, and Zahi A. Fayad. 2008. 'Imaging of atherosclerotic cardiovascular disease', Nature, 451: 953-57.

Schwartzman, D., J. J. Michele, C. T. Trankiem, and J. F. Ren. 2001. 'Electrogram-guided radiofrequency catheter ablation of atrial tissue comparison with thermometry-guide ablation: comparison with thermometry-guide ablation', J Interv Card Electrophysiol, 5: 253-66.

Shah, D. 2011. 'A critical appraisal of cardiac ablation technology for catheter-based treatment of atrial fibrillation', Expert Rev Med Devices, 8: 49-55.

Shah, J., S. Park, S. Aglyamov, T. Larson, L. Ma, K. Sokolov, K. Johnston, T. Milner, and S. Y. Emelianov. 2008. 'Photoacoustic imaging and temperature measurement for photothermal cancer therapy', J Biomed Opt, 13: 034024.

Sousa, J. Eduardo, Marco A. Costa, E. Murat Tuzcu, Jay S. Yadav, and Stephen Ellis. 2005. 'New Frontiers in Interventional Cardiology', Circulation, 111: 671-81.

Su, Jimmy Li-Shin, Bo Wang, and Stanislav Y. Emelianov. 2009. 'Photoacoustic imaging of coronary artery stents', Optics express, 17: 19894-901.

Szabo, Thomas L. 2004. Diagnostic ultrasound imaging: inside out (Academic Press).

Tam, A. C. 1986. 'APPLICATIONS OF PHOTOACOUSTIC SENSING TECHNIQUES', Reviews of Modern Physics, 58: 381-431.

Tassa, Carlos, Stanley Y Shaw, and Ralph Weissleder. 2011. 'Dextran-coated iron oxide nanoparticles: a versatile platform for targeted molecular imaging, molecular diagnostics, and therapy', Accounts of chemical research, 44: 842-52.

Thomsen, S. 1991. 'Pathologic analysis of photothermal and photomechanical effects of laser-tissue interactions', Photochem Photobiol, 53: 825-35.

Thomsen, Sharon L, Steven L Jacques, and Stephen T Flock. 1990. "Microscopic correlates of macroscopic optical property changes during thermal coagulation of myocardium." In OE/LASE'90, 14-19 Jan., Los Angeles, CA, 2-11. International Society for Optics and Photonics.

Tse, Hung-Fat, Sven Reek, Carl Timmermans, Kathy Lai-Fun Lee, J. Christoph Geller, Luz-Maria Rodriguez, Benoit Ghaye, Gregory M. Ayers, Harry J. G. M. Crijns, Helmut U. Klein, and Chu-Pak Lau. 2003. 'Pulmonary vein isolation using transvenous catheter cryoablation for treatment of atrial fibrillation without risk of pulmonary vein stenosis', Journal of the American College of Cardiology, 42: 752-58.

VanderLaan, D., A. Karpiouk, D. Yeager, and S. Emelianov. 2014. "System and integrated catheter for real-time intravascular ultrasound and photoacoustic imaging." In Ultrasonics Symposium (IUS), 2014 IEEE International, 1591-94.

Wang, B., and S. Emelianov. 2011. 'Thermal intravascular photoacoustic imaging', Biomed Opt Express, 2: 3072-8.

Wang, B., A. Karpiouk, D. Yeager, J. Amirian, S. Litovsky, R. Smalling, and S. Emelianov. 2012a. 'Intravascular photoacoustic imaging of lipid in atherosclerotic plaques in the presence of luminal blood', Opt Lett, 37: 1244-6.

Wang, Bo, Andrei Karpiouk, Doug Yeager, James Amirian, Silvio Litovsky, Richard Smalling, and Stanislav Emelianov. 2012b. 'In vivo Intravascular Ultrasound-guided Photoacoustic Imaging of Lipid in Plaques Using an Animal Model of Atherosclerosis', Ultrasound in Medicine & Biology, 38: 2098-103.

Wang, Bo, Jimmy L. Su, James Amirian, Silvio H. Litovsky, Richard Smalling, and Stanislav Emelianov. 2010. 'Detection of lipid in atherosclerotic vessels using ultrasound-guided spectroscopic intravascular photoacoustic imaging', Opt. Express, 18: 4889-97.

Wang, Bo, Evgeniya Yantsen, Timothy Larson, Andrei B. Karpiouk, Shriram Sethuraman, Jimmy L. Su, Konstantin Sokolov, and Stanislav Y. Emelianov. 2009. 'Plasmonic Intravascular Photoacoustic Imaging for Detection of Macrophages in Atherosclerotic Plaques', Nano Letters, 9: 2212-17.

Wang, Li-Sheng, Min-Chieh Chuang, and Ja-an Annie Ho. 2012. 'Nanotheranostics–a review of recent publications', International journal of nanomedicine, 7: 4679.

Wang, Lihong, Steven L Jacques, and Liqiong Zheng. 1995. 'MCML—Monte Carlo modeling of light transport in multi-layered tissues', Computer methods and programs in biomedicine, 47: 131-46.

Wang, Lihong V. 2009. 'Multiscale photoacoustic microscopy and computed tomography', Nature photonics, 3: 503-09.

Wang, Lihong V, and Hsin-i Wu. 2007. Biomedical optics: principles and imaging (John Wiley & Sons).

Wang, X. D., X. Y. Xie, G. N. Ku, and L. H. V. Wang. 2006. 'Noninvasive imaging of hemoglobin concentration and oxygenation in the rat brain using high-resolution photoacoustic tomography', Journal of Biomedical Optics, 11: 9.

Weight, Ryan M., John A. Viator, Paul S. Dale, Charles W. Caldwell, and Allison E. Lisle. 2006. 'Photoacoustic detection of metastatic melanoma cells in the human circulatory system', Optics Letters, 31: 2998-3000.

Welch, A. J., J. A. Pearce, K. R. Diller, G. Yoon, and W. F. Cheong. 1989. 'Heat Generation in Laser Irradiated Tissue', Journal of Biomechanical Engineering, 111: 62-68.

Wikipedia.org. 2016. 'Cardiac action potential --- Wikipedia, The Free Encyclopedia', Accessed July 22. https://en.wikipedia.org/w/index.php?title=Cardiac_action_potential&oldid=722126209.

Wilensky, Robert L. 2013. 'In Search of the Elusive Vulnerable PlaqueReducing the Gap Between Coronary Imaging and Necropsy Findings∗∗', Journal of the American College of Cardiology, 61: 1052-53.

Wilson, B. C., and G. Adam. 1983. 'A Monte Carlo model for the absorption and flux distributions of light in tissue', Medical Physics, 10: 824-30.

Wu, Chun-Hsien, Jason Cook, Stanislav Emelianov, and Konstantin Sokolov. 2014. 'Multimodal magneto-plasmonic nanoclusters for biomedical applications', Advanced Functional Materials, 24: 6862-71.

Wu, Weitai, Ting Zhou, Alexandra Berliner, Probal Banerjee, and Shuiqin Zhou. 2010. 'Smart core− shell hybrid nanogels with Ag nanoparticle core for cancer cell imaging and gel shell for pH-regulated drug delivery', Chemistry of Materials, 22: 1966-76.

Xiang, Liangzhong, Da Xing, Huaimin Gu, Diwu Yang, Lvming Zeng, and Sihua Yang. 2006. "Gold nanoshell-based photoacoustic imaging application in biomedicine." In Biophotonics, Nanophotonics and Metamaterials, 2006. Metamaterials 2006. International Symposium on, 76-79. IEEE.

Yeager, Doug, Yun-Sheng Chen, Silvio Litovsky, and Stanislav Emelianov. 2014. 'Intravascular Photoacoustics for Image-Guidance and Temperature Monitoring During Plasmonic Photothermal Therapy of Atherosclerotic Plaques: A Feasibility Study', Theranostics, 4: 36-46.

Yeager, Doug, Andrei Karpiouk, Bo Wang, James Amirian, Konstantin Sokolov, Richard Smalling, and Stanislav Emelianov. 2012. 'Intravascular photoacoustic imaging of exogenously labeled atherosclerotic plaque through luminal blood', Journal of Biomedical Optics, 17: 106016-16.

Yoon, Soon Joon, Avinash Murthy, Keith P Johnston, Konstantin V Sokolov, and Stanislav Y Emelianov. 2012. 'Thermal stability of biodegradable plasmonic nanoclusters in photoacoustic imaging', Optics express, 20: 29479-87.

Zerda, Adam de la, Zhuang Liu, Sunil Bodapati, Robert Teed, Srikant Vaithilingam, Butrus T Khuri-Yakub, Xiaoyuan Chen, Hongjie Dai, and Sanjiv Sam Gambhir. 2010. 'Ultrahigh sensitivity carbon nanotube agents for photoacoustic molecular imaging in living mice', Nano Letters, 10: 2168-72.

Zhang, E. Z., J. G. Laufer, R. B. Pedley, and P. C. Beard. 2009. 'In vivo high-resolution 3D photoacoustic imaging of superficial vascular anatomy', Physics in Medicine and Biology, 54: 1035.

Zhao, Xue-qin, Tian-xiao Wang, Wen Liu, Cai-ding Wang, Dong Wang, Ting Shang, Li-hua Shen, and Lei Ren. 2011. 'Multifunctional Au@ IPN-pNIPAAm nanogels for cancer cell imaging and combined chemo-photothermal treatment', Journal of Materials Chemistry, 21: 7240-47.

Chapter 2: In Vitro Photoacoustic Sensing Of Calcium Dynamics With Arsenazo III[2]

2.1 ABSTRACT

Imaging of cellular electric potential via calcium-ion sensitive contrast agents is a useful tool, but currently it lacks sufficient depth penetration. We explore contrast-enhanced photoacoustic (PA) imaging, using Arsenazo III dye, to visualize cardiac myocyte depolarization in vitro. Phantom results show strong linearity of PA signal with dye concentration ($R2 > 0.95$), and agree spectrally with extinction measurements with varying calcium concentration. Cell studies indicate a significant (> 100-fold) increase in PA signal for dye-treated cells, as well as a 10-fold increase in peak-to-peak variation during a 30-second window. This suggests contrast-enhanced PA imaging may have sufficient sensitivity and specificity for depth-resolved visualization of tissue depolarization in real-time.

2.2 INTRODUCTION

2.2.1 Calcium function

Calcium-ion (Ca) exchange mediates a wide range of mammalian cellular functions, such as muscle contraction, cell signaling, cell secretion, glycolysis, cell division and growth (Berridge, Lipp, and Bootman 2000). In neuronal and cardiac cells, Ca exchange is essential for electrophysiological activity (Catterall and Few 2008), as well as being responsible for mammalian myocyte inter-cell electro-mechanical coupling. During cardiac myocyte depolarization, cytosolic Ca concentration has been shown to rapidly increase by a factor of 10 or greater (Bers 2002). Cardiomyocytes can sustain

[2] This chapter is adapted in part from a manuscript titled 'In vitro photoacoustic sensing of calcium dynamics with arsenazo III' (Dana, Fowler, Allen, Zoldan, Suggs and Emelianov 2016). Nicholas Dana is the primary author of this manuscript.

these high concentrations for hundreds of milliseconds (Bers 2002). As such, visualization of Ca2+ exchange is a useful tool in the study of cardiac physiology, for evaluating cellular dysfunction, and in assessing the efficacy of medical interventions.

2.2.2 Optical imaging of Ca and current limitations

Optical imaging – one of the most common methods utilized to assess Ca transport – offers high spatio-temporal resolution and a large palette of Ca-sensitive fluorescent dyes (Herron, Lee, and Jalife 2012), though it is not without drawbacks. This method may require clearance of blood from tissue, and often can only be performed ex vivo (Herron, Lee, and Jalife 2012; Sutherland and Hearse 2000). Additionally, due to the reliance on fluorescent emission, observation of electrical activity is often limited to the tissue surface (Herron, Lee, and Jalife 2012). Such methods are unable to capture the full three-dimensional (3D) nature of tissue electrical propagation, which is known to play a role in cardiac arrhythmia disorders (Winfree 1994). The availability of an imaging technique that can visualize electrical propagation throughout a 3D tissue, with high spatio-temporal resolution and high penetration depth, could offer improved insight into electrophysiological dysfunction and the mechanisms of medical interventions.

2.2.3 Arsenazo III dye

Arsenazo III (Asz) is a Ca chelating dye (Rowatt and Williams 1989), which also exhibits a shift in absorbance dependent upon both dye concentration and pH (Palade and Vergara 1983). In the presence of dissolved Ca, Asz exhibits absorption peaks at 600 nm and 655 nm, the prominence of which depends on the ratio of Ca to Asz (Figure 2.1). At 575 nm, Asz shows minor variation (< 10%) in absorbance relative to Ca concentration, indicating 575 nm can be considered an isosbestic point. Asz has been suggested as a PA contrast agent for observation of Ca concentration changes (Cooley et al. 2010), but PA

imaging results have yet to be obtained using electrophysiologically active cells or tissues.

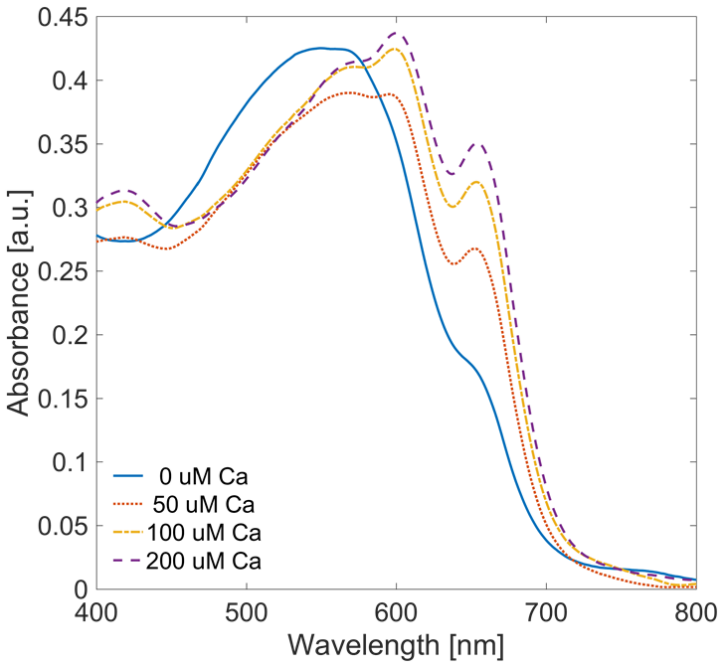

Figure 2.1. Optical extinction of 50 μM Asz dye in buffered saline with varied calcium ion concentration.

2.2.4 Review of photoacoustic imaging

Photoacoustic (PA) imaging relies on optical excitation of endogengous or exogenous chromophores, followed by an ultrasonic detection of the resulting acoustic wave (Beard 2011). Specifically, PA signal is generated by chromophores in the tissue which absorb photons emitted by a pulsed light source. When the pulse duration of the light source is sufficiently short, the absorbed energy results in rapid thermoelastic expansion of the chromophore, which generates an acoustic wave that can be detected using traditional ultrasonic systems (Beard 2011). As such, local PA signal (p_0) is proportional to the absorbed energy, which is a product of local optical absorption (μ_a)

and local fluence (F), both of which are a function of wavelength (λ). PA signal is also proportional to the tissue thermal properties, known as the Grüneisen parameter (Γ) – a function of temperature (T). Combined they result in the photoacoustic equation (Equation 1, shown below:

$$p_0(\vec{r}, \lambda, T) \propto \Gamma(T)\mu_a(\vec{r}, \lambda)F(\vec{r}, \lambda) \qquad \text{Equation 1}$$

The reliance of PA methods on optical absorption make it well suited to monitor absorption-based contrast. For that reason, we investigated PA imaging using Arsenazo III (Asz), a Ca sensitive dye (Rowatt and Williams 1989), to determine the potential for PA based visualization of cytosolic Ca concentration changes resulting from cellular depolarization.

2.3 Materials and Methods

2.3.1 Arsenazo III Dye Preparation

Asz dye (Sigma-Aldrich Inc., St. Louis, MO, USA) was dissolved in stock HEPES buffered normal saline (Sigma-Aldrich Inc., St. Louis, MO, USA). Asz solutions were titrated with NaOH and HCl to a pH of 7.4. Ca solution was obtained by dissolving CaCl2 (Sigma-Aldrich Inc., St. Louis, MO, USA) into the stock buffered saline solution. Ca solution was then added to Asz solution, in varying amounts, to generate different Ca to Asz ratios for extinction measurements and for later PA measurements. Optical extinction measurements were made using a spectrophotometer (UV-3600, Shimadzu Corp., Kyoto, Japan).

2.3.2 Phantom Imaging Studies

Initial studies were conducted on phantom imaging targets containing buffered Asz-Ca solutions to examine PA signal response with respect to varying Asz and Ca concentrations. Asz solution was enclosed in a glass Pasteur pipette and submerged into

degassed water. A 1.5 MHz immersion ultrasound transducer (E1259, Valpey-Fisher, Inc., Hopkinton, MA, USA, 1.5-inch diameter, 1.7-inch spherical focus) was used to receive acoustic signal. The PA signals acquired by the transducer were amplified by an ultrasound pulser/receiver amplifier (5073PR, Olympus NDT Inc., Waltham, MA, USA, gain of 39 dB) in receive mode and digitized using an oscilloscope (CompuScope 12400, Gage Applied Technologies Inc., Lockport, IL, USA) operating at 200 MHz sampling frequency. PA laser excitation was provided by a Q-switched pulsed Nd:YAG laser (Quanta-Ray PRO-290, Spectra-Physics Lasers, Mountain View, CA, USA) pumping a tunable optical parametric oscillator (Spectra-Physics premiScan/MB, GWU-Lasertechnik Vertriebsges, Germany) to select the wavelength. The laser pulse-duration was 5-7 ns, with a pulse repetition rate of 10 Hz and energy varied from approximately 10 mJ – 20 mJ per pulse for the wavelengths used. Samples were irradiated at the approximate isosbestic point (575 nm) and at the two Ca dependent absorption peaks (600 nm and 655 nm). Laser spot size was approximately one cm diameter and light was delivered via air beam. Approximately 5% of laser light energy was redirected and measured with a pyroelectric power meter (Nova II, Ophir Ltd., Jerusalem, Israel) to account for pulse-to-pulse and wavelength dependent energy variation. LabVIEW software (National Instruments, Inc., Austin, TX, USA) was used to integrate components and control data acquisition. This configuration allowed for consistent optical illumination and energy normalization. A diagram of the imaging setup is depicted in Figure 2.2.a.

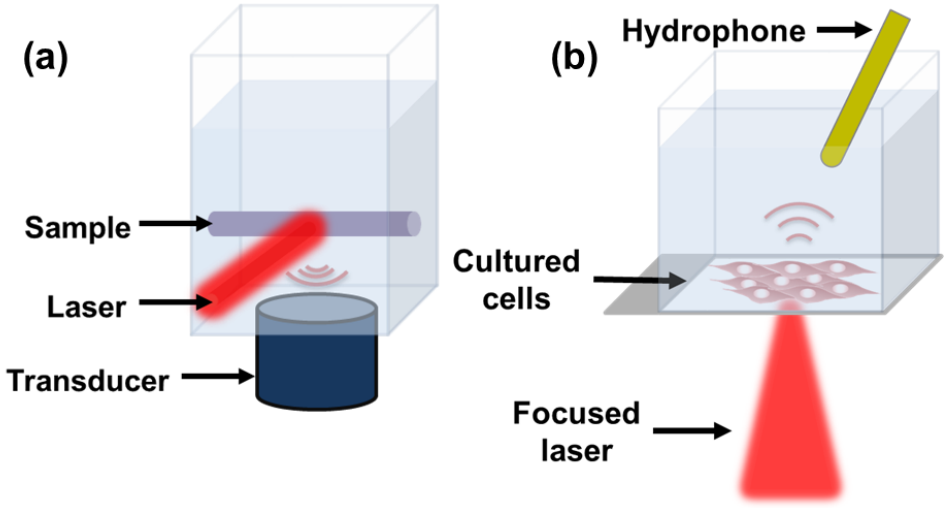

Figure 2.2. Diagram of phantom imaging setup with air-beam laser irradiation and immersion transducer (a). Modified cell-study setup with focused laser and hydrophone (b).

Multiple samples were made by varying Asz dye concentration from 0 µM to 500 µM, as well as using a 500 µM Asz solution and varying the molar ratio of Ca to Asz from 0 to 4. The Asz molar concentration used for PA experiments was 10-fold higher than that used in the UV-Vis extinction curves to achieve a high PA signal. Each sample was injected into the Pasteur pipette and measurements of PA signal amplitude (RF-line) were taken using the system described above, with 300 averages per sample.

2.3.3 HL-1 Culture

HL-1 cardiac myocytes (provided by Dr. William Claycomb, Lousiana State University Health Science Center, New Orleans, LA, USA), which are phenotypically similar to mature cardiomyocytes and exhibit spontaneous depolarization (Claycomb et al. 1998), were used as an in vitro cellular imaging target. HL-1 cell passages 60-80 were maintained in Claycomb medium (Sigma-Aldrich Inc., St. Louis, MO, USA) with 10% fetal bovine serum (Sigma-Aldrich Inc., St. Louis, MO, USA, Lot# 12J001), 1%

Penicillin/Streptomycin (Invitrogen), 1% Glutamax (Invitrogen), and 0.1 mM Norepinephrine (Sigma-Aldrich Inc., St. Louis, MO, USA). Cells were subcultured (1:3) every 4 days (Geuss et al. 2015). Twelve hours before imaging, HL-1 cells were seeded at 80,000 cells/cm^2 in Nunc™ Lab-Tek™ II CC2™ two chamber slides (Thermo Fisher Scientific, Inc., Waltham, MA, USA). Just prior to imaging, cells were rinsed three times and incubated for 20 minutes in Tyrode's solution (Cold Spring Harbor) containing 100 µM Norepinephrine, 200 µM Asz and 10 µM DMSO (Sigma-Aldrich Inc., St. Louis, MO, USA, to improve cellular uptake of Asz). Cells were then thrice rinsed with Tyrode's solution containing Norepinephrine and immediately imaged using either optical or photoacoustic imaging.

2.3.4 Optical and Fluorescent live-cell imaging

In order to optically verify cellular uptake of Asz and observe Asz binding/unbinding of cytosolic Ca, HL-1 cells were treated with Asz and imaged using bright field microscopy (EVOS FL, Thermo Fisher Scientific Inc., Waltham, MA, USA) with a rhodamine cube filter (AMEP4652, Thermo Fisher Scientific Inc., Waltham, MA, USA, emission 593 nm /40 nm FWHM). This setup was able to observe changes in the transmitted light intensity as cytosolic Asz chelates Ca during cellular depolarization (Video S1). Additionally, to independently verify HL-1 myocyte cytosolic Ca dynamics, cells were incubated with a fluo-4 AM calcium assay kit, (F36206, Thermo Fisher Scientific Inc., Waltham, MA, USA) per the manufacturer's instructions, and imaged with fluorescent microscopy using a green fluorescent protein (GFP) cube filter (AMEP4651, Thermo Fisher Scientific Inc., Waltham, MA, USA, emission 525 nm /50 nm FWHM) to verify cellular depolarization (Video S2).

To assess Asz cytoxicity, HL-1 cells were treated with Asz and rinsed, as described above, and immediately incubated using a LIVE/DEAD® cell viability assay kit (L3224, Thermo Fisher Scientific Inc., Waltham, MA, USA) containing calcein-AM and ethidium homodimer-1 (EthD). Cells were incubated for 20 minutes in PBS with 1 μM green-fluorescent calcein-AM to indicate intracellular esterase activity and 2 μM red-fluorescent EthD to indicate a compromised plasma membrane. For comparison, one plate of cells was incubated in PBS with 10 μM DMSO prior to staining with the viability assay kit, as a live control, and an additional plate was incubated in PBS with 70% ethanol (EtOH). Cells were then imaged with fluorescent microscopy using GFP and rhodamine cube filters to visualize calcein-AM and EthD, respectively. Fluorescent images are shown in Figure 2.5.

2.3.5 Photoacoustic Microscopy

PA signal acquisition for cell studies used a photoacoustic microscopy (PAM) system described previously (Cook, Frey, and Emelianov 2013), with a few modifications. The needle hydrophone (Precision Acoustics LTD, Dorchester, UK) was inserted into the slide chamber and positioned just offset from the laser light path, to avoid generation of a PA signal within the hydrophone itself. Hydrophone signals were amplified using an RF amplifier (2100L, Electronics & Innovation, Inc., Rochester, NY, USA, gain of 50 dB). Laser light was directed into the imaging chamber using mirrors and iris apertures, and focused to a spot size of roughly 40 μm by 50 μm (fluence estimated to be 4 kJ/cm^2). Spot size was measured optically at the slide plane using a USAF 1951 positive resolution target (DA009, Max Levy Autograph, Inc., Philadelphia, PA, USA). Figure 2.2.b shows a diagram of the slide chamber, hydrophone and focused laser.

PAM measurements of cells (with and without Asz treatment) were taken in several positions on multiple slides. Once signal at a given position was observed on an oscilloscope, 300 RF-lines were acquired at 10 Hz. RF-lines were bandpass filtered (0.5 MHz/5 MHz) and normalized to fluence using Matlab software (MathWorks, Inc., Natick, MA, USA).

By observing PA signal over a retarded-time 30 second window, we can compare Asz treated and control non-Asz treated cells on time scales that correspond to several depolarization-repolarization cycles. PAM retarded-time data was generated by selecting the region of each RF-line corresponding to the location of the cells. The peak amplitude was sampled from this region for each RF-line and used to construct a 30 second retarded-time signal. This signal was then low-pass filtered at 2 Hz to reduce high-frequency noise while maintaining the signal from cardiac cells, which is expected to be near 1 Hz or below. For Asz treated cells, retarded-time amplitude fluctuations should be proportional to cytosolic Ca concentration. Measurements of retarded-time peak-to-peak values were taken (indicated by the black arrow in Figure 2.6.b) and analyzed from five Asz-treated cell studies and five control cell studies.

2.4 RESULTS

2.4.1 Photoacoustic phantom imaging results

PA phantom results showed linear agreement between PA signal and Asz concentration, as shown in Figure 2.3.a. The coefficient of determination (R2) was 0.99, 0.98 and 0.90 for 575 nm, 600 nm and 655 nm, respectively, with an average R2 = 0.954.

PA phantom spectra with varying Ca to Asz ratio also show general agreement with both extinction data using 50 μM Asz, as well as previous results reported by Rowatt and Williams (Rowatt and Williams 1989). Both data indicate that at a molar

ratio of Ca to Asz equal to one, we expect to see a plateau in the optical extinction at 600 nm, which is reflected in Figure 2.3.b. Data also indicate that extinction at 575 nm should remain generally constant, which is indicated in Figure 2.3.b. Data at 655 nm indicate that extinction should continually increase with increasing Ca to Asz ratio up four, but the increase in PA signal at higher ratios was not as pronounced as that predicted by extinction data.

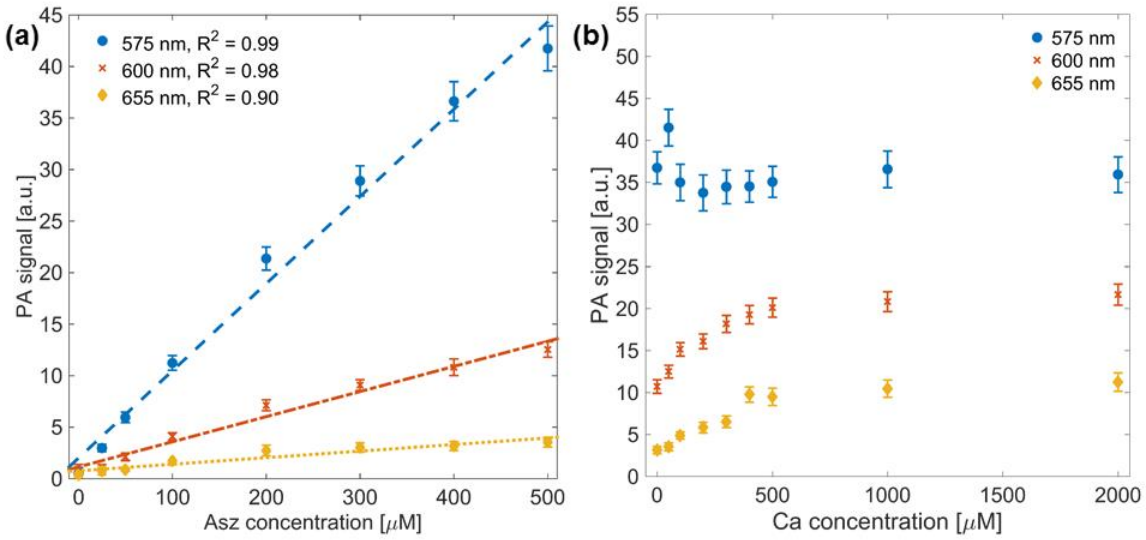

Figure 2.3. PA signal versus Asz concentration with linear fit (dashed line) to PA data (a). with R2 values of 0.99, 0.98 and 0.90 for 575 nm, 600 nm and 655 nm, respectively. PA signal from 500 µM Asz dye with varying Ca:Asz ratio (b). Different colors-markers represent results using 575 nm (blue-circle), 600 nm (red-x) and 655 nm (yellow-diamond) laser light.

2.4.2 Optical imaging results

Cells incubated with the fluo-4 AM and imaged with fluorescence microscopy showed obvious variation in fluorescence emission across time-lapse images (Video S2). This result verified cellular depolarization and cytosolic Ca variation.

Similarly, cells treated with Asz and imaged using bright field microscopy with a rhodamine filter also showed fluctuation in time-lapse series of images (Figure 2.4, Video S1). While these optical changes were less obvious than those observed using fluo-4, these images served as verification that Asz was being successfully incorporated into HL-1 cardiac myocyte cytosol and was responding to dynamic Ca concentration changes.

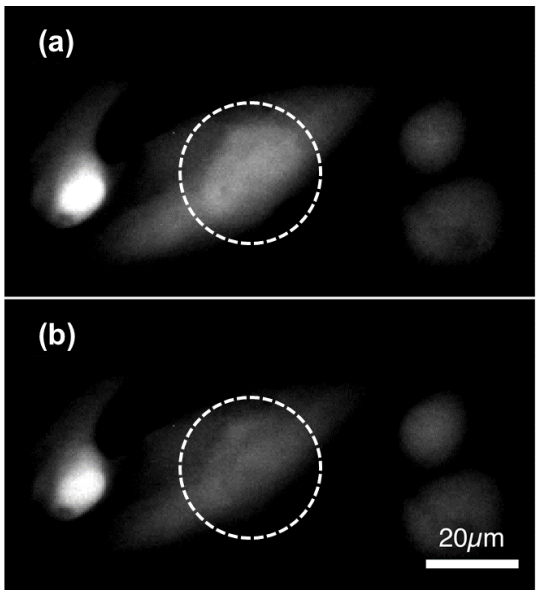

Figure 2.4. Bright field microscopy images, using a red-fluorescent filter, of HL-1 cardiac myocytes incubated with Asz. Images (a) and (b) are part of a time-lapse series, $\Delta t = 10$ seconds.

2.4.3 Cell viability study

Cell viability images indicate that, following 20 minute Asz treatment, most cells exhibit esterase activity and indicate intact plasma membranes (Figure 2.5, Asz row), suggesting most cells are alive immediately following Asz treatment. Though, when compared to live-control images (Figure 2.5, PBS row), viability results suggest that Asz treatment does decrease cell viability, as indicated by the increased EthD stained cells visible in columns a and b of Figure 2.5.

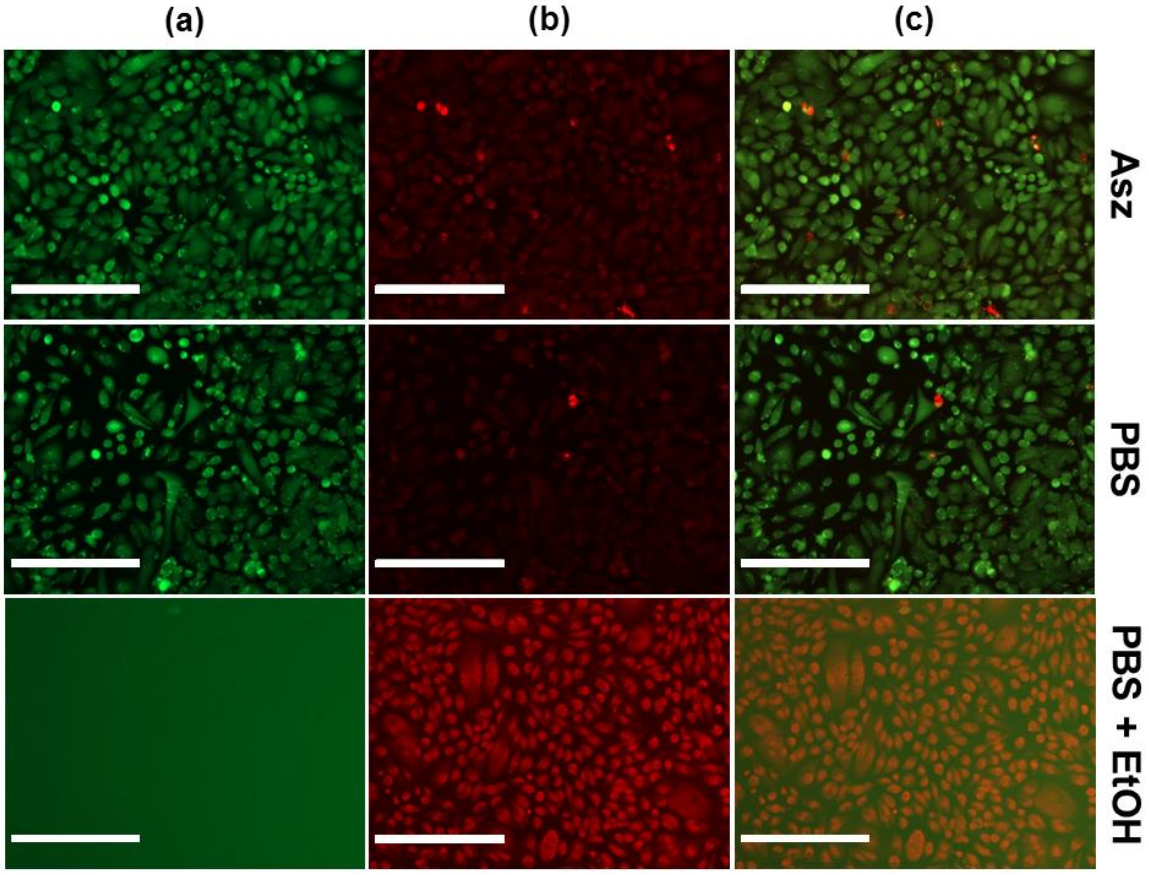

Figure 2.5. Fluorescence microscopy images following cell viability assay for Asz-treated cells (Asz), PBS treated live-control cells (PBS) and Ethanol treated dead-control cells (PBS + EtOH). Green channel (column a) indicates calcein-AM fluorescence (i.e. estera esterase activity/live cells), red channel (column b) indicates DNA-bound EthD fluorescence (i.e. disrupted plasma membrane/dead cells), with overlaid images (column c) for comparison. Micrograph bar indicates 200 μm scale.

2.4.4 Photoacoustic sensing of dynamic calcium concentration

PA RF-line data collected from Asz treated cells and control non-treated cells were compared with respect to their peak PA amplitudes (n = 5, each). RF-line data from Asz treated cells showed, on average, > 100-fold increase in peak RF-line amplitude as compared to control cells (Figure 2.6.a).

Retarded-time PA data (Figure 2.6.b) underwent peak-to-peak analysis, indicated by the black arrow in Figure 2.6.b. Data were compared between Asz treated cells and non-Asz treated cells. For retarded-time data, Asz incubated cells showed, on average, a 10-fold increase in their peak-to-peak standard deviation over the control non-treated cells.

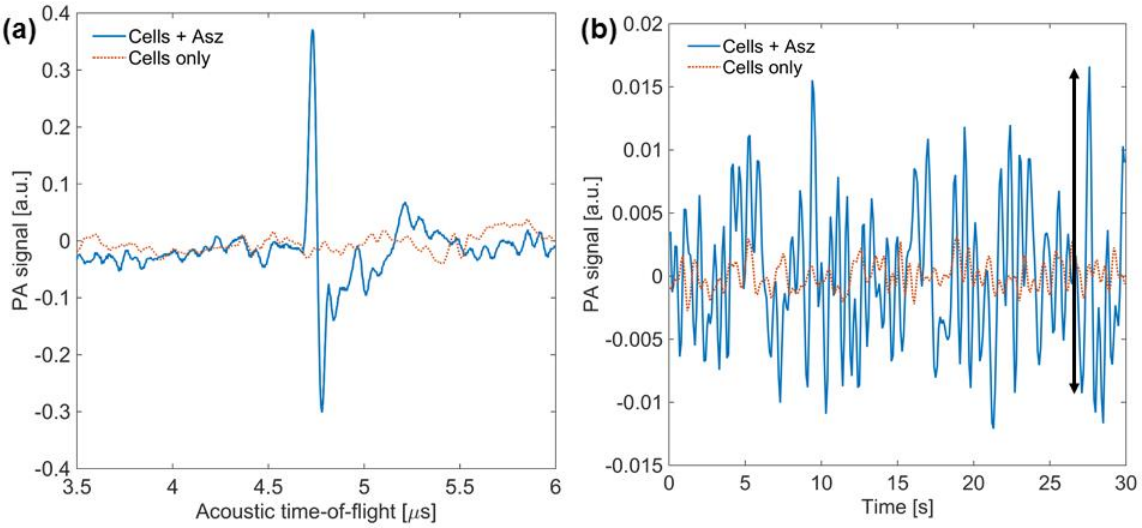

Figure 2.6. PA RF-line of Asz-treated cells and control cells (a). Retarded-time signal of Asz-treated cells and control cells (b). Arrow indicates example of peak-to-peak measurement.

2.5 DISCUSSION

2.5.1 Linearity of phantom-study photoacoustic signal with respect to Arsenazo concentration

PA signal observed during phantom studies showed a strong linear relationship to Asz concentration at 575 nm and 600 nm (R2 = 0.99 and 0.98, respectively), as expected, though PA data at 655 nm did not exhibit as strong a linear relationship to Asz

concentration (R2 = 0.90). This is likely due to low optical absorption of Asz (w/o Ca) at 655 nm, which would reduce signal-to-noise ratio (SNR).

Optical extinction of Asz dye is known to have non-linear absorption based on dye concentration (Palade and Vergara 1983), in addition to those absorption changes dependent on pH and cation concentration. As such, quantitative comparisons between PA measurements from phantom studies and UV-Vis molar extinction coefficients could not be made. Nonetheless, the PA data did show increased signal with increasing Ca to Asz ratio at 600 nm and 655 nm and flat signal at 575 nm (Figure 2.3.b), which qualitatively agrees with UV-Vis data in Figure 2.1. PA signal at 600 nm exhibited an inflection point near a Ca to Asz ratio of one (Figure 2.3.b), which agrees with both UV-Vis data (Figure 2.1) and results from Rowatt, et al. (Rowatt and Williams 1989). At higher ($\geq$ 2) Ca to Asz ratios, UV-Vis data (50 μM Asz concentration) indicates absorption should be greater at 600 nm than at 575 nm, but this was not observed in PA phantom measurements (500 μM Asz concentration). Furthermore, as mentioned above, the PA signal at 655 nm did not increase as much as UV-Vis data would predict for higher Ca to Asz ratios. These results are likely attributable to the higher (10-fold) Asz concentrations used in PA experiments. At these higher concentrations, the non-linear absorption of Asz may become significant. Previous work by Palade, et al, showed that molar extinction, at a given wavelength, differed by approximately a factor of two when comparing Asz samples whose concentrations varied by a factor of 100 (Palade and Vergara 1983). This could account for observed discrepancies between the extinction data and PA phantom results. Unfortunately, initial PA phantom results using matching 50 μM Asz concentration showed poor SNR. To achieve the same SNR using a 10-fold dilute solution, at least 100-fold more averages would be needed, at which point dye

photo-bleaching and photo-chemical reactions may impact results. For that reason, a higher Asz concentration was used in PA phantom imaging studies.

2.5.2 Optical verification of HL-1 depolarization

HL-1 cells stained with both fluo-4, AM (Video S2) and Asz (Figure 2.4, Video S1) showed variations in light intensity as observed using fluorescent and bright field microscopy, respectively. While the quality of the images in Figure 2.4 is low, due to both low light intensity and low contrast, it does indicate that Asz was present in cells and responding to cytosolic Ca concentration. HL-1 cells observed with fluo-4 generally showed poor electrical coupling with their neighbors, which has been observed previously (Geuss et al. 2015). As such, electrical synchronization occurred only on the order of a few cells, at most, which corresponds to a circular region of roughly 40 μm diameter. The PAM system, utilizing highly focused optical excitation (roughly 40 μm diameter spot size), was able to overcome the issues associated with highly localized depolarization, albeit at the cost of lower SNR.

2.5.3 Photoacoustic sensing of calcium transients proof-of-concept

Asz treated cells showed a significant increase over control cells in their maximum RF-line amplitude (Figure 2.6.a), as well as a 10-fold increase in the peak-to-peak values in the retarded-time traces (Figure 2.6.b), suggesting the PAM studies using Asz dye were successful in observing absorption changes resulting from Asz binding/unbinding dynamic cytosolic Ca. It should be noted that peak-to-peak analysis was done without any peak-threshold criteria (i.e. minimum increase over the neighboring values). When any peak-threshold criteria was used, very few “peaks” were observed in control retarded-time data, though data from Asz treated cells still demonstrated multiple peaks in all samples. This suggests this technique may have

sufficient sensitivity for PA imaging of dynamic Ca concentration to visualize ion changes in vivo, once properly adapted.

Because PA signal generation results from absorbed light, it is not limited by ballistic-photon propagation, as other optical techniques are. This technique could potentially allow 3D reconstruction of cellular depolarization at moderate (~ 1 cm) tissue depths. It also has the ability to monitor depolarization in real-time, as was demonstrated herein.

2.6 Conclusion

These results demonstrate proof-of-concept for contrast-enhanced PA imaging to monitor ion-concentration changes resulting from cellular depolarization. While these initial results are promising, work remains to develop non-toxic, NIR-absorbing, ion-sensitive contrast agents. Ideal agents would exhibit a strong absorption shift in the NIR (preferably at 1064 nm) upon ion binding, and have minimal cytotoxicity. This would also allow translation of contrast-enhanced PA monitoring of dynamic ion concentration to animal models, where electric and ionic coupling will be present up to the organ level. Such studies would allow quantitative comparison of PA data to ECG/EMG measurements, and further assess the potential of this technique to spatiotemporally resolve 3D tissue depolarization.

2.7 References

Bers, Donald M. 2002. 'Cardiac excitation-contraction coupling', Nature, 415: 198-205.

Catterall, William A., and Alexandra P. Few. 2008. 'Calcium Channel Regulation and Presynaptic Plasticity', Neuron, 59: 882-901.

Claycomb, William C., Nicholas A. Lanson, Beverly S. Stallworth, Daniel B. Egeland, Joseph B. Delcarpio, Anthony Bahinski, and Nicholas J. Izzo. 1998. 'HL-1 cells: A cardiac muscle cell line that contracts and retains phenotypic characteristics of the adult cardiomyocyte', Proceedings of the National Academy of Sciences, 95: 2979-84.

Cold Spring Harbor. 'Tyrode's solution', Cold Spring Harbor Protocols, 2006.

Cook, Jason R., Wolfgang Frey, and Stanislav Emelianov. 2013. 'Quantitative Photoacoustic Imaging of Nanoparticles in Cells and Tissues', ACS Nano, 7: 1272-80.

Cooley, Erika J., Pieter Kruizinga, Darren W. Branch, and Stanislav Emelianov. 2010. "Evaluation of arsenazo III as a contrast agent for photoacoustic detection of micromolar calcium transients." In, 75761J-61J-8.

Geuss, Laura R., Alicia C. B. Allen, Divya Ramamoorthy, and Laura J. Suggs. 2015. 'Maintenance of HL-1 cardiomyocyte functional activity in PEGylated fibrin gels', Biotechnology and Bioengineering, 112: 1446-56.

Herron, Todd J., Peter Lee, and José Jalife. 2012. 'Optical Imaging of Voltage and Calcium in Cardiac Cells & Tissues', Circulation Research, 110: 609-23.

Palade, P, and J Vergara. 1983. 'Stoichiometries of arsenazo III-Ca complexes.', Biophysical Journal, 43: 355-69.

Rowatt, E., and R. J. Williams. 1989. 'The interaction of cations with the dye arsenazo III', Biochemical Journal, 259: 295-98.

Sutherland, Fiona J., and David J. Hearse. 2000. 'The isolated blood and perfusion fluid perfused heart', Pharmacological Research, 41: 613-27.

Winfree, AT. 1994. 'Electrical turbulence in three-dimensional heart muscle', Science, 266: 1003-06.

Chapter 3: In Vitro Photoacoustic Characterization Of Radiofrequency Cardiac Ablation Lesions[3]

3.1 ABSTRACT

Radiofrequency (RF) ablation to treat atrial arrhythmia is limited by an inability to reliably assess lesion durability and transmurality. In this study, we investigate the feasibility of combined ultrasound (US) and spectroscopic photoacoustic (sPA) imaging to visualize RF ablation lesions in 3-D based on unique differences in the optical absorption spectra between normal and ablated myocardial tissue. We aim to determine feasibility of photoacoustic characterization of myocardial ablation lesions in vitro. Tissue samples were excised from the ventricles of fresh porcine hearts. Lesions were generated using an RF catheter ablation system using 20 - 30 W of power applied for 40 - 60 s. Ablated samples were imaged in the NIR regime (740-780 nm) using a combined PA/US imaging system. Measured PA spectra were correlated to the absorption spectra of deoxy-hemoglobin and ablated tissue to produce a tissue characterization map (TCM) identifying 3-D lesion location and extent. Tissue samples were stained and photographed for gross pathology. TCM and gross pathology images were co-registered to assess TCM accuracy. The TCM reliably characterized ablated and non-ablated tissue up to depths of 3 mm. The TCM also assessed lesion position and extent with sub-millimeter accuracy in multiple dimensions. Segmented TCMs achieved greater than 69% agreement with gross pathology. These results suggest that sPA imaging has the potential to accurately assess RF ablation lesion size and position with sub-millimeter precision and may be well suited to guide trans-catheter RF atrial ablation in clinical practice.

[3] This chapter is adapted in part from a manuscript titled 'In vitro photoacoustic visualization of myocardial ablation lesions', (Dana, Di Biase, Natale, Emelianov and Bouchard, 2014). Nicholas Dana is the primary author of this manuscript.

3.2 INTRODUCTION

3.2.1 Atrial Fibrillation

Atrial fibrillation (AF) is currently the most common arrhythmia encountered in clinical practice, with estimates as high as 6.1 million sufferers in 2010 in the United States alone (Roger et al. 2012; Miyasaka et al. 2006). AF has been implicated in an increased risk of stroke, dementia, heart failure and an excess mortality rate (Roger et al. 2012; Wolf, Abbott, and Kannel 1991; Wolf et al. 1998; Benjamin et al. 1998). Anti-arrhythmic drugs are burdened with significant side effects, toxicity and poor capability to maintain NSR and thus are not the ideal treatment option for AF patients (Shah 2011; Cappato et al. 2010; Santangeli et al. 2011). Radio-frequency (RF) trans-catheter ablation is currently the most effective treatment for AF (Shah 2011) as it can isolate the firing of ectopic foci, typically located around the pulmonary veins (Haissaguerre et al. 1998; Pappone et al. 2000). Unfortunately, RF ablation lesions can vary considerably with catheter contact force, orientation, size and RF energy parameters (Shah 2011; Rosenbaum et al. 1994; Petersen, Chen, Pietersen, Svendsen, and Haunso 1999; Petersen, Chen, Pietersen, Svendsen, and Haunsø 1999). Lesion "reconnection" and "recovery" has been a major cause for procedural failure and can necessitate repeat procedures (Shah 2011; Cappato et al. 2010). Furthermore, ablation procedures carry the risk of severe complications, such as atrio-esophageal fistulae or cardiac tamponade (Shah 2011; Cappato et al. 2010). These limitations of RF trans-catheter ablation will not be significantly improved without a real-time (RT) tool to characterize lesions intraoperatively (Shah 2011).

3.2.2 Guidance of atrial fibrillation treatment

Several attempts have recently been made to address this need by probing changes that occur in tissue as RF energy denatures proteins and disrupts native structure. MRI has been used both to guide RF trans-catheter ablation (Ranjan et al. 2012) and to provide thermographic information (Kolandaivelu et al. 2010). Unfortunately, MRI for these applications tends to suffer from poor spatial resolution and low frame rates (1.8 mm and < 5 frames per second [fps], respectively, for real-time MRI and 1.7 mm and < 1 frame per 4 cardiac cycles, respectively, for MRI thermography) (Ranjan et al. 2012; Kolandaivelu et al. 2010). Additionally, both techniques require the advent of MRI compatible equipment (Ranjan et al. 2012; Kolandaivelu et al. 2010), and long-duration MRI studies can be cost prohibitive.

Optical coherence tomography (OCT) is being investigated as a means to assess lesion formation and provide real-time feedback to physicians during ablation procedures (Fleming et al. 2010). OCT relies on back-scattered light from a coherent source to interrogate tissue optical properties. The reliance on quasi-ballistic photon propagation limits OCT by imposing a maximum imaging depth of approximately 1 mm (Fleming et al. 2010), restricting the use of OCT to only atrial regions where tissue is thinnest and limiting assessment of transmurality. Acoustic radiation force impulse (ARFI) imaging is an ultrasound (US)-based elasticity imaging technology being investigated as a means to intraoperatively identify RF ablation lesions (Eyerly et al. 2010; Eyerly et al. 2012). ARFI imaging interrogates mechanical properties by analyzing the ARFI-induced dynamic response of tissue. ARFI relies on micrometer-order tissue displacement, making it particularly susceptible to motion artifacts, that results in a significant fraction of unusable images (Eyerly et al. 2012).

3.3.3 Photoacoustic imaging

Photoacoustic (PA) imaging is making inroads as a novel medical imaging technique utilizing short-duration laser pulses (Xu and Wang 2006; Beard 2011) which are absorbed by chromophores (such as deoxy-hemoglobin [Hb]) in the tissue, resulting in thermoelastic expansion and generation of an acoustic (Xu and Wang 2006; Beard 2011). These local transients can be imaged using a traditional US transducer (Bouchard et al. 2012; Shah et al. 2008; Wang et al. 2012a), providing an optical absorption map with resolutions on the order of tens of micrometers (or hundreds of micrometers using a 7.5 MHz US probe, which is common for EP intracardiac or transesophageal US applications and comparable to MRI) and at imaging depths in excess of a centimeter (Xu and Wang 2006; Beard 2011; Bouchard et al. 2012; Shah et al. 2008; Wang et al. 2012a).

The peak photoacoustic pressure, generated during thermal and stress confinement, is commonly modeled as:

$$p_0(\vec{r},\lambda,T) \propto \left(\frac{\beta(\vec{r},T)\, v_s^2(\vec{r},T)}{C_p(\vec{r},T)}\right) \mu_{abs}(\vec{r},\lambda)\, F(\vec{r},\lambda) \qquad \text{Equation 2}$$

where $\beta(\vec{r},T)$ [K^{-1}] is the temperature dependent thermal coefficient of volume expansion, $v_s(\vec{r},T)$ [cm s^{-1}] is the sound velocity in tissue, $C_p(\vec{r},T)$ [J kg^{-1} K^{-1}] is the heat capacity at constant pressure, $\mu_{abs}(\vec{r},\lambda)$ [cm^{-1}] is the optical absorption coefficient and $F(\vec{r},\lambda)$ [J cm^{-2}] is the local optical fluence(Xu and Wang 2006; Beard 2011). As such, $\vec{r},\lambda$ and T represent spatial distribution, optical wavelength and temperature, respectively.

PA imaging contrast is provided by variations in optical absorption (μ_{abs}) resulting from variations in the concentration of endogenous or exogenous chromophores. Due to the wavelength dependence of μ_{abs} (Swartling et al. 2003; Thomsen, Jacques, and Flock 1990), spectroscopic photoacoustic imaging (sPA) can be

performed for tissue characterization purposes (Ntziachristos 2010). PA imaging's reliance upon ultrasonic sensing allows straightforward co-registration with anatomical US images, providing molecularly sensitive anatomical PA/US images (Bouchard et al. 2012; Shah et al. 2008; Wang et al. 2012a). For these reasons, PA imaging is being pursued as a powerful medical imaging modality in cancer detection (Mallidi, Luke, and Emelianov 2011), disease staging (Wang et al. 2012b) and therapy monitoring (Shah et al. 2008).

3.3 METHODS

3.3.1 Sample preparation and ablation

Fresh porcine hearts (Sierra for Medical Science, Whittier, CA) were acquired within 24 hours of sacrifice and were never frozen. The ventricles were harvested and samples were excised from these portions to produce approximately 20x20x10 mm^3 sized specimens for ablation. The ablation system consisted of a Stockert 70 RF generator combined with a COOLFLOW® irrigation pump and a THERMOCOOL® irrigated tip catheter (Biosense Webster Inc., Diamond Bar, CA). During each ablation, the catheter was flushed with PBS. RF energy was applied at a rate of 20 - 30 W for 40 - 60 s. Tissue samples were submerged in normal PBS during ablation and then patted dry and returned to an airtight container and refrigerated.

3.3.2 Imaging system setup and procedure

Normal PBS was used to acoustically couple the imaging system with the tissue. Imaging was performed on a combined PA/US imaging system consisting of a Vevo® 2100 US imaging system (FUJIFILM VisualSonics Inc., Toronto, ON, Canada) paired with an LZ-250 transducer (21-MHz center frequency) with integrated fiber optics connected to a pulsed, tunable Nd:YAG laser (680 - 970 nm wavelength range). A single

three-dimensional (3-D) combined PA/US B-mode scan was performed on each sample at 710 nm. From that 3-D volume, a single 2-D plane corresponding to the brightest region of the PA signal was selected for sPA imaging from 680 - 840 in 2-nm steps. Ten frames were averaged into a single PA/US image at each sampled wavelength (e.g. Figures 3.2A and 3.3B). Energy was measured at the fiber bundle output using an external power meter. This protocol was used to image eight ablated samples harvested from two porcine hearts. Later, a full 3-D PA/US volume was acquired for each wavelength from 740 – 780 nm in 5-nm steps. At each wavelength, six PA/US volumes were averaged. The resulting 3-D sPA data were normalized to the average laser energy at each corresponding wavelength. This second protocol was used to image six ablated samples from two additional porcine hearts. A schematic of the imaging system is shown in Figure 3.1.

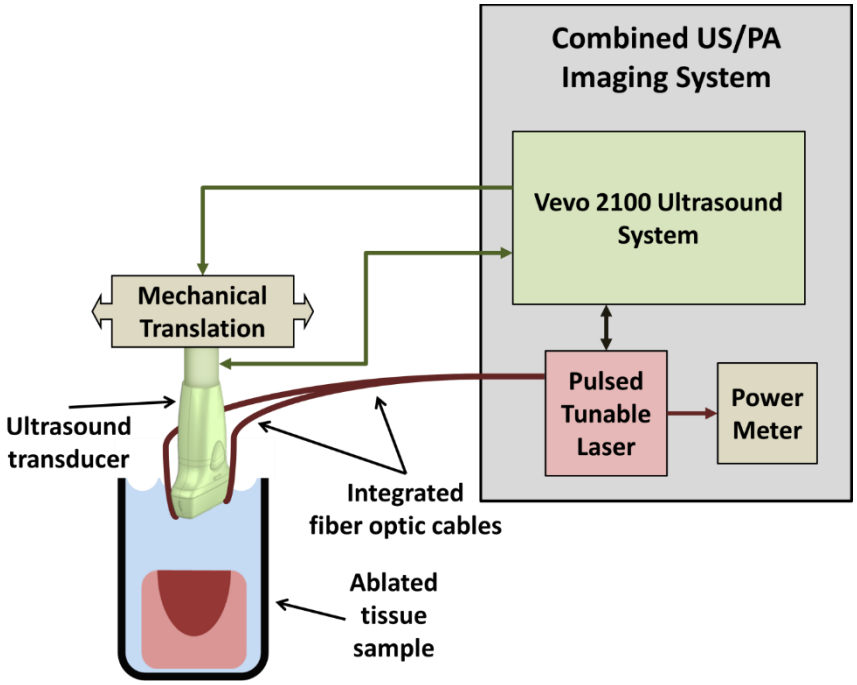

Figure 3.1. Schematic of combined PA/US imaging system.

3.3.3 Sample staining procedure

For the purpose of sample staining, nitro-tetrazolium blue (NTB) salt (Sigma-Aldrich Corp., St. Louis, MO) was chosen to identify macroscopic myocardial tissue necrosis (Ramkissoon 1966). The NTB solution was prepared by dissolving NTB in normal PBS at 0.5 mg ml^{-1} and maintained at 35 C°, as outlined by Ramkissoon (Ramkissoon 1966). All specimens were incubated in the NTB solution for 15 minutes, then patted dry and photographed for gross pathology.

3.3.4 ROI selection and analysis

Equal-sized regions-of-interest (ROIs; 0.04 mm^2) of the PA signal center (Ablated) and a specimen region external to the lesion (Non-ablated) were selected from the 2-D sPA dataset for analysis, as shown in the white boxes in Figure 3.2A.

3.3.5 Contrast and reference spectra

Contrast-to-background ratio (CBR) was calculated using the mean PA signal intensity for the Ablated and Non-ablated ROIs. To obtain PA signal spectra, the mean PA intensities for both ROIs were calculated and plotted as a function of wavelength; Figure 3.2B shows representative spectra observed in Ablated (red) and Non-ablated (blue) myocardium (normalized for display purposes). These spectra differ considerably near 760 nm, where the Non-ablated spectrum has a prominent hump, which correlates well with the extinction spectrum of Hb (Jacques 2013), and is absent from the Ablated spectrum. For this reason, two spectra (Figure 3.2D) were selected for a Pearson correlation test to characterize the two tissue types. Ablated reference spectra were obtained by averaging ROIs from ablated samples (n = 8) harvested from two separate hearts. The known extinction spectrum for Hb was normalized and used as a reference for the non-ablated tissue.

3.3.6 Spectroscopic photoacoustic image processing and correlation

Prior to the correlation test, each sPA dataset was filtered spatially and to reduce noise. For the 3-D sPA data, each 3-D volume was filtered using a 3-D sliding average kernel. Voxel-by-voxel correlation, using both the Ablation-reference and the Hb-reference spectra, was performed on each 2-D and 3-D sPA dataset through 740 - 780 nm. For each sPA dataset, Ablation reference and Hb reference correlation maps were obtained. A final tissue characterization map (TCM, Figure 3.2C) was then generated. Voxels of the TCM showing high ($r \geq 0.65$) Ablation-reference or Hb-reference correlation were displayed as either red or blue, respectively, whereas voxels showing high correlation to both spectra were color coded green. TCM voxels showing poor correlation ($r < 0.65$) to both spectra were not color coded. For each voxel that correlated to either Ablation or Hb reference spectra, the p-value of the correlation was calculated based on the null hypothesis. 3-D rendering of the data (Figure 3.4A and 3.4B) was achieved with Amira (VSG, Burlington, MA); a clipping plane was introduced at the location of the tissue bisection (Figure 3.4B) to compare 3-D TCMs with the side-view gross pathology (Figure 3.4D).

3.3.7 Image registration and comparison

Three-dimensional TCM/US data was co-registered with matching photographed gross pathology. Gross pathology photographs were acquired in top-view and side-view orientations. Both orientations were adjusted so that the gross pathology field of view (FOV) represented the same FOV as the US volume. In the top-view gross pathology images, tissue sample boundaries and the ablated region were manually segmented from the photograph background (Figure 3.3A, blue and red, respectively) and a line was placed to identify the tissue bisection plane. An equivalent top-view orientation was then

reconstructed using the TCM/US volume data with matching segmentations performed on this reconstructed view.

A straightforward rigid image registration was applied to both top- and side-view image sets. Once the top-view gross pathology and matched TCM/US data were co-registered, an image slice was selected from the TCM/US data that corresponded to the tissue bisection plane. A similar segmentation and registration process was then performed on the side-view gross pathology and selected TCM/US data (Figures 3.3C and 3.3D, respectively).

Once both the top- and side-view image sets were co-registered, the accuracy of the TCM was determined. The centroids of the ablated-region segmentations were calculated for each gross pathology and TCM set. For each co-registered set, the lateral, axial and elevation offsets between the centroids were measured. Agreement between the segmentations was assessed by comparing the maximum axial, lateral or elevation extent of the segmented region. The % Area agreement was defined as follows:

$$\%\ \text{Area Agreement} = (I_{TCM} \cap I_{GP} / I_{TCM} \cup I_{GP}) \times 100\% \qquad \text{Equation 3}$$

Where I_{TCM} and I_{GP} represent the segment TCM image and gross pathology image, respectively, and $\cap$ and $\cup$ are the intersect and union sets, respectively. For the side-view co-registered samples, two samples were utilized to assess elevation offset, while four samples were utilized to assess lateral offset; all six side-view co-registered samples were utilized to assess axial offset.

3.4 RESULTS

3.4.1 Single-wavelength analysis

Figure 3.2A shows a representative single-wavelength combined PA/US image acquired at 710 nm. Based on matched gross pathology images of the stained sample, the

red-orange region located at the image center, at approximately 11 mm depth, correlates to the core of the lesion. For Figure 3.2A, $\bar{I}_{Abl}$ = -7.8 ± 3.0 dB, $\bar{I}_{Nabl}$ = -38.6 ± 2.4 dB (both normalized to the PA signal peak intensity at 710 nm), and CBR is 30.7 ± 3.1 dB.

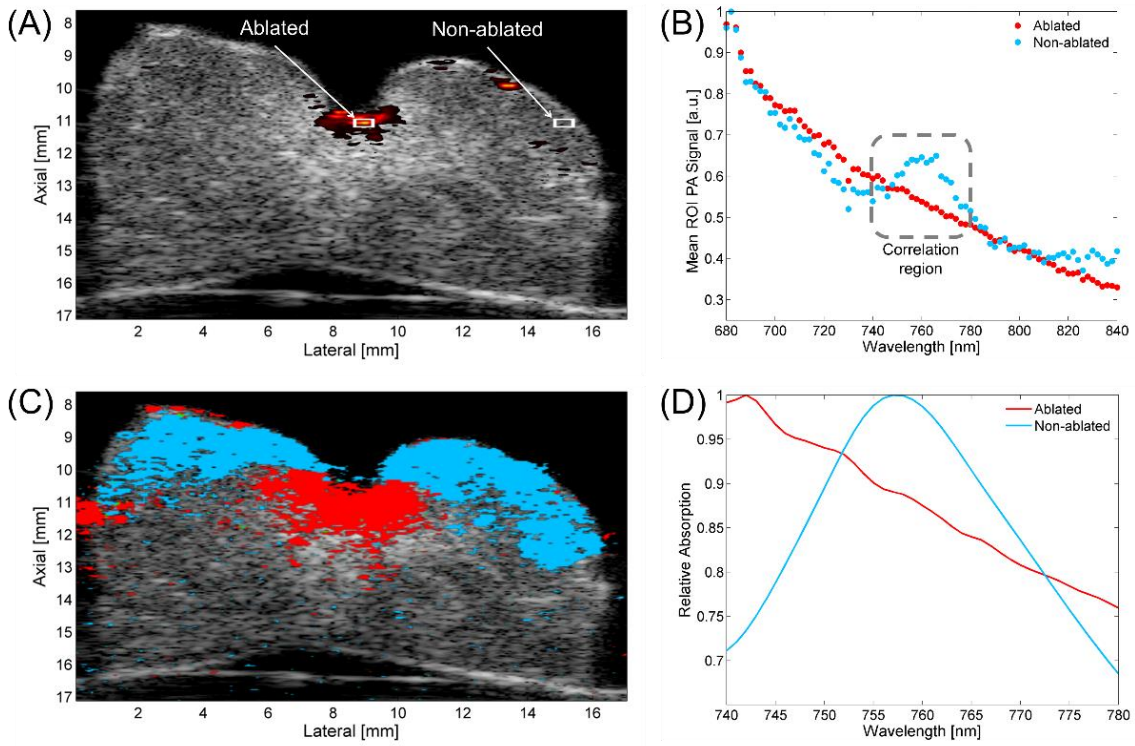

Figure 3.2. Single-wavelength PA image (710 nm) overlaying US image with Ablated and Non-ablated ROIs (A). Mean ROI photoacoustic signal plotted vs. wavelength (B). Tissue characterization map (TCM) (C). Reference spectra for Ablated (averaged over eight samples from two hearts) and Non-ablated (derived from optical extinction data from deoxy-Hb) tissue (D).

3.4.2 Spectroscopic analysis

Both normalized spectra from the ROIs in Figure 3.2A are shown in Figure 3.2B. The Ablated absorption spectrum monotonically decreases, which agrees with results obtained by Swartling, et al. (Swartling et al. 2003) The Non-ablated absorption spectrum agreed well with that of Hb (Jacques 2013), notably displaying a prominent hump near

760 nm. In this wavelength range, Hb is expected to be the dominant absorber in a harvested (i.e. oxygen depleted) myocardial sample.

An example of the TCM overlaying the corresponding B-mode US image is displayed in Figure 3.2C. The correlation maps demonstrate the ability to visualize both ablated and non-ablated tissue at greater depth and extent than that afforded by single-wavelength PA images. Figure 3.2C indicates, at lateral positions of 6 mm and 10.5 mm, the correlation protocol was able to identify 2 - 3 mm of ablated myocardium beneath at least an additional millimeter of non-ablated myocardium. This was typical of both 2-D and 3-D imaged samples, where the sPA data showed good correlation to absorbers up to a depth of 3 mm. The average correlation p-value (as estimated using a two-tailed student's T-test) over all voxels was 0.0104 ± 0.0098, suggesting that the overall correlation was significant.

3.4.3 Lesion dimension statistics

The results of the 3-D segmentation comparison are shown in Table 3.1. For the top-view orientation (Figures 3.3A and 3.3B), good agreement between the gross pathology images and TCM was achieved, with no elevation and low lateral (0.4 mm) offset measured. The absolute difference between the average lateral and elevation extent was 1 mm or less, and well within the standard deviations for both measurements. The mean segmented lesion areas were calculated to be 37.8 ± 15.8 mm^2 and 41.8 ± 16.4 mm^2 for the TCM and gross pathology, respectively. The difference between these areas was 4.0 mm^2 (approximately 10% total lesion area), which is within the standard deviations of both measurements. The % Area Agreement, as defined in Equation 3, was approximately 70% averaged across all 6 samples, indicating good TCM and gross pathology agreement for all 3-D volumes.

Lesion dimension statistics (n = 6 samples total)				
Top-view orientation				
Metric	Axial (mm)	Lateral (mm)	Elevation (mm)	Segmented Area (mm^2)
TCM offset	-	0.4 ± 0.4	0.0 ± 0.7	-
TCM extent	-	7.4 ± 1.8	7.3 ±1.6	37.8 ± 15.8
Gross pathology extent	-	6.5 ±1.9	8.3 ±1.5	41.8 ± 16.4
% Area agreement	-	-	-	69 ± 11%
Side-view orientation				
TCM offset	1.2 ± 0.8	0.1 ± 0.7	0.9 ±1.5	-
TCM extent	3.4 ± 1.0	8.0 ± 1.4	6.3 ± 1.9	14.5 ± 4.9
Gross pathology extent	5.3 ± 1.0	7.8 ± 1.4	10.9 ± 3.7	30.7 ± 10.1
Area agreement	-	-	-	36 ± 18%

Table 3.1. Comparison of lesion segmentation metrics (n = 6 samples total) from top- and side-view gross pathology and TCM/US registrations.

For the side-view orientation (Figures 3.3C and 3.3D), the two samples cut parallel to the elevation axis showed an average of a 0.9-mm offset in that dimension. The samples cut laterally showed good lateral agreement (offset of 0.1 mm). The axial dimension showed the greatest offset, averaging 1.2 mm across all 6 samples. The

average axial extent of the lesion segmentations was 3.4 ± 1.0 mm and 5.3 ± 1.0 mm, for the TCM and gross pathology, respectively. Mean segmented areas were calculated to be 14.5 ± 4.9 mm^2 and 30.7 ± 10.1 mm^2 for the TCM and gross pathology, respectively, while the % Area Agreement was 36% (averaged across 6 samples).

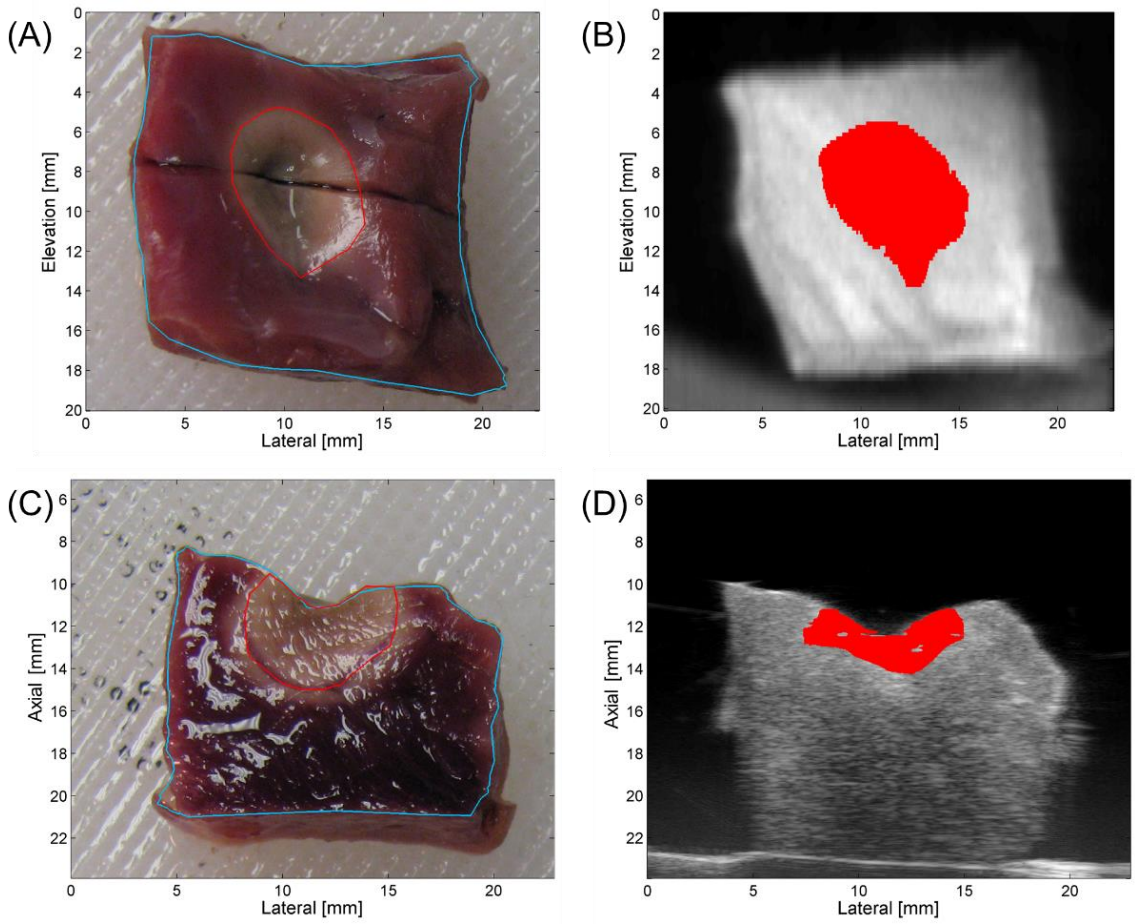

Figure 3.3. Top-view (A) and side-view (C) stained sample gross pathology with sample-boundary (blue) and Ablated-region (red) segmentation. Matching top- (B) and side-view (D) TCM-US images with segmented Ablated region (red).

The 3-D rendered data compared well with the matching gross pathology (Figures 3.4A-D). In this data set, there are two distinct regions of ablated tissue surrounded by

non-ablated tissue and separated by an approximately 2-mm non-ablated gap (Figure 3.4A). The tissue is also consistently identified to depths greater than 2 mm, for both ablated and non-ablated myocardium, and generally agrees well with the matched gross pathology (Figure 3.4C and 3.4D).

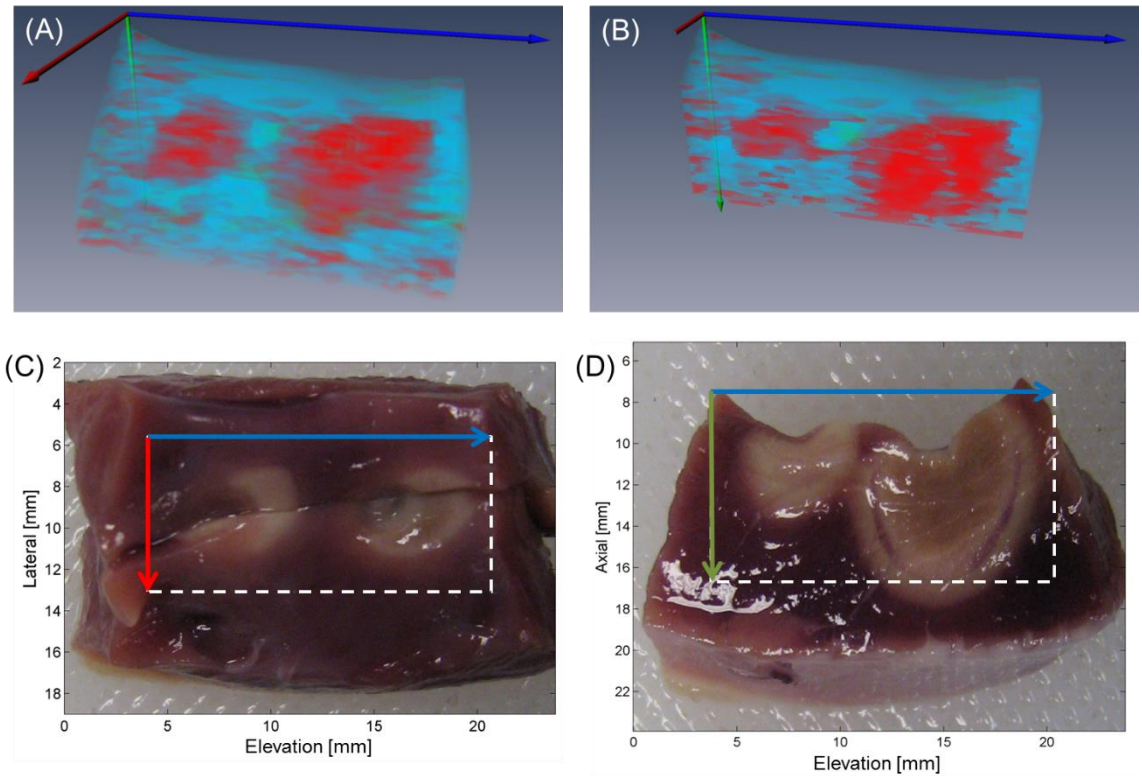

Figure 3.4. Three-dimensional rendering (A) of TCM volume with clipping plane corresponding to tissue bisection (B). Matching top- (C) and side-view (D) gross pathology photographs with axes and FOVs indicated by arrows and boxes, respectively.

3.5 DISCUSSION

3.5.1 Segmentation metrics

Single-wavelength PA imaging shows high contrast from the lesion core, which indicates it may be useful as a pilot scan to locate the approximate lesion center, but it

lacks the ability to fully differentiate ablated vs. non-ablated myocardium. In comparison, the sPA-based TCM demonstrated the ability to reliably identify ablated and non-ablated myocardium with high accuracy and sub-millimeter precision (Figures 3.2C, 3.3B, 3.3D, 3.4A and 3.4B). TCM images of ablated and non-ablated tissue appear relatively uniform across the entire imaged area or volume (Figures 3.2C, 3.3B, 3.3D, 3.4A and 3.4B). All TCM images showed consistent tissue characterization and correlated well to matched images of gross pathology to at least 2 mm in depth (Figures 3.2C, 3.3 and 3.4).

One caveat of PA imaging is that imaging artifacts, resulting from refractive index discontinuities, can occasionally be seen near tissue boundary locations. These artifacts, however, would be minimal in an in vivo environment, as the imaging target would not be an explanted tissue sample with tissue-solution boundaries. Also, spectroscopic-based images, such as a TCM, may further reduce artifacts by correlating multiple wavelengths and reducing the effects of saturated voxel regions by identifying absorbers. It should also be noted that the particular imaging system used has reduced SNR at the left and right frame edges, which also contributes to image artifacts in the TCM as broadband noise weakly correlates with the Ablated spectrum. Given the 3-D datasets (Figures 3.3B, 3.3D, 3.4A and 3.4B) were acquired using only six averages and without laser energy pulse-to-pulse normalization, increased frame averaging, improved energy normalization and increased surface fluence should improve TCM quality and increase depth penetration beyond 3 mm. Given its depth penetration capabilities, PA imaging may be best suited for guidance of trans-catheter ablation of atrial arrhythmia.

3.5.2 Image registration comparison

When considering the segmentation metrics, it should be first noted that a basic rigid registration method was utilized that did not account for tissue deformation, which

will inherently introduce error. Despite this limitation, excellent agreement was achieved with the top-view comparisons, with no elevation and small lateral offset observed. Furthermore, the average top-view segmented areas differed only by 4 mm^2, yielding a % Area Agreement of 69 ± 11%; this area agreement is comparable with other lesion imaging methods currently being developed (Eyerly et al. 2010).

For the side-view orientation, lateral offset was improved when compared to the top-view orientation (0.1 mm vs. to 0.4 mm). The relatively high axial offset (1.2 mm) observed in this orientation is attributable to the limited ability in this initial implementation of sPA imaging to characterize tissue at depths greater than 3 mm; this penetration depth can be increased with improved frame averaging, improved energy normalization and increased laser fluence. With said improvements the ability of this imaging modality to reliably characterize tissue and assess transmurality at depths > 3 mm could be determined. As can be seen in Figure 3.3C and 3.4D, the ablated regions extend axially from approximately 10 mm to 15 mm and 11 mm to 16 mm, respectively (5 mm in both instances). The deepest 2 mm of ablated myocardium was not visualized, so the axial position of the segmented TCM centroid naturally appears shallow compared to the centroid of the segmented lesion from photographed gross pathology. This also accounts for the lower % Area Agreement score (36%) when compared with the top-view results (69%).

3.5.3 Three-dimensional rendering comparison

The 3-D rendering (Figures 3.4A and 3.4B) of the dual-lesion data gave the opportunity to examine the ability of the system to identify adjacent lesions. We can clearly see two distinct regions, approximately 4 mm in diameter each, which correlate strongly to the Ablated reference (red); surrounding these two regions is tissue that

consistently correlates to the Non-ablated reference (blue). This segmentation agrees well with gross pathology images, shown in Figures 3.4C and 3.4D. Additionally, a small region of tissue that correlates to both reference spectra is seen lying between the two lesions in Figure 3.4B (green). This segmentation agrees well with matching gross pathology (Figure 3.4D), as a small isthmus of ambiguous tissue lies between the two lesions (approximately 11 mm in the axial and elevation dimensions). This result emphasizes the ability of sPA to identify regions where lesion contiguity may be in question.

3.5.4 Thermal denaturation effects

Given that the PA spectrum observed in ablated tissue results from bulk hyperthermia-induced protein denaturation, resulting from tissue heating, it is believed that this spectrum would not vary significantly from patient to patient, nor vary significantly between normal or pathologic myocardium. Also, given that thermal damage generally eliminates the observed birefringence resulting from myocardial muscle-fiber orientation, it is believed that PA imaging would be insensitive to fiber orientation.

3.6 CONCLUSION

In conclusion, for this initial study, we demonstrate the feasibility of using sPA imaging to provide 3-D visualizations of ablated and non-ablated myocardium in an excised porcine myocardial ablation model. When compared with co-registered stained gross pathology, sPA imaging achieved sub-millimeter accuracy in identifying lesion position and extent and reliably characterized tissue to depths of 3 mm, including identifying adjacent and non-contiguous lesions. These initial results suggest that sPA

imaging, with its molecular specificity and high spatial resolution, may be well suited as a clinical tool to guide trans-catheter ablation of atrial arrhythmia.

3.7 REFERENCES

Beard, P. 2011. 'Biomedical photoacoustic imaging', Interface Focus, 1: 602-31.

Benjamin, E. J., P. A. Wolf, R. B. D'Agostino, H. Silbershatz, W. B. Kannel, and D. Levy. 1998. 'Impact of atrial fibrillation on the risk of death: the Framingham Heart Study', Circulation, 98: 946-52.

Bouchard, Richard, Nicholas Dana, Luigi Di Biase, Andrea Natale, and Stanislav Emelianov. 2012. "Photoacoustic characterization of radiofrequency ablation lesions." In, edited by A. Oraevsky Alexander and V. Wang Lihong, 82233K. SPIE.

Cappato, R., H. Calkins, S. A. Chen, W. Davies, Y. Iesaka, J. Kalman, Y. H. Kim, G. Klein, A. Natale, D. Packer, A. Skanes, F. Ambrogi, and E. Biganzoli. 2010. 'Updated worldwide survey on the methods, efficacy, and safety of catheter ablation for human atrial fibrillation', Circ Arrhythm Electrophysiol, 3: 32-8.

Eyerly, S. A., T. D. Bahnson, J. I. Koontz, D. P. Bradway, D. M. Dumont, G. E. Trahey, and P. D. Wolf. 2012. 'Intracardiac acoustic radiation force impulse imaging: a novel imaging method for intraprocedural evaluation of radiofrequency ablation lesions', Heart Rhythm, 9: 1855-62.

Eyerly, S. A., S. J. Hsu, S. H. Agashe, G. E. Trahey, Y. Li, and P. D. Wolf. 2010. 'An in vitro assessment of acoustic radiation force impulse imaging for visualizing cardiac radiofrequency ablation lesions', J Cardiovasc Electrophysiol, 21: 557-63.

Fleming, Christine P., Kara J. Quan, Hui Wang, Guy Amit, and Andrew M. Rollins. 2010. 'In vitro characterization of cardiac radiofrequency ablation lesions using optical coherence tomography', Opt. Express, 18: 3079-92.

Haissaguerre, M., P. Jais, D. C. Shah, A. Takahashi, M. Hocini, G. Quiniou, S. Garrigue, A. Le Mouroux, P. Le Metayer, and J. Clementy. 1998. 'Spontaneous initiation of atrial fibrillation by ectopic beats originating in the pulmonary veins', N Engl J Med, 339: 659-66.

Jacques, S. L. 2013. 'Optical properties of biological tissues: a review', Phys Med Biol, 58: R37-61.

Kolandaivelu, Aravindan, Menekhem M. Zviman, Valeria Castro, Albert C. Lardo, Ronald D. Berger, and Henry R. Halperin. 2010. 'Noninvasive Assessment of Tissue Heating During Cardiac Radiofrequency Ablation Using MRI Thermography', Circulation: Arrhythmia and Electrophysiology, 3: 521-29.

Mallidi, S., G. P. Luke, and S. Emelianov. 2011. 'Photoacoustic imaging in cancer detection, diagnosis, and treatment guidance', Trends Biotechnol, 29: 213-21.

Miyasaka, Y., M. E. Barnes, B. J. Gersh, S. S. Cha, K. R. Bailey, W. P. Abhayaratna, J. B. Seward, and T. S. Tsang. 2006. 'Secular trends in incidence of atrial fibrillation in Olmsted County, Minnesota, 1980 to 2000, and implications on the projections for future prevalence', Circulation, 114: 119-25.

Ntziachristos, V. 2010. 'Going deeper than microscopy: the optical imaging frontier in biology', Nat Methods, 7: 603-14.

Pappone, C., S. Rosanio, G. Oreto, M. Tocchi, F. Gugliotta, G. Vicedomini, A. Salvati, C. Dicandia, P. Mazzone, V. Santinelli, S. Gulletta, and S. Chierchia. 2000. 'Circumferential radiofrequency ablation of pulmonary vein ostia: A new anatomic approach for curing atrial fibrillation', Circulation, 102: 2619-28.

Petersen, H. H., X. Chen, A. Pietersen, J. H. Svendsen, and S. Haunso. 1999. 'Temperature-controlled radiofrequency ablation of cardiac tissue: an in vitro study of the impact of electrode orientation, electrode tissue contact pressure and external convective cooling', J Interv Card Electrophysiol, 3: 257-62.

Petersen, Helen Høgh, Xu Chen, Adrian Pietersen, Jesper Hastrup Svendsen, and Stig Haunsø. 1999. 'Lesion Dimensions During Temperature-Controlled Radiofrequency Catheter Ablation of Left Ventricular Porcine Myocardium : Impact of Ablation Site, Electrode Size, and Convective Cooling', Circulation, 99: 319-25.

Ramkissoon, R. A. 1966. 'Macroscopic identification of early myocardial infarction by dehydrogenase alterations', J Clin Pathol, 19: 479-81.

Ranjan, R., E. G. Kholmovski, J. Blauer, S. Vijayakumar, N. A. Volland, M. E. Salama, D. L. Parker, R. MacLeod, and N. F. Marrouche. 2012. 'Identification and acute targeting of gaps in atrial ablation lesion sets using a real-time magnetic resonance imaging system', Circ Arrhythm Electrophysiol, 5: 1130-5.

Roger, V. L., A. S. Go, D. M. Lloyd-Jones, E. J. Benjamin, J. D. Berry, W. B. Borden, D. M. Bravata, S. Dai, E. S. Ford, C. S. Fox, H. J. Fullerton, C. Gillespie, S. M. Hailpern, J. A. Heit, V. J. Howard, B. M. Kissela, S. J. Kittner, D. T. Lackland, J. H. Lichtman, L. D. Lisabeth, D. M. Makuc, G. M. Marcus, A. Marelli, D. B. Matchar, C. S. Moy, D. Mozaffarian, M. E. Mussolino, G. Nichol, N. P. Paynter, E. Z. Soliman, P. D. Sorlie, N. Sotoodehnia, T. N. Turan, S. S. Virani, N. D. Wong, D. Woo, M. B. Turner, Committee American Heart Association Statistics, and Subcommittee Stroke Statistics. 2012. 'Executive summary: heart disease and stroke statistics--2012 update: a report from the American Heart Association', Circulation, 125: 188-97.

Rosenbaum, R., A. J. Greenspon, M. Smith, and P. Walinsky. 1994. 'Advanced radiofrequency catheter ablation in canine myocardium', Am Heart J, 127: 851-7.

Santangeli, P., L. Di Biase, G. Pelargonio, J. D. Burkhardt, and A. Natale. 2011. 'The pharmaceutical pipeline for atrial fibrillation', Ann Med, 43: 13-32.

Shah, D. 2011. 'A critical appraisal of cardiac ablation technology for catheter-based treatment of atrial fibrillation', Expert Rev Med Devices, 8: 49-55.

Shah, J., S. Park, S. Aglyamov, T. Larson, L. Ma, K. Sokolov, K. Johnston, T. Milner, and S. Y. Emelianov. 2008. 'Photoacoustic imaging and temperature measurement for photothermal cancer therapy', J Biomed Opt, 13: 034024.

Swartling, J., S. Pålsson, P. Platonov, S. B. Olsson, and S. Andersson-Engels. 2003. 'Changes in tissue optical properties due to radio-frequency ablation of myocardium', Medical & Biological Engineering & Computing, 41: 403-09.

Thomsen, Sharon L, Steven L Jacques, and Stephen T Flock. 1990. "Microscopic correlates of macroscopic optical property changes during thermal coagulation of myocardium." In OE/LASE'90, 14-19 Jan., Los Angeles, CA, 2-11. International Society for Optics and Photonics.

Wang, B., A. Karpiouk, D. Yeager, J. Amirian, S. Litovsky, R. Smalling, and S. Emelianov. 2012a. 'Intravascular photoacoustic imaging of lipid in atherosclerotic plaques in the presence of luminal blood', Opt Lett, 37: 1244-6.

Wang, Bo, Andrei Karpiouk, Doug Yeager, James Amirian, Silvio Litovsky, Richard Smalling, and Stanislav Emelianov. 2012b. 'In vivo Intravascular Ultrasound-guided Photoacoustic Imaging of Lipid in Plaques Using an Animal Model of Atherosclerosis', Ultrasound in Medicine & Biology, 38: 2098-103.

Wolf, P. A., R. D. Abbott, and W. B. Kannel. 1991. 'Atrial fibrillation as an independent risk factor for stroke: the Framingham Study', Stroke, 22: 983-88.

Wolf, P. A., J. B. Mitchell, C. S. Baker, W. B. Kannel, and R. B. D'Agostino. 1998. 'Impact of atrial fibrillation on mortality, stroke, and medical costs', Arch Intern Med, 158: 229-34.

Xu, Minghua, and Lihong V. Wang. 2006. 'Photoacoustic imaging in biomedicine', Review of Scientific Instruments, 77: 041101.

Chapter 4: In Vitro Photoacoustic Characterization Of High-Intensity Focused Ultrasound Ablation Lesions In Cardiac And Liver Tissues[4]

4.1 ABSTRACT

High intensity focused ultrasound (HIFU) thermal therapies are limited by deficiencies in existing image guidance techniques. Previous studies using single-wavelength photoacoustic (PA) imaging have demonstrated that HIFU lesions generate contrast with respect to native tissues, but have not sufficiently assessed lesion extent. The purpose of this study is to demonstrate feasibility of characterization of in vitro HIFU ablation lesion dimensions using 3D multi-wavelength PA imaging. Fresh porcine cardiac and liver tissue samples were embedded in agar phantoms and ablated using a 2.5-MHz small-animal HIFU system. 2D and 3D multi-wavelength photoacoustic-ultrasonic (PAUS) scans were performed in the NIR range to characterize the change in the absorption spectrum of tissues following ablation and were compared to stained gross pathology to assess treatment margins and lesion extent. Comprehensive 2D multi-wavelength PA imaging yielded a spectrum in ablated tissue that did not display the characteristic local maximum in the optical absorption spectrum of deoxy-hemoglobin (Hb) near 760 nm. 2D tissue characterization map (TCM) images reconstructed from 3D TCM volumes reliably characterized lesion area and showed >70% area-agreement with stained gross pathology. Additionally, tissue samples were heated via water bath and concurrently interrogated with 2D PAUS imaging. PA signal exhibited an initial amplitude increase across all wavelengths, corresponding to an initial temperature increase, before then exhibiting a spectral change. This study suggests that multi-wavelength PA imaging has potential to obtain accurate characterization of HIFU lesion

[4] This chapter is adapted in part from a manuscript titled 'Multi-Wavelength Photoacoustic Visualization of High Intensity Focused Ultrasound Lesions' (Gray, Dana, Dextraze, Maier, Emelianov and Bouchard, 2015). Nicholas Dana is one of two primary co-authors of this manuscript.

extent and may be better suited to guide HIFU ablation therapies during clinical treatments than single-wavelength methods.

4.2 INTRODUCTION

4.2.1 High intensity focused ultrasound

High intensity focused ultrasound (HIFU) is a minimally invasive technique that has developed significantly over the last two decades for the treatment of benign and malignant conditions in soft tissues (Bailey et al. 2003; Kennedy 2005). HIFU treatments use ultrasound transducers with highly controlled beams to instantly achieve destructive temperatures at their focus. This technique has been used to treat targets that may be several centimeters below the skin surface, while preserving healthy tissue since hyperthermal therapy tends to occur at the focus of the beam (Kennedy 2005). HIFU is of clinical interest for several conditions, including atrial fibrillation of cardiac tissue (Lee et al. 2000; Groh et al. 2007), central nervous system disorders of the brain (Jagannathan et al. 2009), treatment of both benign and malignant solid tumors through thermal ablation (Kennedy 2005), and enhanced drug delivery at treatment sites (Dromi et al. 2007). In the United States, HIFU has been indicated for clinical treatment of uterine fibroids and malignant bone metastases (U.S. Food and Drug Administration 2005).

Image guidance is employed during HIFU for treatment planning, tissue temperature, and assessment of tissue damage during and after treatment (i.e. estimating treatment margins) (Kennedy 2005). Real-time image guidance has accommodated adaptive ablation planning, leading to increased efficacy of HIFU treatments and improved precision in estimating treatment margins (Kennedy 2005). Imaging guidance for hyperthermal therapy has been provided by magnetic resonance (MRI) imaging, computed tomography (CT), and ultrasound (US), all of which have been able to

elucidate anatomical structures and heating-probe location (Goldberg et al. 2005). Several of these techniques have demonstrated the capability to monitor tissue temperature changes, yet only MRI is used as a standard-of-care technique for image guidance during clinical treatments (Hynynen et al. 1993; Jolesz 2009).

4.2.2 Photoacoustic imaging

Photoacoustic (PA) imaging is a relatively novel technique that is gaining attention due to its feasibility of implementation as a point-of-care imaging solution, its molecular sensitivity, and its ready compatibility with existing US technology (Dana, Dumani, et al. 2016; Bouchard, Sahin, and Emelianov 2014). PA imaging can be achieved through extracorporeal or interstitial application of near-infrared (NIR) laser pulses, which are absorbed by endogenous chromophores or exogenous contrast agents (Dana, Dumani, et al. 2016). Due to the "optical window," in which optical absorption by water, fat, and blood decreases dramatically in the NIR region (650-1100 nm), imaging depths of several centimeters can be achieved in soft tissues (Smith, Mancini, and Nie 2009). Photon energy absorbed by chromophores is converted into mechanical energy through a rapid thermal expansion, which results in the generation of an acoustic transient that propagates through soft tissue and may be detected by a standard US transducer at the tissue surface (Bouchard, Sahin, and Emelianov 2014; Dana, Dumani, et al. 2016). Detected signals can then be used to estimate a map of optical absorption with sub-millimeter spatial resolution. Since PA signals are detected using an ultrasonic transducer, PA images can be co-registered with US images (Bouchard, Sahin, and Emelianov 2014; Dana, Dumani, et al. 2016). These photoacoustic-ultrasonic (PAUS) images allow for the presentation of anatomical information alongside estimated optical absorption, and thus molecular composition, of the tissue.

The amplitude of PA pressure waves, $p_0(\vec{r}, T, \lambda)$, generated as a result of optical absorption by chromophores in tissue, are dependent on the speed of sound in tissue ($v_s^2(\vec{r}, T)$ [cm s^{-1}]), a temperature-dependent volume expansion coefficient ($\beta(\vec{r}, T)$ [K^{-1}]), the isobaric heat capacity in tissue ($C_p(\vec{r}, T)$ [J kg^{-1} K^{-1}]), the optical absorption coefficient of the tissue ($\mu_{abs}(\vec{r}, \lambda)$ [cm^{-1}]), and the optical fluence ($F(\vec{r}, \lambda)$ [J cm^{-2}]) as (Bouchard, Sahin, and Emelianov 2014; Dana, Dumani, et al. 2016):

$$p_0(\vec{r}, \lambda, T) \propto \left(\frac{\beta(\vec{r}, T)\, v_s^2(\vec{r}, T)}{C_p(\vec{r}, T)}\right) \mu_{abs}(\vec{r}, \lambda)\, F(\vec{r}, \lambda) \qquad \text{Equation 4}$$

Contrast in PA images primarily arises from variations in the optical absorption coefficient, which depends on both the concentration of chromophores in tissue and the wavelength of the laser source. Due to the wavelength dependence of the optical absorption coefficient, multi-wavelength photoacoustic imaging can be performed by tuning the wavelength of the laser through the entire NIR region in order to estimate the optical absorption properties of the tissue (Mallidi, Luke, and Emelianov 2011; Bouchard, Sahin, and Emelianov 2014; Dana, Dumani, et al. 2016). Varying the location of the PAUS transducer or using a 2D transducer array and obtaining PA signals at several wavelengths allows for the generation of a multi-wavelength 3D PAUS volume. Additionally, the temperature dependence of pressure wave generation may allow for real-time monitoring and characterization of temperature change during ablation(Shah et al. 2008; Larin et al. 2000; Irina, Kirill, and Rinat 2005; Pramanik and Wang 2009).

4.2.3 Current image-guidance methods

Image guidance techniques greatly improve the outcome of HIFU treatments by allowing physicians to more accurately and completely estimate treatment margins, yet existing imaging modalities are not entirely satisfactory for treatment guidance

(Schlesinger et al. 2013; Rosenthal et al. 2015). Currently, image guidance of HIFU treatments is performed using several standard imaging modalities. Traditional pulse-echo B-mode US provides excellent anatomical information and can provide short-term identification of hyperechoic regions of tissue corresponding to microbubble formation at the site of the HIFU focus; however, it cannot provide quantification of lesion extent (Vaezy et al. 2001). Elastography can be used to assess and characterize induced lesions, but can be difficult to implement in vivo and provide a significant number of false-positives (Righetti et al. 1999). Magnetic resonance imaging (MRI) allows for excellent identification of treatment targets, treatment planning, and real-time tracking of relative temperature changes at the site of ablation through MRI thermography (Ottenhausen et al. 2013), but it is limited by the high cost and equipment incompatibility imposed by high magnetic field strengths. PA imaging is a promising modality for image guidance of HIFU therapies because of its ready compatibility with existing technology and capability to monitor target and healthy tissue during ablation with sub-millimeter spatial resolution. This level of spatial resolution in fact exceeds the spatial resolution of existing temperature MRI guidance techniques (1-2 mm) (Quesson, de Zwart, and Moonen 2000).

4.2.4 HIFU guidance with PA imaging

PA imaging provides several unique qualities that make it promising as an alternative to existing image-guidance techniques for HIFU. PA imaging is capable of both thermography and spectroscopy (Shah et al. 2008; Lee et al. 2013; Dana et al. 2014), allowing for real-time assessment of temperature changes and tissue state. In practice, conventional US techniques such as Doppler imaging or microbubble-contrast perfusion assessment can also be applied concurrently with PA imaging to assess nearby critical

structures, such as vessels (Dana, Dumani, et al. 2016; Bouchard, Sahin, and Emelianov 2014).

Previous studies of HIFU ablations in vitro and in vivo using PA imaging have shown that PA imaging is capable of providing image contrast in the ablation region (Chitnis et al. 2010; Cui, Staley, and Yang 2010; Cui and Yang 2010, 2011; Sun and O'Neill 2013; Funke et al. 2009). This change in contrast at the ablation site may be attributed to a change in the concentration of chromophores in the tissue as a result of heating (Tanya et al. 2006). However, single-wavelength methods typically fail to provide enough information to reliably quantify the precise position and dimensions of HIFU lesions. Studies using radio-frequency ablation have shown that multi-wavelength PA imaging is capable of detecting changes in the concentration of chromophores—specifically in the concentration of deoxy-hemoglobin (Hb)—following thermal ablation and that these multi-wavelength methods allow PA imaging to identify an optical absorption spectrum specific to ablated tissue and distinct from the typical Hb spectrum (Dana et al. 2014; Sun and O'Neill 2013). In this study, we use the previously described technique (Dana et al. 2014; Sun and O'Neill 2013) in an in vitro environment following HIFU and water-bath ablation of cardiac and liver tissue samples. 2D and 3D multi-wavelength PA data of ablated tissue samples is then correlated to these two absorption spectra to create Tissue Characterization Maps (TCM), which are used to quantitate lesion size for comparison to stained gross pathology. Additionally, we examine the temperature dependence of the PA signal as tissue samples are heated in a PBS bath.

4.3 METHODS

4.3.1 Sample preparation and ablation procedure

Imaging samples were acquired from fresh porcine cardiac and liver tissues (Animal Technologies Inc., Tyler, TX) within 24 hours of sacrifice and were never frozen. Excised tissues from one liver and two hearts were used to make three liver samples and three cardiac samples, each approximately 30x30x20 mm^3 in size. Each specimen was embedded into an agar phantom for HIFU sonication. The HIFU transducer was acoustically coupled to the agar phantoms using ultrasound gel and samples were each sonicated for 120 seconds at power settings between 22 and 30 watts using a LabFUS 2.5-MHz small-animal HIFU system (Image Guided Therapy Inc., Paris, France). Photographs of the HIFU system, HIFU transducer, and imaging system are presented in Figure 4.1. Following ablation, tissue specimens were removed from their agar phantoms, and the uppermost 1.5 – 2 mm of tissue surface was removed in order to expose ablation lesions to allow for tissue-sample photography and later co-registration with imaging data.

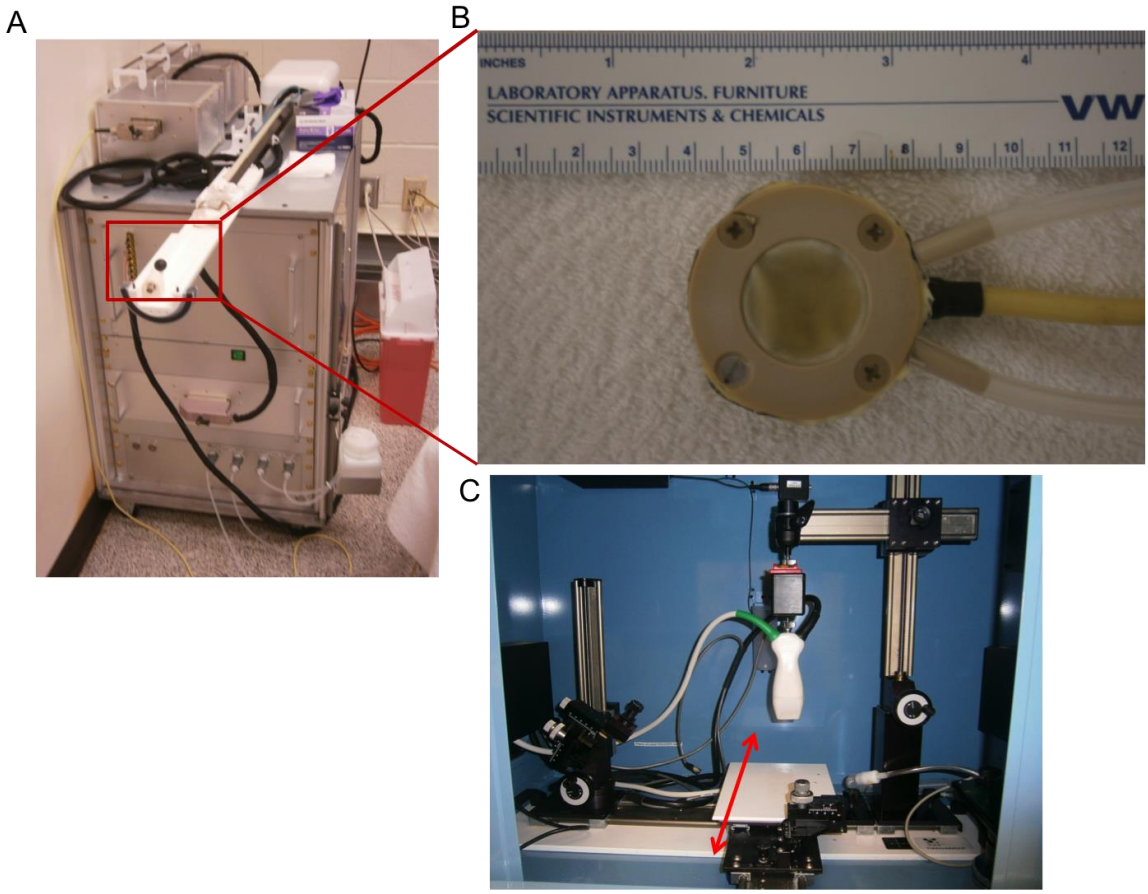

Figure 4.1. Photographs of experimental equipment. A) LabFUS 2.5-MHz small-animal HIFU system. B) Close-up view of eight-element, 2.5-MHz HIFU transducer. C) Vevo LAZR 2100 combined PAUS imaging system. Red arrow indicates motorized platform for elevation scanning during 3D imaging.

Additionally, fresh bovine liver tissues (Animal Technologies Inc., Tyler, TX) were acquired within 24 hours of sacrifice and never frozen. Two samples were excised from one liver and submerged in normal PBS in an imaging chamber containing a heat exchanger. The goal of this experiment was to monitor the tissue PA signal as a function of bath temperature. The tissue sample was located in the center of the copper tubing coil, which comprised the heat exchanger, to generate an approximately isotropic temperature

field. Bath temperature was measured via thermocouple at a location a few millimeters from the upper surface of the tissue imaging plane.

4.3.2 Imaging setup

Following the aforementioned ablation procedure, specimens were anchored in a thin layer of gelatin and submerged in normal phosphate buffered saline (PBS) to achieve acoustic coupling between the tissue sample and the PAUS transducer. PAUS imaging was performed using a Vevo LAZR 2100 imaging system equipped with a 21-MHz US transducer coupled to a pulsed Nd:YAG laser capable of irradiating from 670-970 nm (FUJIFILM VisualSonics Inc., Toronto, Canada). In each sample, a single-wavelength 3D PAUS scan was performed over the extent of the tissue sample in order to identify a single plane containing the ablation lesion. The location of the lesion was chosen by selecting an area in the 3D PAUS scan exhibiting a hyperechoic US signal and high PA contrast. After identification of the lesion, a 2D comprehensive multi-wavelength PA scan was performed on this plane using wavelengths ranging from 680-970 nm in 3-nm steps. A multi-wavelength 3D PAUS scan was then performed on each tissue over a volume including the ablation lesion using five wavelengths in the NIR region (740, 750, 760, 780, 900 nm), corresponding to a distinct feature in the Hb absorption spectrum (Jacques 2013), and averaging eight frames for each wavelength and location.

For the bath-heated samples, multi-wavelength PA imaging was done using five wavelengths in the NIR region (740, 750, 760, 770, 780 nm), corresponding to the same Hb spectral feature. First, a baseline multi-wavelength PA acquisition was performed. The bath-heat exchanger was then activated, and the tissue bath temperature rapidly rose to approximately 60 °C. PA imaging at all wavelengths was conducted at one-minute intervals for the first 30 minutes, then at five-minute intervals thereafter, up to 60

minutes. Bath temperature was measured at each imaging time-point. Immediately post-imaging, the tissue sample was removed from the water bath and bisected at the imaging plane. Photographs were taken of the sample prior to heating, as well as at the point of bisection post-heating.

4.3.3 Staining procedure

Following imaging, samples were stained using triphenyl tetrazolium chloride (TTC) salts for registration and comparison of gross pathology to PAUS data (Sigma-Aldrich Corp., St Louis, MO). TTC is a redox indicator of metabolic activity: the white stain accumulates in cells and is oxidized to a deep red color by a variety of molecules associated with metabolic activity (Berridge et al. 1996). Tissue in the ablation region has undergone necrosis and should become white/gray in color, while metabolically active healthy tissue outside the ablation region will become a deep red. Staining solutions were prepared by dissolving 0.1 mg/ml TTC in normal PBS. Tissue samples were submerged in staining solution and incubated at 37° C for 20 minutes with constant stirring. After staining, tissue samples were patted dry and photographed. Bath-heated tissue samples were not stained as the tissue was clearly coagulated throughout the entire tissue volume.

4.3.4 2D multi-wavelength PA analysis

The comprehensive 2D multi-wavelength scans were analyzed to assess whether HIFU treatment results in a change in the PA spectra of tissue. Regions of interest (ROI) were selected in areas showing high PA contrast and areas showing low PA contrast, corresponding to areas of ablated and non-ablated tissue, respectively. The mean PA signal inside each ROI was calculated for each wavelength scanned and plotted to display the absorption spectra for ablated (liver and cardiac, respectively) and non-ablated tissue (Figure 4.2).

4.3.5 Creation of tissue characterization maps

Tissue characterization maps (TCMs) were generated using a correlation-based algorithm. Reference absorption spectra for ablated and Hb absorbers were obtained from the comprehensive multi-wavelength PA data (liver or cardiac, as appropriate) using previously described methods (Dana et al. 2014). The filtered PA data were compared to two reference spectra (i.e. Hb correlation and a distinct ablated correlation for each tissue type), resulting in two 3D datasets of Pearson correlation coefficients. These two 3D correlation datasets (i.e. Hb correlation coefficients and ablated correlation coefficients) were then processed with a simple thresholding algorithm. Correlation thresholds of 0.6 were used for both Hb and ablated reference spectra. PA voxels were then classified based on the respective thresholds and correlation coefficients. Voxels that correlated strongly (i.e. displayed correlation coefficients above the threshold) to only one reference spectra were classified accordingly (i.e. class 2 for ablated; class 1 for Hb). Voxels that correlated strongly to both were classified according to their greatest correlation coefficient. Voxels that correlated strongly to neither reference spectra were classified as 0 (no correlation). Thus, a trinary 3D TCM was constructed for each PA dataset and compared to photographed gross pathology. For the bath-treated tissue samples, an equivalent process was employed, save that a correlation threshold of 0.65 was used. A 2D TCM was generated at each time point, and the 2D multi-wavelength PA signal was examined as a function of time (i.e. thermal exposure).

4.3.6 Image registration and characterization of ablation size

HIFU 3D TCM data were co-registered with top-view photographs of stained gross pathology by manual registration based on corresponding visual landmarks. Top-view C-scan TCMs were obtained by taking the mode along the depth axis for each voxel at the surface of the TCM volume. Mode calculations were performed from a depth 0.184

mm (corresponding to five voxels, which tended to avoid subsurface fluence artifacts) below the surface of the volume to a depth 1.29 mm (corresponding to 35 voxels) below the surface. Borders between areas of ablation and non-ablation were manually segmented in matched TCMs and pathology photographs by three experts, generating three segmentations for each TCM or pathology photograph. The segmentations for each TCM or photograph were analyzed automatically using MATLAB. Pixel-wise lesion area was calculated from each expert-segmentation of corresponding TCM data and gross pathology photographs. The mean and standard deviation of lesion areas from the expert segmentations were calculated and subsequently converted to physical dimensions (mm^2). Percent area agreement between gross pathology and TCMs was calculated for each tissue sample as:

$$\%\ \text{Area Agreement} = \left[1 - \frac{(I_{TCM} - I_{GP})}{I_{GP}}\right] \times 100\% \qquad \text{Equation 5}$$

An SNR analysis was done, comparing SNR up to 8 mm tissue depth, while varying the number of averages. A 0.21x0.18 mm^2 sliding kernel was used, analyzing signal along a depth line located in the center of the ROI shown in Figure 4.5A. Additionally, a noise image was acquired (degassed water, no laser irradiation) to assess PA image noise at the equivalent depth. Up to 64 averages were used. Analysis was done on beam-formed image data, using the following equation:

$$\text{SNR} = 10 \cdot \log_{10}\left(\frac{\overline{PA}}{\sigma_{noise}}\right) \qquad \text{Equation 6}$$

Where $\overline{PA}$ and σ_{noise} denote the ROI mean PA signal and noise standard deviation, respectively. The SNR threshold was empirically determined by analyzing the depth, and thus corresponding SNR, at which the TCM loses continuity (i.e. the point at

which the gaps in the solid TCM regions become as large as or larger than the spatial averaging kernel used).

4.4 RESULTS

4.4.1 2D multi-wavelength PA analysis

Figure 4.2 displays the results of 2D multi-wavelength PA imaging performed in liver tissue. Figure 4.2A shows an overlay of the single-wavelength PA signal at 710 nm on its matched US image. ROIs shown in Figure 4.2A represent the area averaged at each wavelength to generate the reference spectra from ablated and non-ablated tissue; these spectra are shown in Figure 4.2B. We expect the dominant absorber to be Hb in this wavelength region as the ex vivo tissue samples should be oxygen-depleted. Non-ablated tissue displays an absorption spectrum that agrees well with that of Hb (Dana et al. 2014) as the characteristic local maximum in the absorption spectrum around 760 nm is readily apparent. The absorption spectrum in the ROI corresponding to ablated tissue decreases monotonically with increasing optical wavelength and does not display the characteristic 760-nm local maximum of the Hb absorption spectrum, indicating a likely change in the concentration of Hb absorbers due to hyperthermia.

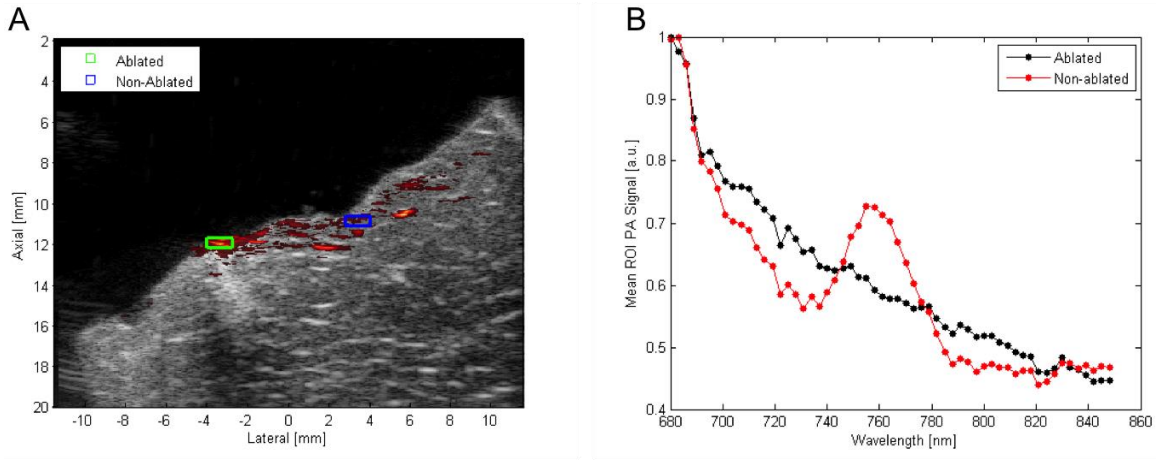

Figure 4.2. Results of 2D comprehensive multi-wavelength PA imaging. A) Overlay of single-wavelength PA data at 710 nm on matched US image. High PA contrast and US hyper-echogenicity exhibited in area where lesion is expected. B) Plot of mean PA signal in each ROI indicated at each wavelength. Mean PA spectrum in areas outside lesion exhibit the characteristic peak of Hb around 760 nm; peak not seen in area of high PA contrast where lesion is expected.

4.4.2 Lesion area statistics

TCMs were created by correlating to wavelengths in the region between 740 and 780 nm; the region where ablated tissue and Hb absorption spectra are most distinct. Tissue characterization was achieved at depths up to 3 mm below the surface of the tissue, while gross pathology indicated that lesions extend 5-7 mm in depth. Examples of 3D TCM volumes overlaid on matching US volumes for liver and cardiac tissues are shown Figure 4.3.

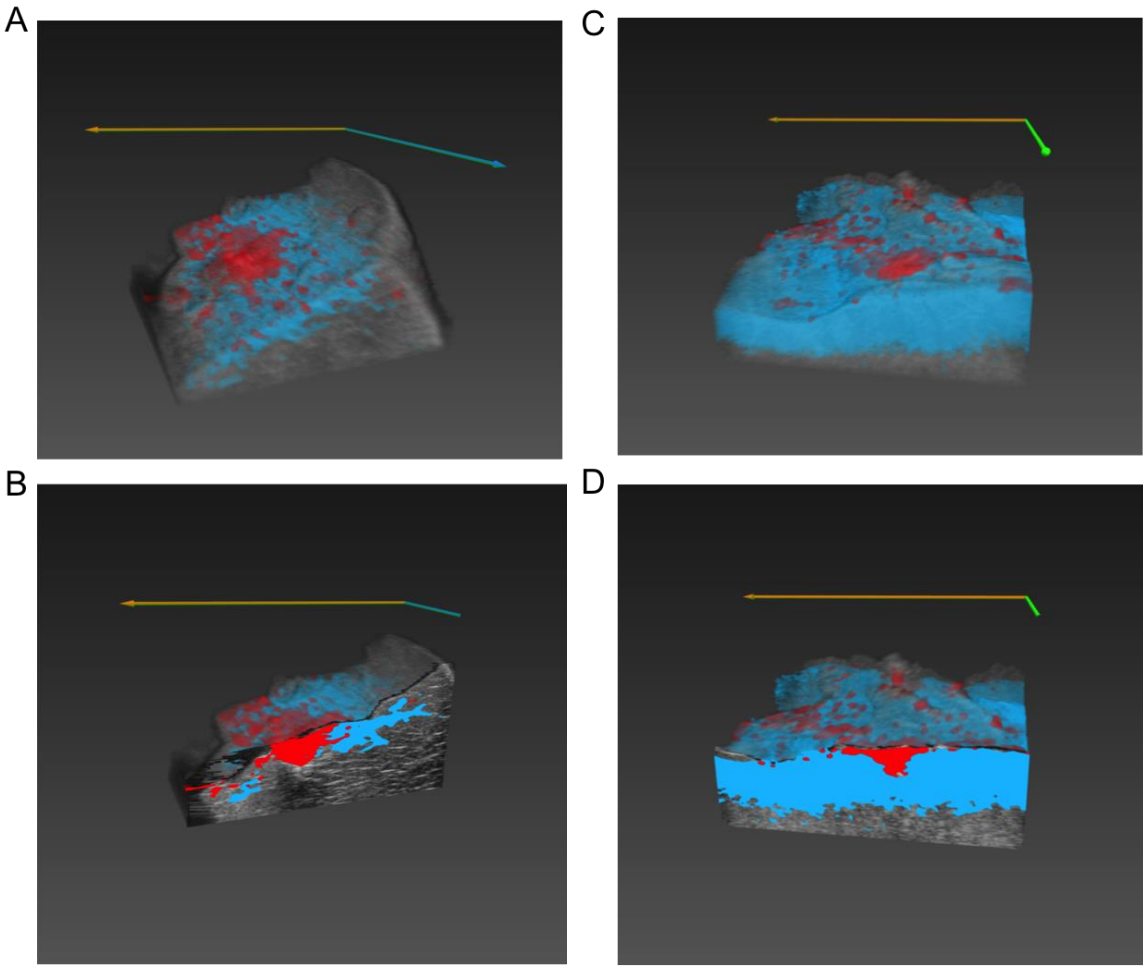

Figure 4.3. Renderings of 3D TCM volumes overlaid matching 3D US volumes. A) Full liver sample 3D volume rendering and B) cut-away view of 2D frame in the interior of the lesion of the same liver volume. C) Full cardiac sample 3D volume rendering and D) cut-away view of 2D frame in the interior of the lesion of same cardiac volume.

Results of area calculations performed on manually segmented lesions in both TCMs and gross pathology photographs can be found in Table 4.1; a representative sample image can be found in Figure 4.4. In TCM volumes, we observed that tissue bordering the areas of strong ablation correlation tended to correlate poorly to both ablated and non-ablated absorption spectra. These areas were segmented in addition to

the area that was primarily classified as the lesion and was also compared to gross pathology.

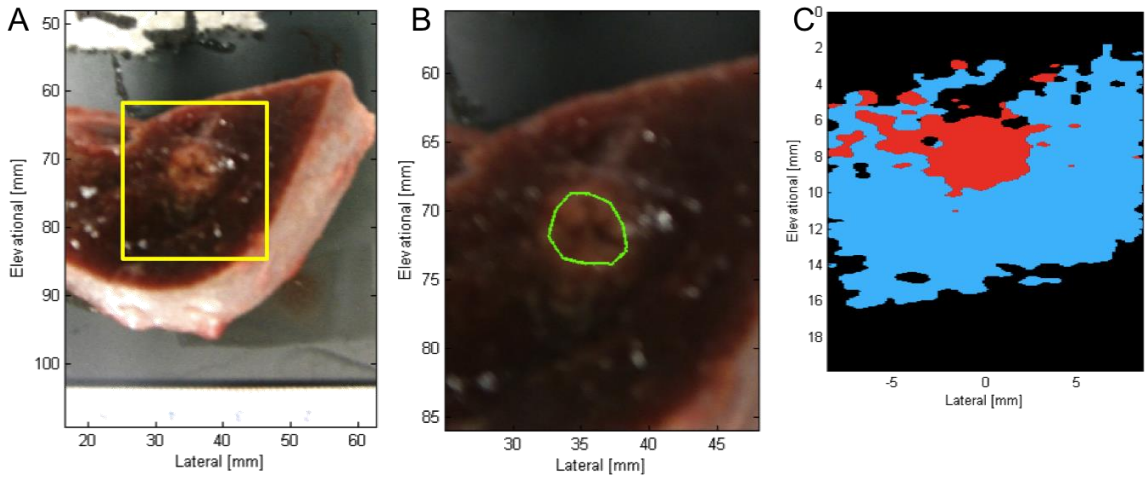

Figure 4.4. Comparison of gross pathology and TCM data for one liver tissue sample. A) Photographed stained gross pathology. Red box indicates area of tissue displayed by 2D TCM data. B) Zoomed in photograph of stained gross pathology. Manual segmentation of gross pathology overlaid in green. C) C-scan 2D TCM plane reconstructed from TCM volume for manual segmentation. Blue indicates Hb correlation, Red indicates ablated spectrum correlation, black indicates correlation to neither spectra.

Metrics	Tissue type					
	Liver			Cardiac		
	#1	#2	#3	#1	#2	#3
Pathology area (mm^2)	16.9±1.8	35.3±3.7	22.2±2.0	11.4±1.0	10.3±0.1	3.5±0.2
Total region (ablated + border) area (mm^2)	15.7±1.9	28.1±0.2	22.2±0.1	11.5±0.4	7.21±0.2	3.2±0.1
% Area Agreement Total region	93.2%	79.8%	99.9%	99.1%	70.0%	91.7%
Ablated region area (mm^2)	8.53±0.1	25.6±0.1	20.0±0.1	11.6±0.6	7.2±0.2	2.1±0.2
% Area Agreement Ablated region	50.6%	72.5%	90.2%	98.3%	70.1%	61.2%

Table 4.1. Lesion registration results.

For the bath-heated samples, Figure 4.5A – E shows a 2D TCM overlaid on co-registered B-Mode US images for five time points, with a rectangular square identifying an ROI for spectral analysis. At baseline (Figure 4.5A) strong correlation to Hb is observed to approximately 4 mm in depth across the entire width of the tissue sample. The depth of this correlation decreases to about 2 mm by 15 minutes (Figure 4.5B). By 30 minutes, a thin layer correlating to ablated tissue can be identified at the tissue surface (Figure 4.5C). At 45 minutes (Figure 4.5D), 1 – 2 mm of ablated tissue is identified at the surface, with only sporadic Hb is identified beneath the surface, and this trend continues at 60 minutes (Figure 4.5E). Figure 4.5F shows a surface plot of the mean PA signal of

the ROI, normalized to baseline, as a function of wavelength and time. The PA signal rapidly increases for the first 5 minutes after heating onset, but still maintains the Hb spectral shape (local maximum at 760 nm). Amplitude decreases slightly, but spectral shape is maintained until approximately 30 minutes, at which point the spectra begins to flatten, correlating more strongly to the ablated reference spectra thereafter (as shown by the surface color). Figure 4.5G allows for better comparison of the spectra at prominent time points. Note that at 5 minutes after heating onset (bath temperature of 52 °C) a PA signal increase of approximately 80% from baseline can been seen across all wavelengths. The signal decreases slightly, but remains relatively constant at roughly 50% above baseline until about 30 minutes after heating onset. At 30 minutes, we can see the PA spectrum flattening out, and by 45 and 60 minutes, we observe a monotonically decreasing spectrum that strongly resembles the ablated reference spectrum for liver.

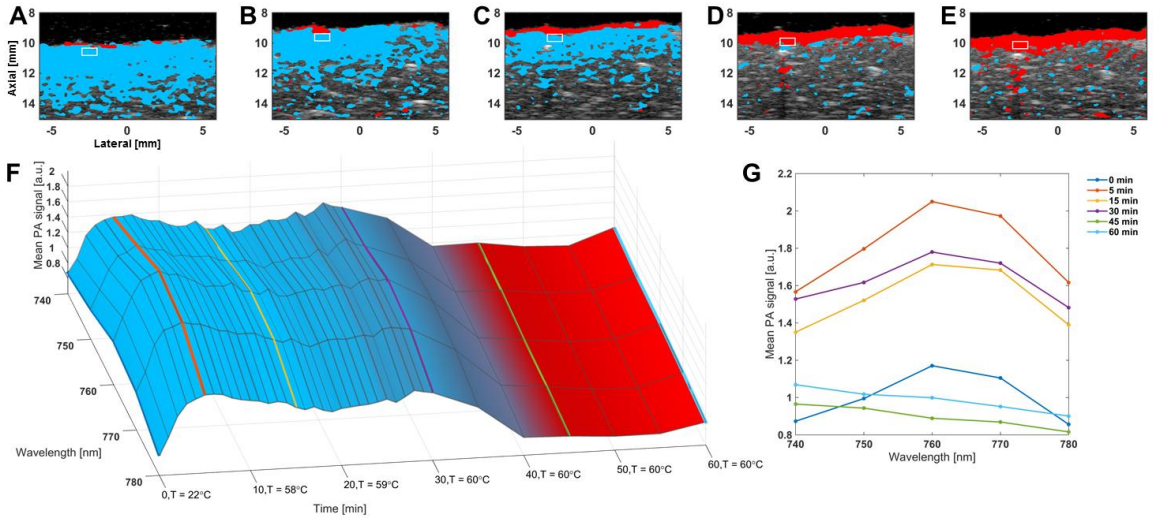

Figure 4.5. Comparison of TCMs (same color-coding as previously stated) and spectra for sample subjected to PBS-bath thermal treatment. A – E) TCMs overlaid on coregistered US B-mode image for time-points 0 (baseline), 15, 30, 45 and 60 minutes of thermal treatment, respectively. White rectangular box denotes a 1x0.5 mm^2 ROI selected for analysis, maintained at constant depth from tissue surface. F) Surface plot of mean PA signal in ROI (normalized to baseline), as a function of wavelength and time. Surface color-map represents mean TCM color value across ROI at each time point. G) PA signal spectra from F for time-points 0, 5, 15, 30, 45 and 60 minutes (time-points at 0, 15, 30, 45 and 60 minutes correspond to images A – E, respectively).

Analysis of TCMs against the SNR results suggests that an SNR of 10 dB is generally sufficient for reliable tissue characterization using this method. By increasing averages, we found SNR using this method can be improved approximately proportional to $\sqrt{\#\ \text{averages}}$, allowing accurate TCMs at greater depths in tissue, though at the cost of increased imaging time.

4.5 DISCUSSION

4.5.1 Tissue characterization map accuracy

In this initial study, we demonstrate that multi-wavelength PA imaging can provide estimates of lesion extent with gross pathology area agreement greater than 79% in liver and greater than 70% in cardiac tissue. As has been shown previously (Cui, Staley, and Yang 2010; Cui and Yang 2011; Funke et al. 2009)and demonstrated in this study (Figure 4.2), high PA signal contrast in the ablated lesion center can be obtained using a single laser wavelength. However, PA imaging data from a single wavelength tends not to be sufficient to completely characterize the extent of the ablation lesion. While single-wavelength PA imaging may be useful to perform a quick 3D scan and obtain a rough identification of the lesion center, multi-wavelength TCMs provide significantly more information about the boundaries and extent of ablation lesions, as shown by comparing Figure 4.2A and Figure 4.3B and Figure 4.5A – E. Focusing on the wavelengths where the absorption spectra of ablated and non-ablated tissue display different features, multi-wavelength TCMs were able to identify HIFU ablation lesions in ex vivo cardiac and liver tissue and obtain area agreement with gross pathology photographs in excess of 70% and with sub-millimeter spatial resolution. TCMs compared well with manually segmented gross pathology photographs (minimum 70% area agreement), demonstrating multi-wavelength PA imaging as a potential tool for HIFU lesion identification and quantification.

4.5.2 Photoacoustic image artifacts

Despite our success in the identification and characterization of HIFU ablation lesions in cardiac and liver tissues, limitations in PA imaging and our experimental setup prevent ideal characterization of lesion dimensions. Imaging artifacts immediately at the

surface of the tissue were observed and are believed to be the result of subsurface photon fluence and refractive index discontinuities between the surface of the tissue and the PBS used to couple the tissue to the ultrasound transducer. In our study, these artifacts were mitigated when creating 2D TCM images of the top-view plane by using a depth 0.184 mm below the tissue surface as the starting point for reconstruction of the C-scan projected views.

4.5.3 Limitations of light penetration and imaging depth

PA based TCMs also underestimated lesion depth in this experiment. Depth of PA imaging is limited by scattering of photons which increases the likelihood of absorption by chromophores at shallower depths in the tissue. In this experiment, imaging depths were limited to no more than 3 mm below the surface of the tissue, yet HIFU lesions extended 5-7 mm in depth. Several techniques could be employed in order to increase the penetration depth of imaging, including increased photon fluence and increased frame averaging to improve the signal-to-noise ratio at depth, as discussed below. Interstitial delivery of light by laser fibers also allows for significantly deeper light delivery to provide image guidance of treatments on deep-lying tissues, such as the liver and kidneys (Mitcham et al. 2013). By employing these methods, it should be possible to extend imaging depth beyond 3 mm in ex vivo experiments. Additionally, penetration depth could possibly be improved in in vivo experiments due to the fact that tissues will be highly oxygenated. Optical absorption by oxygenated hemoglobin is roughly an order of magnitude lower in the NIR spectrum than that of Hb (Mallidi, Luke, and Emelianov 2011; Jacques 2013). This reduction in optical absorption may allow increased optical penetration depth while maintaining energy, but it may require re-optimizing imaging wavelengths to maintain contrast between ablated and native oxygenated tissue.

4.5.4 Lesion peripheral region analysis

A noteworthy effect observed in this experiment was the appearance of a ring of tissue surrounding the area correlating to ablated tissue in TCMs that did not correlate well to either the obtained ablated tissue spectrum or the standard Hb spectrum. This effect was observed in both liver and cardiac tissue in our study and has been reported in previous studies (Dana et al. 2014). In cardiac tissues, the area of non-correlation was not always observed. An example of this effect is seen in Figure 4.4C, where an area of non-correlated tissue (i.e. black) borders the upper area correlating highly to ablated tissue (i.e. red) at the core of the lesion. The segmentation region containing the region of ablation-correlated (red) and non-correlated (e.g. also including the black region extending from 4-6 mm in elevation in Fig. 4C) tissue showed better agreement with segmented ablation regions in gross pathology photographs than the segmentations of the ablation-correlated region alone. Regions of ablation correlation alone tended to underestimate the area extent of lesions when compared to gross pathology segmentations. The change in the PA spectrum in ablated tissue likely results from hyperthermia-induced changes in the Hb chromophore. It is possible that incomplete conversion of Hb occurs at the edge of the ablation region due to reduced increase in local temperature as compared to the core of the lesion, resulting in an absorption spectrum that did not correlate well to either Hb or the lesion core.

4.5.5 Thermographic photoacoustic imaging potential and limitations

The capacity of PA imaging to assess temperature has been previously demonstrated by examining changes in PA amplitude (Shah et al. 2008). By applying similar techniques, we were able to track the relative temperature rise in the bath-heated tissue sample during the first several minutes. As shown in Figure 4.5F, the PA amplitude then decreases slightly after five minutes. We suspect this is primarily a result of changes

in surface fluence. As can be seen in the B-Mode US images in Figure 4.5, the tissue swells initially (B and C), before contracting partially (D and E). This initial tissue swelling is likely the result of increased osmotic pressure in the bath, following temperature increase. The swelling is likely to affect and the surface fluence, due to a change in separation between the tissue and light emission source. The tissue contraction observed in Figure 4.5D and Figure 4.5E is likely due coagulation of ECM proteins, which concurs with the observed strong correlation of the PA signal to the ablated reference spectrum (red region in Figures). These results highlight the potential complementary nature of PA thermography and multi-wavelength analysis. Tissue coagulation may also explain the decrease in PA amplitude after 30 minutes, as increased optical scattering following coagulation will reduce fluence, and thus PA signal, at greater depths. While these factors confound PA thermography in this experiment, these issues may not be as prevalent in clinical applications for several reasons. First, tissue hyperthermal therapy typically occurs on the order of several seconds to a few minutes and is typically much more spatially localized, which may reduce large scale tissue swelling or edema. Lastly, if an optical scattering increase within an ROI correlates to a change in the observed PA spectra, as suggested by this study, it may serve as a partial endpoint for hyperthermal therapy, rather than a mitigating factor to image guidance. Furthermore, if changes in optical fluence and absorption can be accounted for (perhaps by collecting some backscattered light for diffuse reflectance assessment (Hennessy et al. 2013)), PA thermography may be able to quantify thermal dose, comparable to what is currently done using MRI thermography.

4.5.6 Signal-to-noise ratio analysis

The SNR analysis suggests that roughly 10 dB SNR is necessary for reliable TCM analysis. Our particular system showed that, with 64 averages, the SNR up to 5 mm can be improved to allow for reliable TCM analysis. While increased averaging may be prohibitive in some clinical applications, such as cardiac imaging, this analysis suggests a baseline to predict TCM accuracy as a function of depth for a given application and imaging system

4.6 CONCLUSION

We have demonstrated the feasibility of using multi-wavelength PA imaging to create tissue characterization volumes that allow the differentiation of HIFU-induced tissue ablation lesions from non-ablated tissue and to estimate the treatment margins of tissue ablations in 2D planes in ex vivo cardiac and liver tissue samples following a HIFU ablation. Multi-wavelength PA imaging demonstrates that HIFU-induced hyperthermia results in changes in the Hb absorption spectrum that can be leveraged for PA-based segmentation. Multi-wavelength TCMs were used to successfully identify lesion size with a greater accuracy than single-wavelength methods. Multi-wavelength TCMs agreed with gold-standard stained pathology images (70% area agreement) and were able to successfully assess lesion margins with a spatial resolution comparable to existing temperature MRI techniques. Additionally, we demonstrated the complementary nature of PA thermography and multi-wavelength TCMs. Further in vivo experiments concurrent with treatment must be performed to assess PA signal changes in living tissues. These results suggest that multi-wavelength PA imaging and PA thermography present a promising modality for guiding hyperthermia therapies that depend on precise knowledge of temperature and lesion extent in order to preserve critical structures.

4.7 REFERENCES

Bailey, M. R., V. A. Khokhlova, O. A. Sapozhnikov, S. G. Kargl, and L. A. Crum. 2003. 'Physical mechanisms of the therapeutic effect of ultrasound (a review)', Acoustical Physics, 49: 369-88.

Berridge, Michael V, An S Tan, Kathy D McCoy, and Rui Wang. 1996. 'The biochemical and cellular basis of cell proliferation assays that use tetrazolium salts', Biochemica, 4: 14-19.

Bouchard, Richard, Onur Sahin, and Stanislav Emelianov. 2014. 'Ultrasound-guided photoacoustic imaging: current state and future development', IEEE transactions on ultrasonics, ferroelectrics, and frequency control, 61: 450-66.

Chitnis, Parag V., Hans-Peter Brecht, Richard Su, and Alexander A. Oraevsky. 2010. 'Feasibility of optoacoustic visualization of high-intensity focused ultrasound-induced thermal lesions in live tissue', Journal of Biomedical Optics, 15: 021313-13-5.

Cui, Huizhong, Jacob Staley, and Xinmai Yang. 2010. 'Integration of photoacoustic imaging and high-intensity focused ultrasound', Journal of Biomedical Optics, 15: 021312-12-4.

Cui, Huizhong, and Xinmai Yang. 2010. 'In vivo imaging and treatment of solid tumor using integrated photoacoustic imaging and high intensity focused ultrasound system', Medical Physics, 37: 4777-81.

———. 2011. 'Real-time monitoring of high-intensity focused ultrasound ablations with photoacoustic technique: An in vitro study', Medical Physics, 38: 5345-50.

Dana, N., L. Di Biase, A. Natale, S. Emelianov, and R. Bouchard. 2014. 'In vitro photoacoustic visualization of myocardial ablation lesions', Heart Rhythm, 11: 150-7.

Dana, Nicholas P., Diego S. Dumani, Jason R. Cook, and Stanislav Emelianov. 2016. 'Overview of Photoacoustic Imaging.' in Devon J. Godfrey, Jacob Van Dyk, Shiva K. Das, Bruce H. Curran and Anthony B. Wolbarst (eds.), Advances in Medical Physics (Medical Physics Publishing: Madison, WI).

Dromi, Sergio, Victor Frenkel, Alfred Luk, Bryan Traughber, Mary Angstadt, Monica Bur, Jason Poff, Jianwu Xie, Steven K. Libutti, King C. P. Li, and Bradford J. Wood. 2007. 'Pulsed-High Intensity Focused Ultrasound and Low Temperature–Sensitive Liposomes for Enhanced Targeted Drug Delivery and Antitumor Effect', Clinical cancer research : an official journal of the American Association for Cancer Research, 13: 2722-27.

Funke, Arik R., Jean-François Aubry, Mathias Fink, Albert-Claude Boccara, and Emmanuel Bossy. 2009. 'Photoacoustic guidance of high intensity focused

ultrasound with selective optical contrasts and time-reversal', Applied Physics Letters, 94: 054102.

Goldberg, S Nahum, Clement J Grassi, John F Cardella, J William Charboneau, Gerald D Dodd III, Damian E Dupuy, Debra Gervais, Alice R Gillams, Robert A Kane, and Fred T Lee Jr. 2005. 'Standards of Practice-Image-guided Tumor Ablation: Standardization of Terminology and Reporting Criteria', Journal of Vascular and Interventional Radiology, 16: 765-78.

Groh, Mark A, Oliver A Binns, Harry G Burton, Stephen W Ely, and Alan M Johnson. 2007. 'Ultrasonic cardiac ablation for atrial fibrillation during concomitant cardiac surgery: long-term clinical outcomes', The Annals of thoracic surgery, 84: 1978-83.

Hennessy, Ricky, Sam L. Lim, Mia K. Markey, and James W. Tunnell. 2013. 'Monte Carlo lookup table-based inverse model for extracting optical properties from tissue-simulating phantoms using diffuse reflectance spectroscopy', Journal of Biomedical Optics, 18: 037003-03.

Hynynen, K., A. Darkazanli, E. Unger, and J. F. Schenck. 1993. 'MRI-guided noninvasive ultrasound surgery', Medical Physics, 20: 107-15.

Irina, V. Larina, V. Larin Kirill, and O. Esenaliev Rinat. 2005. 'Real-time optoacoustic monitoring of temperature in tissues', Journal of Physics D: Applied Physics, 38: 2633.

Jacques, S. L. 2013. 'Optical properties of biological tissues: a review', Phys Med Biol, 58: R37-61.

Jagannathan, Jay, Narendra K. Sanghvi, Lawrence A. Crum, Chun-Po Yen, Ricky Medel, Aaron S. Dumont, Jason P. Sheehan, Ladislau Steiner, Ferenc Jolesz, and Neal F. Kassell. 2009. 'High intensity focused ultrasound surgery (HIFU) of the brain: A historical perspective, with modern applications', Neurosurgery, 64: 201-11.

Jolesz, Ferenc A. 2009. 'MRI-Guided Focused Ultrasound Surgery', Annual Review of Medicine, 60: 417-30.

Kennedy, James E. 2005. 'High-intensity focused ultrasound in the treatment of solid tumours', Nat Rev Cancer, 5: 321-27.

Larin, Kirill V., Irina V. Larina, Massoud Motamedi, and Rinat O. Esenaliev. 2000. "Monitoring of temperature distribution in tissues with optoacoustic technique in real time." In, 311-21.

Lee, Hannah J., Yang Liu, Jun Zhao, Min Zhou, Richard R. Bouchard, Trevor Mitcham, Michael Wallace, R. Jason Stafford, Chun Li, Sanjay Gupta, and Marites P. Melancon. 2013. 'In vitro and in vivo mapping of drug release after laser ablation thermal therapy with doxorubicin-loaded hollow gold nanoshells using

fluorescence and photoacoustic imaging', Journal of Controlled Release, 172: 152-58.

Lee, Lisa A., Claudio Simon, Edward L. Bove, Ralph S. Mosca, Emad S. Ebbini, Gerald D. Abrams, and Achiau Ludomirsky. 2000. 'High Intensity Focused Ultrasound Effect on Cardiac Tissues: Potential for Clinical Application', Echocardiography, 17: 563-66.

Mallidi, S., G. P. Luke, and S. Emelianov. 2011. 'Photoacoustic imaging in cancer detection, diagnosis, and treatment guidance', Trends Biotechnol, 29: 213-21.

Mitcham, T, T Marques, D Chatterjee, S Krishnan, T Pugh, and R Bouchard. 2013. "Transrectal photoacoustic-ultrasonic imaging enhancement through interstitial irradiation and targeted nanoparticles." In Proceedings of the 2013 IEEE Ultrasonics symposium, Prague, Czech Republic.

Ottenhausen, Malte, Imithri Bodhinayake, Matei Banu, Kartik Kesavabhotla, Ashley Ray, and John A. Boockvar. 2013. 'Industry progress report on neuro-oncology: Biotech update 2013', Journal of Neuro-Oncology, 115: 311-16.

Pramanik, M., and L. V. Wang. 2009. 'Thermoacoustic and photoacoustic sensing of temperature', J Biomed Opt, 14: 054024.

Quesson, Bruno, Jacco A. de Zwart, and Chrit T. W. Moonen. 2000. 'Magnetic resonance temperature imaging for guidance of thermotherapy', Journal of Magnetic Resonance Imaging, 12: 525-33.

Righetti, Raffaella, Faouzi Kallel, R. Jason Stafford, Roger E. Price, Thomas A. Krouskop, John D. Hazle, and Jonathan Ophir. 1999. 'Elastographic characterization of HIFU-induced lesions in canine livers', Ultrasound in Medicine & Biology, 25: 1099-113.

Rosenthal, Eben L., Jason M. Warram, Kirby I. Bland, and Kurt R. Zinn. 2015. 'The Status of Contemporary Image-Guided Modalities in Oncologic Surgery', Annals of Surgery, 261: 46-55.

Schlesinger, David, Stanley Benedict, Chris Diederich, Wladyslaw Gedroyc, Alexander Klibanov, and James Larner. 2013. 'MR-guided focused ultrasound surgery, present and future', Medical Physics, 40: 080901.

Shah, J., S. Park, S. Aglyamov, T. Larson, L. Ma, K. Sokolov, K. Johnston, T. Milner, and S. Y. Emelianov. 2008. 'Photoacoustic imaging and temperature measurement for photothermal cancer therapy', J Biomed Opt, 13: 034024.

Smith, Andrew M., Michael C. Mancini, and Shuming Nie. 2009. 'Bioimaging: Second window for in vivo imaging', Nat Nano, 4: 710-11.

Sun, Yao, and Brian O'Neill. 2013. 'Imaging high-intensity focused ultrasound-induced tissue denaturation by multispectral photoacoustic method: an ex vivo study', Applied optics, 52: 1764-70.

Tanya, D. Khokhlova, M. Pelivanov Ivan, A. Sapozhnikov Oleg, S. Solomatin Vladimir, and A. Karabutov Aleksander. 2006. 'Opto-acoustic diagnostics of the thermal action of high-intensity focused ultrasound on biological tissues: the possibility of its applications and model experiments', Quantum Electronics, 36: 1097.

U.S. Food and Drug Administration, Center for Devices and Radiological Health. 2005. "InSightec ExAblate® System, Model 2000 premarket approval." In.

Vaezy, Shahram, Xuegong Shi, Roy W. Martin, Emil Chi, Peter I. Nelson, Michael R. Bailey, and Lawrence A. Crum. 2001. 'Real-time visualization of high-intensity focused ultrasound treatment using ultrasound imaging', Ultrasound in Medicine & Biology, 27: 33-42.

Chapter 5: Intravascular Photoacoustic Imaging Optimization Using Monte Carlo Optical Modeling And Analysis

5.1 ABSTRACT

Coronary heart disease, typified by the presence of coronary atherosclerotic plaques, is a significant killer in the industrialized world. Percutaneous catheter intervention (PCI) is a common treatment method used to stabilize vulnerable plaques that could otherwise rupture. Intravascular photoacoustic (IVPA) imaging is being explored to improve and guide PCI treatments by characterizing vulnerable plaques, but a clinical IVPA imaging system has yet to be introduced. We utilized a sophisticated Monte Carlo (MC) optical model to simulate IVPA excitation in simulated coronary tissues to identify optimal wavelengths in terms of optical penetration and visualization of lipid. NIR wavelengths from 800 – 1800 nm were simulated and single- and dual-wavelength image data was analyzed utilizing image-subtraction and segmentation. Results indicate light penetration is best in the range of 1050 nm to 1370 nm, where 5% fluence can be readily achieved at clinically relevant depths of 2 mm or more in arteries. Analyses of optical fluence show that, over the arterial lumen, fluence can vary by over an order of magnitude, confounding assessments of lipid content. Segmentation-lipid correlation peaked in single-wavelength images at 1210 nm and 1720 nm, though correlation overall was quite poor. Subtraction-images showed much better correlation between segmentation and lipid content, with several bands of high correlation, the most promising of which utilized 1210 nm as a primary wavelength. Considerations of light penetration, fluence variation and lipid visualization suggest that using a primary wavelength near 1210 nm light, paired with a secondary wavelength near 1360 nm may offer the most promising clinical implementation of IVPA imaging as it allows

differentiation of plaque from luminal blood pool and lining, while optimizing light penetration and reduce fluence variation across images.

5.2 INTRODUCTION

5.2.1 Coronary heart disease and treatment

Coronary heart disease (CHD) affects 6.2% of American adults (aged ≥ 20 years) and contributes to American adults experiencing a myocardial infarction every 43 seconds, on average (Mozaffarian et al. 2015). This exacts an annual financial cost in excess of $200 billion in 2010 (Mozaffarian et al. 2015) and an incalculable toll in human suffering. CHD occurs when lipid accumulates at the endothelium of the coronary arteries, resulting in the formation of an atherosclerotic plaque (Libby 2002). Plaque accumulation can occur over many years, and may result in narrowing of the lumen, which reduces blood flow downstream, or may develop into a vulnerable plaque, which can rupture, resulting in thrombus formation and myocardial infarction (Libby 2002). Coronary-stent placement via percutaneous catheter intervention (PCI) is an accepted treatment method to stabilize vulnerable plaques (Fischman et al. 1994). Much research has been conducted to differentiate vulnerable plaques from their stable counterparts, and several pertinent imaging-related markers have been identified, such as fibrous-cap thickness and the presence of a necrotic core (Fleg et al. 2012; Narula et al. 2013). It has also been shown that patient outcomes improve when PCI stenting-procedures utilize image guidance techniques, such as intravascular ultrasound (IVUS) imaging (Roy et al. 2008). These results highlight the potential for image guidance to improve the outcomes of patients suffering from CAD. Photoacoustic (PA) imaging a novel imaging modality that is being explored to address this need.

5.2.2 Photoacoustic imaging

In brief, PA imaging is a hybrid optic-ultrasonic imaging modality which utilizes short-duration laser pulses (Xu and Wang 2006; Beard 2011; Dana, Dumani, et al. 2016) which are absorbed by chromophores in the tissue, resulting in thermoelastic expansion and generation of an acoustic transient (Xu and Wang 2006; Beard 2011; Dana, Dumani, et al. 2016). These transients can be imaged using a traditional ultrasound (US) transducer (Bouchard et al. 2012; Shah et al. 2008; Wang et al. 2012a) and used to generate an estimate of the distribution of optical absorbers in the tissue, making PA imaging a molecular imaging modality. The peak photoacoustic pressure is commonly modeled as:

$$p_0(\vec{r},\lambda,T) \propto \left(\frac{\beta(\vec{r},T)\, v_s^2(\vec{r},T)}{C_p(\vec{r},T)}\right)\mu_a(\vec{r},\lambda)\, F(\vec{r},\lambda) \qquad \text{Equation 7}$$

$$\Gamma(\vec{r},T) = \left(\frac{\beta(\vec{r},T)\, v_s^2(\vec{r},T)}{C_p(\vec{r},T)}\right) \qquad \text{Equation 8}$$

where $\beta(\vec{r},T)$ [K^{-1}] is the temperature dependent thermal coefficient of volume expansion, $v_s(\vec{r},T)$ [cm s^{-1}] is the sound velocity in tissue, $C_p(\vec{r},T)$ [J kg^{-1} K^{-1}] is the heat capacity at constant pressure, $\mu_a(\vec{r},\lambda)$ [cm^{-1}] is the optical absorption coefficient and $F(\vec{r},\lambda)$ [J cm^{-2}] is the local optical fluence (Xu and Wang 2006; Beard 2011). As such, $\vec{r},\lambda$ and T represent spatial distribution, optical wavelength and temperature, respectively, and the term containing $\beta(\vec{r},T)$, $v_s(\vec{r},T)$ and $C_p(\vec{r},T)$ is often referred to as the Grüneisen parameter, $\Gamma(\vec{r},T)$ [unitless] (Equation 8).

5.2.3 Intravascular photoacoustic imaging

Intravascular photoacoustic (IVPA) imaging, combined with IVUS imaging, has been extensively leveraged as a means to provide image guidance and characterization of atherosclerotic plaques (Wang et al. 2010; Wang and Emelianov 2011; Wang et al. 2012a; Wang et al. 2012b; Yeager et al. 2012; VanderLaan et al. 2014; Yeager et al. 2014; Jansen, van der Steen, et al. 2014; Jansen, Wu, et al. 2014; Allen et al. 2012; Karpiouk, Wang, and Emelianov 2010) and to evaluate coronary stent placement (Su, Wang, and Emelianov 2009). Results have demonstrated the promise of IVPA imaging using both endogenous contrast (Wang et al. 2010; Wang et al. 2012a; Jansen, van der Steen, et al. 2014; Jansen, Wu, et al. 2014) and exogenous contrast agents (Wang et al. 2009; Yeager et al. 2012). Investigations have indicated there are two primary spectral regions, 1210 nm and 1720 nm, that show promise for visualizing the lipid content in plaque (Wang et al. 2012a; Jansen, Wu, et al. 2014; Wang et al. 2010). These various results have propelled IVPA imaging from the research realm toward its development as a clinical imaging modality (VanderLaan et al. 2014; Karpiouk, Wang, and Emelianov 2010; Abran et al. 2014; Li et al. 2015; Piao et al. 2015). While promising, results have yet to demonstrate which of these two spectral regions may provide optimal plaque characterization results and also how said results might best be improved by the addition of secondary wavelengths for imaging. Given the compromises involved in designing an imaging system, such as balancing design, function and cost (Fleg et al. 2012), developing an optimized translatable imaging system is not a trivial task.

For an IVPA/IVUS imaging system to successfully translate into the clinical realm, it must do several things:

1. Demonstrate the ability to reliably and accurately assess coronary diameter and stenosis (Narula et al. 2013; Fleg et al. 2012).

2. Demonstrate reliable and accurate visualization and quantification of plaque burden in the artery, which has been shown to be useful in characterizing vulnerable plaque (Narula et al. 2013; Wilensky 2013; Fleg et al. 2012).
3. Demonstrate the ability to achieve the above results while imaging through several millimeters of blood and tissue, which should be sufficient in most situations, given the average coronary artery diameter of 3.5 mm (Waller et al. 1992).
4. Provide this image guidance and characterization in real-time, preferably at a frame-rate of 30 frames per second.
5. Accomplish all of the above while trying to maximize cost-effectiveness, thus reducing the barrier to clinical translation (Fleg et al. 2012).

5.2.4 Current barriers to translation of intravascular photoacoustic imaging

Many previous results have relied upon an optical parametric oscillator (OPO) to provide tunable wavelength selection for IVPA studies (Wang et al. 2010; Wang and Emelianov 2011; Wang et al. 2012a; Wang et al. 2012b; Yeager et al. 2012; VanderLaan et al. 2014; Yeager et al. 2014; Jansen, van der Steen, et al. 2014; Jansen, Wu, et al. 2014). While versatile and useful in a research setting, this is unlikely to be suitable for a clinical imaging system, as these laser systems typically suffer from slow pulse repetition frequency (~10 Hz) and can be cost-prohibitive. Given the desire to provide real-time imaging, an IVPA system that reconstructs a single image from 128 scan lines will need a laser source with a pulse repetition frequency of several kilohertz (1 laser pulse per scan line x 128 scan lines per frame x 30 frames per second = 3840 laser pulses per second). This number will increase linearly with the number of imaging wavelengths. This laser source must also provide a sufficiently high pulse energy so as to excite a measurable PA

signal at depths in excess of 2 mm through blood and tissue to reliably image within the average coronary artery (Waller et al. 1992). While not impossible, it is unlikely that a laser and optics system or collection of systems would be able to accomplish these tasks while providing illumination at many wavelengths. For that reason, it seems reasonable to consider that an optimized clinical IVPA imaging system provide results using only one or two wavelengths, but no more. With this constraint in mind, we can consider how we might determine an optimal IVPA imaging configuration.

Ideally, in order to develop a clinical IVPA imaging system, one would conduct exhaustive experiments, preferably using IVPA imaging systems currently in development (VanderLaan et al. 2014; Karpiouk, Wang, and Emelianov 2010). This would require using multiple fresh coronary artery samples, with different disease states, with each imaged exhaustively in the NIR, followed by comprehensive histopathology to establish pertinent metrics such as luminal stenosis, plaque burden and cap thickness. Unfortunately, given the dearth and fragility of available tissue samples, such a comprehensive imaging study is unrealistic. Fortunately, other options, such as optical modeling, may offer insight into the details of an optimized clinical IVPA imaging system.

5.2.5 Modeling-based optimization of intravascular photoacoustic imaging

Monte Carlo (MC) optical modeling is a technique in which the probabilistic propagation of photons through a medium simulated and then combined to calculate a final fluence distribution. MC modeling has been used for decades to elucidate light transport and distributions in biomedical applications (Wilson and Adam 1983; Prahl et al. 1989; Wang, Jacques, and Zheng 1995; Fang and Boas 2009; Jacques 2014). In brief,

MC models treat light transport in tissue as a stochastic process, where the optical properties of a given tissue type are modeled by a set of parameters:

1. The probability of a photon being absorbed, defined as the absorption coefficient, μ_a [cm^{-1}].
2. The probability of a photon being scattered, defined as the scattering coefficient, μ_s [cm^{-1}].
3. The average angle of scattering, defined by the anisotropy, g [unitless], and a phase function (the Henyey-Greenstein (Henyey and Greenstein 1941) phase function is commonly used in biomedical applications, though several others have been suggested).
4. The refractive index of the material, n [unitless] (not all models incorporate this information).

Simulations utilize random number generators and, using known or estimated optical properties, determine the path length of a photon packet, the fraction of energy absorbed and the new vector of propagation of a photon after each light-matter interaction (Wilson and Adam 1983; Prahl et al. 1989; Wang, Jacques, and Zheng 1995; Fang and Boas 2009; Jacques 2014). This continues until the energy of a photon packet decreases below a critical threshold, at which point transport of that packet is typically terminated (Wilson and Adam 1983; Prahl et al. 1989; Wang, Jacques, and Zheng 1995; Fang and Boas 2009; Jacques 2014). A new photon packet can then be launched, and the process repeated, until the fluence distribution within the tissue is adequately simulated. MC models have been developed for homogenous (Wilson and Adam 1983) and layered tissues (Wang, Jacques, and Zheng 1995), three-dimensional (3D) voxellated media (Fang and Boas 2009; Jacques 2014) and mesh-based structures (Fang 2010), with simulations optimized to run on CPUs, as well as graphics processing units (GPU) (Fang

and Boas 2009; Fang 2010). The success of MC models can be attributed to their high accuracy when compared to experiments (Flock, Wilson, and Patterson 1989) and their superiority to alternative methods, such as diffusion theory (Flock et al. 1989).

We aim to leverage the accuracy and versatility of MC optical modeling to simulate the fluence distribution in typical IVPA imaging applications and provide insight into which system configurations may provide the best balance of contrast, imaging depth and lipid visualization. We have developed a model to simulate IVPA data across a range of NIR wavelengths, using several different tissue geometries. The goal of this study is not to supplant experimental studies, which are invaluable, but rather to guide them by providing insight into which imaging schemes show the most promise, so that the limited resources available for IVPA imaging studies can be utilized in the most beneficial matter. In this way, we intend the model-based results provided herein to be used alongside future IVPA imaging experiments and to inform IVPA imaging system development going forward.

5.3 METHODS

5.3.1 Overview of Monte Carlo model

MCXLAB, the software used herein for optical modeling, was developed using CUDA (Nickolls et al. 2008) by Fang and Boas (Fang and Boas 2009) and implemented in MATLAB (MathWorks, Inc., Natick, MA). The simulation defines a 3D gridded model space, where each voxel is tagged with an integer that designates the media comprising that voxel. Each media is defined by four optical parameters (μ_a, μ_s, g and n, as described above), which, together, define the optical properties of the entire simulation space (Fang and Boas 2009). The optical properties of the external space were also defined, as well as the conditions at the model-exterior boundary (non-reflective

boundary). The model space used a grid spacing of 20 μm, which was approximately equivalent to the overall minimum mean free path (MFP) across the tissue types and wavelengths used, as suggested by previous models (Wang, Jacques, and Zheng 1995). The result was a voxel volume of 20 x 20 x 20 μm^3, with uniform grid spacing in the X, Y and Z dimensions, with each dimension spanning 8 mm total, for a total simulation space volume of 8 x 8 x 8 mm^3.

Illumination was modeled as a side-firing optical fiber, very similar to what has been described in previous experimental setups (VanderLaan et al. 2014; Jansen, van der Steen, et al. 2014; Karpiouk, Wang, and Emelianov 2010). The side firing source was located in the center of the model volume. The optical source was modeled as a uniform cone, emanating from the side of the fiber (conic-axis parallel to the X-Y plane), with a half-angle of 16.7 degrees (0.292 radians). The side-firing ultrasonic transducer was modeled as being co-localized with the source, with the axis of ultrasonic propagation assumed to be co-linear with optical conic-axis. Using previously reported unfocused transducer parameters (Karpiouk, Wang, and Emelianov 2010), the transducer sampling-volume, corresponding to the 3D "footprint" of the transducer, was estimated in model space by using reported transducer size and frequency characteristics. The transducer footprint was modeled as being equivalent to the transducer area up to the far-field transition zone (d_{ff}), where $d_{\mathrm{ff}} \approx a^2/\lambda_{US} = 1.6$ mm, a is the piston-transducer radius (250 μm) and λ_{US} is the ultrasound wavelength (approximately 38.5 μm at 40 MHz in tissue) (Szabo 2004). In the far-field zone, the transducer footprint was modeled as diverging according to the full-width half-maximum (FWHM) estimation provided by Szabo (Szabo 2004), shown in Equation 9. Figure 5.1 shows a 3D overlay of the optical fiber, light cone and transducer footprint, as well as a fluence cross-section of a simulation done at 1000 nm in water.

$$\text{FWHM} \approx 0.7047\ \lambda_{\text{US}}\ d/a \qquad \text{Equation 9}$$

5.3.2 Consolidation of model output

Once the initial optical simulation was run, a normalized 3D fluence distribution was generated, containing the estimated fluence at each voxel, $F(\vec{r}, \lambda)$. The PA signal at each voxel was modeled by taking the product of the fluence, the optical absorption, $\mu_a(\vec{r}, \lambda)$, and the Grüneisen parameter, $\Gamma(\vec{r}, T)$, for water-based (0.14) or lipid-based (0.81) tissues, which has been reported previously at room temperature (Yao et al. 2014). The result was a 3D distribution of PA amplitudes, $p_0(\vec{r}, \lambda, T)$, equivalent to what is modeled by Equation 1. Those PA signals which overlapped with the transducer footprint (the intersect of the two regions) were recorded. The source and transducer were then rotated in the X-Y plane, which is equivalent to rotating an IVPA imaging catheter in a coronary artery, and the process was repeated. This was done every 2.81 degrees (0.049 radians) to sample the entire 360 degree arc in 128 steps, as this allowed the entire 2D plane to be spatially sampled at least once, with most voxels being sampled multiple times. Once the entire arc had been sampled, the PA signal contributed from each of the 128 simulations was combined, summed across the Z dimension (which corresponded to the coronary artery axis), and then normalized to the number of times each voxel was sampled. The result was an estimated two-dimensional (2D) distribution of PA signal sources which would be observed by the IVPA imaging system, $I_{PA}(x, y, \lambda)$, as well as a 2D fluence distribution, $I_F(x, y, \lambda)$, at a given wavelength. This entire simulation process was performed at wavelengths from 800 nm to 1800 nm, in 10 nm steps, for each of the four simulated tissue samples. Photon packets totaling 3x106 were launched for each simulation, with the average runtime of a single simulation being 12 seconds, and the

total runtime of all simulations totaling 172 hours. Simulations were performed on a Windows 7 (Microsoft, Seattle, WA) computer with 16 GB of RAM, an Intel Core I7-4770 processor (Intel, Inc., Santa Clara, CA) and a NVidia GTX 1080 GPU (NVidia, Inc., Santa Clara, CA). The resulting data was comprised of 404 simulated image sets, across 101 wavelengths and four tissue types.

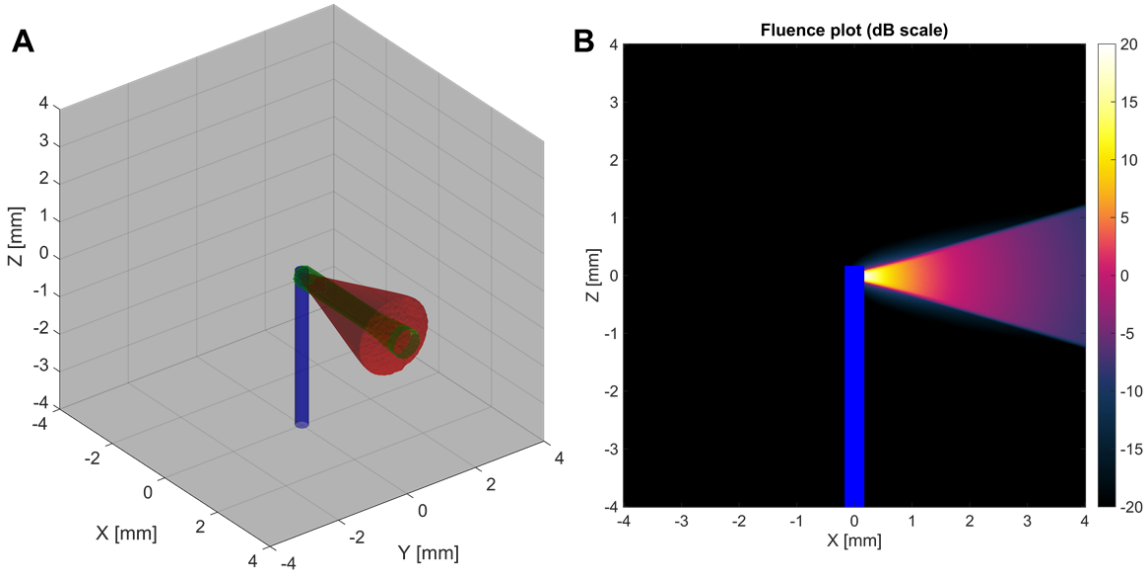

Figure 5.1. (A) Volumetric rendering of optical fiber (blue), light cone (red) and transducer footprint (green). (B) Fluence cross-section (Y = 0 mm, 40 dB scale) of an optical simulation at 1000 nm in water.

5.3.3 Tissue models and optical properties

Four 3D tissue volumes were generated for the model. Two samples were designed that represented vulnerable plaques that would require intervention. The other two samples were designed so as to be unlikely to rupture and produce a thrombus, and thus would not require intervention. A recent study by Narula, et al., examined 295 histopathologic samples of atherosclerotic coronary disease (Narula et al. 2013). Their results indicate that a cap thickness of < 54 µm was the best indicator of plaque type,

followed by macrophage infiltration, necrotic core area (≥ 3.45 mm^2) and that % luminal stenosis did not significantly differentiate stable from vulnerable plaques (Narula et al. 2013). Based on these results, we designed our two vulnerable plaques models as having a thin cap (< 60 μm) and a large lipid-pool (> 3.9 mm^2), as would be expected with a large necrotic core. Conversely our stable plaque sample contained a thicker cap (> 80 μm) and a modest lipid pool (≤ 2.4 mm^2). The last tissue sample modeled was essentially a healthy artery, with minimal fatty streaks and no stenosis. Other tissue properties, such as the thickness of intimal, medial and adventitial tissue, as well as the blood volume, were selected based on average values reported in literature (Waller et al. 1992). The region external to the adventitial tissue was modeled as pericardial (PC) fluid (Ben-Horin et al.). Also, in each tissue sample, extending co-linearly with the Z-axis for 4 mm was a 320 μm diameter optical fiber, as would be needed for light delivery in a catheter implementation. Aside from the fiber optic extending partway into the tissue volume, the tissue samples did not vary along the Z-dimension. Figure 5.2 shows a cross-section of the four tissue types at the slice containing the tip of the optical fiber (Z = 0 mm).

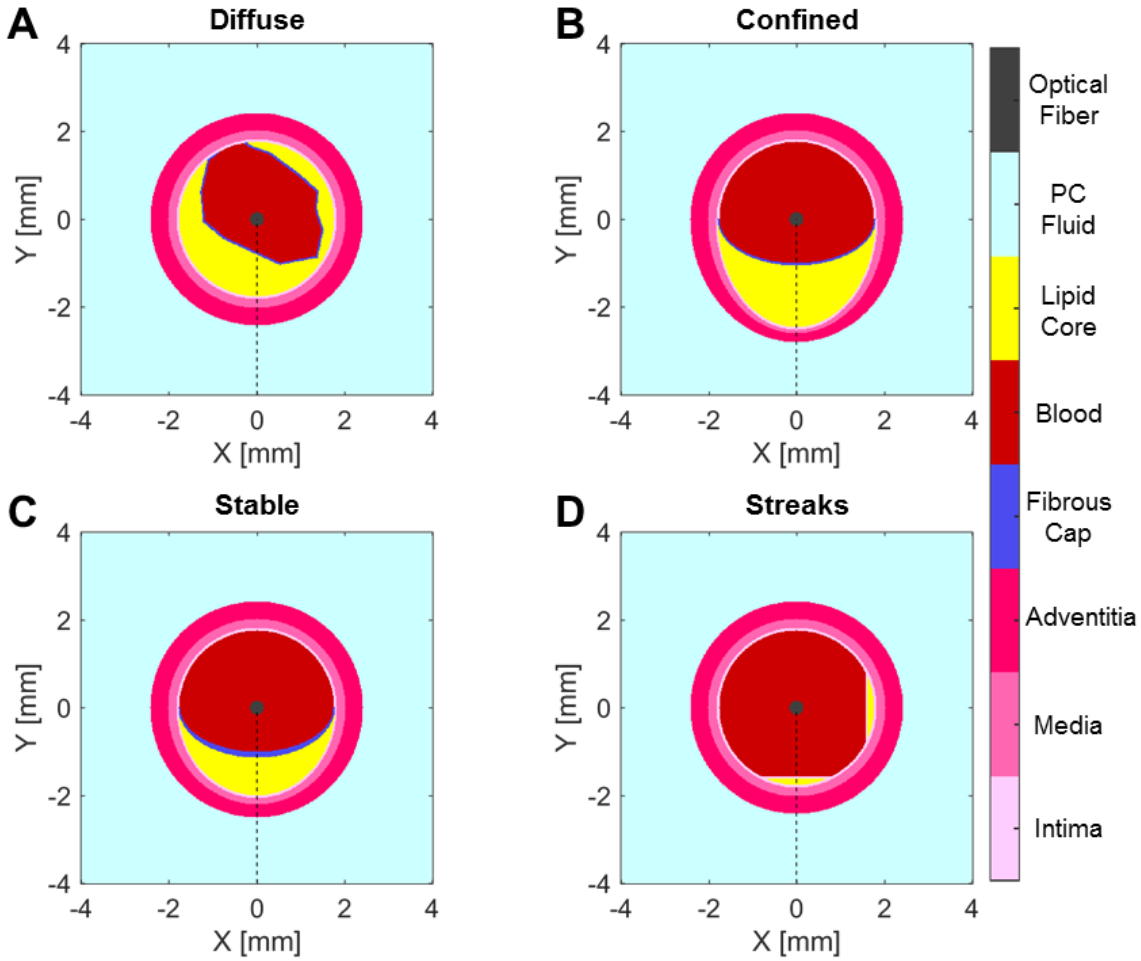

Figure 5.2. Cross-section of modeled tissue volumes at plane Z = 0 mm. Diffuse (A) and Confined (B) represent vulnerable plaques, with large lipid pools and thin caps. Stable (C) represents a stable plaque with a modest lipid pool and a thick cap. Streaks (D) represents a healthy artery with minimal lipid pool. Legend on the right denotes tissue types. Dashed line denotes location where light penetration analysis was done.

The optical properties of the seven tissue constituents in the NIR regime were tabulated from several sources, as described in Table 5.1. Absorption data were extracted from the literature and, if needed, joined and smoothed to provide a continuous spectrum across the desired range. Scattering data were also extracted from the literature and smoothed by fitting data to a two-term function as suggested by Jacques (Jacques 2013).

The optical properties of lipid were estimated based on measurements taken of adipose tissue (Bashkatov et al. 2005b; van Veen et al. 2005; Zamora-Rojas et al. 2013), and fibrous cap properties were estimated based on measurements taken of the thin fibrous layer derived from human aorta (Çilesiz and Welch 1993). PC fluid was modeled based on measurements taken of blood and plasma (Roggan et al. 1999). All other tissue samples were modeled based on optical measurements taken from the tissue themselves, as shown in Table 5.1. Blood was assumed to have an oxygen saturation (SpO2) of 95%. At longer NIR wavelengths (> 1000 nm). The optical absorption of most tissues closely mirrors that of water (Jacques 2013), and so, when literature data were not available at longer wavelengths (typically beyond 1000 nm), the optical absorption of intimal, medial, adventitial tissues and PC fluid was estimated by linearly fitting available data to measurements made of sea water (Hale and Querry 1973) and extrapolating, as has been previously suggested (Jacques 2013). Figure 5.3 shows the final absorption and scattering values used in the model for the 7 tissue types. The optical fiber was assumed to be minimally scattering and absorbing at the modeled wavelengths.

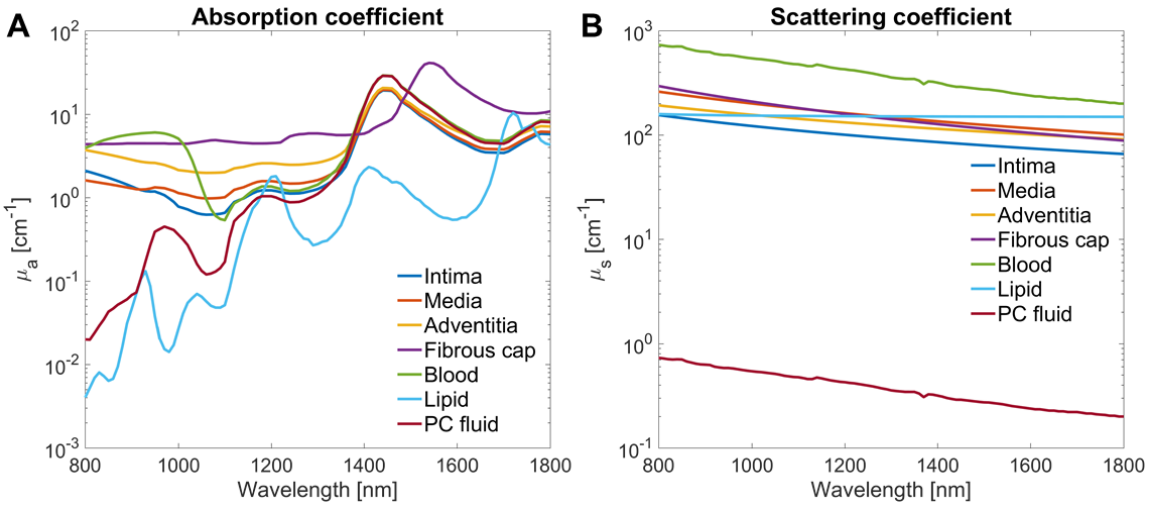

Figure 5.3. Optical absorption (A) and scattering (B) coefficients used to model tissue types. Sources for data can be found in Table 5.1.

Tissue optical parameters and sources (values estimated at 1210 nm)					
Tissue type	$\mu_a(\lambda)$ [cm^{-1}]	$\mu_s(\lambda)$ [cm^{-1}]	$g(\lambda)$	n	Sources
Intima	0.120	9.98	0.89	1.40	(Keijzer et al. 1989) (Hale and Querry 1973)
Media	0.155	16.1	0.86	1.40	(Keijzer et al. 1989) (Hale and Querry 1973)
Adventitia	0.256	13.1	0.89	1.40	(Keijzer et al. 1989) (Hale and Querry 1973)
Fibrous cap	0.453	15.8	0.90	1.40	(Çilesiz and Welch 1993)
Blood	0.132	42.1	0.94	1.35	(Roggan et al. 1999) (Hale and Querry 1973)
Lipid	0.181	15.2	0.93	1.47	(Zamora-Rojas et al. 2013) (van Veen et al. 2005) (Bashkatov et al. 2005b)
PC fluid	0.100	0.0421	0.80	1.34	(Roggan et al. 1999) (Hale and Querry 1973)

Table 5.1. Comparison of tissue optical parameters for absorption, $\mu_a(\lambda)$ [cm^{-1}], scattering, $\mu_s(\lambda)$ [cm^{-1}], anisotropy, $g(\lambda)$ [unitless] and index of refraction, n [unitless], as well as the data sources used to estimate values. Blood was assumed to be 95% oxygen saturated. Anisotropy values typically varied by less than 0.05 across the wavelength range used for a given tissue type. Due to the low dispersion of water and lipid, index of refraction was assumed to be constant for all tissues.

5.3.4 Depth penetration and simulation signal-to-noise analysis

Once the outputs from the simulations were consolidated, several analysis methods were used to determine the quality of expected imaging results. For the 2D fluence distributions, optical penetration depth was assessed by sliding a 100 x 100 μm^2 averaging kernel along the dashed line in Figure 5.2 and recording where fluence attenuated to 5% at each wavelength. SNR in the fluence estimates, which is way to address if the number of simulated photons was sufficient, was calculated by sliding a 100 x 100 μm^2 kernel across each $I_F(x, y, \lambda)$ image and calculating the mean fluence ($\overline{I_F}$) and standard deviation (σ_F) at each position. The SNR at that position was then taken to be the ratio of the two ($\overline{I_F}/\sigma_F$), and then the mean SNR across the entire image was calculated in order to estimate the SNR of the optical simulation process.

5.3.5 Segmentation and correlation analysis

To provide a useful metric to gauge the accuracy of the simulated results to visualize lipid, and thus plaque area, we implemented a simple segmentation algorithm to the IVPA images, $I_{PA}(x, y, \lambda)$, followed by calculation of the Matthew's correlation coefficient (MCC) (Matthews 1975) to determine the quality that imaging scheme to visualize plaque content. The segmentation algorithm used Otsu's method (Otsu 1975) to apply a binary segmentation that designated each voxel of the fluence distribution as either lipid or non-lipid, and then compared those results to the tissue cross-section image as ground truth. Voxels containing lipid were True (the yellow regions in Figure 5.2), all other tissue types were False. By comparing segmentation results with ground truth images voxel by voxel, we calculated true positive (TP), false positive (FP), true negative (TN) and false negative (FN) numbers for each image. These were used to determine the MCC based on the Equation 10:

$$\mathrm{MCC} = \frac{TP \times TN - FP \times FN}{\sqrt{(TP + FP)(TP + FN)(TN + FP)(TN + FN)}} \qquad \text{Equation 10}$$

The MCC is related to the χ^2 statistic and is a good estimator of a binary classifier (Powers 2011). The MCC has an upper and lower bound of 1 and -1, respectively. An MCC of 1 indicates a perfect match between true and measured positive and negative values, while an MCC of -1 indicates a perfect reversal of positive and negative matches, both of which indicate utility in the imaging results. A value for the MCC was calculated for each of the 101 wavelengths, $MCC(\lambda)$, and for each of the four tissue models. A composite MCC was calculated at each wavelength by combining the TP, TN, FP and FN results from all tissue models.

5.3.6 Subtraction-image analysis

Additionally, given that a dual-wavelength IVPA imaging system seemed the most probable implementation of a multi-wavelength IVPA imaging platform, analysis was done to determine which wavelength-pairs may provide the best assessment of plaque content. A simple wavelength-subtraction method was applied to generate a subtraction-image, $I_{\bar{PA}}(x, y, \lambda_1, \lambda_2) = I_{PA}(x, y, \lambda_1) - I_{PA}(x, y, \lambda_2)$. After subtraction, any voxels containing negative intensity values were set to zero. This was done to emphasize primary wavelengths with high-lipid absorption. The data was then processed using the same segmentation method described above, and a single MCC was calculated for each $I_{\bar{PA}}(x, y, \lambda_1, \lambda_2)$ image. The result is a 101 x 101 (wavelength x wavelength) MCC heatmap, $MCC_{hm}(\lambda_1, \lambda_2)$, for each tissue model, and a final composite MCC heatmap using the TP, TN, FP and FN data across all $I_{\bar{PA}}(x, y, \lambda_1, \lambda_2)$ image segmentations.

5.4 RESULTS

5.4.1 Signal-to-noise results

The average SNR in the fluence distributions, $I_F(x, y, \lambda)$, across all wavelengths and tissue geometries was 12.6 ± 2.2, and never fell below 6.3 for any simulation, indicating the number of photon packets launched was sufficient.

5.4.2 Visualization of simulated IVPA results

Figure 5.4 shows simulated IVPA data, $I_{PA}(x, y, \lambda)$, from the four tissue models at 1210 nm, displayed on logarithmic dB scale. Optical absorption of lipid at 1210 nm is a local maximum, and exceeds that of water (as seen in Figure 5.4A), which contributes to the high PA signal seen in the lipid regions in Figure 5.4 (lipid regions are shown in yellow in Figure 5.2). As seen in Figure 5.4, the optical fluence varies by more than an order of magnitude across the lumen and arterial wall.

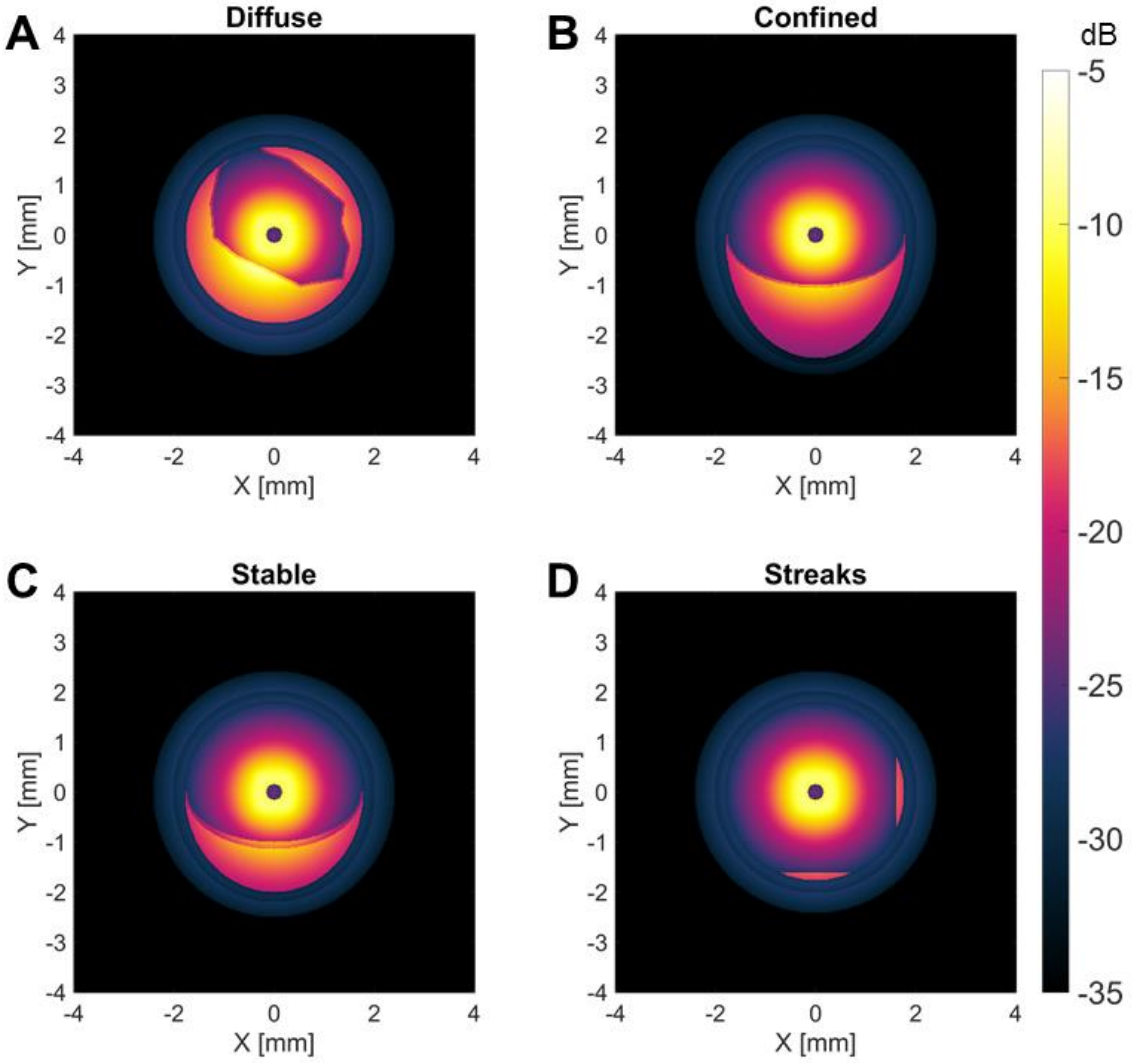

Figure 5.4. Simulated PA data at 1210 nm, $I_{PA}(x, y, 1210\ nm)$, for Diffuse (A), Confined (B), Stable (C) and Streaks (D) tissue models. Images are presented on decibel scale. Note that 1210 nm represents a local absorption maxima of lipid over water, as shown in Figure 5.3A, which is demonstrated by the high-intensity signals in the lipid regions, which are shown in yellow in Figure 5.2.

5.4.3 Variations in depth penetration and single-image segmentation

Figure 5.5 shows the results of the depth penetration analysis (A) and the single-image segmentation results (B). The 5% fluence threshold shown in (A) corresponds to

the probability of a photon transiting across the effective MFP length three times, as one would calculate using a Beer-Lambert approach $\left({I}/{I_0} = e^{-z\cdot\mu_{eff}} \approx 0.05, z = 3\times MFP_{eff}\right)$ (Wang and Wu 2007). For that reason, it is a useful metric to compare between wavelengths and also against other optical modeling results. The 5% fluence threshold varied between 1.5 mm and 2 mm for most wavelengths examined, but the wavelength window from approximately 1050 nm to 1350 nm showed improved depth penetration. The correlation assessment shown in Figure 5.5B indicates modest correlation overall, but the wavelength regions near 1210 nm and 1720 nm, which represent peaks in the lipid optical absorption, show the best correlation overall. This is in agreement with previous studies, which have found IVPA imaging contrast between lipid and water is best at these wavelengths (Wang et al. 2010; Wang et al. 2012a; Wang et al. 2012b; Jansen, van der Steen, et al. 2014; Jansen, Wu, et al. 2014).

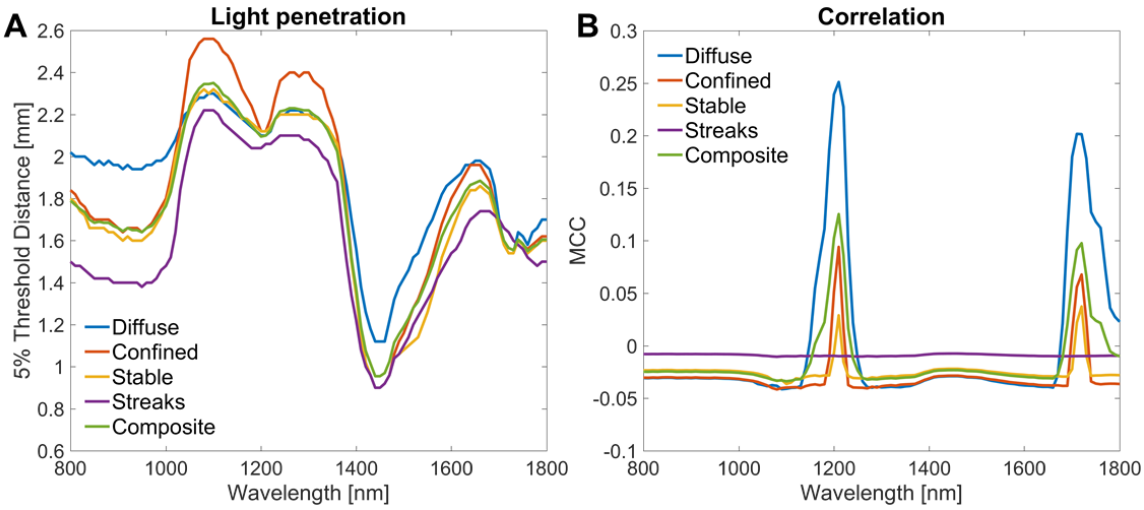

Figure 5.5. Analysis of light penetration across the four tissue types and the composite results (A). A 5% normalized fluence threshold was used, and the average distance of that threshold from the source was calculated for each wavelength and tissue model. Analysis was done along the dashed lines in Figure 5.2, which corresponds to the approximate "center" of the lipid-rich region. Correlation analysis for the segmented $I_{PA}(x, y, 1210\ nm)$ data for the four tissue types and the composite results (B). Two wavelength regions stand out, near 1210 nm and 1720 nm, which correspond to the local absorption maxima of lipid over water.

5.4.4 Results of image-subtraction and segmentation

Figure 5.6 shows an example of the image-subtraction process and the segmentation results obtained. $I_{PA}(x, y, \lambda)$ images are shown on the same linear scale at 1210 nm (Figure 5.6A) and 1530 nm (Figure 5.6B). Note the much higher PA signal observed at 1530 nm, particularly near the light source, as compared to 1210 nm. This is primarily due to the optical absorption of water being roughly an order of magnitude greater than that of lipid at 1530 nm (Figure 5.6A). For this reason, the corresponding subtraction image ($\bar{I_{PA}}(x, y, \lambda_1, \lambda_2)$, Figure 5.6C), with negative values set to zero, emphasizes the lipid-filled regions and deemphasizes other tissue regions, as can be seen.

As a result, the segmented image, shown in Figure 5.6C, strongly correlates to the lipid-filled regions visible in yellow in Figure 5.2A.

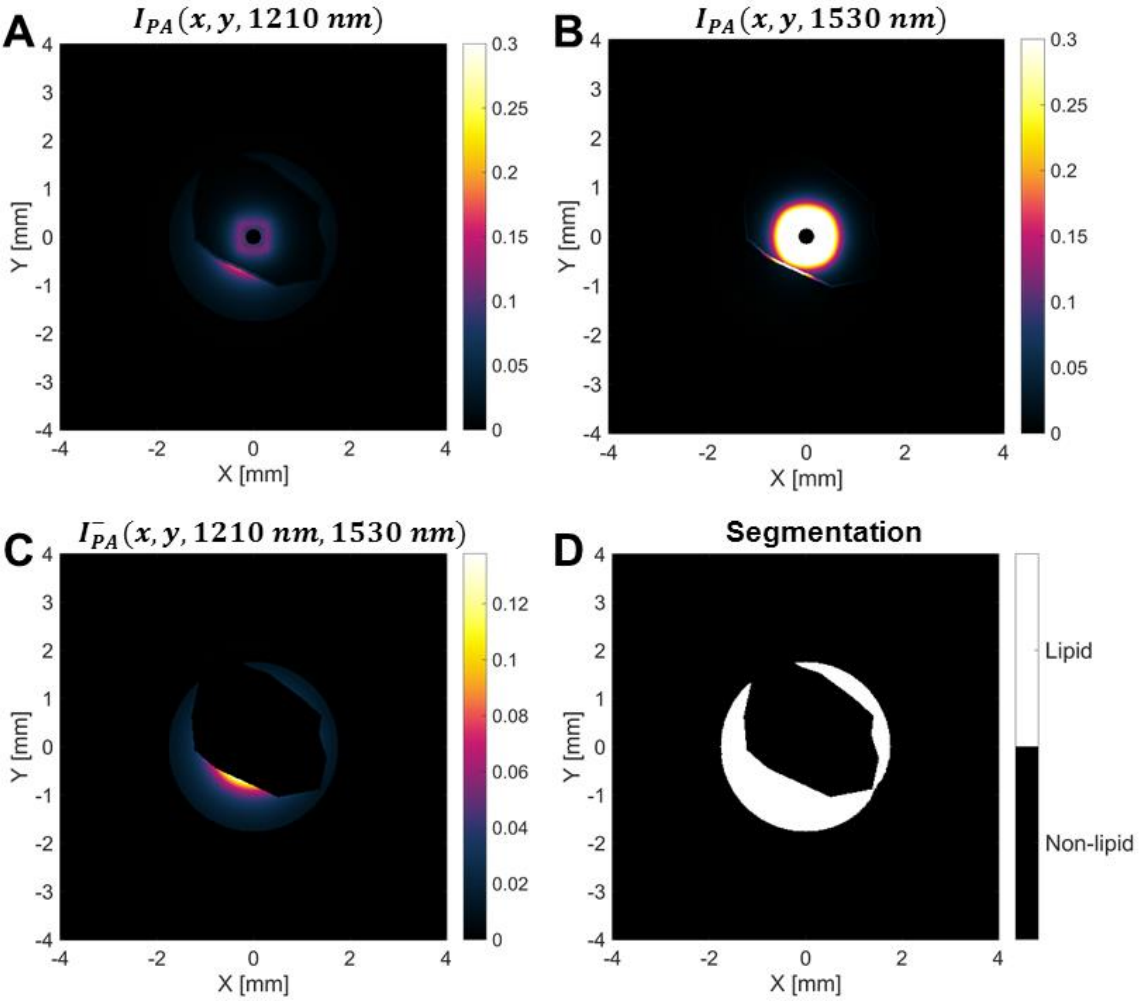

Figure 5.6. Simulated PA data, $I_{PA}(x, y, \lambda)$, for Diffuse tissue model at 1210 nm (A) and 1530 nm (B). Images are displayed on linear scale for comparison. Subtraction image, $I_{\bar{PA}}(x, y, \lambda_1, \lambda_2)$, using data displayed in (A) and (B), shown on a linear scale (C). Note that negative valued-data is set to zero, as described above. Segmented image based on (C), with predicted lipid-rich regions as white (D).

5.4.5 Correlation heatmap results

Results from the image segmentation and correlation analysis on the subtraction-images, $MCC_{hm}(\lambda_1, \lambda_2)$, is shown in Figure 5. for all four tissue models, as well as a composite MCC heatmap (Figure 5.7E). In general, results suggest that using a primary wavelength near 1210 nm showed good correlation using a range of secondary wavelengths, as evidenced by the red horizontal bands centered near λ_1= 1200 nm that are present in all heatmaps shown in Figure 5.7. The peak MCC value of 0.9998 for the composite data occurs at λ_1= 1220 nm and λ_2= 1530 nm, though several MCC values in the aforementioned band are comparable. MCC values centered around the 1720 nm lipid were generally ≥ 0.5, though correlation was poorer at this wavelength compared to results obtained using wavelengths near 1210 nm.

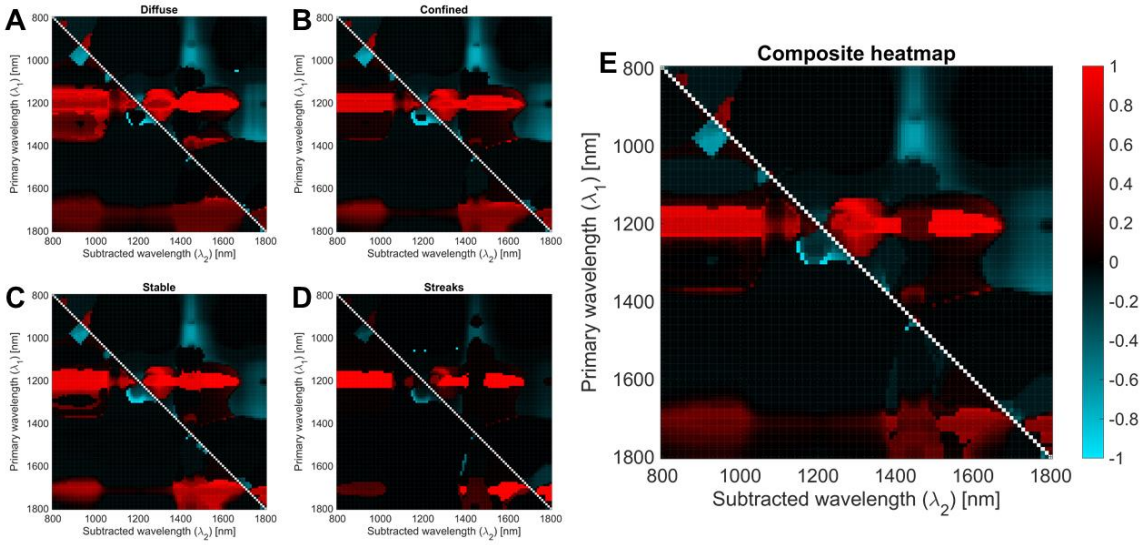

Figure 5.7. MCC heatmap, $MCC_{hm}(\lambda_1, \lambda_2)$, data from analysis of subtraction images, $I_{PA}^{-}(x, y, \lambda_1, \lambda_2)$, for Diffuse (A), Confined (B), Stable (C) and Streaks (D) tissue models, as well as composite MCC analysis from all four tissue types (E). The left and bottom axes represent the primary (λ_1) and secondary (λ_2) wavelengths used, respectively. All images are on the same scale, shown at the right of (E).

5.5 DISCUSSION

It should be noted that the results demonstrated by this work represent the absolute best that an IVPA imaging system may hope to achieve, rather than the expected results from a particular imaging setup. The fluence simulations are normalized to unity across all imaged angles, wavelengths and tissue samples. This would be achieved only if the pulse-to-pulse and wavelength-dependent energy variation of the laser system could be perfectly accounted for. Furthermore, this model presumes that the IVPA imaging system can reconstruct the absorber map to an exquisitely high degree. This model did not account for the attenuation of PA signals as they transit through tissue, nor the introduction of image artifacts due to variations in the speed of sound or refraction at media boundaries, nor for detecting PA signals in the transducer Fresnel zone, nor the transfer function of the detector system, nor noise (Szabo 2004). All of these factors will degrade image quality to some extent, and thus the results presented here are a generalized ideal. The model discussed can be modified or expanded to account for each of these factors, in turn.

5.5.1 Signal-to-noise ratio and computation time

The fact that the mean SNR never fell below 6.3 across all simulations suggests that the number of photon packets launched and the computation time were sufficient to provide modeled fluence distributions with minimal discontinuities and noise. The smoothness of that data can be seen in Figure 5.4, where sharp variations in intensity are visible only at tissue boundaries. Results suggest that sufficiently high SNRs can reliably be accomplished while either significantly reducing the number of photon packets launched, which would reduce computation time, or by maintaining computation time while using a GPU with reduced the processing. Given the current generation of NVidia GPUs (1000 series) show a roughly 60% increase in efficiency compared to the previous

generation (900 series) (Fang 2016), implementation of this model may be done on older hardware without sacrificing SNR or requiring excessive runtimes.

5.5.2 Discussion of general imaging results

Examination of data simulated at 1210 nm, shown in Figure 5.4, indicates that IVPA signals may vary by an order of magnitude within the same tissue and region (e.g. blood-filled lumen in Streaks, Figure 5.4D). Note that the optical absorption between lipid and blood varies by less than a factor of 2 at 1210 nm (Figure 5.3A), and that the Grüneisen parameter does not vary with wavelength. Given this realization, it may be that the spatial variation in fluence may dominate the subtler variation in optical absorption between tissue types, and end up being the primary contrast mechanism in image generation. While not completely unexpected, this finding runs contrary to an ideal molecular imaging modality, one whose contrast depends primarily upon the molecular imaging target (i.e. tissue optical absorption). IVUS imaging may partly allay these concerns, as it can provide additional context to morphology and tissue content (Wang et al. 2011).

5.5.3 Optical depth penetration and wavelength selection

As can be seen in Figure 5.5A, the 5% fluence threshold exceeded 2 mm, on average, in the wavelength region from 1050 nm to 1370 nm. Given that the average coronary artery has a diameter of approximately 3.5 mm (Waller et al. 1992), this wavelength window may represent the optimal imaging region in terms of achieving sufficient light delivery throughout the coronary artery. At wavelengths below 1050 nm the increased optical absorption of hemoglobin (Hb) in blood (Figure 5.3A) strongly attenuates light, as seen in the analysis of the Streaks sample (purple line), which shows reduce depth penetration across most wavelengths. Additionally, the high optical

absorption of water at wavelengths past 1370 nm results in the same strong light attenuation, this time across all tissue models. It is serendipitous that the 1210 nm optical absorption peak of lipid should fall in the middle of the window of reduced optical attenuation. Though the optical absorption difference (contrast) between lipid and water is greater at 1720 nm than at 1210 nm (Figure 5.3A), given the overall strong light attenuation at the former wavelength, achieving real-time IVPA imaging with sufficient SNR across the entire imaging area at 1720 nm may prove challenging. This analysis suggests that efforts should focus on developing IVPA imaging systems designed to operate in the 1050 nm to 1370 nm range. Still, as laser pulse energy and ultrasonic-detector sensitivity vary across systems, it may be possible to achieve adequate IVPA signal generation at increased depths while imaging at 1720 nm.

5.5.4 Single-wavelength correlation discussion

Overall MCC values for single-wavelength images showed peaks at 0.125 (1210 nm) and at 0.098 (1720 nm). While these findings confirm previous results that indicated 1210 nm and 1720 nm optimized lipid-water contrast, ideal MCC values would be near 1 (or -1). The most likely reason for this is that, at most wavelengths, the fluence spatial variations exceed those of optical absorption, and thus dominate the imaging results. While easy to account for visually, this is likely to confound an automated global-segmentation algorithm like the one used, which attempts to separate the entire image-space into a bimodal histogram for segmentation (Otsu 1975). Indeed, in addition to IVPA imaging at multiple wavelengths, it may be possible to implement an adaptive segmentation algorithm that significantly improves segmentation correlation. Once a clinical IVPA imaging system is in further development and imaging wavelength(s) are determined, such an optimized algorithm could be implemented.

5.5.5 Image-subtraction and heatmap discussion

Figure 5.4 (A and B) displays the difference in imaging results obtained at different wavelengths, due to both differences in the fluence distribution, as well as differences in optical absorption. This highlights the fact that selection of an IVPA imaging wavelength must strike a balance between optical absorption, depth penetration and fluence variation. Since initial studies have indicated the potential of IVPA imaging at 1210 nm and 1720 nm (Wang et al. 2010; Wang et al. 2012a; Wang et al. 2012b; Jansen, van der Steen, et al. 2014; Jansen, Wu, et al. 2014), it is logical to build upon previous findings by implementing a segmentation algorithm that selects for primary wavelengths (λ_1) in these wavelength regions. Our segmentation scheme accomplished this using image-subtraction, which has the potential to yield negative pixel intensities, with any negative values clipped to zero. This scheme ensures that information is only retained in IVPA images where the PA intensity $\left(\Gamma(T)\,\mu_a(\vec{r},\lambda)\,F(\vec{r},\lambda)\right)$ at the primary wavelength exceeds that of the secondary wavelength. Given that ground truth is defined by the presence or absence of lipid in a voxel, this method selects for primary wavelengths where the PA signal from lipid is the highest, which is likeliest to occur near 1210 nm and 1720 nm. This explains the 1210 nm and 1720 nm horizontal bands of strong MCCs observed in Figure 5.7. This also explains why the heatmaps are imperfectly reflected across the diagonal, as one would normally expect by inverting the primary and secondary wavelengths. The peak composite MCC occurs at λ_1= 1220 nm and λ_2= 1530 nm, the latter of which the optical absorption of water (λ_2) exceeds that of fat by a factor of 10. The fact that the MCC maximum occurs at λ_1= 1220 nm and λ_2= 1530 is the result of the negative-value clipping process, rather than due to information contained within the simulated IVPA imaging data. This was evidenced when examining the histogram (not shown) of the image in Figure 5.6C, which showed an excess of

intensity values at or near zero. As such, evaluation of MCC heatmaps should be weighed against considerations of fluence variation and optical penetration depth.

Figure 5.8 gives an example of applying the same image-subtraction and segmentation process at wavelengths where depth penetration is comparable (~2 mm), 1210 nm (Figure 5.8A) and 1360 nm (Figure 5.8B). While IVPA intensity is still dominated by water at 1360 nm (Figure 5.8B), the difference is not as drastic as in Figure 5.6 (note the different scale used). Segmentation correlation is still very high using this wavelength pair (MCC >0.99), and light penetration depth is improved compared to 1530 nm. These results are not obvious from a cursory examination of the optical properties shown in Figure 5.3, but rather seem to derive from the complex nature of light interaction with the particular geometry of coronary arteries, as well as the imaging target of lipid-rich plaques. Because the only extended tissue component likely to intervene between the IVPA imaging catheter and an atherosclerotic plaque is blood, a two-wavelength IVPA imaging system will excel if it is able to suppress signal from blood and minimize imaging artifacts resulting from fluence variation across laser-pulses and wavelengths. While, in principle, this could be done for nearly any combination of wavelengths, it is most practical to accomplish when fluence distributions remain relatively constant across two wavelengths. For this reason, the overall results suggest that the 1050 – 1370 nm wavelength range seems the most promising. In this range the optical absorption of water-based tissues remains relatively constant, as does the resulting fluence distribution, while the contrast between lipid and water scales by a factor of five or more (Figure 5.3A).

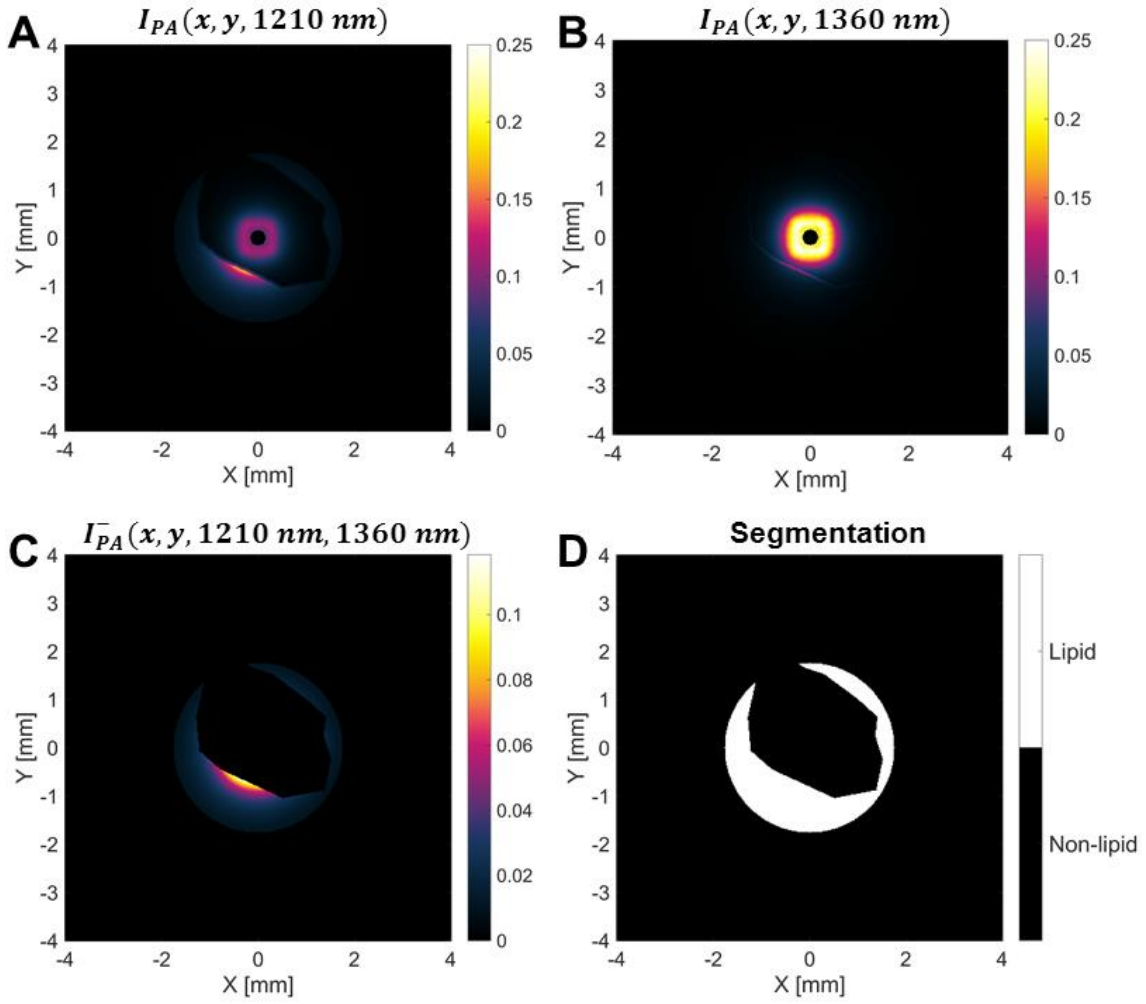

Figure 5.8. Simulated PA data, $I_{PA}(x, y, \lambda)$, for Diffuse tissue model at 1210 nm (A) and 1360 nm (B). Images are displayed on linear scale for comparison. Subtraction image, $I_{PA}^{-}(x, y, \lambda_1, \lambda_2)$, using data displayed in (A) and (B), shown on a linear scale (C). Segmented image based on (C), with predicted lipid-rich regions as white (D). Note that very high correlation can be observed using the same segmentation process at wavelengths where depth penetration is comparable.

As such, for a generalized IVPA imaging system, the optimal two-wavelength imaging solution may occur using a primary imaging wavelength of 1210 nm, and a secondary wavelength of 1360 nm. Should implementation of IVPA imaging at 1360 nm be limited by available laser sources, analysis suggests IVPA imaging at 1210 nm could

be complemented by a number of wavelengths in the 1050 – 1370 nm window. What will likely determine the implementation of a dual-wavelength IVPA clinical imaging system is the cost and availability of laser sources. Nd:YAG lasers produce high-energy pulses at 1064 nm 1320 nm and can be used as pump lasers for solid-state lasing mediums, as well as dye-based mediums and Raman lasing mediums. While together these lasing materials cover a broad wavelength range (Wikipedia.com 2015), dye-based lasers can require frequent maintenance and thus solid-state or Raman lasers present the most viable candidates to achieve the desired laser wavelengths. Indeed, a Ba(NO3)2 Raman laser at 1197 nm has already been demonstrated for IVPA imaging applications, operating at 2 kHz with 2 mJ pulse energy (Wang et al. 2014). This setup, coupled with a primary or secondary diamond Raman laser (McKay et al. 2012) operating at 1240 nm or 1490 nm, respectively, may prove the optimal implementation for a dual-wavelength clinical IVPA imaging solution capable of real-time characterization of atherosclerotic plaque.

5.6 CONCLUSION

In this work we describe a sophisticated optical model to simulate IVPA imaging results in the NIR regime, with the goal of improving the translation of optimized real-time IVPA imaging to the clinical realm. IVPA imaging was modeled in four coronary artery tissue samples from 800 nm to 1800 nm in 10 nm steps. Optical depth penetration was evaluated and a segmentation algorithm was employed to evaluate single-wavelength and dual-wavelength subtraction IVPA imaging capabilities for identifying lipid-rich regions. Comparisons between segmentation results and ground truth tissue cross-sections yielded MCCs to determine the quality of imaging results. Optical depth penetration is highest in the wavelength range of 1050 – 1370 nm, where the 5% fluence threshold extends beyond 2 mm from the optical source. MCC results indicate that single-

wavelength IVPA imaging of atherosclerotic plaque is best at 1210 nm and 1720 nm, at which the former wavelength lies within the increased optical penetration range. Subtraction-image results suggest there are several secondary wavelengths that may adequately compliment primary IVPA imaging at 1210 nm which significantly improve the segmentation correlation. When these results are weighed against considerations of optical depth penetration and fluence variation across wavelength, it seems the 1210 nm and 1360 nm wavelength pairing may prove an optimal IVPA imaging implementation, though the availability of laser sources will likely affect a final imaging solution. Validation of these results with matched experiments is vital to both confirming these findings and expanding the use of this model for additional IVPA imaging applications.

5.7 REFERENCES

Abran, M., G. Cloutier, M. H. R. Cardinal, B. Chayer, J. C. Tardif, and F. Lesage. 2014. 'Development of a Photoacoustic, Ultrasound and Fluorescence Imaging Catheter for the Study of Atherosclerotic Plaque', Biomedical Circuits and Systems, IEEE Transactions on, 8: 696-703.

Allen, Thomas J., Andrew Hall, Amar P. Dhillon, James S. Owen, and Paul C. Beard. 2012. 'Spectroscopic photoacoustic imaging of lipid-rich plaques in the human aorta in the 740 to 1400 nm wavelength range', Journal of Biomedical Optics, 17: 0612091-06120910.

Bashkatov, A. N., É. A. Genina, V. I. Kochubey, and V. V. Tuchin. 2005. 'Optical properties of the subcutaneous adipose tissue in the spectral range 400–2500 nm', Optics and Spectroscopy, 99: 836-42.

Beard, P. 2011. 'Biomedical photoacoustic imaging', Interface Focus, 1: 602-31.

Ben-Horin, Shomron, Ami Shinfeld, Erez Kachel, Angela Chetrit, and Avi Livneh. 'The composition of normal pericardial fluid and its implications for diagnosing pericardial effusions', The American Journal of Medicine, 118: 636-40.

Bouchard, Richard, Nicholas Dana, Luigi Di Biase, Andrea Natale, and Stanislav Emelianov. 2012. "Photoacoustic characterization of radiofrequency ablation lesions." In, edited by A. Oraevsky Alexander and V. Wang Lihong, 82233K. SPIE.

Çilesiz, Inci F., and Ashley J. Welch. 1993. 'Light dosimetry: effects of dehydration and thermal damage on the optical properties of the human aorta', Applied optics, 32: 477-87.

Dana, Nicholas P., Diego S. Dumani, Jason R. Cook, and Stanislav Emelianov. 2016. 'Overview of Photoacoustic Imaging.' in Devon J. Godfrey, Jacob Van Dyk, Shiva K. Das, Bruce H. Curran and Anthony B. Wolbarst (eds.), Advances in Medical Physics (Medical Physics Publishing: Madison, WI).

Fang, Qianqian. 2010. 'Mesh-based Monte Carlo method using fast ray-tracing in Plücker coordinates', Biomedical Optics Express, 1: 165-75.

———. 2016. 'MCX GPU Benchmark/Contest', Accessed September 30, 2016. http://mcx.space/gpubench/.

Fang, Qianqian, and David A. Boas. 2009. 'Monte Carlo Simulation of Photon Migration in 3D Turbid Media Accelerated by Graphics Processing Units', Optics express, 17: 20178-90.

Fischman , David L., Martin B. Leon , Donald S. Baim , Richard A. Schatz , Michael P. Savage , Ian Penn , Katherine Detre , Lisa Veltri , Donald Ricci , Masakiyo Nobuyoshi , Michael Cleman , Richard Heuser , David Almond , Paul S. Teirstein , R. David Fish , Antonio Colombo , Jeffrey Brinker , Jeffrey Moses , Alex Shaknovich , John Hirshfeld , Stephen Bailey , Stephen Ellis , Randal Rake , and Sheldon Goldberg 1994. 'A Randomized Comparison of Coronary-Stent Placement and Balloon Angioplasty in the Treatment of Coronary Artery Disease', New England Journal of Medicine, 331: 496-501.

Fleg, Jerome L., Gregg W. Stone, Zahi A. Fayad, Juan F. Granada, Thomas S. Hatsukami, Frank D. Kolodgie, Jacques Ohayon, Roderic Pettigrew, Marc S. Sabatine, Guillermo J. Tearney, Sergio Waxman, Michael J. Domanski, Pothur R. Srinivas, and Jagat Narula. 2012. 'Detection of High-Risk Atherosclerotic Plaque: Report of the NHLBI Working Group on Current Status and Future Directions', JACC: Cardiovascular Imaging, 5: 941-55.

Flock, S. T., M. S. Patterson, B. C. Wilson, and D. R. Wyman. 1989. 'Monte Carlo modeling of light propagation in highly scattering tissues. I. Model predictions and comparison with diffusion theory', Biomedical Engineering, IEEE Transactions on, 36: 1162-68.

Flock, S. T., B. C. Wilson, and M. S. Patterson. 1989. 'Monte Carlo modeling of light propagation in highly scattering tissues. II. Comparison with measurements in phantoms', IEEE Transactions on Biomedical Engineering, 36: 1169-73.

Hale, George M., and Marvin R. Querry. 1973. 'Optical Constants of Water in the 200-nm to 200-μm Wavelength Region', Applied optics, 12: 555-63.

Henyey, Louis G, and Jesse Leonard Greenstein. 1941. 'Diffuse radiation in the galaxy', The Astrophysical Journal, 93: 70-83.

Jacques, S. L. 2013. 'Optical properties of biological tissues: a review', Phys Med Biol, 58: R37-61.

Jacques, Steven L. 2014. 'Coupling 3D Monte Carlo light transport in optically heterogeneous tissues to photoacoustic signal generation', Photoacoustics, 2: 137-42.

Jansen, Krista, Antonius F. W. van der Steen, Min Wu, Heleen M. M. van Beusekom, Geert Springeling, Xiang Li, Qifa Zhou, K. Kirk Shung, Dominique P. V. de Kleijn, and Gijs van Soest. 2014. 'Spectroscopic intravascular photoacoustic imaging of lipids in atherosclerosis', Journal of Biomedical Optics, 19: 026006-06.

Jansen, Krista, Min Wu, Antonius F. W. van der Steen, and Gijs van Soest. 2014. 'Photoacoustic imaging of human coronary atherosclerosis in two spectral bands', Photoacoustics, 2: 12-20.

Karpiouk, Andrei B., Bo Wang, and Stanislav Y. Emelianov. 2010. 'Development of a catheter for combined intravascular ultrasound and photoacoustic imaging', Review of Scientific Instruments, 81: 014901.

Keijzer, Marleen, Rebecca R. Richards-Kortum, Steven L. Jacques, and Michael S. Feld. 1989. 'Fluorescence spectroscopy of turbid media: Autofluorescence of the human aorta', Applied optics, 28: 4286-92.

Li, Yan, Xiaojing Gong, Chengbo Liu, Riqiang Lin, William Hau, Xiaosong Bai, and Liang Song. 2015. 'High-speed intravascular spectroscopic photoacoustic imaging at 1000 A-lines per second with a 0.9-mm diameter catheter', Journal of Biomedical Optics, 20: 065006-06.

Libby, Peter. 2002. 'Inflammation in atherosclerosis', Nature, 420: 868-74.

Matthews, B. W. 1975. 'Comparison of the predicted and observed secondary structure of T4 phage lysozyme', Biochimica et Biophysica Acta (BBA) - Protein Structure, 405: 442-51.

McKay, Aaron, Ondrej Kitzler, Hua Liu, David Fell, and Richard P. Mildren. 2012. "High average power (11 W) eye-safe diamond Raman laser." In, 85510U-10U-8.

Mozaffarian, Dariush, Emelia J. Benjamin, Alan S. Go, Donna K. Arnett, Michael J. Blaha, Mary Cushman, Sarah de Ferranti, Jean-Pierre Després, Heather J. Fullerton, Virginia J. Howard, Mark D. Huffman, Suzanne E. Judd, Brett M. Kissela, Daniel T. Lackland, Judith H. Lichtman, Lynda D. Lisabeth, Simin Liu, Rachel H. Mackey, David B. Matchar, Darren K. McGuire, Emile R. Mohler, Claudia S. Moy, Paul Muntner, Michael E. Mussolino, Khurram Nasir, Robert W. Neumar, Graham Nichol, Latha Palaniappan, Dilip K. Pandey, Mathew J. Reeves, Carlos J. Rodriguez, Paul D. Sorlie, Joel Stein, Amytis Towfighi, Tanya N. Turan, Salim S. Virani, Joshua Z. Willey, Daniel Woo, Robert W. Yeh, and Melanie B.

Turner. 2015. 'Heart Disease and Stroke Statistics—2015 Update: A Report From the American Heart Association', Circulation, 131: e29-e322.

Narula, Jagat, Masataka Nakano, Renu Virmani, Frank D. Kolodgie, Rita Petersen, Robert Newcomb, Shaista Malik, Valentin Fuster, and Aloke V. Finn. 2013. 'Histopathologic Characteristics of Atherosclerotic Coronary Disease and Implications of the Findings for the Invasive and Noninvasive Detection of Vulnerable Plaques', Journal of the American College of Cardiology, 61: 1041-51.

Nickolls, John, Ian Buck, Michael Garland, and Kevin Skadron. 2008. 'Scalable Parallel Programming with CUDA', Queue, 6: 40-53.

Otsu, Nobuyuki. 1975. 'A threshold selection method from gray-level histograms', Automatica, 11: 23-27.

Piao, Zhonglie, Teng Ma, Jiawen Li, Maximilian T. Wiedmann, Shenghai Huang, Mingyue Yu, K. Kirk Shung, Qifa Zhou, Chang-Seok Kim, and Zhongping Chen. 2015. 'High speed intravascular photoacoustic imaging with fast optical parametric oscillator laser at 1.7 μm', Applied Physics Letters, 107: 083701.

Powers, David Martin Ward. 2011. 'Evaluation: from precision, recall and F-measure to ROC, informedness, markedness and correlation', International Journal of Machine Learning Technology, 2: 37-63.

Prahl, Scott A, Marleen Keijzer, Steven L Jacques, and Ashley J Welch. 1989. 'A Monte Carlo model of light propagation in tissue', Dosimetry of laser radiation in medicine and biology, 5: 102-11.

Roggan, A., M. Friebel, K. Do Rschel, A. Hahn, and G. Mu Ller. 1999. 'Optical Properties of Circulating Human Blood in the Wavelength Range 400-2500 nm', J Biomed Opt, 4: 36-46.

Roy, Probal, Daniel H. Steinberg, Steven J. Sushinsky, Teruo Okabe, Tina L. Pinto Slottow, Kimberly Kaneshige, Zhenyi Xue, Lowell F. Satler, Kenneth M. Kent, William O. Suddath, Augusto D. Pichard, Neil J. Weissman, Joseph Lindsay, and Ron Waksman. 2008. 'The potential clinical utility of intravascular ultrasound guidance in patients undergoing percutaneous coronary intervention with drug-eluting stents', European Heart Journal.

Shah, J., S. Park, S. Aglyamov, T. Larson, L. Ma, K. Sokolov, K. Johnston, T. Milner, and S. Y. Emelianov. 2008. 'Photoacoustic imaging and temperature measurement for photothermal cancer therapy', J Biomed Opt, 13: 034024.

Su, Jimmy Li-Shin, Bo Wang, and Stanislav Y. Emelianov. 2009. 'Photoacoustic imaging of coronary artery stents', Optics express, 17: 19894-901.

Szabo, Thomas L. 2004. Diagnostic ultrasound imaging: inside out (Academic Press).

van Veen, R. L. P., Hjcm Sterenborg, A. Pifferi, A. Torricelli, E. Chikoidze, and R. Cubeddu. 2005. 'Determination of visible near-IR absorption coefficients of

mammalian fat using time- and spatially resolved diffuse reflectance and transmission spectroscopy', Journal of Biomedical Optics, 10: 6.

VanderLaan, D., A. Karpiouk, D. Yeager, and S. Emelianov. 2014. "System and integrated catheter for real-time intravascular ultrasound and photoacoustic imaging." In Ultrasonics Symposium (IUS), 2014 IEEE International, 1591-94.

Waller, Bruce F., Charles M. Orr, John D. Slack, Cass A. Pinkerton, James Van Tassel, and Thomas Peters. 1992. 'Anatomy, histology, and pathology of coronary arteries: A review relevant to new interventional and imaging techniques—Part I', Clinical Cardiology, 15: 451-57.

Wang, B., and S. Emelianov. 2011. 'Thermal intravascular photoacoustic imaging', Biomed Opt Express, 2: 3072-8.

Wang, B., A. Karpiouk, D. Yeager, J. Amirian, S. Litovsky, R. Smalling, and S. Emelianov. 2012a. 'Intravascular photoacoustic imaging of lipid in atherosclerotic plaques in the presence of luminal blood', Opt Lett, 37: 1244-6.

Wang, Bo, Andrei Karpiouk, Doug Yeager, James Amirian, Silvio Litovsky, Richard Smalling, and Stanislav Emelianov. 2012b. 'In vivo Intravascular Ultrasound-guided Photoacoustic Imaging of Lipid in Plaques Using an Animal Model of Atherosclerosis', Ultrasound in Medicine & Biology, 38: 2098-103.

Wang, Bo, Jimmy Su, Andrei Karpiouk, Doug Yeager, and Stanislav Emelianov. 2011. 'Intravascular Photoacoustic and Ultrasound Imaging: From Tissue Characterization to Molecular Imaging to Image-Guided Therapy.' in Jasjit S. Suri, Chirinjeev Kathuria and Filippo Molinari (eds.) (Springer New York).

Wang, Bo, Jimmy L. Su, James Amirian, Silvio H. Litovsky, Richard Smalling, and Stanislav Emelianov. 2010. 'Detection of lipid in atherosclerotic vessels using ultrasound-guided spectroscopic intravascular photoacoustic imaging', Opt. Express, 18: 4889-97.

Wang, Bo, Evgeniya Yantsen, Timothy Larson, Andrei B. Karpiouk, Shriram Sethuraman, Jimmy L. Su, Konstantin Sokolov, and Stanislav Y. Emelianov. 2009. 'Plasmonic Intravascular Photoacoustic Imaging for Detection of Macrophages in Atherosclerotic Plaques', Nano Letters, 9: 2212-17.

Wang, Lihong, Steven L Jacques, and Liqiong Zheng. 1995. 'MCML—Monte Carlo modeling of light transport in multi-layered tissues', Computer methods and programs in biomedicine, 47: 131-46.

Wang, Lihong V, and Hsin-i Wu. 2007. Biomedical optics: principles and imaging (John Wiley & Sons).

Wang, Pu, Teng Ma, Mikhail N. Slipchenko, Shanshan Liang, Jie Hui, K. Kirk Shung, Sukesh Roy, Michael Sturek, Qifa Zhou, Zhongping Chen, and Ji-Xin Cheng. 2014. 'High-speed Intravascular Photoacoustic Imaging of Lipid-laden

Atherosclerotic Plaque Enabled by a 2-kHz Barium Nitrite Raman Laser', Scientific Reports, 4: 6889.

Wikipedia.com. 2015. 'List of laser sources', Wikipedia, The Free Encyclopedia., Accessed 28 September. https://en.wikipedia.org/w/index.php?title=List_of_laser_types&oldid=678949182.

Wilensky, Robert L. 2013. 'In Search of the Elusive Vulnerable PlaqueReducing the Gap Between Coronary Imaging and Necropsy Findings∗∗', Journal of the American College of Cardiology, 61: 1052-53.

Wilson, B. C., and G. Adam. 1983. 'A Monte Carlo model for the absorption and flux distributions of light in tissue', Medical Physics, 10: 824-30.

Xu, Minghua, and Lihong V. Wang. 2006. 'Photoacoustic imaging in biomedicine', Review of Scientific Instruments, 77: 041101.

Yao, Da-Kang, Chi Zhang, Konstantin Maslov, and Lihong V. Wang. 2014. 'Photoacoustic measurement of the Grüneisen parameter of tissue', Journal of Biomedical Optics, 19: 017007-07.

Yeager, Doug, Yun-Sheng Chen, Silvio Litovsky, and Stanislav Emelianov. 2014. 'Intravascular Photoacoustics for Image-Guidance and Temperature Monitoring During Plasmonic Photothermal Therapy of Atherosclerotic Plaques: A Feasibility Study', Theranostics, 4: 36-46.

Yeager, Doug, Andrei Karpiouk, Bo Wang, James Amirian, Konstantin Sokolov, Richard Smalling, and Stanislav Emelianov. 2012. 'Intravascular photoacoustic imaging of exogenously labeled atherosclerotic plaque through luminal blood', Journal of Biomedical Optics, 17: 106016-16.

Zamora-Rojas, Eduardo, Ben Aernouts, Ana Garrido-Varo, Dolores Pérez-Marín, José Emilio Guerrero-Ginel, and Wouter Saeys. 2013. 'Double integrating sphere measurements for estimating optical properties of pig subcutaneous adipose tissue', Innovative Food Science & Emerging Technologies, 19: 218-26.

Chapter 6: Summary And Future Directions Of Photoacoustic Imaging For Cardiovascular Applications

6.1 Abstract

While photoacoustic (PA) imaging has seen many advances in the realm of cardiovascular imaging, work remains to establish determine the full impact of PA imaging in this regime. In general, remaining work can be divided into two categories: development of improved contrast agents and development and testing of clinical imaging systems. The work explored herein using PA techniques to sense calcium dynamics in myocytes utilized a dye with known cytotoxicity issues, which proved to be a limiting factor in the study. Development and characterization of calcium-sensitive, biocompatible PA contrast agents is necessary for PA sensing of calcium dynamics to move beyond this initial stage. For applications exploring PA imaging to guide and characterize cardiac thermal ablation procedures, studies thus far have largely focused on ex vivo studies. For this technology to have any clinical impact, research must translate into studies using in vivo cardiac animal models, preferably using catheter-based PA imaging implementations. Intravascular photoacoustic (IVPA) imaging applications have already seen testing using catheter implementations in animal models. However, the IVPA imaging results discussed herein were obtained solely using optical modeling. The next step is to validate these results with a matching experiment, ideally using plaque-bearing coronary tissue samples or in vivo animal model studies. Such results could confirm our findings and are necessary before these results can impact future clinical IVPA system development.

6.2 INTRODUCTION

The work discussed in this dissertation focuses on photoacoustic (PA) imaging in cardiovascular applications, particularly as they apply for image guidance and tissue characterization. These applications, while promising, still reside in the arena of research, though inroads are being made to translate findings into the clinical realm. In this chapter we discuss some of the obstacles to that translation, and the direction future work must undergo to overcome this limitation.

6.3 PHOTOACOUSTIC SENSING OF CELLULAR CALCIUM DYNAMICS

In Chapter 2 results obtained investigating a PA method to detect cellular calcium dynamics was discussed (Dana, Fowler, et al. 2016). This study utilized arsenazo III (Asz), a calcium chelating dye, as a PA contrast agent. This proof-of-concept study successfully established the possibility of using PA methods to sense cytosolic calcium exchange (Dana, Fowler, et al. 2016), however, there are limitations to this study that can be addressed by future work.

6.3.1 Limitations of current calcium-sensitive dyes as photoacoustic contrast agents

The main limitation of this work, as it stands, involves the use of Asz dye as a contrast agent. Cytosolic Asz dye is known to bind to cellular proteins (Beeler, Schibeci, and Martonosi 1980) and produce free radicals (Docampo, Moreno, and Mason 1983). As such it likely impairs cell viability. We observed, using optical imaging and PA imaging, that cellular activity rapidly decreased after Asz treatment, resulting in a very narrow imaging window (10-20 minutes after completion of Asz treatment). While this window provided sufficient time to conduct our study, the use of a cytotoxic contrast agent is counter to the overarching goal of this study, which is to develop a non-invasive or minimally invasive PA technique to assess cardiac electrophysiology (EP), preferably for

longitudinal studies. For that reason, development of non-toxic, ion-sensitive contrast agents is essential to exploring this technique in an in vivo model.

One potential candidate for such development involves using an organically bound transition metal that absorbs strongly in the NIR (Marshall et al. 2006). Such agents have shown a high degree of optical tunability and very strong optical absorption (Marshall et al. 2006). However, their use of a metallic ion may subject them to the same cytotoxicity concerns afflicting Asz. Cyanine derivatives have been developed that absorb strongly in the NIR, and are already being investigated as PA contrast agents (Temma et al. 2014). These agents may alleviate concerns with cytotoxicity and can likely be easily functionalized for calcium sensitivity. What remains to be seen is how that functionalization may translate into sensitivity of the final agent, and whether that can be visualized with PA imaging. Several organic chromophores have been investigated for use in OLEDs (Qian et al. 2009), and they may have potential as PA contrast agents. Such materials have the benefit of strong absorption out past 900 nm (Qian et al. 2009), and can likely be easily functionalized. They have yet to be investigated as PA contrast agents, though, so questions about their biocompatibility have not been addressed. Indeed, it may prove difficult to solubilize or encapsulate these agents without affecting their absorption or limiting their exposure to cytosolic calcium. Still another possibility exists by exploiting the potential of calcium-sensitive polymers. Studies have shown that alginate gels exhibit tunable properties in response to calcium concentration (Stowers, Allen, and Suggs 2015). It may be possible to modify such gels to exhibit swelling in the presence or absence of calcium. If such gels were laden with plasmonic nanoparticles (Luke, Yeager, and Emelianov 2012), such volume changes could modulate plasmon-coupling between particles, thereby providing wavelength-dependent changes in optical absorption. Alternatively, such gels have exhibited changes

in stiffness as a result of calcium concentration (Stowers, Allen, and Suggs 2015). It may be possible to incorporate into such gels phase-changing PA contrast agents, like those investigated by Hannah, et al.,(Hannah et al. 2014). It may be that such gel stiffness dynamics modulate the rate, and thus the frequency content, of nanodroplets. If that is the case, RF analysis of such signals may be able to determine the stiffness dynamics of the gel, and thus the underlying calcium dynamics driving them. Investigations have yet to be done on many of the contrast agents and systems discussed above, yet with such a diverse field of contrast agent candidates, it is likely that future studies will yield promising results that can move this work forward.

If such a candidate is found, it will need to be fully characterized as a contrast agent. Ideally, direct comparisons of PA data to optical absorption, rather than optical extinction, would be made for a given contrast agent. Such comparisons require comprehensive measurement of absorption and scattering, at multiple dye concentrations and dye to cation ratios. This would allow for quantification of optical properties and stability, as well as ion-sensitivity. Biocompatibility would also have to be examined for any such dye to be impactful on in vivo studies, which ultimately is the goal of this technique.

6.3.2 Future applications of photoacoustic sensing of ion dynamics

Once appropriate dyes are identified translating this method into an in vivo study to visualize ion-dynamics in live tissue is the goal. The promise of this technique to provide non-invasive assessment of EP function on the cellular and tissue scale is quite promising for applications involving pharmacologic efficacy or side-effects. Even if such methods prove too difficult to translate into the clinical realm, the potential of contrast-enabled PA imaging of EP function as a research tool holds great promise.

Finally, beyond the scope of cardiac EP, such dyes may extend these techniques to any EP application, if they can be functionalized to report on the appropriate biological substrate. Such applications may offer improved spatial resolution and depth penetration over current techniques, if suitable contrast-agents can be found.

6.4 PHOTOACOUSTIC IMAGE GUIDANCE AND CHARACTERIZATION OF CARDIAC ABLATION

6.4.1 Realization of real-time imaging

There are several still unexamined aspects of using PA imaging to guide trans-catheter ablation of atrial arrhythmia. Clearly any tool used to guide trans-catheter ablation must be real-time (RT) or near-RT, and in the work described in Chapter 3 and Chapter 4 we have not examined using PA imaging during radiofrequency (RF) lesion creation. PA imaging frame rate is practically limited by the pulse repetition frequency of the irradiating laser. Our initial system is capable of providing near-RT imaging (1-2 frames per second each consisting of several optical wavelengths with no averaging), and many laser systems, operating at kHz frequencies, are currently available that could provide RT PA imaging. Once studies have demonstrated which wavelengths are optimal for in vivo imaging, a system could be constructed using select wavelengths, operating at kHz pulse repetition rates, to provide frame rates well in excess of 30 frames per second.

6.4.2 Translating toward in vivo and eventual clinical imaging

Corroboration of these results in an in vivo model is necessary in order to confirm that the findings reported here are relevant to further clinical application. One recent study (Chitnis et al. 2010) has reported inconclusive findings, showing that while most single-wavelength ex vivo studies reported positive PA contrast in the ablation lesion, it is possible to observe negative contrast in ablation lesions in vivo. One proposed

explanation is that variations in thermal deposition between in vivo and ex vivo models may lead to a different distribution of chromophores between the two environments. As our method relies upon correlation to multiple laser wavelengths, it may be possible to identify a difference in the chromophores present in the ablated regions of in vivo and ex vivo models. While the data in this study suggests Hb is present in significant quantities before ablation and is significantly reduced following ablation, it is not clear which chromophore(s) is generating PA signal in the ablated region. Previous work has suggested that increased temperatures during thermal therapy may give rise to a variety of hemoglobin derivatives, which may account for the observed contrast between normal and ablated tissue (Tanya et al. 2006; Farahani et al. 1999; Black and Barton 2004). While production of hemoglobin derivatives is often cited as a potential source of contrast in ablated tissues, to our knowledge, no study has shown definitively that the proposed derivatives are produced in significant concentrations in tissue. Studies of the thermal unfolding and aggregation process of hemoglobin using 2D infrared spectroscopy have shown that thermal degradation is a complex, multi-step process that is irreversible once local tissues reach a certain temperature threshold: initial destabilizations in the structure of hemoglobin occur at low temperatures between 30-44° C; complete thermal unfolding occurs between 44-54° C; and irreversible aggregation of the denatured protein occurs at temperatures above 54° C (Yan et al. 2004). This complex, three-stage denaturation process involves several potentially irreversible conformation changes in the structure of hemoglobin. Given the dependence of protein absorption on the 3D structure of the protein, these irreversible, temperature-dependent structural changes in hemoglobin may explain the observed elimination of the 760-nm peak in the Hb spectrum in ablated tissue. Partial unfolding of Hb may yield a range of different absorption spectra in ablated tissues rather than a single absorption spectrum

corresponding to a single chromophore. This range of unfolding states could explain the observed correlation discrepancies at the edges of tissue lesions and could be developed to benchmark levels of partial tissue coagulation. In future studies, it would be useful to submit samples of ablated and non-ablated tissues to hemopathological and chemical assays in order to identify with confidence which chromophores are present and in what concentration before and after ablation.

6.4.3 Visualization of cryoablation lesions

Also still unexamined is the feasibility of using PA imaging to characterize cryoablation lesions. As mentioned above, the denaturation process in Hb is highly temperature dependent. Since little research has been done to directly compare the optical absorption of hyper- versus hypothermia-induced myocardial lesions, further studies must be conducted to assess the feasibility of using this method to characterize cardiac cryoablation lesions, which may yield an entirely different absorption spectrum upon ablation.

6.4.4 Development of a clinical imaging device

Development of in vivo imaging solutions will be necessary to apply PA imaging clinically for guidance of cryo-, RF and high-intensity focused ultrasound (HIFU) ablation treatments. Although development of an in vivo system for PAUS imaging will not be a trivial task, building upon previous work by Cui et al. (Cui and Yang 2010; Cui, Staley, and Yang 2010; Cui and Yang 2011) and Prost et al. (Prost et al. 2012) may improve single-device integration, which allows straightforward co-registration of PA and ultrasound (US) imaging spaces, as well as the possible integration of an HIFU energy source also. Another avenue for development of such a clinical probe may benefit from recent advances in combined RF-US catheters (Wright et al. 2011) and the

development of light delivery mechanisms utilized for intracardiac laser ablation (Dukkipati et al. 2012). Still another is to implement PA imaging by adapting an intracardiac echocardiography catheter. These devices have served to implement US-based elastography imaging to characterize cardiac ablation lesions (Eyerly et al. 2010; Eyerly et al. 2012), and by the modest addition of an optical fiber to the catheter, it may be possible add PA imaging capabilities onto the US and elastography capabilities already implemented. Such a device would be capable of a variety of imaging modalities, potentially offering physicians a wealth of information with little disruption to current technology. Regardless of which devices prove most advantageous, by capitalizing on shared optical and ultrasonic system components, such a system may add considerable functionality while minimizing the increased cost associated with added hardware. This would overcome a significant hurdle for clinical translation.

6.4.5 Addition of photoacoustic thermography

Additionally, due to the temperature dependence of $\beta(\vec{r}, T)$, thermographic PA (tPA) mapping with high thermal and temporal resolutions (< 1 K and ~ 1 s, respectively) is possible (Shah et al. 2008; Pramanik and Wang 2009; Beard 2011). Guidance of myocardial ablation procedures represents an ideal application of tPA mapping as PA imaging has the potential to provide thermographic information co-registered with anatomical (US) and molecular (sPA) information. A previous study (Hsiao, Wang, and Deng 2013) monitored the PA signal ratio at two different wavelengths during tissue heating, verifying that PA signal variations occur consistently across wavelengths until the tissue undergoes a change of state (i.e. thermal coagulation), as we observed. By adapting such complementary PA-signal amplitude analysis to the multi-wavelength techniques described herein, a comprehensive PA thermographic and tissue

characterization image guidance system may be realized. This feature of PA imaging has tremendous potential for cryo-, RF and HIFU ablation guidance, both in the cardiac regime and beyond

6.5 MONTE CARLO MODELING IN INTRAVASCULAR PHOTOACOUSTIC IMAGING

6.5.1 Validation of modeling-based results

While the validity of MC optical modeling has long been established, subtle changes in tissue optical properties and geometry can yield large differences in results. For this reason, the most obvious work yet remaining is to corroborate these results with a set of matched simulation-experimentation trials. Ideally, to validate these findings, IVPA imaging could be done on post-mortem coronary artery samples, which could then be sectioned, stained and imaged with a light microscopy to determine their tissue constituents. Microscopy images could then be digitized and the 3D tissue geometry specific to each sample could be recreated in the model space. Thus, direct comparisons using the same tissue geometry and composition can be made between experimental and modeling results. If this proves impractical, matched experiments can be done using ex vivo tissue samples of animal origin, or even with tissue mimicking phantoms, provided they recreate the geometry and optical properties pertinent to coronary artery imaging applications. This would need to be done at several wavelengths in the NIR, if not across the entire 1000 nm range analyzed. Specifically, some key wavelengths (e.g. 1210 nm, 1360 nm, 1530 nm and 1720 nm) must be included in this simulation-experimentation comparison as they represent critical findings discussed herein. Experimental validation of these findings is vital to these results having a significant impact on developing IVPA clinical imaging systems.

6.5.2 Expanding the scope of the described optical model

Beyond validation of these results, the modeling software provided by Fang and Boas (Fang and Boas 2009) can be easily adapted for various IVPA applications. Thus, this modeling scheme can be used to simulate different optical fiber configurations so as to optimize the fluence distribution within the transducer footprint. It could be adapted to simulate different rotation rates and A-line sampling schemes to the optimal balance between imaging frame rate and line density. Simulations could be done involving contrast agents to identify macrophage infiltration, which is a significant vulnerable plaque indicator (Narula et al. 2013). Such studies could identify the optimal absorption characteristics of tunable contrast agents to balance sensitivity, specificity and imaging depth for IVPA imaging applications. Various aspects of imaging system development that would otherwise be tedious or cost-prohibitive to explore experimentally can be investigated using this modeling.

6.5.3 Unification of optical and acoustic modeling

The next, and perhaps most exciting, step would be to couple this optical simulation with an acoustic model. Previous efforts have seen success using such methods in PA applications (Jacques 2014) and adapting these techniques to IVPA imaging should not prove onerous. Such a model could account for the various aspects of IVPA imaging that were ignored in this model, such as the attenuation, diffraction, refraction and interference of ultrasonic signals as they propagate from source to detector. Acoustic wavelengths at 40 MHz in tissue (~40 μm) is on the same order of magnitude as the MFP of photons and the voxel size used in this model (20 μm), easing the adaptation of optical simulation results to the acoustic simulation regime. Preferably, such a combined PA model would be used in tandem with matched experiments, as described above, providing the most accurate fusion of IVPA experimental and modeling schemes.

6.5.4 Toward real-time modeling for enhancement of photoacoustic imaging

Lastly, as computational power improves, it may be possible to implement such an optical model in real-time or near real-time, perhaps using a pre-compiled lookup-table method (Hennessy et al. 2013). Such a technique may incorporate information from IVUS and IVPA imaging to estimate in real-time the 3D distribution of optical absorption, and thus provide the absolute chemical composition of the tissue. While not currently available, such possibilities may be feasible by the time clinical IVPA imaging systems are in the latter stages of clinical trials. Such an application represents the ideal fusion of modeling and medical imaging in order to improve patient outcomes.

6.6 SUMMARY

The work discussed in this dissertation covers a broad range of PA imaging as it pertains to cardiovascular applications, including research at different stages of development. Despite this breadth, due to the similarity of the imaging applications and goals, developments in one application often translate into advancements in all. For example, the optical model discussed in Chapter 5 could be easily adapted to provide insight into the PA imaging of cardiac ablation lesions. Additionally, the signal and image processing algorithms discussed in Chapter 3 and Chapter 4 could be adapted to IVPA imaging applications, or to visualization of EP signals. It may be that, in the not too distant future, a composite cardiac PA imaging suite, capable of imaging a handful of NIR wavelengths, is able to provide image guidance and tissue characterization in a range of cardiac applications. The work described in these chapters should serve as progress toward realization of such an imaging system.

6.7 REFERENCES

Beard, P. 2011. 'Biomedical photoacoustic imaging', Interface Focus, 1: 602-31.

Beeler, Troy J., Angelo Schibeci, and A. Martonosi. 1980. 'The binding of arsenazo III to cell components', Biochimica et Biophysica Acta (BBA) - General Subjects, 629: 317-27.

Black, John F, and Jennifer Kehlet Barton. 2004. 'Chemical and structural changes in blood undergoing laser photocoagulation', Photochemistry and photobiology, 80: 89-97.

Chitnis, Parag V., Hans-Peter Brecht, Richard Su, and Alexander A. Oraevsky. 2010. 'Feasibility of optoacoustic visualization of high-intensity focused ultrasound-induced thermal lesions in live tissue', Journal of Biomedical Optics, 15: 021313-13-5.

Cui, Huizhong, Jacob Staley, and Xinmai Yang. 2010. 'Integration of photoacoustic imaging and high-intensity focused ultrasound', Journal of Biomedical Optics, 15: 021312-12-4.

Cui, Huizhong, and Xinmai Yang. 2010. 'In vivo imaging and treatment of solid tumor using integrated photoacoustic imaging and high intensity focused ultrasound system', Medical Physics, 37: 4777-81.

———. 2011. 'Real-time monitoring of high-intensity focused ultrasound ablations with photoacoustic technique: An in vitro study', Medical Physics, 38: 5345-50.

Dana, N., R. A. Fowler, A. Allen, J. Zoldan, L. Suggs, and S. Emelianov. 2016. 'In vitro photoacoustic sensing of calcium dynamics with arsenazo III', Laser Physics Letters, 13: 075603.

Docampo, R, S N Moreno, and R P Mason. 1983. 'Generation of free radical metabolites and superoxide anion by the calcium indicators arsenazo III, antipyrylazo III, and murexide in rat liver microsomes', Journal of Biological Chemistry, 258: 14920-25.

Dukkipati, S. R., P. Neuzil, J. Kautzner, J. Petru, D. Wichterle, J. Skoda, R. Cihak, P. Peichl, A. Dello Russo, G. Pelargonio, C. Tondo, A. Natale, and V. Y. Reddy. 2012. 'The durability of pulmonary vein isolation using the visually guided laser balloon catheter: multicenter results of pulmonary vein remapping studies', Heart Rhythm, 9: 919-25.

Eyerly, S. A., T. D. Bahnson, J. I. Koontz, D. P. Bradway, D. M. Dumont, G. E. Trahey, and P. D. Wolf. 2012. 'Intracardiac acoustic radiation force impulse imaging: a novel imaging method for intraprocedural evaluation of radiofrequency ablation lesions', Heart Rhythm, 9: 1855-62.

Eyerly, S. A., S. J. Hsu, S. H. Agashe, G. E. Trahey, Y. Li, and P. D. Wolf. 2010. 'An in vitro assessment of acoustic radiation force impulse imaging for visualizing cardiac radiofrequency ablation lesions', J Cardiovasc Electrophysiol, 21: 557-63.

Fang, Qianqian, and David A. Boas. 2009. 'Monte Carlo Simulation of Photon Migration in 3D Turbid Media Accelerated by Graphics Processing Units', Optics express, 17: 20178-90.

Farahani, Keyvan, Romaine E Saxton, Hyo–Chun Yoon, Antonio AF De Salles, Keith L Black, and Robert B Lufkin. 1999. 'MRI of thermally denatured blood: methemoglobin formation and relaxation effects', Magnetic resonance imaging, 17: 1489-94.

Hannah, Alexander S., Donald VanderLaan, Yun-Sheng Chen, and Stanislav Y. Emelianov. 2014. 'Photoacoustic and ultrasound imaging using dual contrast perfluorocarbon nanodroplets triggered by laser pulses at 1064 nm', Biomedical Optics Express, 5: 3042-52.

Hennessy, Ricky, Sam L. Lim, Mia K. Markey, and James W. Tunnell. 2013. 'Monte Carlo lookup table-based inverse model for extracting optical properties from tissue-simulating phantoms using diffuse reflectance spectroscopy', Journal of Biomedical Optics, 18: 037003-03.

Hsiao, Yi-Sing, Xueding Wang, and Cheri X Deng. 2013. 'Dual-wavelength photoacoustic technique for monitoring tissue status during thermal treatments', Journal of Biomedical Optics, 18: 067003-03.

Jacques, Steven L. 2014. 'Coupling 3D Monte Carlo light transport in optically heterogeneous tissues to photoacoustic signal generation', Photoacoustics, 2: 137-42.

Luke, G. P., D. Yeager, and S. Y. Emelianov. 2012. 'Biomedical Applications of Photoacoustic Imaging with Exogenous Contrast Agents', Annals of biomedical engineering, 40: 422-37.

Marshall, K. L., G. Painter, K. Lotito, A. G. Noto, and P. Chang. 2006. 'Transition Metal Dithiolene Near-IR Dyes and Their Applications in Liquid Crystal Devices', Molecular Crystals and Liquid Crystals, 454: 47/[449]-79/[81].

Narula, Jagat, Masataka Nakano, Renu Virmani, Frank D. Kolodgie, Rita Petersen, Robert Newcomb, Shaista Malik, Valentin Fuster, and Aloke V. Finn. 2013. 'Histopathologic Characteristics of Atherosclerotic Coronary Disease and Implications of the Findings for the Invasive and Noninvasive Detection of Vulnerable Plaques', Journal of the American College of Cardiology, 61: 1041-51.

Pramanik, M., and L. V. Wang. 2009. 'Thermoacoustic and photoacoustic sensing of temperature', J Biomed Opt, 14: 054024.

Prost, Amaury, Arik Funke, MickaÃŦl Tanter, and Emmanuel Bossy. 2012. 'Photoacoustic-guided ultrasound therapy with a dual-mode ultrasound array', Journal of Biomedical Optics, 17: 0612051-56.

Qian, Gang, Ze Zhong, Min Luo, Dengbin Yu, Zhiqiang Zhang, Zhi Yuan Wang, and Dongge Ma. 2009. 'Simple and Efficient Near-Infrared Organic Chromophores for Light-Emitting Diodes with Single Electroluminescent Emission above 1000 nm', Advanced Materials, 21: 111-16.

Shah, J., S. Park, S. Aglyamov, T. Larson, L. Ma, K. Sokolov, K. Johnston, T. Milner, and S. Y. Emelianov. 2008. 'Photoacoustic imaging and temperature measurement for photothermal cancer therapy', J Biomed Opt, 13: 034024.

Stowers, Ryan S., Shane C. Allen, and Laura J. Suggs. 2015. 'Dynamic phototuning of 3D hydrogel stiffness', Proceedings of the National Academy of Sciences, 112: 1953-58.

Tanya, D. Khokhlova, M. Pelivanov Ivan, A. Sapozhnikov Oleg, S. Solomatin Vladimir, and A. Karabutov Aleksander. 2006. 'Opto-acoustic diagnostics of the thermal action of high-intensity focused ultrasound on biological tissues: the possibility of its applications and model experiments', Quantum Electronics, 36: 1097.

Temma, Takashi, Satoru Onoe, Kengo Kanazaki, Masahiro Ono, and Hideo Saji. 2014. 'Preclinical evaluation of a novel cyanine dye for tumor imaging with in vivo photoacoustic imaging', Journal of Biomedical Optics, 19: 090501-01.

Wright, Matthew, Erik Harks, Szabolcs Deladi, Freek Suijver, Maya Barley, Anneke van Dusschoten, Steven Fokkenrood, Fei Zuo, Frédéric Sacher, Mélèze Hocini, Michel Haïssaguerre, and Pierre Jaïs. 2011. 'Real-time lesion assessment using a novel combined ultrasound and radiofrequency ablation catheter', Heart Rhythm, 8: 304-12.

Yan, Yong-Bin, Qi Wang, Hua-Wei He, and Hai-Meng Zhou. 2004. 'Protein thermal aggregation involves distinct regions: sequential events in the heat-induced unfolding and aggregation of hemoglobin', Biophysical Journal, 86: 1682-90.

Appendix A: Brief History And Background Of Photoacoustic Imaging[5]

A.1 Introduction

Photoacoustic (PA) imaging (also called optoacoustic imaging) is a hybrid optical-ultrasound imaging modality that relies on optical excitation to generate ultrasonic waves in tissue. PA signal generation depends upon the optical absorption properties of the imaging target, making PA imaging a molecular imaging modality. By observing PA pressure transients using an ultrasound (US) system, and because PA signal generation relies only on absorbed photons, PA imaging is able to overcome the imaging depth limitations common to optical techniques. It is also well suited to take advantage of the reduced tissue optical absorption in the near-infrared (NIR), as well as utilize various contrast agents for improved imaging. For these reasons it has become a promising medical imaging modality, with applications including the evaluation of coronary heart disease (CHD), stem cell treatment monitoring, cancer diagnosis, and treatment guidance, just to name a few. In order to provide additional context for the results discussed in this dissertation, a brief history of the development PA imaging is provided in this appendix.

A.2 History of Photoacoustic Imaging

A.2.1 Discovery of the photoacoustic effect

Discovery of the PA effect predates even the discovery of X-rays, arguably making it one of the oldest medical imaging modalities. Alexander Graham Bell was the first to document the PA effect, in the late 19th century (Bell 1881). Bell conducted several experiments and devised an apparatus (see Figure 1) to make observations on the PA effect. Bell postulated that the modulated light caused “a wave of condensation… and

[5] This appendix is adapted in part from a textbook chapter 'Overview of Photoacoustic Imaging' (Dana, Dumani, Cook and Emelianov, 2016). Nicholas Dana is the primary author of this textbook chapter.

a wave of rarefaction" (Bell 1881), recognizing what would later be formalized as a PA pressure wave (Tam 1986). Bell also observed that varying the material produced different sound intensities, as did altering the optical wavelength. Despite these initial discoveries, it would be nearly a century before the first medical applications utilizing PA phenomena would emerge.

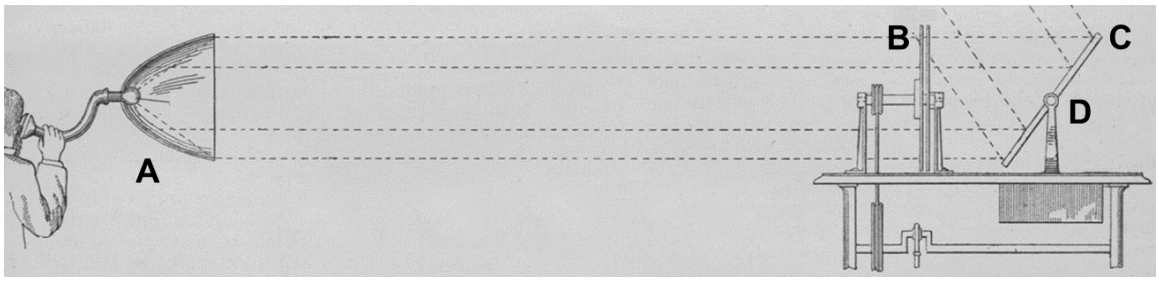

Figure A.1: Device developed by Bell to reflect sunlight via mirror (C), onto parabolic, reflective receiver containing sample (A). Light may be modulated by rotating disk (B) or by adjusting mirror angle (D). Adapted from (Bell 1881).

A.2.2 First studies applying photoacoustic methods to biological materials

In order to efficiently generate a PA signal, a brief pulse of light is necessary (Tam 1986). Furthermore, accurate spectroscopic studies require a narrow optical emission band (i.e. high monochromaticity). For these reasons, advances in PA applications were forestalled until optical and laser technology had sufficiently matured. By the 1970's technology was available to apply PA spectroscopy to the study of biological materials. Studies done by Rosencwaig and Pines (Rosencwaig and Pines 1977) (Figure A.2) demonstrated the utility of PA spectroscopy as a means to estimate biological material optical absorption properties.

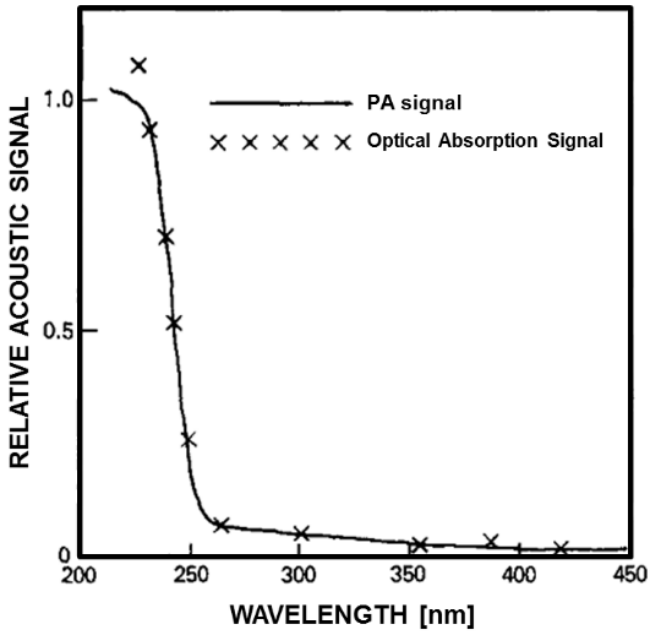

Figure A.2: Photoacoustic and optical absorption spectra of a poly(L-glutamic acid) membrane in the ultraviolet range. Adapted from (Rosencwaig and Pines 1977).

A.2.3 Experimental validation of theoretical models

Early studies done by Diebold et al. (Diebold, Sun, and Khan 1991) (Figure A.3) using pulsed laser irradiation in conjunction with dyed methanol and benzaldehyde phantoms as tissue surrogates showed good agreement with theoretical predictions (Tam 1986).

A.2.4 Expanding the application of photoacoustic methods to biological materials

During the early 1990's work continued, showing that PA techniques were capable of measuring varying concentrations of glucose in whole blood, albeit using a mid-IR laser source (Christison and MacKenzie 1993), and later, using a gelatin tissue phantom and an NIR Nd:YAG laser source (Quan et al. 1993). NIR laser sources are desirable as they operate within the wavelength regime of low optical absorption by

Hemoglobin-variants, often referred to as the “biological window”, “optical window” or “NIR window”. Later Oraevsky et al. (Oraevsky, Jacques, and Tittel 1997) verified that PA measurements of absolute optical absorption using tissue samples were accurate when done in conjunction with diffuse reflectance to quantify optical fluence and estimate the amount of scattered light.

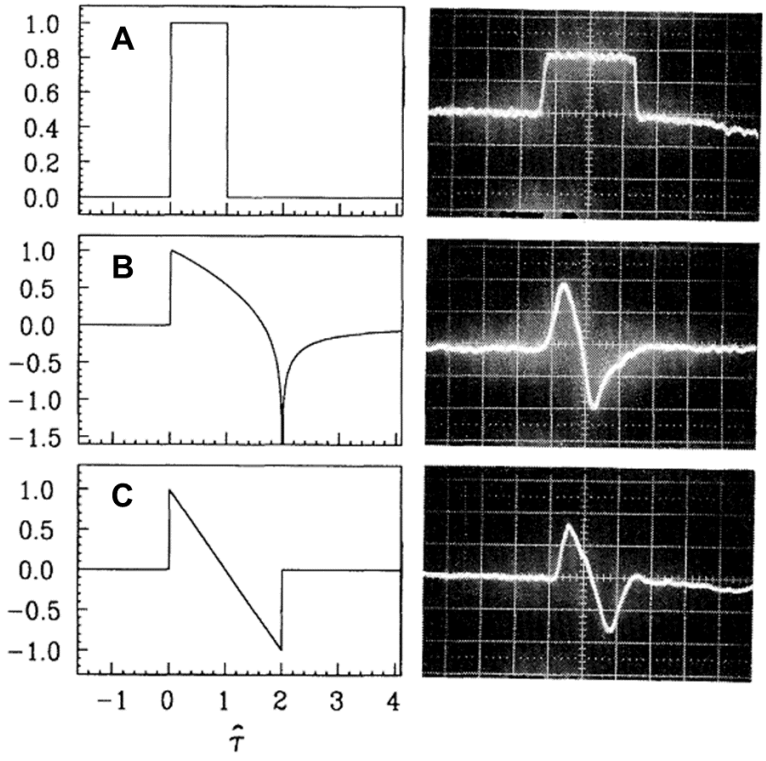

Figure A.3: PA wave forms from short duration laser pulses. Left column: PA pressure (P, in arbitrary units) vs. dimensionless time ($\hat{\tau}$) for a fluid layer (A), a cylinder (B) and a sphere (C). Right column: Experimental wave forms obtained by irradiation of a 3-mm thick layer (A), a 150-µm-radius cylinder (B) and a 500-µm-radius droplet (C). Adapted from (Diebold, Sun, and Khan 1991).

A.2.5 Adaptation of photoacoustic methods to imaging applications

These early studies had focused on using PA techniques to estimate optical properties (i.e. optical absorption) and characterize absorbers. Work by Kruger (Kruger 1994) began to establish PA as an imaging technique by combining optical excitation with an US transducer and using US time-of-flight analysis to estimate absorber size. This led to formal photoacoustic tomography (PAT) methods, using techniques similar to those of X-ray tomography (Kruger et al. 1995).

A.2.6 Early exploration of clinical applications of photoacoustic imaging

As PA imaging and combined photoacoustic-ultrasound (PAUS) imaging became more prevalent, research began to focus on clinical applications of such imaging. Given that hemoglobin (Hb) and oxyhemoglobin (HbO2) are informative endogenous chromophores, studies began to focus on imaging Hb variants both ex vivo and in vivo. Work done by Viator et al. (Viator et al. 2002) demonstrated that, using a 532 nm laser, PA imaging could determine the depth of a port wine stain in vivo. Not long after, early three-dimensional (3D) PA images were acquired by Siphanto et al. (Siphanto et al. 2004) visualizing rat mesenteric vasculature (Figure A.4). This latter study utilized an X-Y two-dimensional (2D) motor stage to raster scan an optical fiber for PA, and used US time-of-flight to estimate the absorber axial position, achieving a 3D image space with sub-millimeter resolution, which is now common in contemporary PA applications.

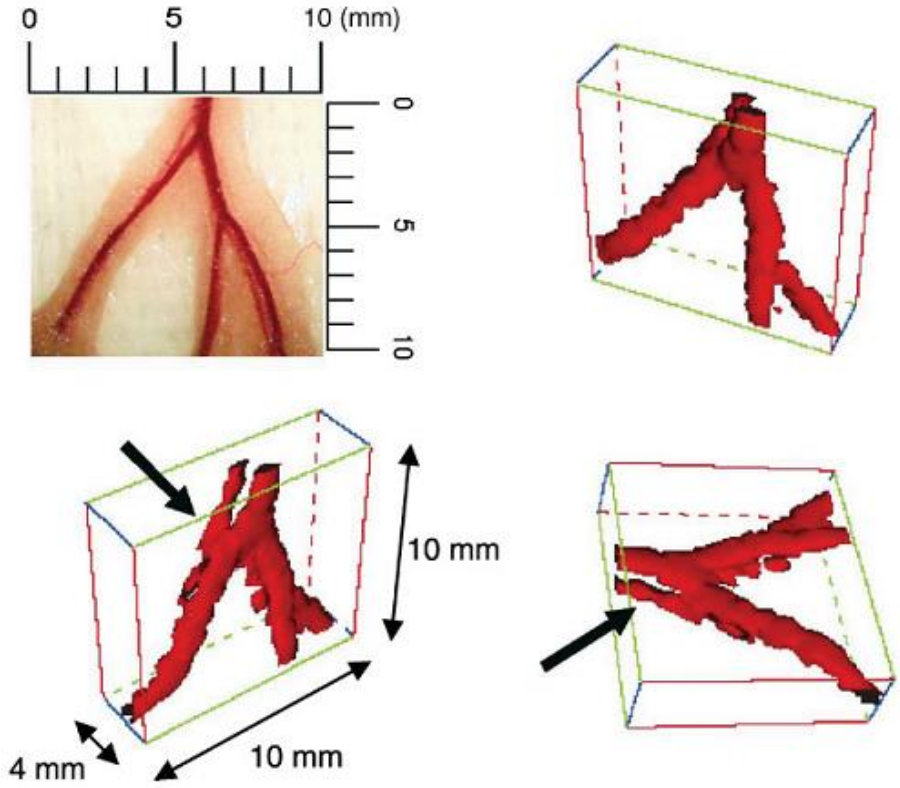

Figure A.4: 3D volume-rendering of PA imaging of rat mesenteric vasculature. Part of the artery which is below the veins, (indicated by the arrows) becomes visible by rotating the three-dimensional image. Voxel size is (X-Y-Z) 400x200x100 µm. Adapted from (Siphanto et al. 2004).

A.2.7 Functional photoacoustic imaging

Hb and HbO2 possess unique absorption spectra which are used to assess oxygen saturation percentage (SpO2), as is done with pulse oximetry. PA imaging contrast is absorption based, making it a good candidate for estimating SpO2. Wang et al. utilized PAT to assess tissue function and SpO2 using a whisker stimulation rat model (Wang et al. 2003). With image subtraction, they visualized hemodynamic changes using a single-wavelength (532 nm, Figure A.5). Later, this same group demonstrated that spectroscopic PA (sPA) imaging could estimate tissue SpO2 non-invasively and transcranially using an

in vivo rat model (Wang et al. 2006). Similar techniques were used to visualize angiogenesis and vascular disruption associated with tumor growth in an in vivo rat brain tumor model (Ku et al. 2005). Investigations into intravascular photoacoustic (IVPA) imaging (Sethuraman et al. 2007), and medical PA thermography (Shah et al. 2008), were also underway.

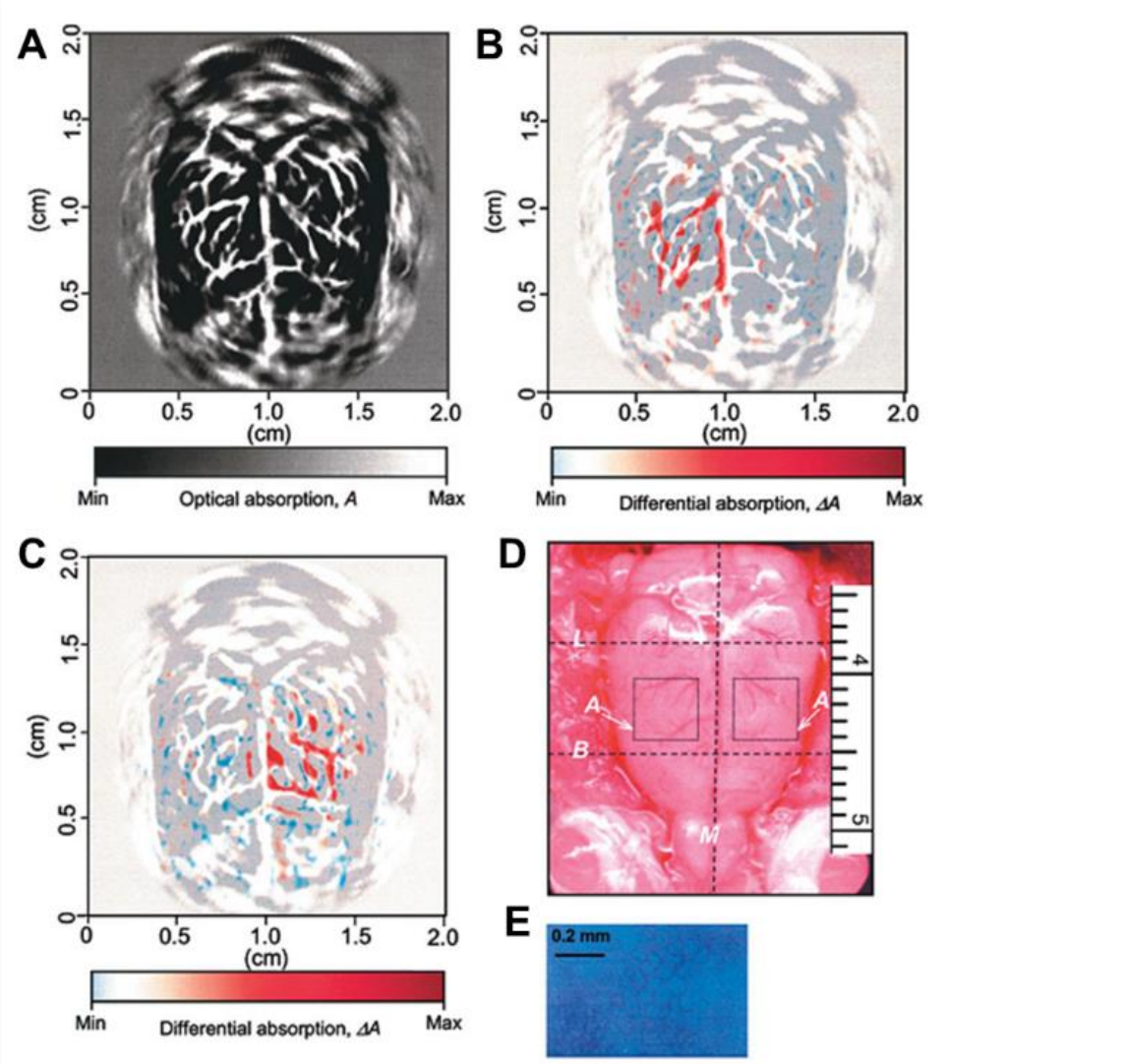

Figure A.5: Functional imaging of cerebral hemodynamic changes in response to whisker stimulation. (A) Noninvasive PAT image of the vascular pattern in the superficial layer of the rat cortex (B, C). Functional PAT images corresponding to left-side and right-side whisker stimulation, respectively. These two maps of functional representations of whiskers are superimposed on the image of the vascular pattern in the superficial cortex shown in a. (D) Open-skull photograph of the rat cortical surface. B, bregma; L, lambda; M, midline; A, activated regions corresponding to whisker stimulation (4 mm × 4 mm). (E) Histology of normal lamina IV cortical barrels, located in regions A, representing the large mystacial vibrissae of the rat somatosensory system (40× magnification). Adapted from (Wang et al. 2003).

A.2.8 Evolution of photoacoustic imaging methods and reconstruction

During this time, more research into image reconstruction methods were taking place. A weighted delay-and-sum method was tested with a PA imaging phantom, achieving approximately a 20 x 200 μm (axial x lateral) field of view by scanning a high-bandwidth hydrophone in an X-Y plane (Hoelen and de Mul 2000). Kruger, et al. (Kruger, Reinecke, and Kruger 1999), demonstrating thermoacoustic imaging (using microwave excitation) with a hemispherical array of detectors commonly called a bowl-array. Bowl-arrays are particularly well suited to breast imaging, dubbed photoacoustic mammography, due to the geometry of the target tissue. Other PA imaging geometries include spiral-scanning (Kruger et al. 2013), rotating radial-scanning (Wang and Emelianov 2011) and cylindrical-scanning systems (Gamelin et al. 2008), to name a few.

A.2.9 Maturation of hybrid photoacoustic imaging systems

As PA imaging technology matured, the research focus shifted to combining PA imaging's excellent molecular sensitivity with additional modalities for complementary structural, mechanical, elastic or optical property information. PA imaging is a hybrid optical-acoustic modality, making it well suited to integrate with similar modalities. Work to develop a combined PA, US and elastography imaging system was performed (Park et al. 2006). Additionally, magneto-photo-acoustic imaging was introduced by combining US and PA imaging with magneto-motive US (MMUS), which utilizes varying magnetic fields to acoustically excite contrast agents (Qu et al. 2011). PA imaging has also been integrated with an optical coherence tomography (OCT) system, which combines optical absorption sensitivity (PA) with optical scattering sensitivity (OCT), while sharing many optical components (Li et al. 2009). A combined PA and fluorescence tomography system was also explored, utilizing PA imaging to inform a finite element (FE) optical diffusion-based model for reconstructed fluorescence

(Razansky and Ntziachristos 2007). These represent just a few examples of combined multimodal PA imaging systems.

A.2.10 Addition of photoacoustic contrast agents

Developing PA imaging contrast agents has also been an active area of research. An ideal PA contrast agent is typified by strong, narrow-band optical absorption, high thermal- and optical-stability, high bio-compatibility and the potential for functionalization. Early work characterized the PA response from a solid sphere (Khan and Diebold 1995), which is commonly used as a contrast agent model. Gold nanoparticles (NPs), due to plasmon-resonance, demonstrate very high optical absorption (Jain et al. 2006) and low cytotoxicity, making them promising contrast agents. Dual-contrast agents are also useful for combined imaging (Hannah et al. 2014; Yang et al. 2013), while theranostic agents can help deliver or monitor therapy (Wang et al. 2013; Lee et al. 2013; Seungsoo et al. 2014). In addition to gold, other contrast agent materials include dyes, silver, iron oxide and graphene (Luke, Yeager, and Emelianov 2012), to name a few. Advances in contrast agent targeting and biocompatibility have also aided PA functional imaging (Nie and Chen 2014).

A.3 CURRENT STATUS

With PA imaging firmly established as a molecularly sensitive pre-clinical imaging tool, much current research focuses on the translation of PA imaging to the clinical arena. Recent PA mammography studies using clinical systems have highlighted the utility of PA imaging for clinical (Kitai et al. 2014; Heijblom, Steenbergen, and Manohar 2015) tasks (Kitai et al. 2014; Heijblom, Steenbergen, and Manohar 2015), while progress continues in other applications. Current research focuses on translation of

contrast agents to the clinical environment, as well as the development of smart agents for targeted drug delivery or theranostic applications.

A.4 REFERENCES

Bell, Alexander Graham. 1881. Upon the Production of Sound by Radiant Energy (Gibson Brothers, printers).

Christison, G. B., and H. A. MacKenzie. 1993. 'Laser photoacoustic determination of physiological glucose concentrations in human whole blood', Medical and Biological Engineering and Computing, 31: 284-90.

Diebold, G. J., T. Sun, and M. I. Khan. 1991. 'Photoacoustic monopole radiation in one, two, and three dimensions', Physical Review Letters, 67: 3384-87.

Gamelin, John, Andres Aguirre, Anastasios Maurudis, Fei Huang, Diego Castillo, Lihong V. Wang, and Quing Zhu. 2008. 'Curved array photoacoustic tomographic system for small animal imaging', Journal of Biomedical Optics, 13: 024007-07-10.

Hannah, Alexander S., Donald VanderLaan, Yun-Sheng Chen, and Stanislav Y. Emelianov. 2014. 'Photoacoustic and ultrasound imaging using dual contrast perfluorocarbon nanodroplets triggered by laser pulses at 1064 nm', Biomedical Optics Express, 5: 3042-52.

Heijblom, M., W. Steenbergen, and S. Manohar. 2015. 'Clinical Photoacoustic Breast Imaging: The Twente experience', Pulse, IEEE, 6: 42-46.

Hoelen, Christoph G. A., and Frits F. M. de Mul. 2000. 'Image reconstruction for photoacoustic scanning of tissue structures', Applied optics, 39: 5872-83.

Jain, Prashant K., Kyeong Seok Lee, Ivan H. El-Sayed, and Mostafa A. El-Sayed. 2006. 'Calculated Absorption and Scattering Properties of Gold Nanoparticles of Different Size, Shape, and Composition: Applications in Biological Imaging and Biomedicine', The Journal of Physical Chemistry B, 110: 7238-48.

Khan, M. I., and G. J. Diebold. 1995. 'The photoacoustic effect generated by an isotropic solid sphere', Ultrasonics, 33: 265-69.

Kitai, Toshiyuki, Masae Torii, Tomoharu Sugie, Shotaro Kanao, Yoshiki Mikami, Tsuyoshi Shiina, and Masakazu Toi. 2014. 'Photoacoustic mammography: initial clinical results', Breast Cancer, 21: 146-53.

Kruger, Robert A. 1994. 'Photoacoustic ultrasound', Medical Physics, 21: 127-31.

Kruger, Robert A., Cherie M. Kuzmiak, Richard B. Lam, Daniel R. Reinecke, Stephen P. Del Rio, and Doreen Steed. 2013. 'Dedicated 3D photoacoustic breast imaging', Medical Physics, 40: 113301.

Kruger, Robert A., Pingyu Liu, Yuncai ‘‘Richard’’ Fang, and C. Robert Appledorn. 1995. 'Photoacoustic ultrasound (PAUS)—Reconstruction tomography', Medical Physics, 22: 1605-09.

Kruger, Robert A., Daniel R. Reinecke, and Gabe A. Kruger. 1999. 'Thermoacoustic computed tomography–technical considerations', Medical Physics, 26: 1832-37.

Ku, Geng, Xueding Wang, Xueyi Xie, George Stoica, and Lihong V. Wang. 2005. 'Imaging of tumor angiogenesis in rat brains in vivo by photoacoustic tomography', Applied optics, 44: 770-75.

Lee, Hannah J., Yang Liu, Jun Zhao, Min Zhou, Richard R. Bouchard, Trevor Mitcham, Michael Wallace, R. Jason Stafford, Chun Li, Sanjay Gupta, and Marites P. Melancon. 2013. 'In vitro and in vivo mapping of drug release after laser ablation thermal therapy with doxorubicin-loaded hollow gold nanoshells using fluorescence and photoacoustic imaging', Journal of Controlled Release, 172: 152-58.

Li, Li, Konstantin Maslov, Geng Ku, and Lihong V. Wang. 2009. 'Three-dimensional combined photoacoustic and optical coherence microscopy for in vivo microcirculation studies', Optics express, 17: 16450-55.

Luke, G. P., D. Yeager, and S. Y. Emelianov. 2012. 'Biomedical Applications of Photoacoustic Imaging with Exogenous Contrast Agents', Annals of biomedical engineering, 40: 422-37.

Nie, Liming, and Xiaoyuan Chen. 2014. 'Structural and functional photoacoustic molecular tomography aided by emerging contrast agents', Chemical Society Reviews, 43: 7132-70.

Oraevsky, Alexander A., Steven L. Jacques, and Frank K. Tittel. 1997. 'Measurement of tissue optical properties by time-resolved detection of laser-induced transient stress', Applied optics, 36: 402-15.

Park, S., J. Shah, S. R. Aglyamov, A. B. Karpiouk, S. Mallidi, A. Gopal, H. Moon, X. J. Zhang, W. G. Scott, and S. Y. Emelianov. 2006. "Integrated system for ultrasonic, photoacoustic and elasticity imaging." In, 61470H-70H-8.

Qu, Min, Srivalleesha Mallidi, Mohammad Mehrmohammadi, Ryan Truby, Kimberly Homan, Pratixa Joshi, Yun-Sheng Chen, Konstantin Sokolov, and Stanislav Emelianov. 2011. 'Magneto-photo-acoustic imaging', Biomedical Optics Express, 2: 385-96.

Quan, K. M., G. B. Christison, H. A. MacKenzie, and P. Hodgson. 1993. 'Glucose determination by a pulsed photoacoustic technique: an experimental study using a gelatin-based tissue phantom', Physics in Medicine and Biology, 38: 1911.

Razansky, Daniel, and Vasilis Ntziachristos. 2007. 'Hybrid photoacoustic fluorescence molecular tomography using finite-element-based inversion', Medical Physics, 34: 4293-301.

Rosencwaig, Allan, and Eli Pines. 1977. 'A photoacoustic study of newborn rat stratum corneum', Biochimica et Biophysica Acta (BBA) - Protein Structure, 493: 10-23.

Sethuraman, S., S. R. Aglyamov, J. H. Amirian, R. W. Smalling, and S. Y. Emelianov. 2007. 'Intravascular photoacoustic imaging using an IVUS imaging catheter', Ultrasonics, Ferroelectrics, and Frequency Control, IEEE Transactions on, 54: 978-86.

Seungsoo, Kim, Chen Yun-sheng, G. P. Luke, and S. Y. Emelianov. 2014. 'In-vivo ultrasound and photoacoustic image- guided photothermal cancer therapy using silica-coated gold nanorods', Ultrasonics, Ferroelectrics, and Frequency Control, IEEE Transactions on, 61: 891-97.

Shah, J., S. Park, S. Aglyamov, T. Larson, L. Ma, K. Sokolov, K. Johnston, T. Milner, and S. Y. Emelianov. 2008. 'Photoacoustic imaging and temperature measurement for photothermal cancer therapy', J Biomed Opt, 13: 034024.

Siphanto, Ronald I., Roy G. M. Kolkman, Arjan Huisjes, Magdalena C. Pilatou, Frits F. M. de Mul, Wiendelt Steenbergen, and Leon N. A. van Adrichem. 2004. 'Imaging of small vessels using photoacoustics: An in vivo study', Lasers in surgery and medicine, 35: 354-62.

Tam, A. C. 1986. 'APPLICATIONS OF PHOTOACOUSTIC SENSING TECHNIQUES', Reviews of Modern Physics, 58: 381-431.

Viator, John A., Gigi Au, Guenther Paltauf, Steven L. Jacques, Scott A. Prahl, Hongwu Ren, Zhongping Chen, and J. Stuart Nelson. 2002. 'Clinical testing of a photoacoustic probe for port wine stain depth determination', Lasers in surgery and medicine, 30: 141-48.

Wang, B., and S. Emelianov. 2011. 'Thermal intravascular photoacoustic imaging', Biomed Opt Express, 2: 3072-8.

Wang, X. D., Y. J. Pang, G. Ku, X. Y. Xie, G. Stoica, and L. H. V. Wang. 2003. 'Noninvasive laser-induced photoacoustic tomography for structural and functional in vivo imaging of the brain', Nature Biotechnology, 21: 803-06.

Wang, X. D., X. Y. Xie, G. N. Ku, and L. H. V. Wang. 2006. 'Noninvasive imaging of hemoglobin concentration and oxygenation in the rat brain using high-resolution photoacoustic tomography', Journal of Biomedical Optics, 11: 9.

Wang, Yi-Wei, Yu-Ying Fu, Qiaoli Peng, Shan-Shan Guo, Gang Liu, Juan Li, Huang-Hao Yang, and Guo-Nan Chen. 2013. 'Dye-enhanced graphene oxide for photothermal therapy and photoacoustic imaging', Journal of Materials Chemistry B, 1: 5762-67.

Yang, Hung-Wei, Hao-Li Liu, Meng-Lin Li, I. Wen Hsi, Chih-Tai Fan, Chiung-Yin Huang, Yu-Jen Lu, Mu-Yi Hua, Hsin-Yi Chou, Jiunn-Woei Liaw, Chen-Chi M. Ma, and Kuo-Chen Wei. 2013. 'Magnetic gold-nanorod/ PNIPAAmMA nanoparticles for dual magnetic resonance and photoacoustic imaging and targeted photothermal therapy', Biomaterials, 34: 5651-60.

References

Abran, M., G. Cloutier, M. H. R. Cardinal, B. Chayer, J. C. Tardif, and F. Lesage. 2014. 'Development of a Photoacoustic, Ultrasound and Fluorescence Imaging Catheter for the Study of Atherosclerotic Plaque', *Biomedical Circuits and Systems, IEEE Transactions on*, 8: 696-703.

Akers, Walter J, Chulhong Kim, Mikhail Berezin, Kevin Guo, Ralph Fuhrhop, Gregory M Lanza, Georg M Fischer, Ewald Daltrozzo, Andreas Zumbusch, and Xin Cai. 2010. 'Noninvasive photoacoustic and fluorescence sentinel lymph node identification using dye-loaded perfluorocarbon nanoparticles', *ACS Nano*, 5: 173-82.

Allen, Thomas J., Andrew Hall, Amar P. Dhillon, James S. Owen, and Paul C. Beard. 2012. 'Spectroscopic photoacoustic imaging of lipid-rich plaques in the human aorta in the 740 to 1400 nm wavelength range', *Journal of Biomedical Optics*, 17: 0612091-06120910.

Andreas, H. Hielscher, E. Alcouffe Raymond, and L. Barbour Randall. 1998. 'Comparison of finite-difference transport and diffusion calculations for photon migration in homogeneous and heterogeneous tissues', *Physics in Medicine and Biology*, 43: 1285.

Bailey, M. R., V. A. Khokhlova, O. A. Sapozhnikov, S. G. Kargl, and L. A. Crum. 2003. 'Physical mechanisms of the therapeutic effect of ultrasound (a review)', *Acoustical Physics*, 49: 369-88.

Bashkatov, A. N., E. A. Genina, V. I. Kochubey, and V. V. Tuchin. 2005a. 'Optical properties of human skin, subcutaneous and mucous tissues in the wavelength range from 400 to 2000 nm', *Journal of Physics D: Applied Physics*, 38: 2543.

Bashkatov, A. N., É. A. Genina, V. I. Kochubey, and V. V. Tuchin. 2005b. 'Optical properties of the subcutaneous adipose tissue in the spectral range 400–2500 nm', *Optics and Spectroscopy*, 99: 836-42.

Bayer, Carolyn L., Yun-Sheng Chen, Seungsoo Kim, Srivalleesha Mallidi, Konstantin Sokolov, and Stanislav Emelianov. 2011. 'Multiplex photoacoustic molecular imaging using targeted silica-coated gold nanorods', *Biomedical Optics Express*, 2: 1828-35.

Beard, P. 2011. 'Biomedical photoacoustic imaging', *Interface Focus*, 1: 602-31.

Beeler, Troy J., Angelo Schibeci, and A. Martonosi. 1980. 'The binding of arsenazo III to cell components', *Biochimica et Biophysica Acta (BBA) - General Subjects*, 629: 317-27.

Bell, Alexander Graham. 1881. *Upon the Production of Sound by Radiant Energy* (Gibson Brothers, printers).

Ben-Horin, Shomron, Ami Shinfeld, Erez Kachel, Angela Chetrit, and Avi Livneh. 'The composition of normal pericardial fluid and its implications for diagnosing pericardial effusions', *The American Journal of Medicine*, 118: 636-40.

Benjamin, E. J., P. A. Wolf, R. B. D'Agostino, H. Silbershatz, W. B. Kannel, and D. Levy. 1998. 'Impact of atrial fibrillation on the risk of death: the Framingham Heart Study', *Circulation*, 98: 946-52.

Berridge, Michael J., Peter Lipp, and Martin D. Bootman. 2000. 'The versatility and universality of calcium signalling', *Nat Rev Mol Cell Biol*, 1: 11-21.

Berridge, Michael V, An S Tan, Kathy D McCoy, and Rui Wang. 1996. 'The biochemical and cellular basis of cell proliferation assays that use tetrazolium salts', *Biochemica*, 4: 14-19.

Bers, Donald M. 2002. 'Cardiac excitation-contraction coupling', *Nature*, 415: 198-205.

Bhattacharyya, Sibaprasad, Shuyan Wang, Daniel Reinecke, William Kiser Jr, Robert A Kruger, and Timothy R DeGrado. 2008. 'Synthesis and evaluation of near-infrared (NIR) dye− herceptin conjugates as photoacoustic computed tomography (PCT) probes for HER2 expression in breast cancer', *Bioconjugate chemistry*, 19: 1186-93.

Black, John F, and Jennifer Kehlet Barton. 2004. 'Chemical and structural changes in blood undergoing laser photocoagulation', *Photochemistry and photobiology*, 80: 89-97.

Bouchard, Richard, Nicholas Dana, Luigi Di Biase, Andrea Natale, and Stanislav Emelianov. 2012. "Photoacoustic characterization of radiofrequency ablation lesions." In, edited by A. Oraevsky Alexander and V. Wang Lihong, 82233K. SPIE.

Bouchard, Richard, Onur Sahin, and Stanislav Emelianov. 2014. 'Ultrasound-guided photoacoustic imaging: current state and future development', *IEEE transactions on ultrasonics, ferroelectrics, and frequency control*, 61: 450-66.

Cannon, Christopher P., Benjamin A. Steinberg, Sabina A. Murphy, Jessica L. Mega, and Eugene Braunwald. 2006. 'Meta-Analysis of Cardiovascular Outcomes Trials Comparing Intensive Versus Moderate Statin Therapy', *Journal of the American College of Cardiology*, 48: 438-45.

Cappato, R., H. Calkins, S. A. Chen, W. Davies, Y. Iesaka, J. Kalman, Y. H. Kim, G. Klein, A. Natale, D. Packer, A. Skanes, F. Ambrogi, and E. Biganzoli. 2010. 'Updated worldwide survey on the methods, efficacy, and safety of catheter ablation for human atrial fibrillation', *Circ Arrhythm Electrophysiol*, 3: 32-8.

Catterall, William A., and Alexandra P. Few. 2008. 'Calcium Channel Regulation and Presynaptic Plasticity', *Neuron*, 59: 882-901.

Chavez, Patricia, Franz H Messerli, Abel Casso Dominguez, Emad F Aziz, Tina Sichrovsky, Daniel Garcia, Connor D Barrett, and Stephan Danik. 2015. 'Atrioesophageal fistula following ablation procedures for atrial fibrillation: systematic review of case reports', *Open Heart*, 2.

Chen, Jingyi, Fusayo Saeki, Benjamin J Wiley, Hu Cang, Michael J Cobb, Zhi-Yuan Li, Leslie Au, Hui Zhang, Michael B Kimmey, and Xingde Li. 2005. 'Gold nanocages: bioconjugation and their potential use as optical imaging contrast agents', *Nano Letters*, 5: 473-77.

Chitnis, Parag V., Hans-Peter Brecht, Richard Su, and Alexander A. Oraevsky. 2010. 'Feasibility of optoacoustic visualization of high-intensity focused ultrasound-induced thermal lesions in live tissue', *Journal of Biomedical Optics*, 15: 021313-13-5.

Christison, G. B., and H. A. MacKenzie. 1993. 'Laser photoacoustic determination of physiological glucose concentrations in human whole blood', *Medical and Biological Engineering and Computing*, 31: 284-90.

Çilesiz, Inci F., and Ashley J. Welch. 1993. 'Light dosimetry: effects of dehydration and thermal damage on the optical properties of the human aorta', *Applied optics*, 32: 477-87.

Claycomb, William C., Nicholas A. Lanson, Beverly S. Stallworth, Daniel B. Egeland, Joseph B. Delcarpio, Anthony Bahinski, and Nicholas J. Izzo. 1998. 'HL-1 cells: A cardiac muscle cell line that contracts and retains phenotypic characteristics of the adult cardiomyocyte', *Proceedings of the National Academy of Sciences*, 95: 2979-84.

Cold Spring Harbor. 'Tyrode's solution', *Cold Spring Harbor Protocols*, 2006.

Cook, Jason R., Wolfgang Frey, and Stanislav Emelianov. 2013. 'Quantitative Photoacoustic Imaging of Nanoparticles in Cells and Tissues', *ACS Nano*, 7: 1272-80.

Cooley, Erika J., Pieter Kruizinga, Darren W. Branch, and Stanislav Emelianov. 2010. "Evaluation of arsenazo III as a contrast agent for photoacoustic detection of micromolar calcium transients." In, 75761J-61J-8.

Cui, Huizhong, Jacob Staley, and Xinmai Yang. 2010. 'Integration of photoacoustic imaging and high-intensity focused ultrasound', *Journal of Biomedical Optics*, 15: 021312-12-4.

Cui, Huizhong, and Xinmai Yang. 2010. 'In vivo imaging and treatment of solid tumor using integrated photoacoustic imaging and high intensity focused ultrasound system', *Medical Physics*, 37: 4777-81.

———. 2011. 'Real-time monitoring of high-intensity focused ultrasound ablations with photoacoustic technique: An in vitro study', *Medical Physics*, 38: 5345-50.

Dana, N., L. Di Biase, A. Natale, S. Emelianov, and R. Bouchard. 2014. 'In vitro photoacoustic visualization of myocardial ablation lesions', *Heart Rhythm*, 11: 150-7.

Dana, N., R. A. Fowler, A. Allen, J. Zoldan, L. Suggs, and S. Emelianov. 2016. 'In vitro photoacoustic sensing of calcium dynamics with arsenazo III', *Laser Physics Letters*, 13: 075603.

Dana, Nicholas P., Diego S. Dumani, Jason R. Cook, and Stanislav Emelianov. 2016. 'Overview of Photoacoustic Imaging.' in Devon J. Godfrey, Jacob Van Dyk, Shiva K. Das, Bruce H. Curran and Anthony B. Wolbarst (eds.), *Advances in Medical Physics* (Medical Physics Publishing: Madison, WI).

Dana, Nicholas; Bouchard, Richard; Di Biase, Luigi; Natale, Andrea; Emelianov, Stanislav. 2014. "Characterization of myocardial ablation lesions using multi-wavelength photoacoustic imaging." In *SPIE Photons Plus Ultrasound: Imaging and Sensing 2014*. San Francisco, California United States.

Davies, M. J., N. Woolf, P. Rowles, and P. D. Richardson. 1994. 'Lipid and cellular constituents of unstable human aortic plaques.' in, *Arteriosclerosis* (Springer).

Diebold, G. J., and T. Sun. 1994. 'PROPERTIES OF PHOTOACOUSTIC WAVES IN ONE-DIMENSION, 2-DIMENSION, AND 3-DIMENSION', *Acustica*, 80: 339-51.

Diebold, G. J., T. Sun, and M. I. Khan. 1991. 'Photoacoustic monopole radiation in one, two, and three dimensions', *Physical Review Letters*, 67: 3384-87.

Docampo, R, S N Moreno, and R P Mason. 1983. 'Generation of free radical metabolites and superoxide anion by the calcium indicators arsenazo III, antipyrylazo III, and murexide in rat liver microsomes', *Journal of Biological Chemistry*, 258: 14920-25.

Dromi, Sergio, Victor Frenkel, Alfred Luk, Bryan Traughber, Mary Angstadt, Monica Bur, Jason Poff, Jianwu Xie, Steven K. Libutti, King C. P. Li, and Bradford J. Wood. 2007. 'Pulsed-High Intensity Focused Ultrasound and Low Temperature–Sensitive Liposomes for Enhanced Targeted Drug Delivery and Antitumor Effect', *Clinical cancer research : an official journal of the American Association for Cancer Research*, 13: 2722-27.

Duck, Francis A. 1990a. 'Chapter 8 - Nuclear Magnetism of Tissue.' in Francis A. Duck (ed.), *Physical Properties of Tissues* (Academic Press: London).

———. 1990b. 'Chapter 9 - Tissue Composition.' in Francis A. Duck (ed.), *Physical Properties of Tissues* (Academic Press: London).

Dukkipati, S. R., P. Neuzil, J. Kautzner, J. Petru, D. Wichterle, J. Skoda, R. Cihak, P. Peichl, A. Dello Russo, G. Pelargonio, C. Tondo, A. Natale, and V. Y. Reddy. 2012. 'The durability of pulmonary vein isolation using the visually guided laser

balloon catheter: multicenter results of pulmonary vein remapping studies', *Heart Rhythm*, 9: 919-25.

El-Sayed, Mostafa A. 2001. 'Some interesting properties of metals confined in time and nanometer space of different shapes', *Accounts of chemical research*, 34: 257-64.

Elezi, Shpend, Adnan Kastrati, Franz-Josef Neumann, Martin Hadamitzky, Josef Dirschinger, and Albert Schömig. 1998. 'Vessel Size and Long-Term Outcome After Coronary Stent Placement', *Circulation*, 98: 1875-80.

Eyerly, S. A., T. D. Bahnson, J. I. Koontz, D. P. Bradway, D. M. Dumont, G. E. Trahey, and P. D. Wolf. 2012. 'Intracardiac acoustic radiation force impulse imaging: a novel imaging method for intraprocedural evaluation of radiofrequency ablation lesions', *Heart Rhythm*, 9: 1855-62.

Eyerly, S. A., S. J. Hsu, S. H. Agashe, G. E. Trahey, Y. Li, and P. D. Wolf. 2010. 'An in vitro assessment of acoustic radiation force impulse imaging for visualizing cardiac radiofrequency ablation lesions', *J Cardiovasc Electrophysiol*, 21: 557-63.

Fang, Qianqian. 2010. 'Mesh-based Monte Carlo method using fast ray-tracing in Plücker coordinates', *Biomedical Optics Express*, 1: 165-75.

———. 2016. 'MCX GPU Benchmark/Contest', Accessed September 30, 2016. http://mcx.space/gpubench/.

Fang, Qianqian, and David A. Boas. 2009. 'Monte Carlo Simulation of Photon Migration in 3D Turbid Media Accelerated by Graphics Processing Units', *Optics express*, 17: 20178-90.

Farahani, Keyvan, Romaine E Saxton, Hyo–Chun Yoon, Antonio AF De Salles, Keith L Black, and Robert B Lufkin. 1999. 'MRI of thermally denatured blood: methemoglobin formation and relaxation effects', *Magnetic resonance imaging*, 17: 1489-94.

Fischman , David L., Martin B. Leon , Donald S. Baim , Richard A. Schatz , Michael P. Savage , Ian Penn , Katherine Detre , Lisa Veltri , Donald Ricci , Masakiyo Nobuyoshi , Michael Cleman , Richard Heuser , David Almond , Paul S. Teirstein , R. David Fish , Antonio Colombo , Jeffrey Brinker , Jeffrey Moses , Alex Shaknovich , John Hirshfeld , Stephen Bailey , Stephen Ellis , Randal Rake , and Sheldon Goldberg 1994. 'A Randomized Comparison of Coronary-Stent Placement and Balloon Angioplasty in the Treatment of Coronary Artery Disease', *New England Journal of Medicine*, 331: 496-501.

Fleg, Jerome L., Gregg W. Stone, Zahi A. Fayad, Juan F. Granada, Thomas S. Hatsukami, Frank D. Kolodgie, Jacques Ohayon, Roderic Pettigrew, Marc S. Sabatine, Guillermo J. Tearney, Sergio Waxman, Michael J. Domanski, Pothur R. Srinivas, and Jagat Narula. 2012. 'Detection of High-Risk Atherosclerotic Plaque: Report of the NHLBI Working Group on Current Status and Future Directions', *JACC: Cardiovascular Imaging*, 5: 941-55.

Fleming, Christine P., Kara J. Quan, Hui Wang, Guy Amit, and Andrew M. Rollins. 2010. 'In vitro characterization of cardiac radiofrequency ablation lesions using optical coherence tomography', *Opt. Express*, 18: 3079-92.

Flock, S. T., M. S. Patterson, B. C. Wilson, and D. R. Wyman. 1989. 'Monte Carlo modeling of light propagation in highly scattering tissues. I. Model predictions and comparison with diffusion theory', *Biomedical Engineering, IEEE Transactions on*, 36: 1162-68.

Flock, S. T., B. C. Wilson, and M. S. Patterson. 1989. 'Monte Carlo modeling of light propagation in highly scattering tissues. II. Comparison with measurements in phantoms', *IEEE Transactions on Biomedical Engineering*, 36: 1169-73.

Fogoros, Richard N. 1999. *Electrophysiologic Testing* (Blackwell Publishing).

Funke, Arik R., Jean-François Aubry, Mathias Fink, Albert-Claude Boccara, and Emmanuel Bossy. 2009. 'Photoacoustic guidance of high intensity focused ultrasound with selective optical contrasts and time-reversal', *Applied Physics Letters*, 94: 054102.

Galanzha, Ekaterina I, Evgeny V Shashkov, Thomas Kelly, Jin-Woo Kim, Lily Yang, and Vladimir P Zharov. 2009. 'In vivo magnetic enrichment and multiplex photoacoustic detection of circulating tumour cells', *Nature nanotechnology*, 4: 855-60.

Gamelin, John, Andres Aguirre, Anastasios Maurudis, Fei Huang, Diego Castillo, Lihong V. Wang, and Quing Zhu. 2008. 'Curved array photoacoustic tomographic system for small animal imaging', *Journal of Biomedical Optics*, 13: 024007-07-10.

Geuss, Laura R., Alicia C. B. Allen, Divya Ramamoorthy, and Laura J. Suggs. 2015. 'Maintenance of HL-1 cardiomyocyte functional activity in PEGylated fibrin gels', *Biotechnology and Bioengineering*, 112: 1446-56.

Go, Alan S, Dariush Mozaffarian, Véronique L Roger, Emelia J Benjamin, Jarett D Berry, William B Borden, Dawn M Bravata, Shifan Dai, Earl S Ford, and Caroline S Fox. 2013. 'Heart disease and stroke statistics—2013 update a report from the American Heart Association', *Circulation*, 127: e6-e245.

Goel, Shreya, Feng Chen, and Weibo Cai. 2014. 'Synthesis and biomedical applications of copper sulfide nanoparticles: from sensors to theranostics', *Small*, 10: 631-45.

Goldberg, S Nahum, Clement J Grassi, John F Cardella, J William Charboneau, Gerald D Dodd III, Damian E Dupuy, Debra Gervais, Alice R Gillams, Robert A Kane, and Fred T Lee Jr. 2005. 'Standards of Practice-Image-guided Tumor Ablation: Standardization of Terminology and Reporting Criteria', *Journal of Vascular and Interventional Radiology*, 16: 765-78.

Gray, J. P., N. Dana, K. L. Dextraze, F. Maier, S. Emelianov, and R. R. Bouchard. 2015. 'Multi-Wavelength Photoacoustic Visualization of High Intensity Focused Ultrasound Lesions', *Ultrasonic Imaging*.

Groh, Mark A, Oliver A Binns, Harry G Burton, Stephen W Ely, and Alan M Johnson. 2007. 'Ultrasonic cardiac ablation for atrial fibrillation during concomitant cardiac surgery: long-term clinical outcomes', *The Annals of thoracic surgery*, 84: 1978-83.

Haissaguerre, M., P. Jais, D. C. Shah, A. Takahashi, M. Hocini, G. Quiniou, S. Garrigue, A. Le Mouroux, P. Le Metayer, and J. Clementy. 1998. 'Spontaneous initiation of atrial fibrillation by ectopic beats originating in the pulmonary veins', *N Engl J Med*, 339: 659-66.

Hale, George M., and Marvin R. Querry. 1973. 'Optical Constants of Water in the 200-nm to 200-μm Wavelength Region', *Applied optics*, 12: 555-63.

Hannah, Alexander, Geoffrey Luke, Katheryne Wilson, Kimberly Homan, and Stanislav Emelianov. 2013. 'Indocyanine green-loaded photoacoustic nanodroplets: dual contrast nanoconstructs for enhanced photoacoustic and ultrasound imaging', *ACS Nano*, 8: 250-59.

Hannah, Alexander S., Donald VanderLaan, Yun-Sheng Chen, and Stanislav Y. Emelianov. 2014. 'Photoacoustic and ultrasound imaging using dual contrast perfluorocarbon nanodroplets triggered by laser pulses at 1064 nm', *Biomedical Optics Express*, 5: 3042-52.

Haraldsson, Börje, Jenny Nyström, and William M. Deen. 2008. 'Properties of the Glomerular Barrier and Mechanisms of Proteinuria', *Physiological Reviews*, 88: 451-87.

Heijblom, M., W. Steenbergen, and S. Manohar. 2015. 'Clinical Photoacoustic Breast Imaging: The Twente experience', *Pulse, IEEE*, 6: 42-46.

Hellings, Willem E., Wouter Peeters, Frans L. Moll, Sebastiaan R.D. Piers, Jessica van Setten, Peter J. Van der Spek, Jean-Paul P.M. de Vries, Kees A. Seldenrijk, Peter C. De Bruin, Aryan Vink, Evelyn Velema, Dominique P.V. de Kleijn, and Gerard Pasterkamp. 2010. 'Composition of Carotid Atherosclerotic Plaque Is Associated With Cardiovascular Outcome: A Prognostic Study', *Circulation*, 121: 1941-50.

Hennessy, Ricky, Sam L. Lim, Mia K. Markey, and James W. Tunnell. 2013. 'Monte Carlo lookup table-based inverse model for extracting optical properties from tissue-simulating phantoms using diffuse reflectance spectroscopy', *Journal of Biomedical Optics*, 18: 037003-03.

Henyey, Louis G, and Jesse Leonard Greenstein. 1941. 'Diffuse radiation in the galaxy', *The Astrophysical Journal*, 93: 70-83.

Herron, Todd J., Peter Lee, and José Jalife. 2012. 'Optical Imaging of Voltage and Calcium in Cardiac Cells & Tissues', *Circulation Research*, 110: 609-23.

Hoelen, Christoph G. A., and Frits F. M. de Mul. 2000. 'Image reconstruction for photoacoustic scanning of tissue structures', *Applied optics*, 39: 5872-83.

Hsiao, Yi-Sing, Xueding Wang, and Cheri X Deng. 2013. 'Dual-wavelength photoacoustic technique for monitoring tissue status during thermal treatments', *Journal of Biomedical Optics*, 18: 067003-03.

Hsu, Li-Fern, Pierre JaÏS, MÉLÈZe Hocini, Prashanthan Sanders, Christophe ScavÉE, Frederic Sacher, Yoshihide Takahashi, Martin Rotter, Jean-Luc Pasquie, Jacques ClÉMenty, and Michel HaÏSsaguerre. 2005. 'Incidence and Prevention of Cardiac Tamponade Complicating Ablation for Atrial Fibrillation', *Pacing and Clinical Electrophysiology*, 28: S106-S09.

Hu, Xiaoge, Chen-Wei Wei, Jinjun Xia, Ivan Pelivanov, Matthew O'Donnell, and Xiaohu Gao. 2013. 'Trapping and Photoacoustic Detection of CTCs at the Single Cell per Milliliter Level with Magneto-Optical Coupled Nanoparticles', *Small (Weinheim an der Bergstrasse, Germany)*, 9: 2046-52.

Hynynen, K., A. Darkazanli, E. Unger, and J. F. Schenck. 1993. 'MRI-guided noninvasive ultrasound surgery', *Medical Physics*, 20: 107-15.

Irina, V. Larina, V. Larin Kirill, and O. Esenaliev Rinat. 2005. 'Real-time optoacoustic monitoring of temperature in tissues', *Journal of Physics D: Applied Physics*, 38: 2633.

Jacques, S. L. 2013. 'Optical properties of biological tissues: a review', *Phys Med Biol*, 58: R37-61.

Jacques, Steven L. 2014. 'Coupling 3D Monte Carlo light transport in optically heterogeneous tissues to photoacoustic signal generation', *Photoacoustics*, 2: 137-42.

Jagannathan, Jay, Narendra K. Sanghvi, Lawrence A. Crum, Chun-Po Yen, Ricky Medel, Aaron S. Dumont, Jason P. Sheehan, Ladislau Steiner, Ferenc Jolesz, and Neal F. Kassell. 2009. 'High intensity focused ultrasound surgery (HIFU) of the brain: A historical perspective, with modern applications', *Neurosurgery*, 64: 201-11.

Jain, Mukesh K., and Paul M. Ridker. 2005. 'Anti-Inflammatory Effects of Statins: Clinical Evidence and Basic Mechanisms', *Nat Rev Drug Discov*, 4: 977-87.

Jain, Prashant K., Kyeong Seok Lee, Ivan H. El-Sayed, and Mostafa A. El-Sayed. 2006. 'Calculated Absorption and Scattering Properties of Gold Nanoparticles of Different Size, Shape, and Composition: Applications in Biological Imaging and Biomedicine', *The Journal of Physical Chemistry B*, 110: 7238-48.

Jansen, Krista, Antonius F. W. van der Steen, Min Wu, Heleen M. M. van Beusekom, Geert Springeling, Xiang Li, Qifa Zhou, K. Kirk Shung, Dominique P. V. de

Kleijn, and Gijs van Soest. 2014. 'Spectroscopic intravascular photoacoustic imaging of lipids in atherosclerosis', *Journal of Biomedical Optics*, 19: 026006-06.

Jansen, Krista, Min Wu, Antonius F. W. van der Steen, and Gijs van Soest. 2014. 'Photoacoustic imaging of human coronary atherosclerosis in two spectral bands', *Photoacoustics*, 2: 12-20.

Ji, Xiaohui, Xiangning Song, Jun Li, Yubai Bai, Wensheng Yang, and Xiaogang Peng. 2007. 'Size control of gold nanocrystals in citrate reduction: the third role of citrate', *Journal of the American Chemical Society*, 129: 13939-48.

Jolesz, Ferenc A. 2009. 'MRI-Guided Focused Ultrasound Surgery', *Annual Review of Medicine*, 60: 417-30.

Karpiouk, Andrei B., Bo Wang, and Stanislav Y. Emelianov. 2010. 'Development of a catheter for combined intravascular ultrasound and photoacoustic imaging', *Review of Scientific Instruments*, 81: 014901.

Keijzer, Marleen, Rebecca R. Richards-Kortum, Steven L. Jacques, and Michael S. Feld. 1989. 'Fluorescence spectroscopy of turbid media: Autofluorescence of the human aorta', *Applied optics*, 28: 4286-92.

Kelly, K Lance, Eduardo Coronado, Lin Lin Zhao, and George C Schatz. 2003. 'The optical properties of metal nanoparticles: the influence of size, shape, and dielectric environment', *The Journal of Physical Chemistry B*, 107: 668-77.

Kennedy, James E. 2005. 'High-intensity focused ultrasound in the treatment of solid tumours', *Nat Rev Cancer*, 5: 321-27.

Khan, M. I., and G. J. Diebold. 1995. 'The photoacoustic effect generated by an isotropic solid sphere', *Ultrasonics*, 33: 265-69.

Kim, Chulhong, Kwang Hyun Song, Feng Gao, and Lihong V Wang. 2010. 'Sentinel lymph nodes and lymphatic vessels: noninvasive dual-modality in vivo mapping by using indocyanine green in rats—volumetric spectroscopic photoacoustic imaging and planar fluorescence imaging 1', *Radiology*, 255: 442-50.

Kim, Gwangseong, Sheng-Wen Huang, Kathleen C Day, Matthew O'Donnell, Rodney R Agayan, Mark A Day, Raoul Kopelman, and Shai Ashkenazi. 2007. 'Indocyanine-green-embedded PEBBLEs as a contrast agent for photoacoustic imaging', *Journal of Biomedical Optics*, 12: 044020-20-8.

Kim, S., Y. S. Chen, G. P. Luke, and S. Y. Emelianov. 2011. 'In vivo three-dimensional spectroscopic photoacoustic imaging for monitoring nanoparticle delivery', *Biomed Opt Express*, 2: 2540-50.

Kitai, Toshiyuki, Masae Torii, Tomoharu Sugie, Shotaro Kanao, Yoshiki Mikami, Tsuyoshi Shiina, and Masakazu Toi. 2014. 'Photoacoustic mammography: initial clinical results', *Breast Cancer*, 21: 146-53.

Kolandaivelu, Aravindan, Menekhem M. Zviman, Valeria Castro, Albert C. Lardo, Ronald D. Berger, and Henry R. Halperin. 2010. 'Noninvasive Assessment of Tissue Heating During Cardiac Radiofrequency Ablation Using MRI Thermography', *Circulation: Arrhythmia and Electrophysiology*, 3: 521-29.

Kruger, Robert A. 1994. 'Photoacoustic ultrasound', *Medical Physics*, 21: 127-31.

Kruger, Robert A., Cherie M. Kuzmiak, Richard B. Lam, Daniel R. Reinecke, Stephen P. Del Rio, and Doreen Steed. 2013. 'Dedicated 3D photoacoustic breast imaging', *Medical Physics*, 40: 113301.

Kruger, Robert A., Pingyu Liu, Yuncai ‘‘Richard’’ Fang, and C. Robert Appledorn. 1995. 'Photoacoustic ultrasound (PAUS)—Reconstruction tomography', *Medical Physics*, 22: 1605-09.

Kruger, Robert A., Daniel R. Reinecke, and Gabe A. Kruger. 1999. 'Thermoacoustic computed tomography–technical considerations', *Medical Physics*, 26: 1832-37.

Kruizinga, Pieter, Antonius F. W. van der Steen, Nico de Jong, Geert Springeling, Jan Lukas Robertus, Aad van der Lugt, and Gijs van Soest. 2014. 'Photoacoustic imaging of carotid artery atherosclerosis', *Journal of Biomedical Optics*, 19: 110504-04.

Ku, Geng, Xueding Wang, Xueyi Xie, George Stoica, and Lihong V. Wang. 2005. 'Imaging of tumor angiogenesis in rat brains in vivo by photoacoustic tomography', *Applied optics*, 44: 770-75.

Ku, Geng, Min Zhou, Shaoli Song, Qian Huang, John Hazle, and Chun Li. 2012. 'Copper sulfide nanoparticles as a new class of photoacoustic contrast agent for deep tissue imaging at 1064 nm', *ACS Nano*, 6: 7489-96.

Kumar, S, J Aaron, and K Sokolov. 2008. 'Directional conjugation of antibodies to nanoparticles for synthesis of multiplexed optical contrast agents with both delivery and targeting moieties', *Nature Protocols*, 3: 314-20.

Larin, Kirill V., Irina V. Larina, Massoud Motamedi, and Rinat O. Esenaliev. 2000. "Monitoring of temperature distribution in tissues with optoacoustic technique in real time." In, 311-21.

Laufer, Jan, Edward Zhang, and Paul Beard. 2010. 'Evaluation of absorbing chromophores used in tissue phantoms for quantitative photoacoustic spectroscopy and imaging', *Selected Topics in Quantum Electronics, IEEE Journal of*, 16: 600-07.

Lee, Hannah J., Yang Liu, Jun Zhao, Min Zhou, Richard R. Bouchard, Trevor Mitcham, Michael Wallace, R. Jason Stafford, Chun Li, Sanjay Gupta, and Marites P. Melancon. 2013. 'In vitro and in vivo mapping of drug release after laser ablation thermal therapy with doxorubicin-loaded hollow gold nanoshells using

fluorescence and photoacoustic imaging', *Journal of Controlled Release*, 172: 152-58.

Lee, Lisa A., Claudio Simon, Edward L. Bove, Ralph S. Mosca, Emad S. Ebbini, Gerald D. Abrams, and Achiau Ludomirsky. 2000. 'High Intensity Focused Ultrasound Effect on Cardiac Tissues: Potential for Clinical Application', *Echocardiography*, 17: 563-66.

Lehman, William, Roger Craig, and Peter Vibert. 1994. 'Ca2+-induced tropomyosin movement in Limulus thin filaments revealed by three-dimensional reconstruction', *Nature*, 368: 65-67.

Li, Li, Konstantin Maslov, Geng Ku, and Lihong V. Wang. 2009. 'Three-dimensional combined photoacoustic and optical coherence microscopy for in vivo microcirculation studies', *Optics express*, 17: 16450-55.

Li, Yan, Xiaojing Gong, Chengbo Liu, Riqiang Lin, William Hau, Xiaosong Bai, and Liang Song. 2015. 'High-speed intravascular spectroscopic photoacoustic imaging at 1000 A-lines per second with a 0.9-mm diameter catheter', *Journal of Biomedical Optics*, 20: 065006-06.

Libby, Peter. 2002. 'Inflammation in atherosclerosis', *Nature*, 420: 868-74.

Longmire, Michelle, Peter L Choyke, and Hisataka Kobayashi. 2008. 'Clearance properties of nano-sized particles and molecules as imaging agents: considerations and caveats'.

Luke, G. P., D. Yeager, and S. Y. Emelianov. 2012. 'Biomedical Applications of Photoacoustic Imaging with Exogenous Contrast Agents', *Annals of biomedical engineering*, 40: 422-37.

Luke, Geoffrey P., Seung Yun Nam, and Stanislav Y. Emelianov. 2013. 'Optical wavelength selection for improved spectroscopic photoacoustic imaging', *Photoacoustics*, 1: 36-42.

MacNeill, Briain D., Harry C. Lowe, Masamichi Takano, Valentin Fuster, and Ik-Kyung Jang. 2003. 'Intravascular Modalities for Detection of Vulnerable Plaque: Current Status', *Arteriosclerosis, Thrombosis, and Vascular Biology*, 23: 1333-42.

Mallidi, S., G. P. Luke, and S. Emelianov. 2011. 'Photoacoustic imaging in cancer detection, diagnosis, and treatment guidance', *Trends Biotechnol*, 29: 213-21.

Marrouche, N. F., D. O. Martin, O. Wazni, A. M. Gillinov, A. Klein, M. Bhargava, E. Saad, D. Bash, H. Yamada, W. Jaber, R. Schweikert, P. Tchou, A. Abdul-Karim, W. Saliba, and A. Natale. 2003. 'Phased-array intracardiac echocardiography monitoring during pulmonary vein isolation in patients with atrial fibrillation: impact on outcome and complications', *Circulation*, 107: 2710-6.

Marshall, K. L., G. Painter, K. Lotito, A. G. Noto, and P. Chang. 2006. 'Transition Metal Dithiolene Near-IR Dyes and Their Applications in Liquid Crystal Devices', *Molecular Crystals and Liquid Crystals*, 454: 47/[449]-79/[81].

Matthews, B. W. 1975. 'Comparison of the predicted and observed secondary structure of T4 phage lysozyme', *Biochimica et Biophysica Acta (BBA) - Protein Structure*, 405: 442-51.

McKay, Aaron, Ondrej Kitzler, Hua Liu, David Fell, and Richard P. Mildren. 2012. "High average power (11 W) eye-safe diamond Raman laser." In, 85510U-10U-8.

Mitcham, T, T Marques, D Chatterjee, S Krishnan, T Pugh, and R Bouchard. 2013. "Transrectal photoacoustic-ultrasonic imaging enhancement through interstitial irradiation and targeted nanoparticles." In *Proceedings of the 2013 IEEE Ultrasonics symposium, Prague, Czech Republic*.

Mitnovetski, S., A. A. Almeida, J. Goldstein, A. W. Pick, and J. A. Smith. 2009. 'Epicardial high-intensity focused ultrasound cardiac ablation for surgical treatment of atrial fibrillation', *Heart Lung Circ*, 18: 28-31.

Miyasaka, Y., M. E. Barnes, B. J. Gersh, S. S. Cha, K. R. Bailey, W. P. Abhayaratna, J. B. Seward, and T. S. Tsang. 2006. 'Secular trends in incidence of atrial fibrillation in Olmsted County, Minnesota, 1980 to 2000, and implications on the projections for future prevalence', *Circulation*, 114: 119-25.

Mozaffarian, Dariush, Emelia J. Benjamin, Alan S. Go, Donna K. Arnett, Michael J. Blaha, Mary Cushman, Sarah de Ferranti, Jean-Pierre Després, Heather J. Fullerton, Virginia J. Howard, Mark D. Huffman, Suzanne E. Judd, Brett M. Kissela, Daniel T. Lackland, Judith H. Lichtman, Lynda D. Lisabeth, Simin Liu, Rachel H. Mackey, David B. Matchar, Darren K. McGuire, Emile R. Mohler, Claudia S. Moy, Paul Muntner, Michael E. Mussolino, Khurram Nasir, Robert W. Neumar, Graham Nichol, Latha Palaniappan, Dilip K. Pandey, Mathew J. Reeves, Carlos J. Rodriguez, Paul D. Sorlie, Joel Stein, Amytis Towfighi, Tanya N. Turan, Salim S. Virani, Joshua Z. Willey, Daniel Woo, Robert W. Yeh, and Melanie B. Turner. 2015. 'Heart Disease and Stroke Statistics—2015 Update: A Report From the American Heart Association', *Circulation*, 131: e29-e322.

Muller, James E, George S Abela, Richard W Nesto, and Geoffrey H Tofler. 1994. 'Triggers, acute risk factors and vulnerable plaques: the lexicon of a new frontier', *Journal of the American College of Cardiology*, 23: 809-13.

Nam, Seung Yun, Laura M Ricles, Laura J Suggs, and Stanislav Y Emelianov. 2012. 'Nonlinear photoacoustic signal increase from endocytosis of gold nanoparticles', *Optics Letters*, 37: 4708-10.

Narula, Jagat, Masataka Nakano, Renu Virmani, Frank D. Kolodgie, Rita Petersen, Robert Newcomb, Shaista Malik, Valentin Fuster, and Aloke V. Finn. 2013. 'Histopathologic Characteristics of Atherosclerotic Coronary Disease and

Implications of the Findings for the Invasive and Noninvasive Detection of Vulnerable Plaques', *Journal of the American College of Cardiology*, 61: 1041-51.

Natale, Andrea, Larry Breeding, Gery Tomassoni, Kathleen Rajkovich, Mark Richey, Salwa Beheiry, Katie Martinez, Lisa Cromwell, Brandon Wides, and Fabio Leonelli. 1998. 'Ablation of right and left ectopic atrial tachycardias using a three-dimensional nonfluoroscopic mapping system', *The American Journal of Cardiology*, 82: 989-92.

Nickolls, John, Ian Buck, Michael Garland, and Kevin Skadron. 2008. 'Scalable Parallel Programming with CUDA', *Queue*, 6: 40-53.

Nie, Liming, and Xiaoyuan Chen. 2014. 'Structural and functional photoacoustic molecular tomography aided by emerging contrast agents', *Chemical Society Reviews*, 43: 7132-70.

Niidome, Takuro, Masato Yamagata, Yuri Okamoto, Yasuyuki Akiyama, Hironobu Takahashi, Takahito Kawano, Yoshiki Katayama, and Yasuro Niidome. 2006. 'PEG-modified gold nanorods with a stealth character for in vivo applications', *Journal of Controlled Release*, 114: 343-47.

Nikoobakht, Babak, and Mostafa A El-Sayed. 2003. 'Preparation and growth mechanism of gold nanorods (NRs) using seed-mediated growth method', *Chemistry of Materials*, 15: 1957-62.

Ntziachristos, V. 2010. 'Going deeper than microscopy: the optical imaging frontier in biology', *Nat Methods*, 7: 603-14.

Oraevsky, Alexander A., Steven L. Jacques, and Frank K. Tittel. 1997. 'Measurement of tissue optical properties by time-resolved detection of laser-induced transient stress', *Applied optics*, 36: 402-15.

Otsu, Nobuyuki. 1975. 'A threshold selection method from gray-level histograms', *Automatica*, 11: 23-27.

Ottenhausen, Malte, Imithri Bodhinayake, Matei Banu, Kartik Kesavabhotla, Ashley Ray, and John A. Boockvar. 2013. 'Industry progress report on neuro-oncology: Biotech update 2013', *Journal of Neuro-Oncology*, 115: 311-16.

Palade, P, and J Vergara. 1983. 'Stoichiometries of arsenazo III-Ca complexes.', *Biophysical Journal*, 43: 355-69.

Pappone, C., S. Rosanio, G. Oreto, M. Tocchi, F. Gugliotta, G. Vicedomini, A. Salvati, C. Dicandia, P. Mazzone, V. Santinelli, S. Gulletta, and S. Chierchia. 2000. 'Circumferential radiofrequency ablation of pulmonary vein ostia: A new anatomic approach for curing atrial fibrillation', *Circulation*, 102: 2619-28.

Park, S., J. Shah, S. R. Aglyamov, A. B. Karpiouk, S. Mallidi, A. Gopal, H. Moon, X. J. Zhang, W. G. Scott, and S. Y. Emelianov. 2006. "Integrated system for ultrasonic, photoacoustic and elasticity imaging." In, 61470H-70H-8.

Petersen, H. H., X. Chen, A. Pietersen, J. H. Svendsen, and S. Haunso. 1999. 'Temperature-controlled radiofrequency ablation of cardiac tissue: an in vitro study of the impact of electrode orientation, electrode tissue contact pressure and external convective cooling', *J Interv Card Electrophysiol*, 3: 257-62.

Petersen, Helen Høgh, Xu Chen, Adrian Pietersen, Jesper Hastrup Svendsen, and Stig Haunsø. 1999. 'Lesion Dimensions During Temperature-Controlled Radiofrequency Catheter Ablation of Left Ventricular Porcine Myocardium : Impact of Ablation Site, Electrode Size, and Convective Cooling', *Circulation*, 99: 319-25.

Piao, Zhonglie, Teng Ma, Jiawen Li, Maximilian T. Wiedmann, Shenghai Huang, Mingyue Yu, K. Kirk Shung, Qifa Zhou, Chang-Seok Kim, and Zhongping Chen. 2015. 'High speed intravascular photoacoustic imaging with fast optical parametric oscillator laser at 1.7 μm', *Applied Physics Letters*, 107: 083701.

Powers, David Martin Ward. 2011. 'Evaluation: from precision, recall and F-measure to ROC, informedness, markedness and correlation', *International Journal of Machine Learning Technology*, 2: 37-63.

Prahl, Scott. 1999. 'Optical absorption of hemoglobin', *Oregon Medical Laser Center, http://omlc. ogi. edu/spectra/hemoglobin/index. html*, 15.

Prahl, Scott A, Marleen Keijzer, Steven L Jacques, and Ashley J Welch. 1989. 'A Monte Carlo model of light propagation in tissue', *Dosimetry of laser radiation in medicine and biology*, 5: 102-11.

Pramanik, M., and L. V. Wang. 2009. 'Thermoacoustic and photoacoustic sensing of temperature', *J Biomed Opt*, 14: 054024.

Pramanik, Manojit, Magdalena Swierczewska, Danielle Green, Balaji Sitharaman, and Lihong V Wang. 2009. 'Single-walled carbon nanotubes as a multimodal-thermoacoustic and photoacoustic-contrast agent', *Journal of Biomedical Optics*, 14: 034018-18-8.

Prost, Amaury, Arik Funke, MickaÃŦl Tanter, and Emmanuel Bossy. 2012. 'Photoacoustic-guided ultrasound therapy with a dual-mode ultrasound array', *Journal of Biomedical Optics*, 17: 0612051-56.

Qian, Gang, Ze Zhong, Min Luo, Dengbin Yu, Zhiqiang Zhang, Zhi Yuan Wang, and Dongge Ma. 2009. 'Simple and Efficient Near-Infrared Organic Chromophores for Light-Emitting Diodes with Single Electroluminescent Emission above 1000 nm', *Advanced Materials*, 21: 111-16.

Qu, Min, Srivalleesha Mallidi, Mohammad Mehrmohammadi, Ryan Truby, Kimberly Homan, Pratixa Joshi, Yun-Sheng Chen, Konstantin Sokolov, and Stanislav Emelianov. 2011. 'Magneto-photo-acoustic imaging', *Biomedical Optics Express*, 2: 385-96.

Quan, K. M., G. B. Christison, H. A. MacKenzie, and P. Hodgson. 1993. 'Glucose determination by a pulsed photoacoustic technique: an experimental study using a gelatin-based tissue phantom', *Physics in Medicine and Biology*, 38: 1911.

Quesson, Bruno, Jacco A. de Zwart, and Chrit T. W. Moonen. 2000. 'Magnetic resonance temperature imaging for guidance of thermotherapy', *Journal of Magnetic Resonance Imaging*, 12: 525-33.

Rajian, Justin Rajesh, Mario L. Fabiilli, J. Brian Fowlkes, Paul L. Carson, and Xueding Wang. 2011. 'Drug delivery monitoring by photoacoustic tomography with an ICG encapsulated double emulsion', *Optics express*, 19: 14335-47.

Ramkissoon, R. A. 1966. 'Macroscopic identification of early myocardial infarction by dehydrogenase alterations', *J Clin Pathol*, 19: 479-81.

Ranjan, R., E. G. Kholmovski, J. Blauer, S. Vijayakumar, N. A. Volland, M. E. Salama, D. L. Parker, R. MacLeod, and N. F. Marrouche. 2012. 'Identification and acute targeting of gaps in atrial ablation lesion sets using a real-time magnetic resonance imaging system', *Circ Arrhythm Electrophysiol*, 5: 1130-5.

Razansky, Daniel, and Vasilis Ntziachristos. 2007. 'Hybrid photoacoustic fluorescence molecular tomography using finite-element-based inversion', *Medical Physics*, 34: 4293-301.

Righetti, Raffaella, Faouzi Kallel, R. Jason Stafford, Roger E. Price, Thomas A. Krouskop, John D. Hazle, and Jonathan Ophir. 1999. 'Elastographic characterization of HIFU-induced lesions in canine livers', *Ultrasound in Medicine & Biology*, 25: 1099-113.

Roger, V. L., A. S. Go, D. M. Lloyd-Jones, E. J. Benjamin, J. D. Berry, W. B. Borden, D. M. Bravata, S. Dai, E. S. Ford, C. S. Fox, H. J. Fullerton, C. Gillespie, S. M. Hailpern, J. A. Heit, V. J. Howard, B. M. Kissela, S. J. Kittner, D. T. Lackland, J. H. Lichtman, L. D. Lisabeth, D. M. Makuc, G. M. Marcus, A. Marelli, D. B. Matchar, C. S. Moy, D. Mozaffarian, M. E. Mussolino, G. Nichol, N. P. Paynter, E. Z. Soliman, P. D. Sorlie, N. Sotoodehnia, T. N. Turan, S. S. Virani, N. D. Wong, D. Woo, M. B. Turner, Committee American Heart Association Statistics, and Subcommittee Stroke Statistics. 2012. 'Executive summary: heart disease and stroke statistics--2012 update: a report from the American Heart Association', *Circulation*, 125: 188-97.

Roggan, A., M. Friebel, K. Do Rschel, A. Hahn, and G. Mu Ller. 1999. 'Optical Properties of Circulating Human Blood in the Wavelength Range 400-2500 nm', *J Biomed Opt*, 4: 36-46.

Rosenbaum, R., A. J. Greenspon, M. Smith, and P. Walinsky. 1994. 'Advanced radiofrequency catheter ablation in canine myocardium', *Am Heart J*, 127: 851-7.

Rosencwaig, Allan, and Eli Pines. 1977. 'A photoacoustic study of newborn rat stratum corneum', *Biochimica et Biophysica Acta (BBA) - Protein Structure*, 493: 10-23.

Rosenthal, Eben L., Jason M. Warram, Kirby I. Bland, and Kurt R. Zinn. 2015. 'The Status of Contemporary Image-Guided Modalities in Oncologic Surgery', *Annals of Surgery*, 261: 46-55.

Rowatt, E., and R. J. Williams. 1989. 'The interaction of cations with the dye arsenazo III', *Biochemical Journal*, 259: 295-98.

Roy, Probal, Daniel H. Steinberg, Steven J. Sushinsky, Teruo Okabe, Tina L. Pinto Slottow, Kimberly Kaneshige, Zhenyi Xue, Lowell F. Satler, Kenneth M. Kent, William O. Suddath, Augusto D. Pichard, Neil J. Weissman, Joseph Lindsay, and Ron Waksman. 2008. 'The potential clinical utility of intravascular ultrasound guidance in patients undergoing percutaneous coronary intervention with drug-eluting stents', *European Heart Journal*.

Santangeli, P., L. Di Biase, G. Pelargonio, J. D. Burkhardt, and A. Natale. 2011. 'The pharmaceutical pipeline for atrial fibrillation', *Ann Med*, 43: 13-32.

Sanz, Javier, and Zahi A. Fayad. 2008. 'Imaging of atherosclerotic cardiovascular disease', *Nature*, 451: 953-57.

Schlesinger, David, Stanley Benedict, Chris Diederich, Wladyslaw Gedroyc, Alexander Klibanov, and James Larner. 2013. 'MR-guided focused ultrasound surgery, present and future', *Medical Physics*, 40: 080901.

Schwartzman, D., J. J. Michele, C. T. Trankiem, and J. F. Ren. 2001. 'Electrogram-guided radiofrequency catheter ablation of atrial tissue comparison with thermometry-guide ablation: comparison with thermometry-guide ablation', *J Interv Card Electrophysiol*, 5: 253-66.

Sethuraman, S., S. R. Aglyamov, J. H. Amirian, R. W. Smalling, and S. Y. Emelianov. 2007. 'Intravascular photoacoustic imaging using an IVUS imaging catheter', *Ultrasonics, Ferroelectrics, and Frequency Control, IEEE Transactions on*, 54: 978-86.

Seungsoo, Kim, Chen Yun-sheng, G. P. Luke, and S. Y. Emelianov. 2014. 'In-vivo ultrasound and photoacoustic image- guided photothermal cancer therapy using silica-coated gold nanorods', *Ultrasonics, Ferroelectrics, and Frequency Control, IEEE Transactions on*, 61: 891-97.

Shah, D. 2011. 'A critical appraisal of cardiac ablation technology for catheter-based treatment of atrial fibrillation', *Expert Rev Med Devices*, 8: 49-55.

Shah, J., S. Park, S. Aglyamov, T. Larson, L. Ma, K. Sokolov, K. Johnston, T. Milner, and S. Y. Emelianov. 2008. 'Photoacoustic imaging and temperature measurement for photothermal cancer therapy', *J Biomed Opt*, 13: 034024.

Siphanto, Ronald I., Roy G. M. Kolkman, Arjan Huisjes, Magdalena C. Pilatou, Frits F. M. de Mul, Wiendelt Steenbergen, and Leon N. A. van Adrichem. 2004. 'Imaging of small vessels using photoacoustics: An in vivo study', *Lasers in surgery and medicine*, 35: 354-62.

Smith, Andrew M., Michael C. Mancini, and Shuming Nie. 2009. 'Bioimaging: Second window for in vivo imaging', *Nat Nano*, 4: 710-11.

Sousa, J. Eduardo, Marco A. Costa, E. Murat Tuzcu, Jay S. Yadav, and Stephen Ellis. 2005. 'New Frontiers in Interventional Cardiology', *Circulation*, 111: 671-81.

Stowers, Ryan S., Shane C. Allen, and Laura J. Suggs. 2015. 'Dynamic phototuning of 3D hydrogel stiffness', *Proceedings of the National Academy of Sciences*, 112: 1953-58.

Su, Jimmy Li-Shin, Bo Wang, and Stanislav Y. Emelianov. 2009. 'Photoacoustic imaging of coronary artery stents', *Optics express*, 17: 19894-901.

Sun, Yao, and Brian O'Neill. 2013. 'Imaging high-intensity focused ultrasound-induced tissue denaturation by multispectral photoacoustic method: an ex vivo study', *Applied optics*, 52: 1764-70.

Sutherland, Fiona J., and David J. Hearse. 2000. 'The isolated blood and perfusion fluid perfused heart', *Pharmacological Research*, 41: 613-27.

Swartling, J., S. Pålsson, P. Platonov, S. B. Olsson, and S. Andersson-Engels. 2003. 'Changes in tissue optical properties due to radio-frequency ablation of myocardium', *Medical & Biological Engineering & Computing*, 41: 403-09.

Szabo, Thomas L. 2004. *Diagnostic ultrasound imaging: inside out* (Academic Press).

Tam, A. C. 1986. 'APPLICATIONS OF PHOTOACOUSTIC SENSING TECHNIQUES', *Reviews of Modern Physics*, 58: 381-431.

Tanya, D. Khokhlova, M. Pelivanov Ivan, A. Sapozhnikov Oleg, S. Solomatin Vladimir, and A. Karabutov Aleksander. 2006. 'Opto-acoustic diagnostics of the thermal action of high-intensity focused ultrasound on biological tissues: the possibility of its applications and model experiments', *Quantum Electronics*, 36: 1097.

Tassa, Carlos, Stanley Y Shaw, and Ralph Weissleder. 2011. 'Dextran-coated iron oxide nanoparticles: a versatile platform for targeted molecular imaging, molecular diagnostics, and therapy', *Accounts of chemical research*, 44: 842-52.

Temma, Takashi, Satoru Onoe, Kengo Kanazaki, Masahiro Ono, and Hideo Saji. 2014. 'Preclinical evaluation of a novel cyanine dye for tumor imaging with in vivo photoacoustic imaging', *Journal of Biomedical Optics*, 19: 090501-01.

Thomsen, S. 1991. 'Pathologic analysis of photothermal and photomechanical effects of laser-tissue interactions', *Photochem Photobiol*, 53: 825-35.

Thomsen, Sharon L, Steven L Jacques, and Stephen T Flock. 1990. "Microscopic correlates of macroscopic optical property changes during thermal coagulation of myocardium." In *OE/LASE'90, 14-19 Jan., Los Angeles, CA*, 2-11. International Society for Optics and Photonics.

Tse, Hung-Fat, Sven Reek, Carl Timmermans, Kathy Lai-Fun Lee, J. Christoph Geller, Luz-Maria Rodriguez, Benoit Ghaye, Gregory M. Ayers, Harry J. G. M. Crijns, Helmut U. Klein, and Chu-Pak Lau. 2003. 'Pulmonary vein isolation using transvenous catheter cryoablation for treatment of atrial fibrillation without risk of pulmonary vein stenosis', *Journal of the American College of Cardiology*, 42: 752-58.

U.S. Food and Drug Administration, Center for Devices and Radiological Health. 2005. "InSightec ExAblate® System, Model 2000 premarket approval." In.

Vaezy, Shahram, Xuegong Shi, Roy W. Martin, Emil Chi, Peter I. Nelson, Michael R. Bailey, and Lawrence A. Crum. 2001. 'Real-time visualization of high-intensity focused ultrasound treatment using ultrasound imaging', *Ultrasound in Medicine & Biology*, 27: 33-42.

van Veen, R. L. P., Hjcm Sterenborg, A. Pifferi, A. Torricelli, E. Chikoidze, and R. Cubeddu. 2005. 'Determination of visible near-IR absorption coefficients of mammalian fat using time- and spatially resolved diffuse reflectance and transmission spectroscopy', *Journal of Biomedical Optics*, 10: 6.

VanderLaan, D., A. Karpiouk, D. Yeager, and S. Emelianov. 2014. "System and integrated catheter for real-time intravascular ultrasound and photoacoustic imaging." In *Ultrasonics Symposium (IUS), 2014 IEEE International*, 1591-94.

Viator, John A., Gigi Au, Guenther Paltauf, Steven L. Jacques, Scott A. Prahl, Hongwu Ren, Zhongping Chen, and J. Stuart Nelson. 2002. 'Clinical testing of a photoacoustic probe for port wine stain depth determination', *Lasers in surgery and medicine*, 30: 141-48.

Waller, Bruce F., Charles M. Orr, John D. Slack, Cass A. Pinkerton, James Van Tassel, and Thomas Peters. 1992. 'Anatomy, histology, and pathology of coronary arteries: A review relevant to new interventional and imaging techniques—Part I', *Clinical Cardiology*, 15: 451-57.

Wang, B., and S. Emelianov. 2011. 'Thermal intravascular photoacoustic imaging', *Biomed Opt Express*, 2: 3072-8.

Wang, B., A. Karpiouk, D. Yeager, J. Amirian, S. Litovsky, R. Smalling, and S. Emelianov. 2012a. 'Intravascular photoacoustic imaging of lipid in atherosclerotic plaques in the presence of luminal blood', *Opt Lett*, 37: 1244-6.

Wang, Bo, Andrei Karpiouk, Doug Yeager, James Amirian, Silvio Litovsky, Richard Smalling, and Stanislav Emelianov. 2012b. 'In vivo Intravascular Ultrasound-guided Photoacoustic Imaging of Lipid in Plaques Using an Animal Model of Atherosclerosis', *Ultrasound in Medicine & Biology*, 38: 2098-103.

Wang, Bo, Jimmy Su, Andrei Karpiouk, Doug Yeager, and Stanislav Emelianov. 2011. 'Intravascular Photoacoustic and Ultrasound Imaging: From Tissue Characterization to Molecular Imaging to Image-Guided Therapy.' in Jasjit S. Suri, Chirinjeev Kathuria and Filippo Molinari (eds.) (Springer New York).

Wang, Bo, Jimmy L. Su, James Amirian, Silvio H. Litovsky, Richard Smalling, and Stanislav Emelianov. 2010. 'Detection of lipid in atherosclerotic vessels using ultrasound-guided spectroscopic intravascular photoacoustic imaging', *Opt. Express*, 18: 4889-97.

Wang, Bo, Evgeniya Yantsen, Timothy Larson, Andrei B. Karpiouk, Shriram Sethuraman, Jimmy L. Su, Konstantin Sokolov, and Stanislav Y. Emelianov. 2009. 'Plasmonic Intravascular Photoacoustic Imaging for Detection of Macrophages in Atherosclerotic Plaques', *Nano Letters*, 9: 2212-17.

Wang, Li-Sheng, Min-Chieh Chuang, and Ja-an Annie Ho. 2012. 'Nanotheranostics–a review of recent publications', *International journal of nanomedicine*, 7: 4679.

Wang, Lihong, Steven L Jacques, and Liqiong Zheng. 1995. 'MCML—Monte Carlo modeling of light transport in multi-layered tissues', *Computer methods and programs in biomedicine*, 47: 131-46.

Wang, Lihong V. 2009. 'Multiscale photoacoustic microscopy and computed tomography', *Nature photonics*, 3: 503-09.

Wang, Lihong V, and Hsin-i Wu. 2007. *Biomedical optics: principles and imaging* (John Wiley & Sons).

Wang, Pu, Teng Ma, Mikhail N. Slipchenko, Shanshan Liang, Jie Hui, K. Kirk Shung, Sukesh Roy, Michael Sturek, Qifa Zhou, Zhongping Chen, and Ji-Xin Cheng. 2014. 'High-speed Intravascular Photoacoustic Imaging of Lipid-laden Atherosclerotic Plaque Enabled by a 2-kHz Barium Nitrite Raman Laser', *Scientific Reports*, 4: 6889.

Wang, X. D., Y. J. Pang, G. Ku, X. Y. Xie, G. Stoica, and L. H. V. Wang. 2003. 'Noninvasive laser-induced photoacoustic tomography for structural and functional in vivo imaging of the brain', *Nature Biotechnology*, 21: 803-06.

Wang, X. D., X. Y. Xie, G. N. Ku, and L. H. V. Wang. 2006. 'Noninvasive imaging of hemoglobin concentration and oxygenation in the rat brain using high-resolution photoacoustic tomography', *Journal of Biomedical Optics*, 11: 9.

Wang, Yi-Wei, Yu-Ying Fu, Qiaoli Peng, Shan-Shan Guo, Gang Liu, Juan Li, Huang-Hao Yang, and Guo-Nan Chen. 2013. 'Dye-enhanced graphene oxide for

photothermal therapy and photoacoustic imaging', *Journal of Materials Chemistry B*, 1: 5762-67.

Weight, Ryan M., John A. Viator, Paul S. Dale, Charles W. Caldwell, and Allison E. Lisle. 2006. 'Photoacoustic detection of metastatic melanoma cells in the human circulatory system', *Optics Letters*, 31: 2998-3000.

Welch, A. J., J. A. Pearce, K. R. Diller, G. Yoon, and W. F. Cheong. 1989. 'Heat Generation in Laser Irradiated Tissue', *Journal of Biomechanical Engineering*, 111: 62-68.

Wikipedia.com. 2015. 'List of laser sources', Wikipedia, The Free Encyclopedia., Accessed 28 September. https://en.wikipedia.org/w/index.php?title=List_of_laser_types&oldid=678949182.

Wikipedia.org. 2016. 'Cardiac action potential --- Wikipedia, The Free Encyclopedia', Accessed July 22. https://en.wikipedia.org/w/index.php?title=Cardiac_action_potential&oldid=722126209.

Wilensky, Robert L. 2013. 'In Search of the Elusive Vulnerable PlaqueReducing the Gap Between Coronary Imaging and Necropsy Findings∗∗', *Journal of the American College of Cardiology*, 61: 1052-53.

Wilson, B. C., and G. Adam. 1983. 'A Monte Carlo model for the absorption and flux distributions of light in tissue', *Medical Physics*, 10: 824-30.

Winfree, AT. 1994. 'Electrical turbulence in three-dimensional heart muscle', *Science*, 266: 1003-06.

Wolf, P. A., R. D. Abbott, and W. B. Kannel. 1991. 'Atrial fibrillation as an independent risk factor for stroke: the Framingham Study', *Stroke*, 22: 983-88.

Wolf, P. A., J. B. Mitchell, C. S. Baker, W. B. Kannel, and R. B. D'Agostino. 1998. 'Impact of atrial fibrillation on mortality, stroke, and medical costs', *Arch Intern Med*, 158: 229-34.

Wright, Matthew, Erik Harks, Szabolcs Deladi, Freek Suijver, Maya Barley, Anneke van Dusschoten, Steven Fokkenrood, Fei Zuo, Frédéric Sacher, Mélèze Hocini, Michel Haïssaguerre, and Pierre Jaïs. 2011. 'Real-time lesion assessment using a novel combined ultrasound and radiofrequency ablation catheter', *Heart Rhythm*, 8: 304-12.

Wu, Chun-Hsien, Jason Cook, Stanislav Emelianov, and Konstantin Sokolov. 2014. 'Multimodal magneto-plasmonic nanoclusters for biomedical applications', *Advanced Functional Materials*, 24: 6862-71.

Wu, Weitai, Ting Zhou, Alexandra Berliner, Probal Banerjee, and Shuiqin Zhou. 2010. 'Smart core− shell hybrid nanogels with Ag nanoparticle core for cancer cell

imaging and gel shell for pH-regulated drug delivery', *Chemistry of Materials*, 22: 1966-76.

Xiang, Liangzhong, Da Xing, Huaimin Gu, Diwu Yang, Lvming Zeng, and Sihua Yang. 2006. "Gold nanoshell-based photoacoustic imaging application in biomedicine." In *Biophotonics, Nanophotonics and Metamaterials, 2006. Metamaterials 2006. International Symposium on*, 76-79. IEEE.

Xu, Minghua, and Lihong V. Wang. 2006. 'Photoacoustic imaging in biomedicine', *Review of Scientific Instruments*, 77: 041101.

Yan, Yong-Bin, Qi Wang, Hua-Wei He, and Hai-Meng Zhou. 2004. 'Protein thermal aggregation involves distinct regions: sequential events in the heat-induced unfolding and aggregation of hemoglobin', *Biophysical Journal*, 86: 1682-90.

Yang, Hung-Wei, Hao-Li Liu, Meng-Lin Li, I. Wen Hsi, Chih-Tai Fan, Chiung-Yin Huang, Yu-Jen Lu, Mu-Yi Hua, Hsin-Yi Chou, Jiunn-Woei Liaw, Chen-Chi M. Ma, and Kuo-Chen Wei. 2013. 'Magnetic gold-nanorod/ PNIPAAmMA nanoparticles for dual magnetic resonance and photoacoustic imaging and targeted photothermal therapy', *Biomaterials*, 34: 5651-60.

Yao, Da-Kang, Chi Zhang, Konstantin Maslov, and Lihong V. Wang. 2014. 'Photoacoustic measurement of the Grüneisen parameter of tissue', *Journal of Biomedical Optics*, 19: 017007-07.

Yeager, Doug, Yun-Sheng Chen, Silvio Litovsky, and Stanislav Emelianov. 2014. 'Intravascular Photoacoustics for Image-Guidance and Temperature Monitoring During Plasmonic Photothermal Therapy of Atherosclerotic Plaques: A Feasibility Study', *Theranostics*, 4: 36-46.

Yeager, Doug, Andrei Karpiouk, Bo Wang, James Amirian, Konstantin Sokolov, Richard Smalling, and Stanislav Emelianov. 2012. 'Intravascular photoacoustic imaging of exogenously labeled atherosclerotic plaque through luminal blood', *Journal of Biomedical Optics*, 17: 106016-16.

Yoon, Soon Joon, Avinash Murthy, Keith P Johnston, Konstantin V Sokolov, and Stanislav Y Emelianov. 2012. 'Thermal stability of biodegradable plasmonic nanoclusters in photoacoustic imaging', *Optics express*, 20: 29479-87.

Zamora-Rojas, Eduardo, Ben Aernouts, Ana Garrido-Varo, Dolores Pérez-Marín, José Emilio Guerrero-Ginel, and Wouter Saeys. 2013. 'Double integrating sphere measurements for estimating optical properties of pig subcutaneous adipose tissue', *Innovative Food Science & Emerging Technologies*, 19: 218-26.

Zerda, Adam de la, Zhuang Liu, Sunil Bodapati, Robert Teed, Srikant Vaithilingam, Butrus T Khuri-Yakub, Xiaoyuan Chen, Hongjie Dai, and Sanjiv Sam Gambhir. 2010. 'Ultrahigh sensitivity carbon nanotube agents for photoacoustic molecular imaging in living mice', *Nano Letters*, 10: 2168-72.

Zhang, E. Z., J. G. Laufer, R. B. Pedley, and P. C. Beard. 2009. 'In vivo high-resolution 3D photoacoustic imaging of superficial vascular anatomy', *Physics in Medicine and Biology*, 54: 1035.

Zhao, Xue-qin, Tian-xiao Wang, Wen Liu, Cai-ding Wang, Dong Wang, Ting Shang, Li-hua Shen, and Lei Ren. 2011. 'Multifunctional Au@ IPN-pNIPAAm nanogels for cancer cell imaging and combined chemo-photothermal treatment', *Journal of Materials Chemistry*, 21: 7240-47.